THE UNIVERSITY OF ASTON IN BIRMINGHAM

"A study of the elastic scattering of fast neutrons by potassium and lithium"

Thesis submitted for the degree of Doctor of Philosophy

by

David Holland

Department of Physics

September, 1974.

SUMMARY

The elastic scattering of fast neutrons by ^{39}K and ^{7}Li has been studied at an incident neutron energy of 14.1 MeV, using a neutron spectrometer employing the associated particle time of flight technique. The source neutrons were produced by the $^{3}H(d,n)^{4}He$ reaction at an incident deuteron energy of 120 KeV. The time of origin of the source neutron is determined by detecting the associated helium particle, and the neutron energy is determined by measuring electronically its flight time over a fixed flight path.

Differential elastic scattering cross section measurements were made on ^{39}K in order to obtain better agreement between optical model predictions and experiment than the one previous measurement by Frasca et al. Improved agreement between theory and experiment was obtained, following the suggestion of Cassola and Koshel that a derivative surface absorption term should be used for potassium. Differential elastic scattering cross section measurements were also made on ^{7}Li in order to investigate the discrepancies in the previous measurements by Armstrong et al, using nuclear emulsions, and Wong et al, using the pulsed beam method, and to investigate the validity of the optical model for light nuclei. A comparison of the angular distributions obtained for both elements was made with the predictions of the nuclear optical model.

Finally, in parallel with the work at 14.1 MeV, an associated particle time of flight spectrometer was developed for use with the $^{2}H(d,n)^{3}He$ reaction, to enable neutron differential scattering cross section measurements to be made at an incident neutron energy of 2.5 MeV, this being suitable for experiments related to reactor design.

ACKNOWLEDGEMENTS

I am very much indebted to my supervisor, Dr. A.J. Cox, for his continued guidance and encouragement throughout the research project and I thank Professor S.E. Hunt, Head of the Department of Physics, for his interest throughout the work.

I wish to acknowledge the staff of the Nuclear Physics Group for many useful discussions; Dr. J.A. Archer-Hall for help with the construction of the samples, and the technical staff of the laboratory and workshop for their help.

I thank the Science Research Council for the three year grant which enabled the research to be carried out.

Finally, I would like to thank Rhoda Finch for typing the thesis.

CONTENTS

CHAPTER 1

Introduction

1.1 Introduction

The interaction between one nucleon and a nucleus is clearly of central importance in the studies of nuclear structure and reactions. For nuclear structure it is the potential of the shell model that explains the specific features, while for nuclear reactions it is the interaction between an incident nucleon and a target nucleus that determines how the nucleon is scattered by the nucleus. There are two ways of determining the nucleon-nucleus potential; by deduction from the nucleon-nucleon potential or by induction from experimental data. It is found that individually these methods are inadequate, but taken together they are able to give a good representation of the interaction. This is indicated schematically in figure 1.1.,

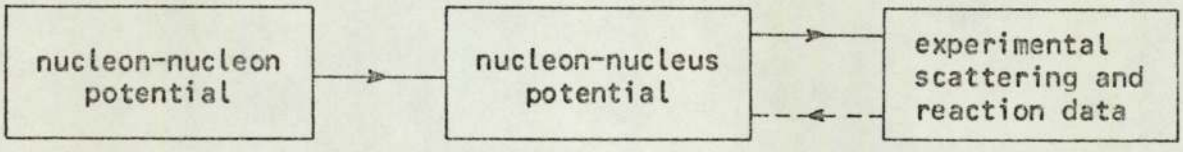

Figure 1.1

where the solid arrows indicate deduction and the dotted arrow induction.

The treatment of even the simplest process of elastic scattering is very complicated. The incident particle interacts with each nucleon in the target nucleus, and a complete treatment of the interaction between just two nucleons is exceedingly difficult. The determination of the nucleon-nucleus potential from experimental data is subject to another type of difficulty. If a one body potential is assumed, the expected scattering cross sections can be calculated, and the parameters of the assumed potential may be adjusted to optimise the fit to the

experimental data. It is found, however, that many potentials can be made to fit the data in this way, and there is no experimental method of distinguishing between them. These two methods can be combined to describe the interaction; the deduction method giving the over-all shape of the potential and the analysis of experimental data the numerical parameters.

The simplest model of the nucleon-nucleus interaction replaces the nucleus by a real potential well specified by a radius and a depth. The consequences of such a model were studied by Bethe[1], and it was found that the predicted non-elastic cross sections and the change of cross sections with energy, were not in accord with experiment. The model was superseded by the compound nucleus model of Bohr[2], which accounted successfully for the observed non-elastic cross sections, but was inadequate to explain the forward peaking shown by elastic scattering at higher energies. It was later found by Le Levier and Saxon[3], and Feshbach et al[4], that the old potential with the addition of an imaginary component, was able to give a good account of the data at energies greater than 10 MeV. Physically, this is equivalent to treating the nucleus as if it were made of a material of complex refractive index, so that it both absorbs and refracts the incident waves.

1.2 Elastic Scattering and the Optical Model

At energies greater than approximately 10 MeV it is found that some nuclear reactions can take place immediately, without passing through the compound nucleus stage: these are known as direct reactions[5]. More precisely a direct reaction may be defined as one that passes at once from the initial to the final stage, without any intermediate compound nucleus stage.

In the initial stage the incident particle interacts with the target nucleus by means of an average nuclear potential. While it is under the influence of this average potential, the incident

particle will either be elastically scattered or it will be absorbed by the target nucleus. If the former process occurs, i.e., a direct reaction, it is referred to as "shape elastic" or "potential" scattering. If the particle is absorbed by the target nucleus a number of possibilities must be considered. For example, the absorbed particle may collide with a nucleon in the target causing the struck nucleon to be raised to an excited state and the absorbed particle to be emitted from the nucleus via the appropriate inelastic channel, or the particle may undergo multiple inelastic collisions before being emitted. Another possibility also exists. The absorbed particle and the target nucleus may coalesce to form a compound nucleus[2]. At energies less than 6 MeV the number of exit channels which are available for the decay of the compound nucleus is quite small, and there is a high probability that the decay will take place through the entrance channel. This type of elastic scattering is referred to as "compound elastic" scattering. At higher energies more inelastic modes of decay become available and it is then more probable for the system to decay by some inelastic process[5][6]. The final stage of the nuclear reaction consists of the separation of the reaction products. Here, as in the initial stage, the interaction between the particles can be described in terms of an average potential.

The new model thus occupies an intermediate position between the shell model with its weak absorption, and the compound nucleus model with its strong absorption. This model is called the Optical Model and was first proposed by Fernbach et al[7]. The nuclear potential is expressed as a complex interaction potential, both the real and imaginary parts being responsible for elastic scattering, assumed direct, and the imaginary part for absorption leading to reactions and inelastic scattering. Therefore, it is not possible to treat elastic scattering on its own without considering the accompanying absorption process. However, to a good approximation

they can all be considered together and treated just as a process which removes particles from the incident beam.

Neutron Elastic Scattering

Neutron elastic scattering has become interesting because of the success of the optical model which gives good agreement with experiment. In the last decade a large number of measurements of cross sections for elastic scattering of neutrons have been published, and in view of the quantity of experimental data available it was considered beyond the scope of this work to present a detailed review for the entire range of elements.

For comparison with the optical model, neutron experiment are preferable because there is no Coulomb interaction with the nucleus. Neutron elastic scattering data can be interpreted successfully using the optical model with a complex potential of the form:

$$U_{OPT}(r) = U_R(r) + iU_I(r) + U_{SO}(r) \qquad \ldots\ldots\ldots \quad 1.1$$

where $U_R(r)$ and $U_I(r)$ are the real and imaginary parts respectively, and $U_{SO}(r)$ represents the spin orbit potential. The most widely adopted form for the real potential is that of the Woods-Saxon well, i.e.,

$$U_R(r) = - V_R \left\{ 1 + \exp\left(\frac{r - R}{a} \right) \right\}^{-1} \qquad \ldots\ldots\ldots \quad 1.2$$

The radius R is similar to the nuclear radius, and it is usual to write $R = r_o A^{-1/3}$, where $r_o \sim 1.3$ fm. The parameter 'a' is a measure of the rapidity of fall-off of the potential, or of its surface diffuseness, 'a' $\sim$ 0.6 fm. The imaginary potential may take a number of different forms, Woods-Saxon for volume absorption, derivative Woods-Saxon or Gaussian for surface absorption being the most widely

adopted forms. Detailed comparison with experimental data enables the parameters of these potentials to be more precisely determined.

If the shape elastic cross section is denoted by σ_{SE}, the total absorption cross section by σ_A, and the total cross section for all processes by σ_T, then:

$$\sigma_T = \sigma_{SE} + \sigma_A \quad \ldots\ldots\ldots 1.3$$

However, $$\sigma_A = \sigma_{CE} + \sigma_R \quad \ldots\ldots\ldots 1.4$$

and $$\sigma_E = \sigma_{CE} + \sigma_{SE} \quad \ldots\ldots\ldots 1.5$$

where σ_R is the reaction cross section, i.e., that part of the total absorption cross section which leads tononelastic processes, σ_{CE} is the compound elastic cross section, and σ_E is the total elastic cross section.

For incident neutron energies above 10 MeV compound elastic scattering is negligible. Hence, equations 1.3, 1.4 and 1.5 give:

$$\sigma_T = \sigma_{SE} + \sigma_R = \sigma_E + \sigma_R \quad \ldots\ldots\ldots 1.6$$

The optical model enables the quantities in equation 1.6 to be calculated, as well as the differential cross section $\sigma(\theta)$.

1.3 The Research Programme

The principal aim of the present work was to study neutron elastic scattering at an incident neutron energy of 14 MeV. The data on angular distributions from elastic scattering of 14 MeV neutrons is as yet available for a limited number of nuclei only, and there is a need for accurate differential cross section measurements,

especially on separated isotopes, in order to reduce ambiguities in optical model parameters. At this energy theoretical considerations assume that processes involving compound nucleus formation can be neglected. Differential cross section measurements were made employing the widely used associated particle time of flight technique, and the 14 MeV neutrons produced in the $^{3}H(d,n)^{4}He$ reaction.

In the literature search undertaken at the beginning of the research programme, it was apparent that the optical model has been more successful for neutron differential elastic scattering cross section measurements for heavy and medium weight nuclei than for light nuclei, as the former more nearly approach the limit of uniform nuclear matter.

The elements chosen for study were Potassium and Lithium. They were chosen for a number of reasons. Separated isotopes are extremely expensive but the common isotope of each of these elements namely, ^{39}K and ^{7}Li, have isotopic abundances of 93%. Potassium and lithium are also of enormous practical importance with regard to reactor physics calculations, i.e., in the use of sodium-potassium alloy as a coolant in fast reactors; and the use of lithium as the breeder blanket in a fusion reactor.

Differential elastic scattering cross section measurements for potassium at 14 MeV have been reported only by Frasca et al[8]. This work also included measurements on calcium, boron and carbon. The results for these other three elements are in good agreement with those obtained by other workers[9,10,11,12]. It was found, however, that the optical model with gaussian surface absorption was unable to provide equally good fits for the potassium and calcium angular distributions. This was a surprising result in so far as potassium is adjacent to calcium in the periodic table. In an attempt to improve the agreement between theory and experiment, it has been

suggested by Cassola and Koshel[13] that a derivative surface absorption term should be used in place of the gaussian absorption.

A number of differential elastic scattering cross section measurements have been reported for light nuclei ($A < 15$), and have been successfully interpreted in terms of the optical model. Good examples are the measurements of Nakada et al[14] on beryllium and carbon, Bouchez et al[12] on carbon, the boron data of Tesch[11], and the nitrogen and oxygen data of Bauer et al[15]. Differential elastic scattering cross section measurements have been reported for lithium by Armstrong et al[16], and Wong et al[17]. The results obtained by the two groups differ somewhat, as is shown in figure 1.2. The data of Armstrong et al[16] was not in very good agreement with optical model predictions; the data of Wong et al[17] was not analysed in terms of the model.

The aim of the research programme was to investigate the discrepancies discussed for both potassium and lithium, and in the case of lithium to add to the existing data on light nuclei, in order to try and extend the validity of the optical model for light nuclei. A comparison of the angular distributions obtained was made with the theoretical predictions. To make this comparison the computer programme RAROMP[18] was used.

The literature search also revealed an absence of elastic scattering data around incident neutron energies of 2.5 MeV. At this energy compound elastic scattering becomes significant and any experimental measurements would have to be corrected accordingly. A well known source of 2.5 MeV neutrons is the $^{2}H(d,n)^{3}He$ reaction. A major reason the associated particle technique has not been exploited with the $^{2}H(d,n)^{3}He$ reaction until recently, was the difficulty of performing accurate spectrometry on the recoil nuclei. This difficulty has been removed by the rapid development of semi-conductor detectors.

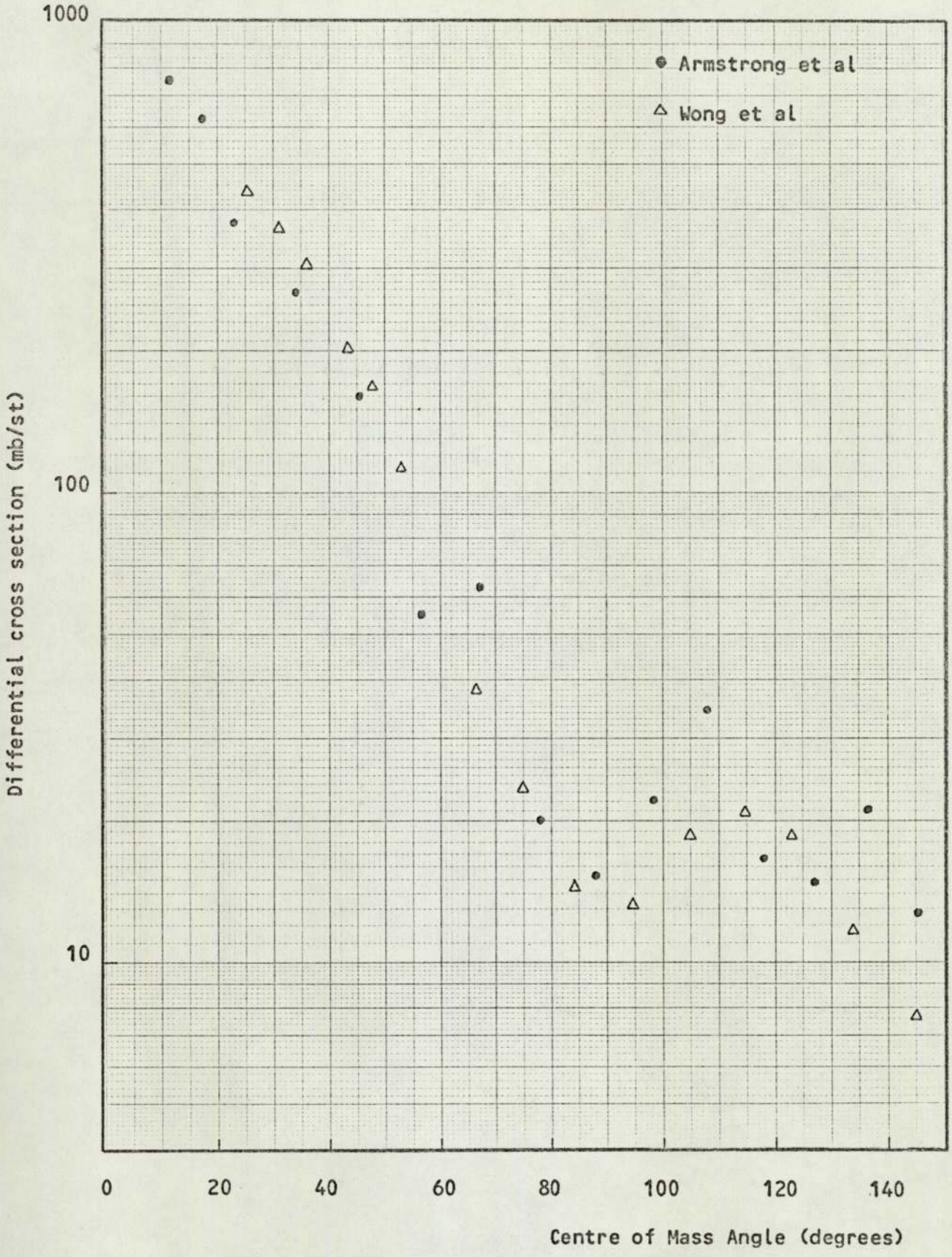

Figure 1.2. Previous measurements of the differential elastic scattering cross section from ^{7}Li at 14.1 MeV.

Therefore, in parallel with the work at 14 MeV, an associated particle time of flight system was developed to enable neutron differential elastic scattering cross section measurements to be made at an incident neutron energy of 2.5 MeV.

1.4 Scattering Geometries

In the measurement of neutron differential cross sections the placement and shape of the source, scattering material, detector, and shield are usually chosen as a compromise between the need for a good signal to background ratio and the need to reduce the magnitude of the corrections which must be made to the data. The three most commonly used arrangements, the ring geometry, cylindrical geometry, and flat plate geometry are indicated in figures 1.3(a), 1.3(b) and 1.3(c).

Ring Geometry

In the ring geometry as shown in figure 1.3(a), a ring of the scattering material is placed with its axis on the line passing through the centre of both the source and detector, and a shadow shield of some form is used to attenuate the direct beam. Scattering at various angles is measured by moving either the scatterer or detector along the axis, or by using rings with different diameters. The principal advantage of this geometry is that, for a given angular resolution and thickness of scatterer, more material can be used and hence a greater scattered intensity can be obtained than with any other arrangement.

There are several disadvantages of ring geometry. Since the distances between the source, scatterer, and detector change with scattering angle, these distances must be determined separately for each angle, necessitating a recalibration of the spectrometer in each case, and due to the compactness of the system the angular resolution is poor. Also, the angular range over which measurements can be made is limited.

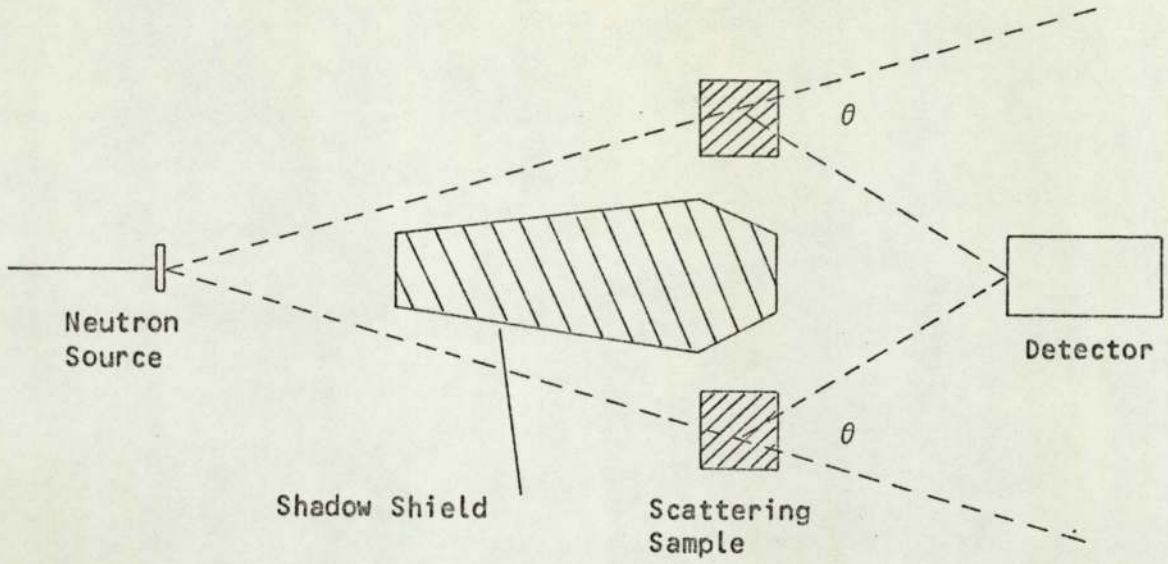

Figure 1.3(a). Ring Geometry.

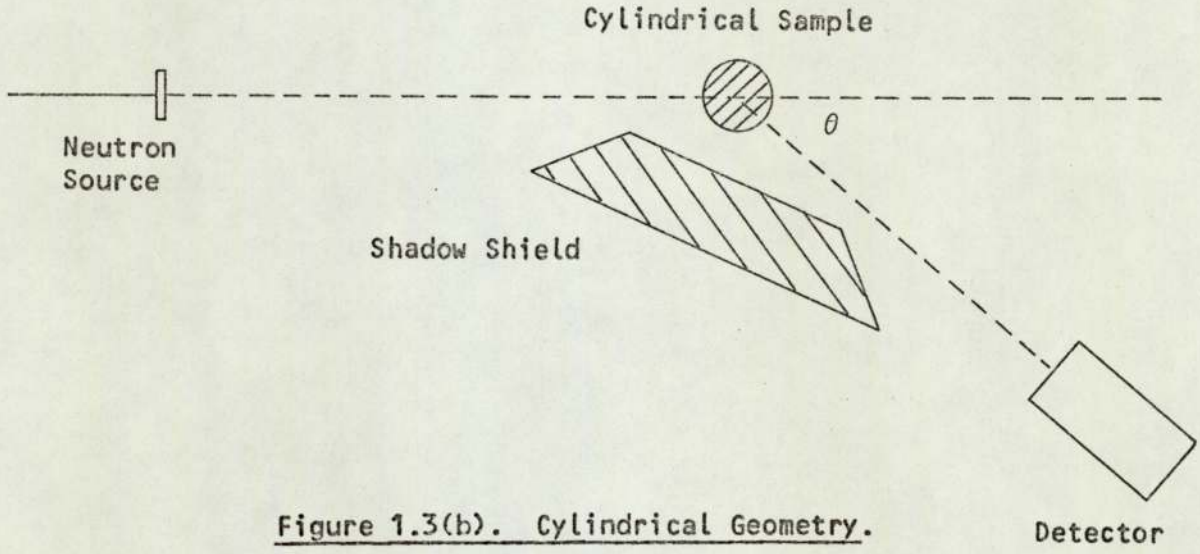

Figure 1.3(b). Cylindrical Geometry.

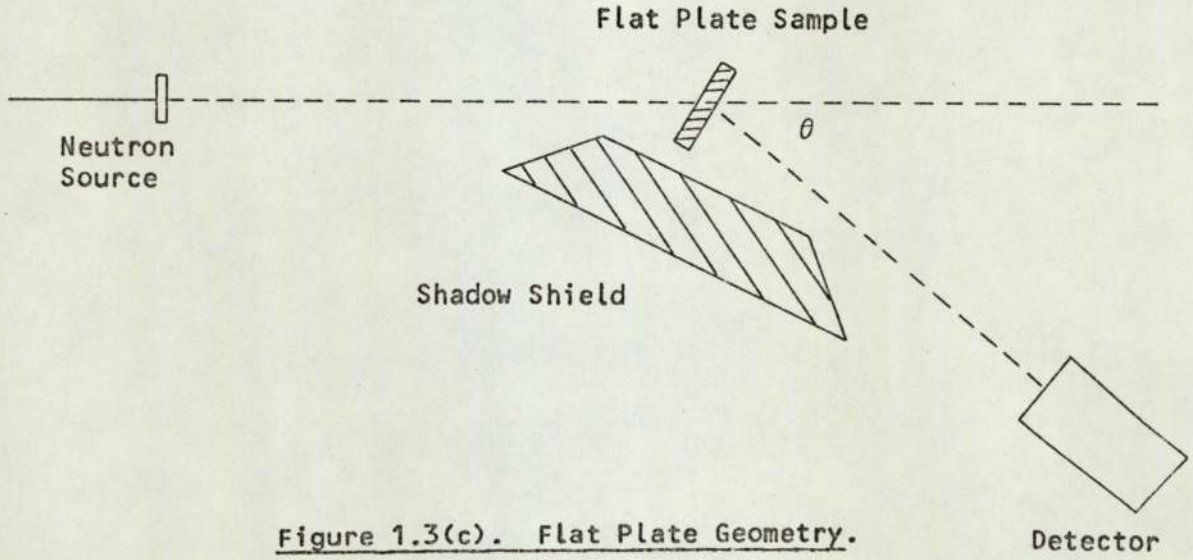

Figure 1.3(c). Flat Plate Geometry.

Cylindrical and Flat Plate Geometry

These two sample geometries can be used with the associated particle time of flight technique. With cylindrical geometry the sample is made in the form of a cylinder or sphere as shown in figure 1.3(b); and with flat plate geometry the sample is in the form of a thin rectangular slab of material, figure 1.3(c). Shielding is usually in the form of a shadow bar and collimator around the detector, and the detector is rotated about the scattering sample to obtain the angular distribution. Good angular resolution is obtained by using small scattering samples positioned between 100 mm to 300 mm from the source. The resolution is defined by the angle subtended at the source by the sample as the detector is considerably further away from the sample.

Flat plate geometry is generally used to reduce multiple scattering contributions while maintaining an adequate signal to background ratio, and has several advantages for use with the associated particle technique. The scattering sample can be made to completely subtend the neutron beam defined by the associated alpha particles. This can be done easily with a flat plate sample but not always with a cylindrical sample. Also, when using flat plate geometry if the sample is made slightly wider than the defined neutron beam, then a small error in the positioning of the sample does not alter the effective sample thickness compared with the use of a cylindrical sample, where an error in positioning the sample alters the effective thickness.

In view of these advantages flat plate geometry was used in the present work.

CHAPTER 2

Neutron Detection and Shielding

2.1 Neutron Detection

The detection of neutrons is a much more complex problem than the detection of charged particles, because neutrons do not carry any electric charge and cause no direct ionization. The neutron interacts with the nucleus and observation of the interaction products provides a means of detection. The detection or measurement technique depends on the neutron energy range.

Neutrons interact with nuclei by scattering or absorption. In the former, the neutron collides with a nucleus, and a fraction of the neutron energy is transferred to the recoil nucleus. In the latter the neutron is absorbed by the nucleus. The most important scattering process for fast neutrons is the elastic scattering by protons, i.e., the $^{1}H(n,n)^{1}H$ reaction. Neutrons are elastically scattered by all nuclei, but the energy transfer to the recoil nucleus is a maximum for neutron-proton scattering, and this process is most widely used for detection of fast neutrons.

Organic scintillators are efficient detectors of fast neutrons because of their high hydrogen content and the relatively large cross section for neutron-proton elastic scattering. This class of scintillator includes plastics, organic liquids and organic crystals such as anthracene or stilbene. Elastic scattering by hydrogen is isotropic in the centre of mass system for neutron energies up to 20 MeV, hence, the spectrum of recoil protons from monoenergetic neutrons of energy E_o is a continuous distribution in energy from zero to E_o. Neglecting other effects, the pulse height spectrum from monoenergetic neutrons on an organic scintillator consists of a flat distribution of pulses up to the pulse height corresponding to E_o,

at which point it drops to zero.

In practice, the drop to zero is not perfectly sharp due to a number of effects including the resolution of the scintillation counter and the non linear response of organic scintillators to protons. These effects are discussed in section 2.3

2.2 Plastic Scintillator NE 102A

The scintillator used in the series of experiments undertaken was a plastic scintillator type NE 102A, manufactured by Nuclear Enterprises Ltd. It has an excellent combination of properties: high light output, good light transmission, fast response and decay times ($\sim 10^{-9}$ secs)[19] all of which are desirable features for high speed time of flight experiments. For neutrons incident on a thin plastic scintillator, single elastic neutron-proton scattering is the most probable reaction. If the scintillator thickness is increased to obtain higher detection efficiency, double and multiple scattering can occur within the scintillator and also the increased thickness introduces a timing uncertainty due to the variation in flight times to different detection points within the scintillator. Allowing for a timing uncertainty of 1 ns for 14.1 MeV neutrons required the use of a scintillator 50.8 mm thick. Using this same scintillator for 2.5 MeV neutrons incurred a timing uncertainty of 2.2 ns.

Before the measurement of scattering cross sections could be made it was necessary to calculate, and check by experimental measurement the efficiency of the scintillator as a function of neutron energy. The experimental measurements are discussed in section 5.5

2.3 Scintillator Efficiency

The efficiency of an organic scintillator is conveniently defined as the ratio of the number of recoil protons to the number of incident neutrons[20]. The efficiency of a scintillator consisting

entirely of carbon and hydrogen can be calculated under the assumption that only single scattering occurs. The number of recoil protons produced in a scintillator of length L, exposed to a flux of N_o neutrons all of energy E_o is:

$$N_1(E_o,L) = N_o n_H \sigma_H L \{ [1 - \exp(-aL)]/aL \} \quad \ldots\ldots \quad 2.1$$

where n_H = number of hydrogen atoms per cm^3 of scintillator, 5.25×10^{22}
σ_H = neutron-proton scattering cross section at neutron energy E_o;
and

$$a = n_H \sigma_H + n_c \sigma_c$$

where n_c = number of carbon atoms per cm^3 of scintillator, 4.75×10^{22}; and σ_c = neutron-carbon cross section at neutron energy E_o. The efficiency for single scattering is then:

$$\epsilon_1(E_o,L) = N_1(E_o,L)/N_o = n_H \sigma_H L f(aL) \quad \ldots\ldots \quad 2.2$$

with $$f(aL) = [1 - \exp(-aL)]/aL \quad \ldots\ldots \quad 2.3$$

the factor f(aL) allows for attenuation of the neutron beam in passing through the scintillator.

The efficiency curve obtained by applying equation 2.2 to a 50.8 mm thick NE 102A scintillator is shown in figure 2.1. Unfortunately, it is found that organic scintillators are also efficient as detectors of low energy background neutrons and γ rays. Therefore, some form of discrimination was necessary to remove these background effects. The factors which modify the scintillator efficiency are found by considering the energy distribution of the recoil protons and the non-linear response of NE 102A scintillator exposed to fast neutrons.

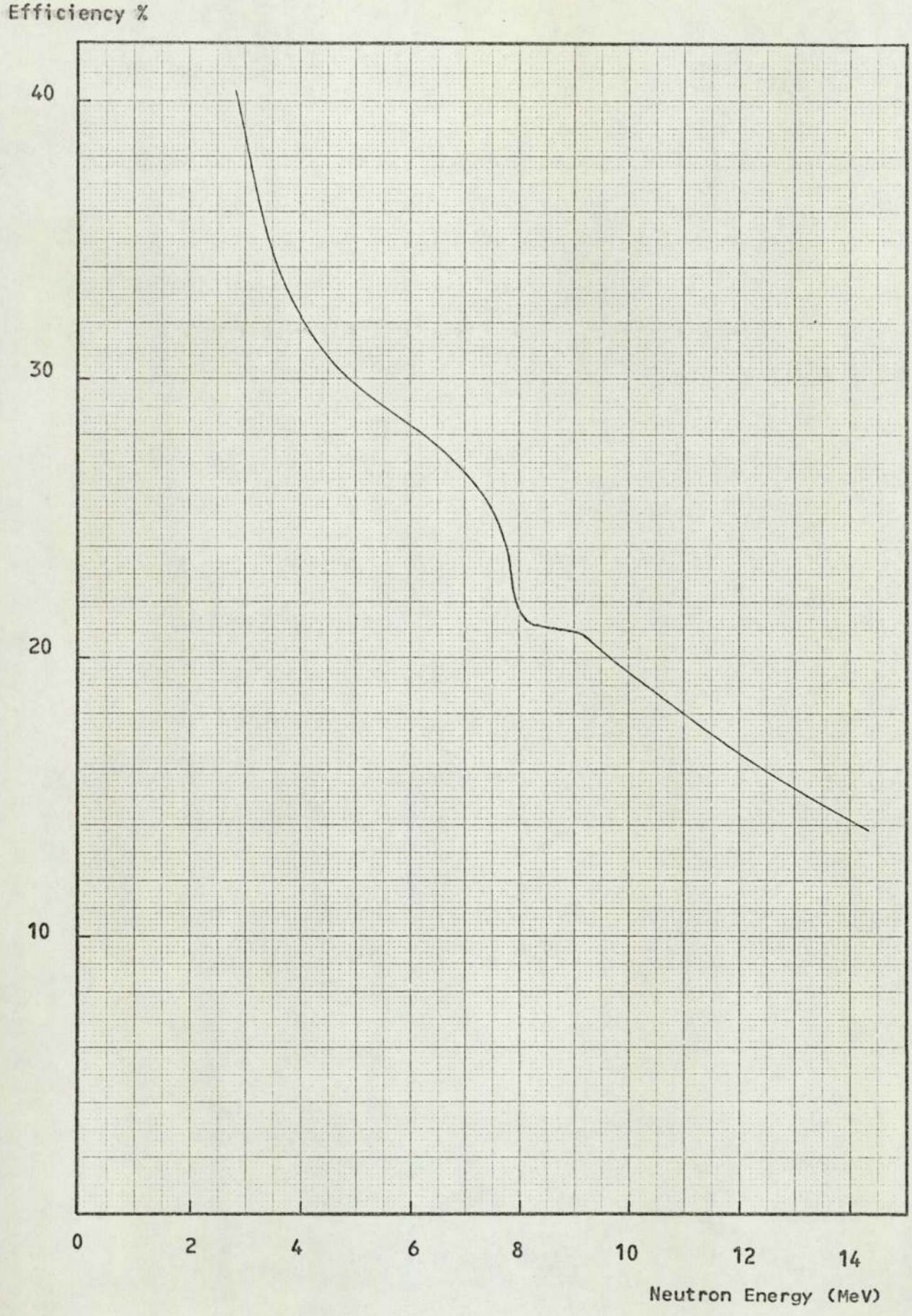

Figure 2.1. Calculated efficiency of a 50.8 mm NE 102A scintillator.

Energy Spectrum of Recoil Protons

Consider the elastic scattering of a neutron, mass unity, initial energy E_n, by a nucleus of mass A, initially at rest in the laboratory system. From the kinematics of the collision it can be shown that the energy of the recoil nucleus E_r is given by:

$$E_r = \frac{4AE_n}{(A+1)^2}\cos^2\alpha = \frac{2AE_n}{(A+1)^2}(1+\cos\beta) \quad \ldots 2.4$$

where α and β are the angles of recoil in the laboratory and centre of mass systems respectively ($\beta = 2\alpha$). E_r is a maximum for a head on collision ($\alpha = \beta = 0$) when the recoil nucleus receives energy:

$$E_{max} = \frac{4A}{(A+1)^2}E_n \quad \ldots 2.5$$

Thus for a proton (A = 1) the entire neutron energy is transferred ($E_{max} = E_n$) in a head on collision, while for a carbon nucleus (A = 12) $E_{max} \sim 0.3\ E_n$. For neutron-proton scattering, equation 2.4 takes the simple form:

$$E_p = E_n\cos^2\alpha \quad \ldots 2.6$$

Barshall and Kanner[21] have shown that the energy distribution of recoil protons in the laboratory system is the same as the angular distribution of neutrons scattered in the centre of mass system. For neutron-proton collisions below E_n = 20 MeV, it has been found experimentally that the scattering is isotropic in the centre of mass system[22]. Hence the energy distribution of recoil protons is uniform from $E_p = 0$ to $E_p = E_n$ as shown in figure 2.2.

Non-Linear Response of NE 102A Scintillator

The quantity directly recorded in the scintillation method is the pulse-height spectrum. Under appropriate conditions, the

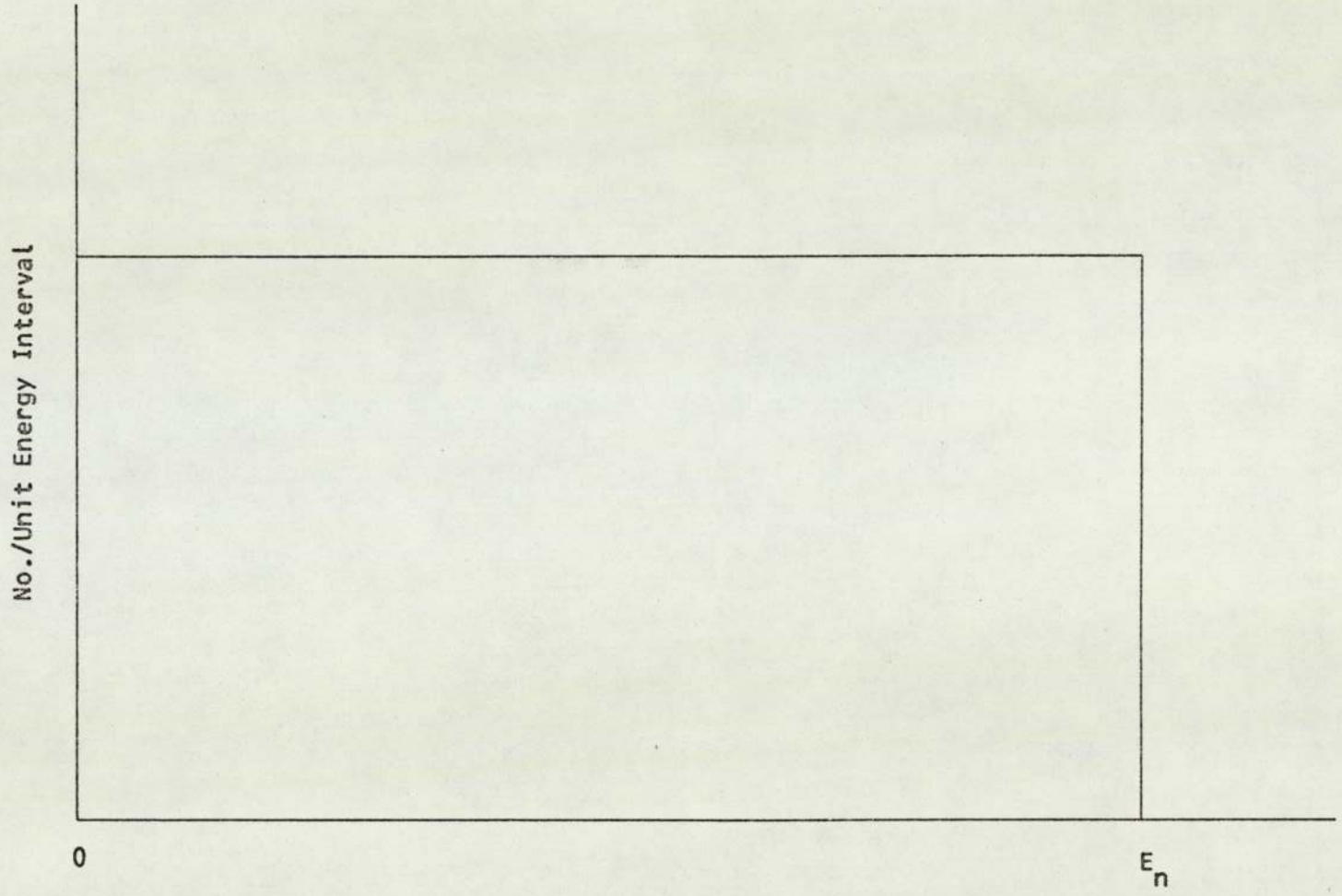

Figure 2.2. Energy spectrum of recoil protons produced by mono-energetic neutrons of energy E_o in an organic scintillator.

photomultiplier output is directly proportional to the luminous output of the scintillator. The scintillator response for charged particles is well represented by the semi-theoretical formula of Birks[23]:

$$\frac{dS}{dr} = \frac{A\ dE/dr}{1 + kB\ dE/dr} \qquad \ldots\ldots \quad 2.7$$

where S = luminous output of the scintillator; r = path length of the particle in the scintillator; E = particle energy; and A and kB are constants for a given scintillator.

To avoid dependence on specific units for the measurement of S, it is convenient to represent the scintillator output by the variable P = S/A, so that equation 2.7 can be re-written in terms of dP/dE, i.e;

$$\frac{dP}{dE} = A^{-1}\frac{dS}{dE} = (1 + kB\ dE/dr)^{-1} \qquad \ldots\ldots\ldots \quad 2.8$$

where P and E now have the same units.

For electrons with energies up to 2 MeV, dE/dr is very small so that kB dE/dr can be neglected, then

$$\frac{dP}{dE} = 1 \qquad \text{i.e. } P = E_e \qquad \ldots\ldots\ldots \quad 2.9$$

where E_e is the electron energy. For protons with energies greater than 2 MeV, however, dE/dr cannot be neglected. Evans and Bellamy[24] have shown that for NE 102A, taking the range-energy relationship of protons in the plastic as that for CH, given by the tables of Rich and Madey[25], the most consistent results are obtained with the value: $kB = 1.0 \times 10^{-2}$ g cm^{-2} MeV^{-1}. With the value of kB known, numerical integration of equation 2.8 gives the pulse height for a given proton

energy E_p. Using the value of kB given overleaf, table 2.1 lists dP/dE and pulse height P as a function of proton energy for NE 102A scintillator; also the range-energy relationship for protons in CH.

If the number of recoil protons with energies between E and E + dE is written as dN = N(E)dE, and the number with pulse height between P and P + dP as dN = N(P)dP; then since the total area under the two curves must be the same, the two spectra are related by:

$$N(E) = N(P) \frac{dP}{dE} \qquad \ldots\ldots\ldots \quad 2.10$$

Using equation 2.10 and the proton pulse height data of table 2.1, figure 2.3 shows the distortion of the pulse height spectrum by the non linear response of plastic scintillator NE 102A for neutrons of 14.1 MeV.

Double Scattering

In the discussion so far, it has been assumed that only single scattering events occur within the scintillator. Recoil protons can also be produced by neutrons which have already been scattered one or more times, by carbon or by hydrogen. The corrections for multiple scattering are difficult to calculate accurately. However, it is possible to estimate the effects of second scattering events on the efficiency of the scintillator.

Some of the neutrons scattered by collisions with carbon nuclei produce recoil protons in a second scattering event. The number of neutrons scattered once by carbon in a scintillator of length L is given by:

$$N_C(E_o, L) = N_o n_C \sigma_C L f(aL) \qquad \ldots\ldots\ldots \quad 2.11$$

where the terms are as defined for equation 2.1. To estimate the

Table 2.1

Response of Plastic Scintillator NE 102A to Protons

Proton Energy E_p (MeV)	dE/dr MeV/g.cm^{-2}	dP/dE	Pulse Height P(MeV)
15	33.50	0.749	8.58
14	-	0.739*	7.84
13	-	0.725*	7.10
12	40.24	0.713	6.37
11	-	0.695*	5.68
10	46.72	0.682	5.01
9	50.93	0.663	4.32
8	56.06	0.641	3.67
7	62.49	0.615	3.03
6	70.80	0.585	2.44
5	82.00	0.549	1.80
4	98.02	0.505	1.35
3	123.10	0.448	0.87
2	168.60	0.372	0.46
1	276.30	0.266	0.16

*Interpolated Values

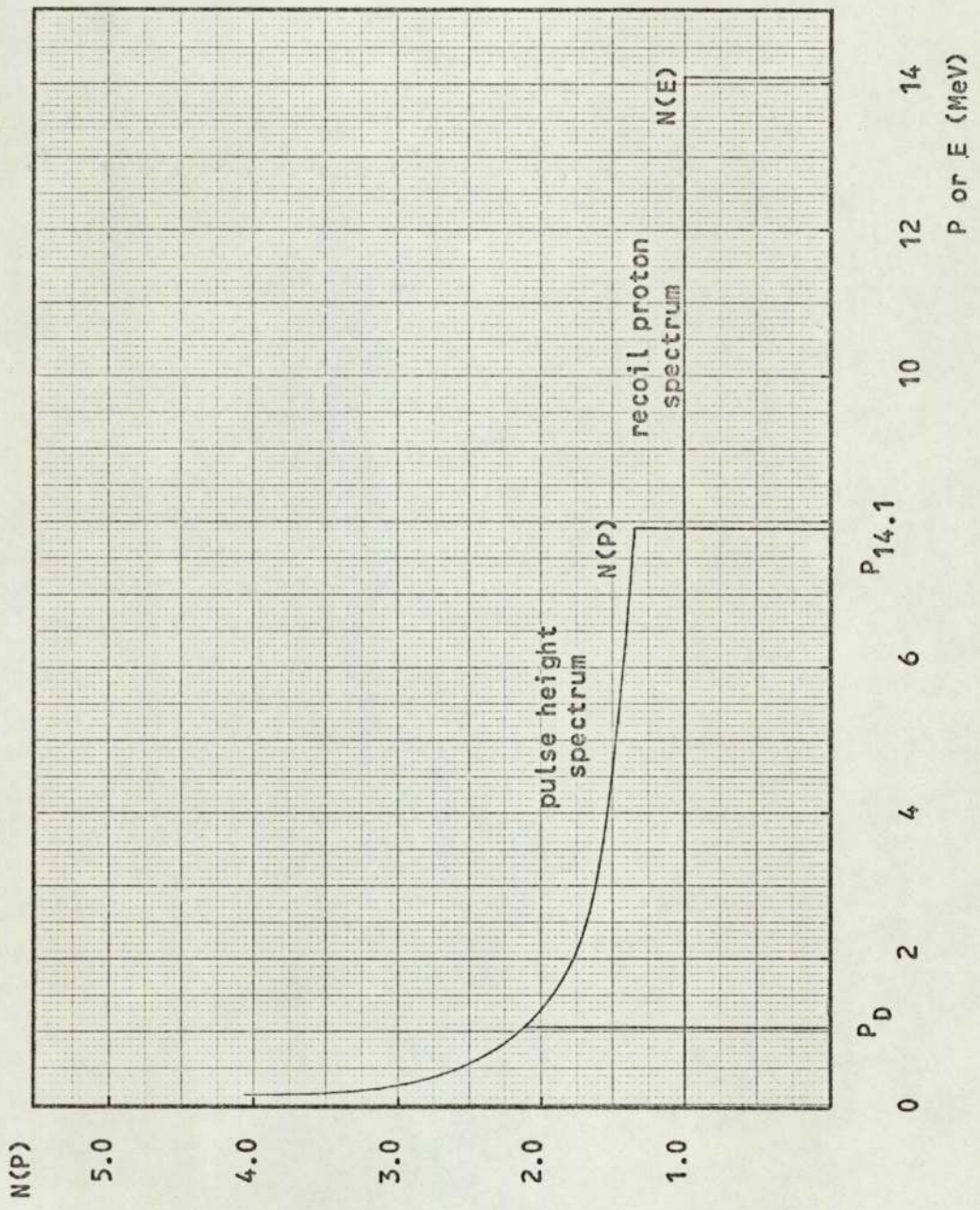

Figure 2.3. Distortion of the Pulse Height Spectrum by the non-linear response of plastic scintillator NE 102A.

number of recoil protons produced by second scattering events, the energy of these neutrons is represented by its average value, which is about 0.85 E_o. It is then assumed that the neutrons traverse an average path length L_1 in the scintillator. As there is very little attenuation of the neutron beam in passing through the scintillator, a very good approximation to L_1 is obtained by taking this average path length to be half the thickness of the scintillator i.e., 25.4 mm. The number of recoil protons produced in this process is then given by:

$$N_{2C}(E_o, L, L_1) = N_C n_H \sigma_{H_1} L_1 f(a_1 L_1) = N_C \epsilon_1(E_1, L_1) \quad \ldots 2.12$$

where σ_{H_1} = the neutron-proton scattering cross section at neutron energy E_1; $a_1 = a(E_1)$ and E_1 = average energy of neutrons after scattering by carbon.

The total number of recoil protons is now $N_1 + N_{2C}$, where N_1 is the number calculated by equation 2.1 i.e., for single scattering only. The efficiency of the scintillator, including double scattering can then be written as:

$$\epsilon_2(E_o, L, L_1) = \epsilon_1(E_o, L)[1 + N_{2C}/N_1] \quad \ldots\ldots 2.13$$

where $\epsilon_1(E_o, L)$ is the efficiency calculated from equation 2.1. The curve obtained by applying equation 2.13 to a 50.8 mm thick NE 102A scintillator is shown in figure 2.4.

The carbon scattering event itself produces a negligible pulse from the scintillator. In double scattering from hydrogen, two recoil protons are produced in such rapid succession that they are recorded as a single event, and hence the number of recoil protons recorded remains the same. Second scattering events and the loss of protons from the sides of the scintillator also result in a distortion

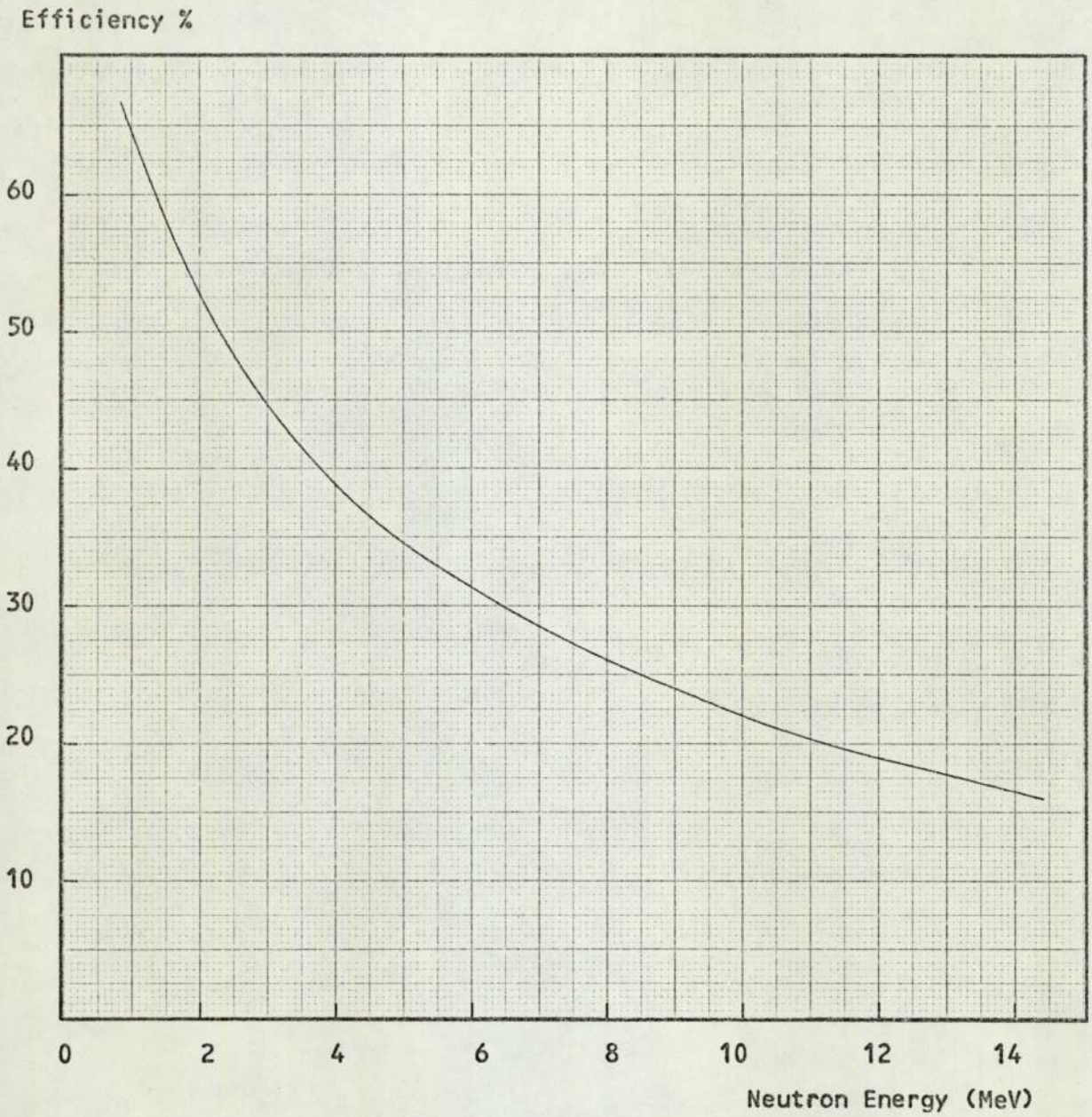

Figure 2.4. Calculated efficiency including double scattering.

of the pulse height spectrum; however, for a scintillator of the dimensions used in the present work these effects are usually negligible

2.4 Scintillator Efficiency with Discrimination

In order to eliminate pulses arising from photomultiplier noise, low energy background neutrons, and γ rays, it is necessary to employ some form of discrimination. This results in the rejection of some recoil proton pulses which have so far been included in the calculations of efficiency. With a discriminator designed to reject pulses of less than a given amplitude P_D, the scintillator efficiency for 14.1 MeV neutrons is given by:

$$\epsilon(14.1) = \epsilon_2(14.1, L, L_1) \left(\frac{A_{14.1} - A_D}{A_T} \right) \quad \ldots\ldots \quad 2.14$$

where $\epsilon_2(14.1, L, L_1)$ = 14.1 MeV efficiency without discrimination, as calculated from equation 2.13; $(A_{14.1} - A_D)$ = area under the pulse height spectrum between ordinates P_D and $P_{14.1}$; A_T = total area under the pulse height spectrum = area under recoil proton energy spectrum; P_D = discriminator level, and $P_{14.1}$ = pulse height due to 14.1 MeV protons. Hence the scintillator efficiency for neutrons of energy E_o can be written as:

$$\epsilon_3(E_o, L, L_1) = \epsilon_2(E_o, L, L_1) \left(\frac{A_{E_o} - A_D}{A_T} \right) \cdot \frac{14.1}{E_o} \quad \ldots \quad 2.15$$

The discriminator level was chosen such that while rejecting background pulses, it was not at such a level as to reject significant neutron inelastic scattering data as well. It was also necessary for it to be fixed at a consistently reproducible known pulse height. This condition was fulfilled by setting the discriminator to reject pulses due to γ rays from a specific source. The source used was Na^{22}, which emits γ rays of 1.274 MeV. At this energy, γ rays interact with

plastic scintillator primarily via the Compton effect. The energies of the recoil electrons in Compton collisions range from zero up to a maximum value E_{max} given by:

$$E_{max} = \frac{E}{1 + (1/2\alpha)} \qquad \ldots\ldots 2.16$$

where E = the incident γ ray energy in MeV and $\alpha = E/m_oC^2$. E_{max}, the maximum energy of the recoil Compton electrons is known as the Compton edge. Applying equation 2.16 to Na^{22} γ rays of energy 1.274 MeV gives E_{max} = 1.068 MeV. Therefore, a discriminator set to reject pulses due to γ rays from Na^{22}, resulted in the rejection of pulses due to 1.068 MeV electrons. From the discussion in section 2.3, equation 2.9 shows that a 1.068 MeV electron produces an equivalent proton pulse height P = 1.068 MeV. Interpolation of the proton pulse heights given in table 2.1 showed a pulse P = 1.068 MeV to be equivalent to a proton of energy 3.5 MeV. With a discriminator set to reject pulses from Na^{22} γ rays, this resulted in the rejection of pulses due to neutrons with energy less than 3.5 MeV.

Figure 2.5 shows the efficiency curve obtained by applying equation 2.15 with a discriminatory pulse height of P = 1.068 MeV.

2.5 The Scintillator-Photomultiplier Combination

For fast neutron time of flight experiments a suitable photomultiplier tube must have a fast transit time with good time resolution. This requirement limits the choice of tube to one with a focused dynode structure, as this type has a much smaller spread in electron transit time.

The photomultiplier tube used was a Philips 56 AVP, having an electron transit time spread of less than 0.5 ns. With fourteen stages of amplification, the 56 AVP is a high gain photomultiplier tube with a current gain of 10^8, capable of producing peak anode

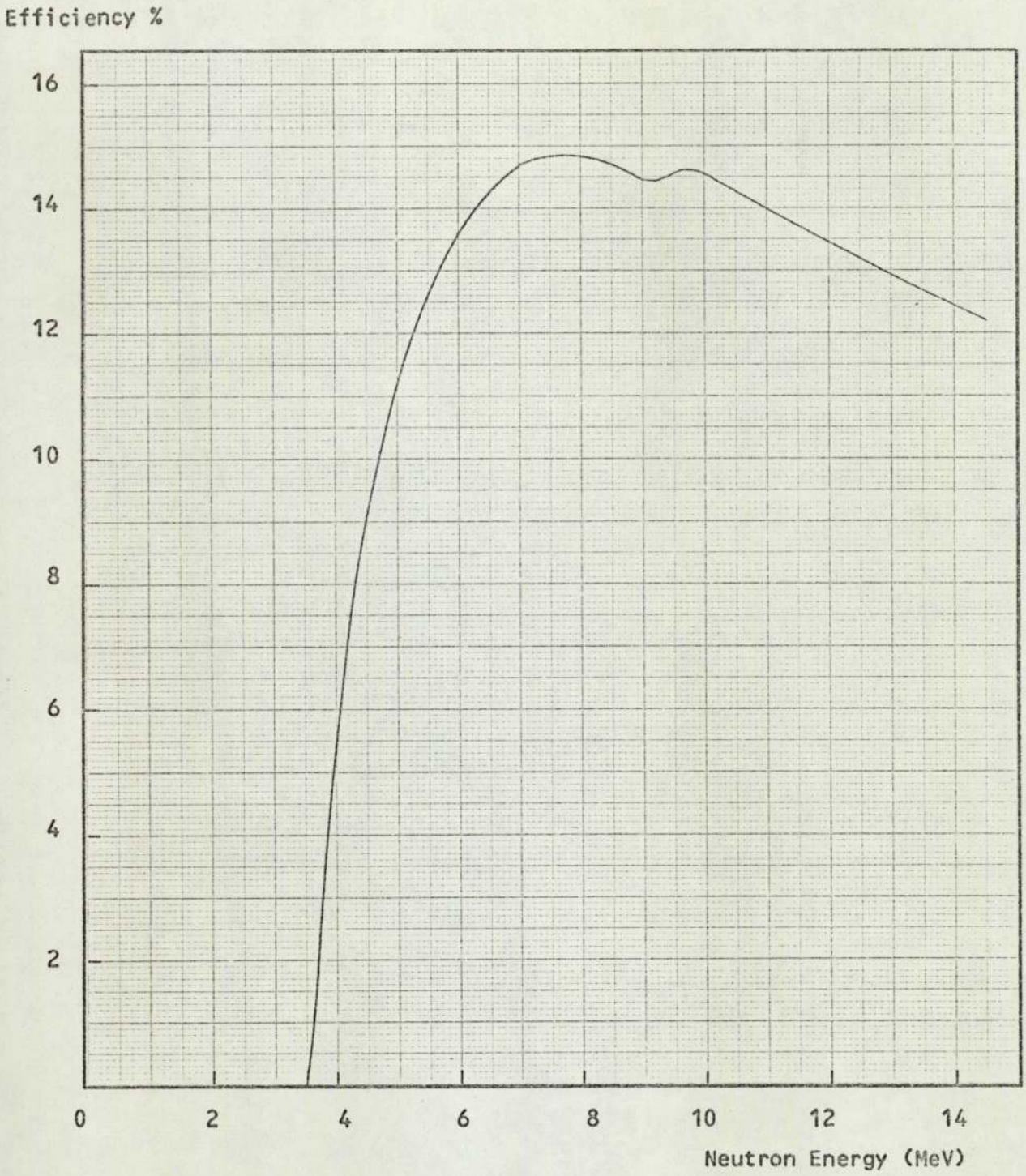

Figure 2.5. Calculated efficiency of a 50.8 mm NE 102A scintillator with a discriminator level of 3.5 MeV.

currents up to 1A. The manufacturers state that to achieve a stability of 1% the ratio of the current through the voltage divider chain to that through the heaviest loaded stage of the tube should be 100:1[24]. For moderate intensities of radiation this requires a dynode chain current of about 3 mA.

The manufacturers recommend two types of voltage divider chains; type (i) has an equal voltage across the last twelve dynode stages and type (ii) has progressively increasing voltages across the last nine dynode stages. Voltage divider type (i) gives a higher gain, but a higher anode current with better time characteristics can be obtained with divider type (ii). The last dynodes of the tube are decoupled by means of capacitors to avoid fluctuations in the dynode potentials.

In view of the higher gain, a dynode chain of type (i) was used for the neutron detector, and the resistor chain is shown in figure 2.6. The current through the dynode chain was 2.3 mA at an operating voltage of 2 kV. A current of 3 mA was the maximum current delivered by the H.T. unit, Isotope Developments type 1617A, used. The capacitors used to decouple the last dynode stages are shown in the figure. The output resistor and H.T. capacitor were chosen to have a small time constant; the values were 2000 Ω and 34 pF.

The time of flight electronics were 7m from the experimental area, and this length of coaxial cable was required to connect the neutron channel discriminator to the detector. To avoid reflections in this long cable the anode signals were matched into the cable via an emitter follower at the base of the photomultiplier. The single transistor emitter follower circuit is shown in figure 2.7. The output impedance of the circuit was 82 Ω and matched the negative pulses into the 70 Ω impedance coaxial cable. When the cable was correctly terminated no reflections were observed.

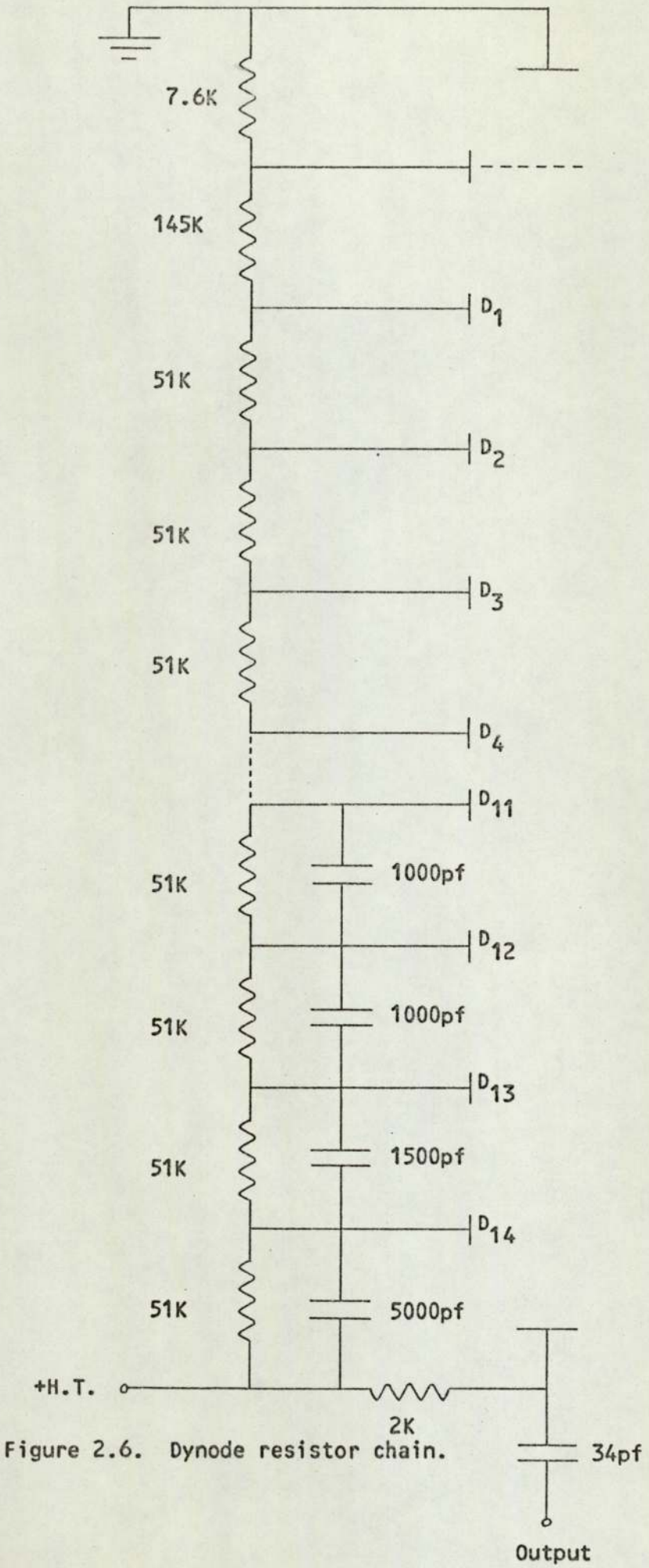

Figure 2.6. Dynode resistor chain.

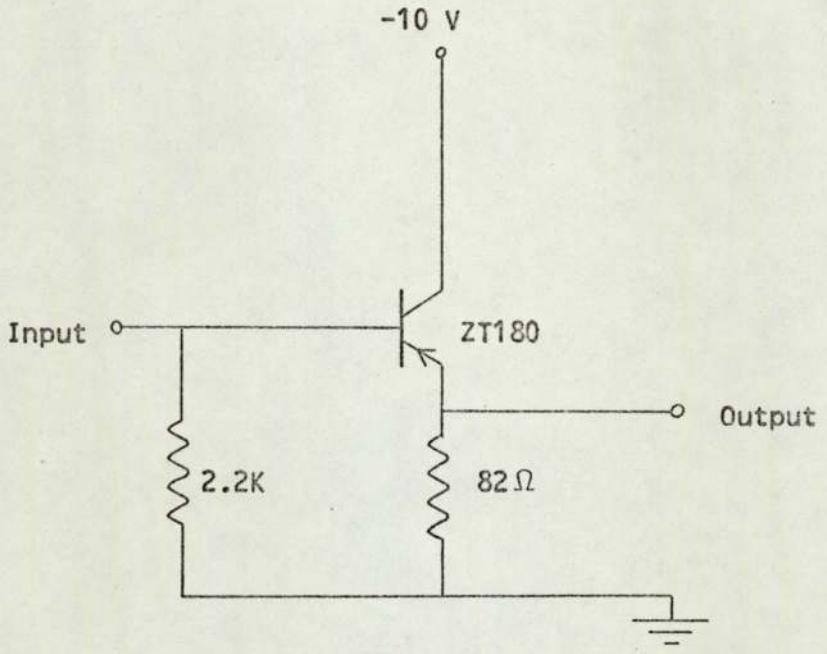

Figure 2.7. Single transistor emitter follower circuit.

Photomultiplier tubes with a focused dynode structure are particularly sensitive to magnetic fields. This effect has been reported by Engstrom[27] and Connor[28]. They have shown that even weak magnetic fields can cause a marked reduction in gain. The earth's magnetic field is not usually troublesome if the tube is operated in a fixed position throughout an experiment, however, in the present work it was required to rotate the detector about the sample, so that shielding from the earth's magnetic field was essential for stable performance.

The electron trajectories from the cathode to the first dynode are most sensitive to magnetic fields. The photomultiplier tube was therefore placed inside a cylindrical mu-metal magnetic shield, No. 56131 recommended by the manufacturers, so that the first dynode stages and the photocathode were adequately shielded. The use of a mu-metal shield, besides giving optimum tube gain, gives minimum transit time spread.

To ensure maximum light collection by the photocathode, care must be taken with the optics of the system. Minimum light loss occurs when the scintillator is coupled directly to the photomultiplier. As the scintillator used had a larger diameter than the photomultiplier tube, a light pipe was employed to make an efficient optical coupling. In this case it is important to minimise light losses, which occur by absorption in the guide and through the sides of the guide. Tove[29] has shown that light absorption is usually only significant for light pipes greater than about 0.5 m. In the present work the light guide was made of perspex and was 70 mm long, converging from the scintillator of diameter 101.6 mm, to the photomultiplier tube face of diameter 46 mm. Cylindrical light guides operate on the principle of total internal reflection, for which there is no light loss through the sides of the guide when the surfaces are smooth.

The optical contact between the scintillator and light guide was made using NE 580 optical cement, which is a clear colourless epoxy resin, having a refractive index close to that of NE 102A scintillator (μ = 1.58). The contact between the light guide and photomultiplier tube consisted of a non-drying silicon immersion oil.

The complete neutron detector assembly and housing is shown in figure 2.8.

2.6 Detector Shielding

The purpose of shielding is to reduce background effects caused by unwanted neutrons and γ rays to a reasonably small fraction of the effects due to the neutrons of interest.

Neutron scattering experiments require careful shielding of the detector from the neutron source. The shielding usually consists of a shadow bar and a collimator surrounding the detector. The shadow bar reduces the number of source neutrons incident on the detector, whilst the collimator reduces the background caused by neutrons and γ rays scattered into the detector from the floor and surrounding walls. In the present work the sources were 10 mm line sources of 14.1 MeV and 2.5 MeV neutrons, so that the detector had to be shielded from the direct flux and from the scattered neutrons of lower energies.

An efficient shield should attenuate fast neutrons producing a minimum of secondary penetrating γ radiation without causing a build up of activity in the shielding material. This is achieved by first moderating the fast neutrons and then absorbing the secondary penetrating radiation i.e. γ rays.

Shielding Materials

The neutrons were moderated by paraffin wax which is an efficient fast neutron moderator and as the inelastic process does not occur with hydrogen it has a low secondary γ ray production. Thermal neutron capture by hydrogen produces a single γ ray of 2.23 MeV from the

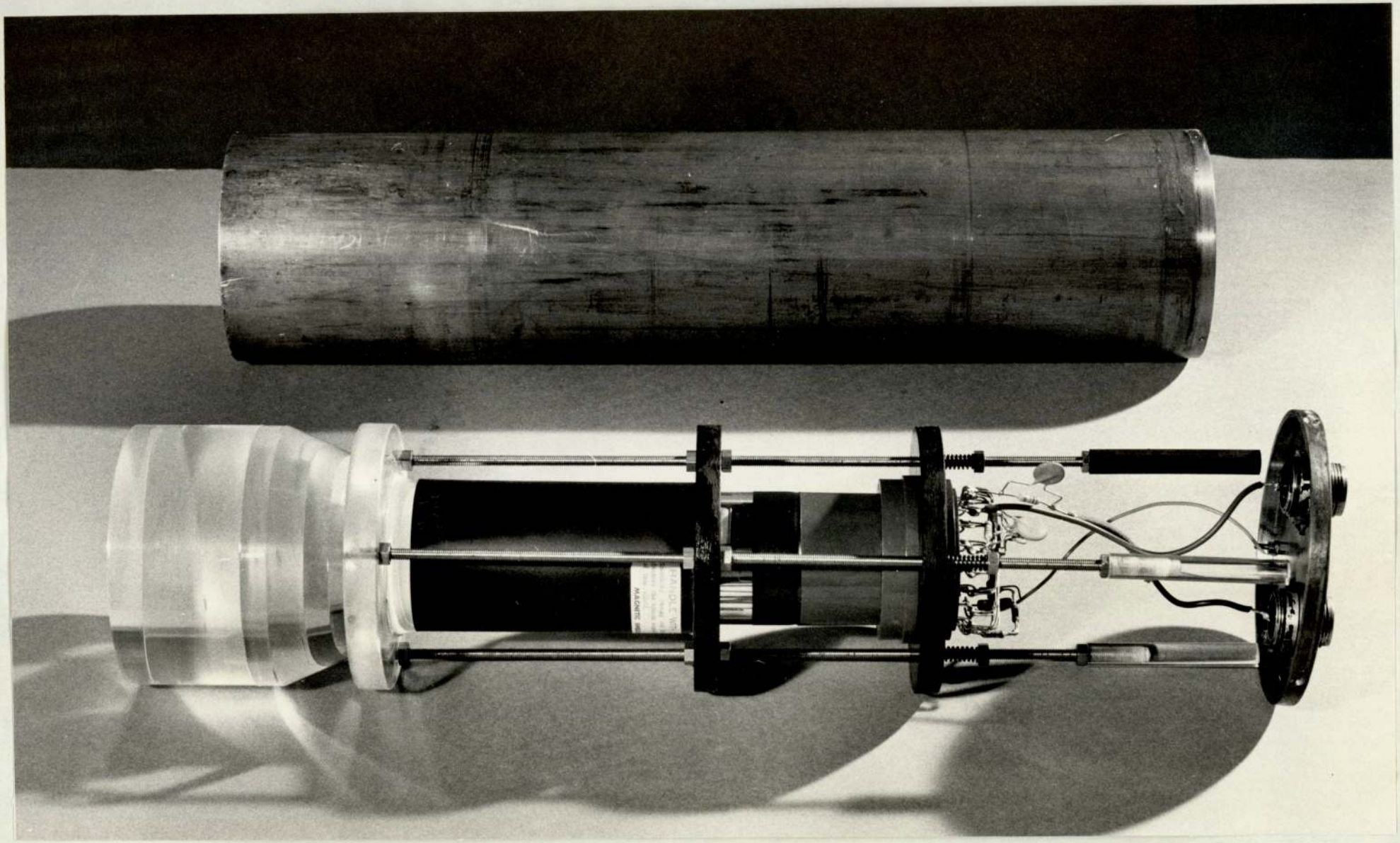

Figure 2.8. The Neutron Detector Assembly.

reaction $^{1}H(n,\gamma)^{2}H$. The cross section for this reaction is 330 mb for thermal neutrons. In using paraffin wax, scattering by its carbon content produces 4.43 MeV γ rays in the reaction $^{12}C(n,n'\gamma)^{12}C$, but the cross section for this reaction is very much less than for elastic scattering by hydrogen and carbon.

It is possible to reduce the γ ray production in the paraffin wax due to the two reactions mentioned above. This can be achieved by loading the paraffin wax with a good slow neutron absorbing material. Suitable materials are ^{6}Li and ^{10}B, generally used in the form of a compound, typically lithium carbonate and boric oxide. Both materials have a large cross section for the (n,α) reaction but the former tends to be the most effective since no γ rays are emitted in the reaction $^{6}Li(n,\alpha)^{3}H$; in the $^{10}B(n,\alpha)^{7}Li$ reaction 0.47 MeV γ rays are emitted. Ashe et al[30] mixed lithium carbonate with paraffin wax, but a mixture must be rich in lithium carbonate for a substantial reduction in γ radiation from neutron capture in the hydrogen. However, this reduces the density of hydrogen in the shield and consequently the neutron shield is less efficient. As a compromise between size, weight, and efficiency of the shield, the paraffin wax was not loaded with lithium or boron compound.

The innermost part of the shield consisted of a suitable γ ray absorbing material. Invariably lead is used for this purpose because of its density and high atomic number. This shielded the detector from γ rays produced by reactions in the shielding material and from the general γ ray background. A cross section of the complete collimator shield is shown in figure 2.9(a).

Shielding from the source neutrons was provided by means of a shadow bar. Neutron target shadow bars are usually made of hydrogenous material or heavy metal e.g., tungsten, copper, iron, lead. The elastic differential cross sections for heavy metals are very sharply

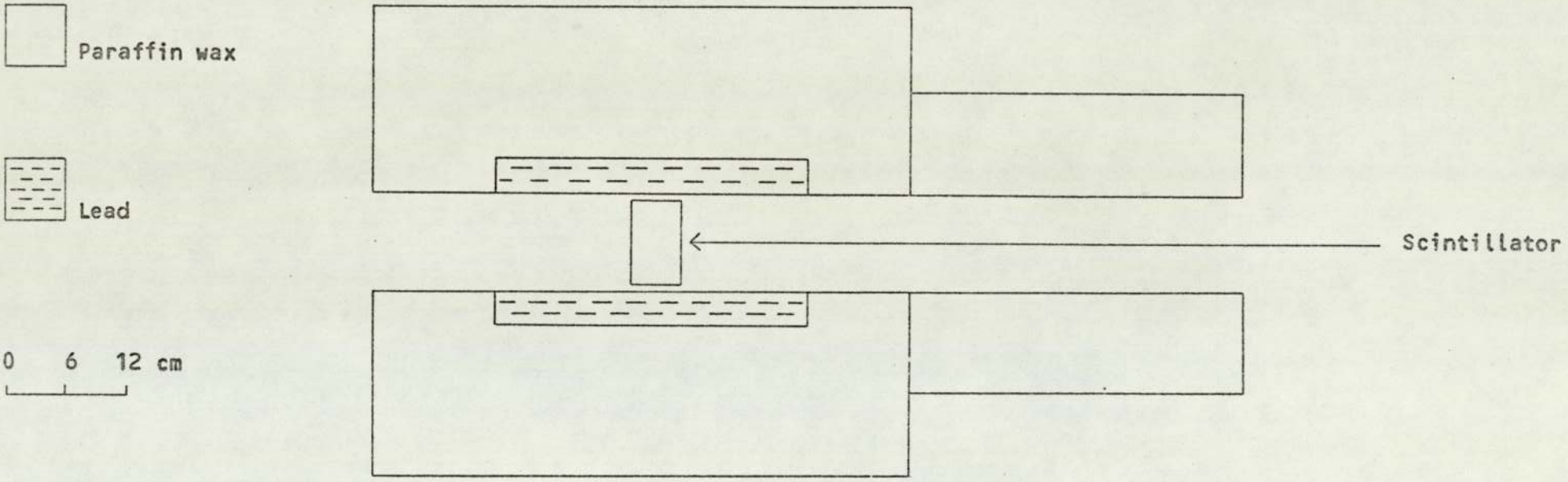

Figure 2.9(a). Neutron detector collimator shield.

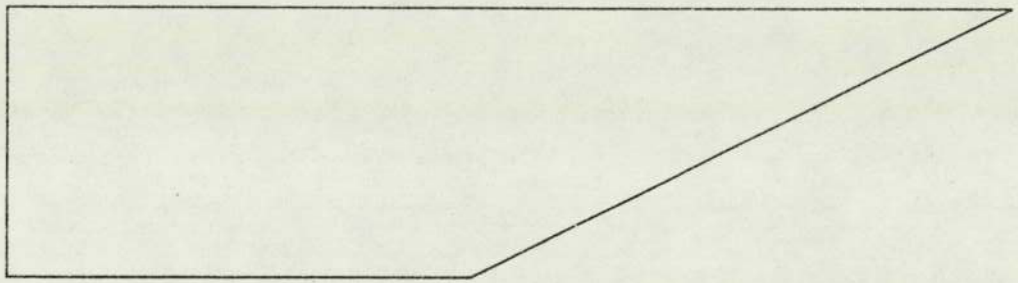

Figure 2.9(b). Shadow bar.

forward peaked, and for attenuation purposes the entire elastic cross section may be neglected. The non-elastic processes either absorb or degrade in energy the incident neutrons. Materials suitable for shadow bars have been investigated by Hopkins et al[31]. They found that for neutrons above 6 MeV the heavy metals are more efficient than hydrogenous material in terms of attenuation per unit thickness of the shield, but when total weight is a consideration, hydrogenous materials are more effective. For lower neutron energies hydrogenous material was the most efficient. Since it was necessary to shield against the direct source for both 14.1 MeV and 2.5 MeV neutrons, on the basis of the above considerations the shadow bar used was made of paraffin wax. A cross section of the shadow bar is shown in fig 2.9(b).

Location and Efficiency of the Shadow Bar

Proper location of the shadow bar was essential. There are several criteria concerning a suitable location for the shadow bar. It should not intercept neutrons between the target and the scattering sample, or between the scattering sample and detector. The entrance of the collimator should not be exposed to the target, and the shadow bar face nearest the target and scattering sample should not be visible to the detector. Within these limitations which may be mutually exclusive at certain very small or very large angles, the shadow bar should occupy as much space as possible between the target and detector.

To test the efficiency of the shadow bar the following experiment was performed. The axis of the detector was positioned so as to coincide with the direct beam from the source. The number of coincidences for a fixed neutron yield was then recorded, with and without the shadow bar in position. The spectra obtained are shown in fig 2.10.

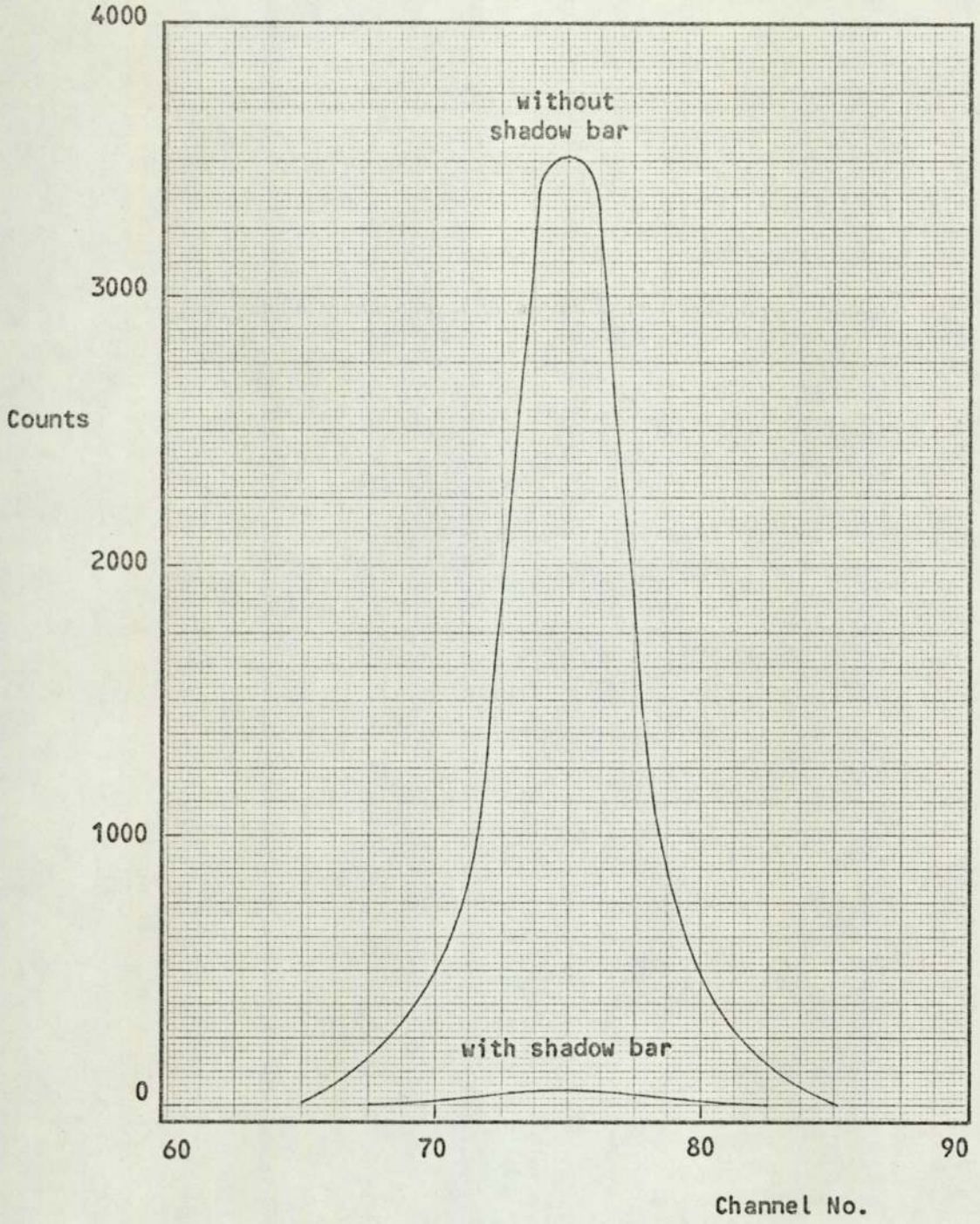

Figure 2.10. Test of the efficiency of the shadow bar.

CHAPTER 3

Experimental Methods for use with the reaction $^{3}H(d,n)^{4}He$

3.1 The Time of Flight Technique

In recent years the time of flight technique has become widely used for the measurement of fast neutron differential cross sections as a function of energy. This technique was developed independently by Alvarez[32], Fertel et al[33] and Milatz[34]. Although it has been greatly improved, the principle remains the same, i.e., the neutron energy is determined by measuring its flight time over a fixed flight path. An essential part of the time of flight measurement is the precise determination of the time of origin of the particles. For neutron time of flight measurements with low energy accelerators two approaches are available; (i) the pulsed beam technique and; (ii) the associated particle technique. These methods differ in the way the neutron time of origin is obtained.

In the pulsed beam technique, the source is usually a nuclear reaction induced by ion bombardment. The solution requires that first of all the time of origin of a neutron be localised by producing the neutrons in bursts of short time duration, say, δt. A specific neutron can then be said to have originated at a given point at a certain time with an uncertainty δt. If the neutrons are produced by positive ions bombarding a target to induce a nuclear reaction, it is sufficient to produce ions in bursts of time δt. This technique was first applied to neutron energy measurement by Cranberg and Levin[35], using the $^{3}H(p,n)^{3}He$ reaction, producing neutrons of energy 2.5 MeV. The pulsed beam technique can be used for all reactions in which the neutrons are produced by an ion beam; hence a wide range of neutron energies can be covered by the use of different charged particle reactions.

In contrast, the associated particle technique, can be used

only with the $^{3}H(d,n)^{4}He$ and $^{2}H(d,n)^{3}He$ neutron producing reactions. Here, the time of origin of the source neutron is defined by detecting the associated helium particle, which can be detected with 100% efficiency. The uncertainty in the time of origin is a function of the energy loss of the helium particles in escaping the target and the time resolution of the helium particle detector. The angle between the helium particle and the neutron is fixed by the kinematics of the nuclear reaction. Consequently, the solid angle subtended at the target by the helium particle detector defines a corresponding cone of associated neutrons. The technique has two main advantages; (i) a continuous accelerator beam is used; and (ii) with the scattering sample positioned so that it subtends all of the defined neutron beam, a neutron start signal is obtained only when a neutron penetrates the sample, thus giving a good signal to background ratio. The associated particle technique was first employed in neutron scattering studies by O'Neill[36]. The technique has been used by Frasca et al[8] for differential cross section measurements on potassium; and by others[9,10,13].

A comparison of these time of flight techniques shows that the versatility of the pulsed beam technique represents its main advantage over that of the associated particle. In the pulsed beam technique the target current burst requires a high peak value to obtain a workable signal to background ratio. Such current pulses can be achieved only with a sophisticated beam chopping and bunching system e.g., a Mobley-type magnet or a klystron buncher. As neither space nor facilities were available for such systems, the associated particle technique was employed for neutrons produced by both the reactions $^{3}H(d,n)^{4}He$ and $^{2}H(d,n)^{3}He$.

3.2 The SAMES Accelerator

The deuteron beam was produced by a SAMES type J accelerator,

as shown in figure 3.1. The SAMES electrostatic generator is housed in a hermetically sealed unit in a hydrogen atmosphere and at 150 kV has a stability of 1%. The accelerator ion source is a 100 MHz oscillator supplied with deuterium gas through a thermally activated palladium leak. The ions are extracted by a potential variable from 0 to +6 kV; the maximum output current from the ion source is 600μA. The extracted beam has a two stage potential drop to earth potential; the intermediate potential applied to the focusing electrode, is variable from 0 to +45 kV. The power for the focusing electrode is produced by an oil-immersed Cockcroft-Walton generator situated inside the high voltage terminal of the accelerator.

3.3 Beam Tube and Target Assembly

The positioning of other experimental facilities in the laboratory required the use of a beam tube 5m in length. The beam tube was evacuated to a pressure of 2×10^{-6} torr. The main pumping stage was included in the main accelerator assembly, but because of the volume of the long beam tube, an auxiliary stage was provided at the target end of the tube. The pumps were backed oil diffusion pumps with liquid nitrogen refrigerated baffles. A liquid nitrogen cold finger was positioned above the auxiliary pumping stage to maintain a good vacuum in the target assembly and to stop oil etc., depositing on the target.

Additional beam focusing was required in view of the length of the beam tube. To supply this, a pair of electrostatic quadrupole lenses was used to focus the beam. The focusing has been described by Baynham[37]. The quadrupoles gave optimum focusing with potentials of $\pm$ 2.08 kV. A pair of electrostatic deflector plates, situated between the quadrupoles and target, enabled the target current to be optimised.

The 90° branched, stainless steel target assembly was supplied

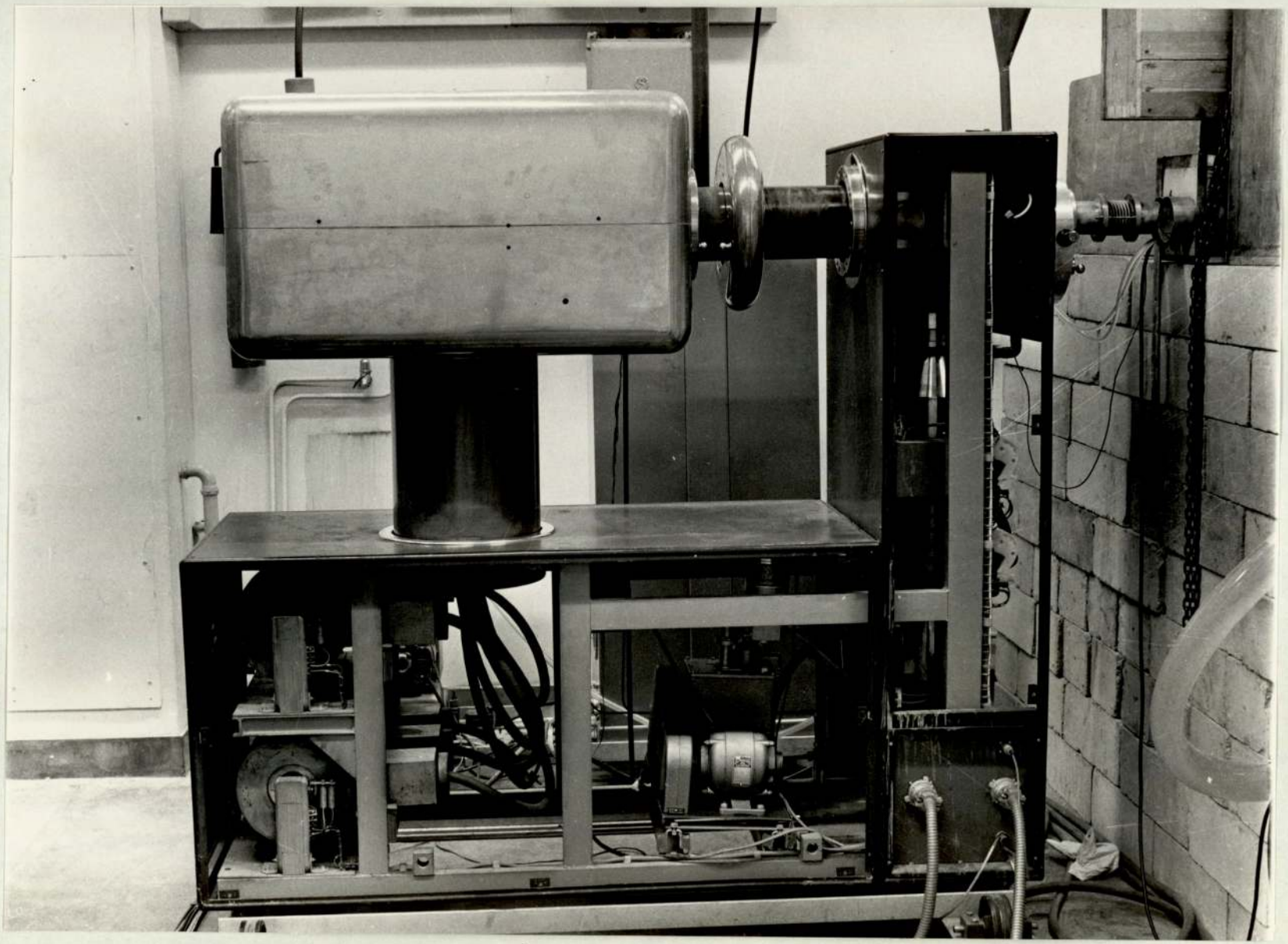

Figure 3.1. The SAMES Accelerator.

by Multivolt Ltd., and housed an annular shaped target. The target assembly is shown in figure 3.2. The area of the target bombarded by the deuteron beam was restricted by an aperture plate defining a line source 10 mm in the vertical plane and 2 mm in the horizontal plane, approximating to a point neutron source in the horizontal plane. The aperture plate was in two parts, as shown in figure 3.2, to enable efficient pumping of the target. The target and diaphragm were water cooled. A comprehensive study of the heating effects of tritium targets under deuteron bombardment in an accelerator has been reported by Smith[38].

Under deuteron bombardment, electrons are ejected from the target and diaphragm. To prevent these electrons backstreaming to the accelerator the diaphragm and target were self suppressed, i.e., the electrons were prevented from escaping by raising the target and diaphragm potentials to +200 volts. As shown in figure 3.2, the aperture flange and the main beam tube were insulated by araldite spacing flanges so as to maintain the suppression potentials, which were produced by taking the target and diaphragm currents to earth via large resistors. Micro-ammeters in series with these resistors enabled the currents to be monitored.

The alpha particle detector was positioned in the arm of the target assembly at right angles to the main beam tube.

3.4 The Alpha Particle Detector

A suitable alpha particle detector should have the following properties, (i) a high detection efficiency for alpha particles, (ii) a low detection efficiency for neutrons and γ rays and; (iii) a fast response time. Two types of detector meet these requirements, scintillation detectors and semi-conductor detectors. A suitable scintillation detector is plastic scintillator NE 102A. It is available in very thin sheets, thus having a low detection efficiency

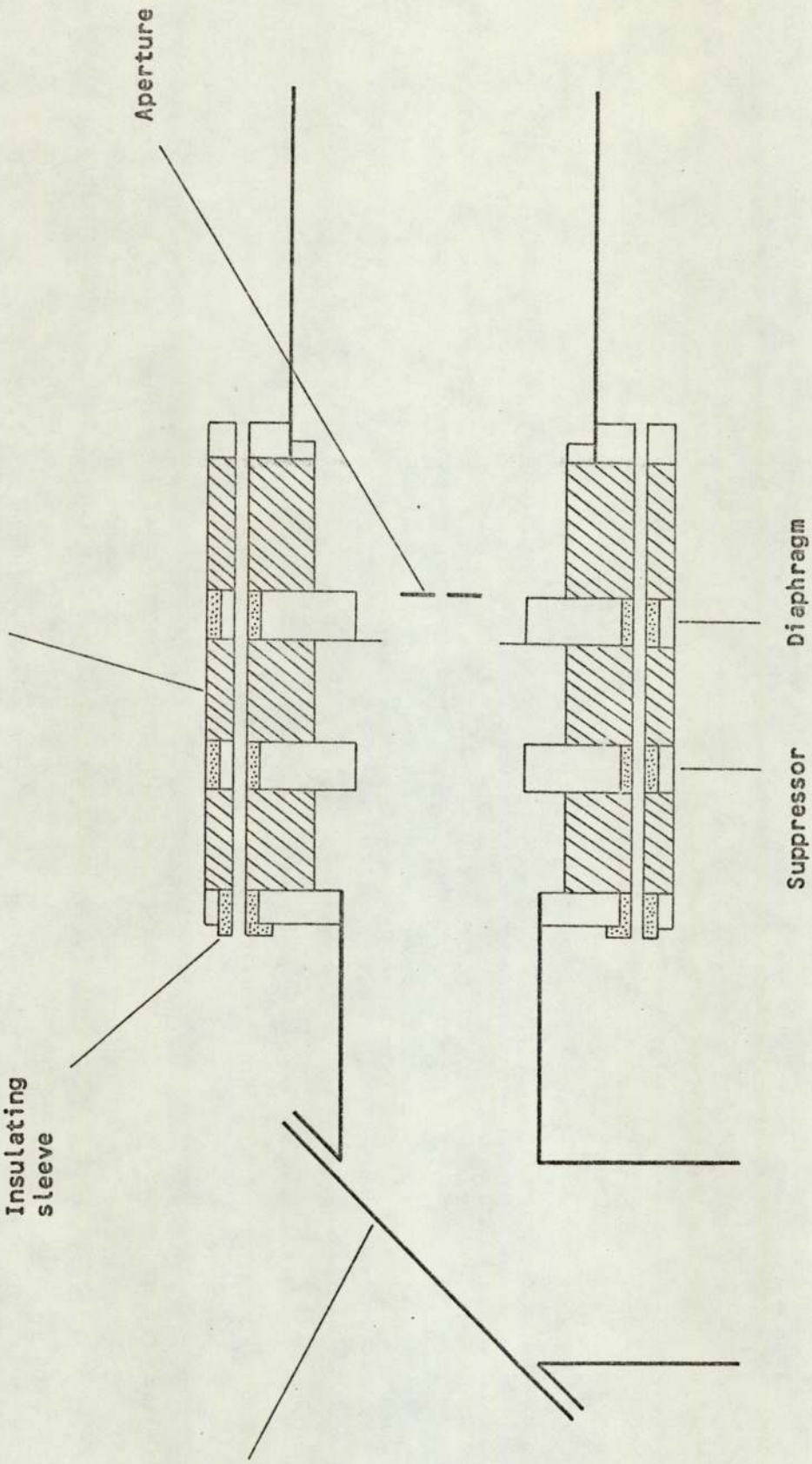

Figure 3.2. The target assembly.

for neutrons and γ rays. The properties of NE 102A have been discussed in section 2.2. When used in conjunction with a high gain focused photomultiplier tube it meets the timing requirements for the associated particle technique.

The silicon surface barrier semi-conductor detector is widely used for alpha particle detection in the $^{3}H(d,n)^{4}He$ reaction. It has a complex detection efficiency for neutrons and γ rays due to the very thin sensitive region and has a fast response time.

A comparison of these two types of detector shows two advantages in using plastic scintillator. Firstly, its use with a high gain focused photomultiplier tube dispenses with a pulse amplifier which is required with the semi-conductor detector; secondly, the scintillation detector is less susceptible to radiation damage than the semi-conductor detector detector[39]. In view of these advantages, plastic scintillator NE 102A was used for the alpha particle detector.

For an incident deuteron energy of 120 KeV, the alpha particles emitted at 90^{o} to the deuteron beam direction in the $^{3}H(d,n)^{4}He$ reaction have an energy of 3.52 MeV. The range of a 3.5 MeV alpha particle in NE 102A is stated by the manufacturers to be 0.025 mm i.e., this thickness of scintillator would be 100% efficient. The scintillator used was 0.5 mm thick and was used in conjunction with a Philips 56 AVP photomultiplier tube, the characteristics of which have been discussed in section 2.5. The dynode chain was similar to that used in the neutron detector assembly. Since the position of the photomultiplier was fixed with respect to the earth's magnetic field, a mu-metal shield was not placed around the photomultiplier.

To avoid the problem of housing the photomultiplier tube inside the evacuated target assembly, a similar system to that reported by O'Neill[36] was used. The thin NE 102A sheet was attached to a perspex light pipe with the light pipe forming the vacuum sealing flange.

The photomultiplier viewed the side of the perspex flange outside the vacuum system. The alpha particle detector arrangement is shown in figure 3.3. The scintillator was positioned 90 mm from the reaction point of the target and was attached to the perspex flange by NE 580 optical cement. The photomultiplier was spring loaded onto the perspex flange, using a non-drying silicon immersion oil to make a good optical contact.

Detector Shielding

The alpha particle detector had to be shielded against two sources of background radiation; deuterons and β particles. The deuteron background resulted from scattering of the deuteron beam by target nuclei and had a maximum energy of 113 KeV; the β particles were produced by the decay of tritium in the target and had a maximium energy of 18.6 KeV. The range of 18.6 KeV β particles in aluminium is 0.0022 mm[40], so this thickness of aluminium would completely shield the scintillator. Data on the range of deuterons in aluminium can be obtained by scaling proton range data derived from the relationship:

$$\left(\frac{dE}{dx}\right)_{\text{proton(E)}} = \left(\frac{dE}{dx}\right)_{\text{deuteron(2E)}} \quad \ldots\ldots 3.1$$

i.e., the deuteron range is twice the range of a proton with the same velocity. Mean proton ranges in aluminium have been tabulated by Whaling[40]. A 100 KeV proton has a range in aluminium of 0.26 $mg.cm^{-2}$ (0.001 mm) so a 200 KeV deuteron has a range in aluminium of 0.52 $mg.cm^{-2}$ (0.002 mm).

The foil used was 0.0044 mm thick, which completely shielded the scintillator from the β particles and scattered deuterons, but was not of sufficient thickness to stop the alpha particles. An

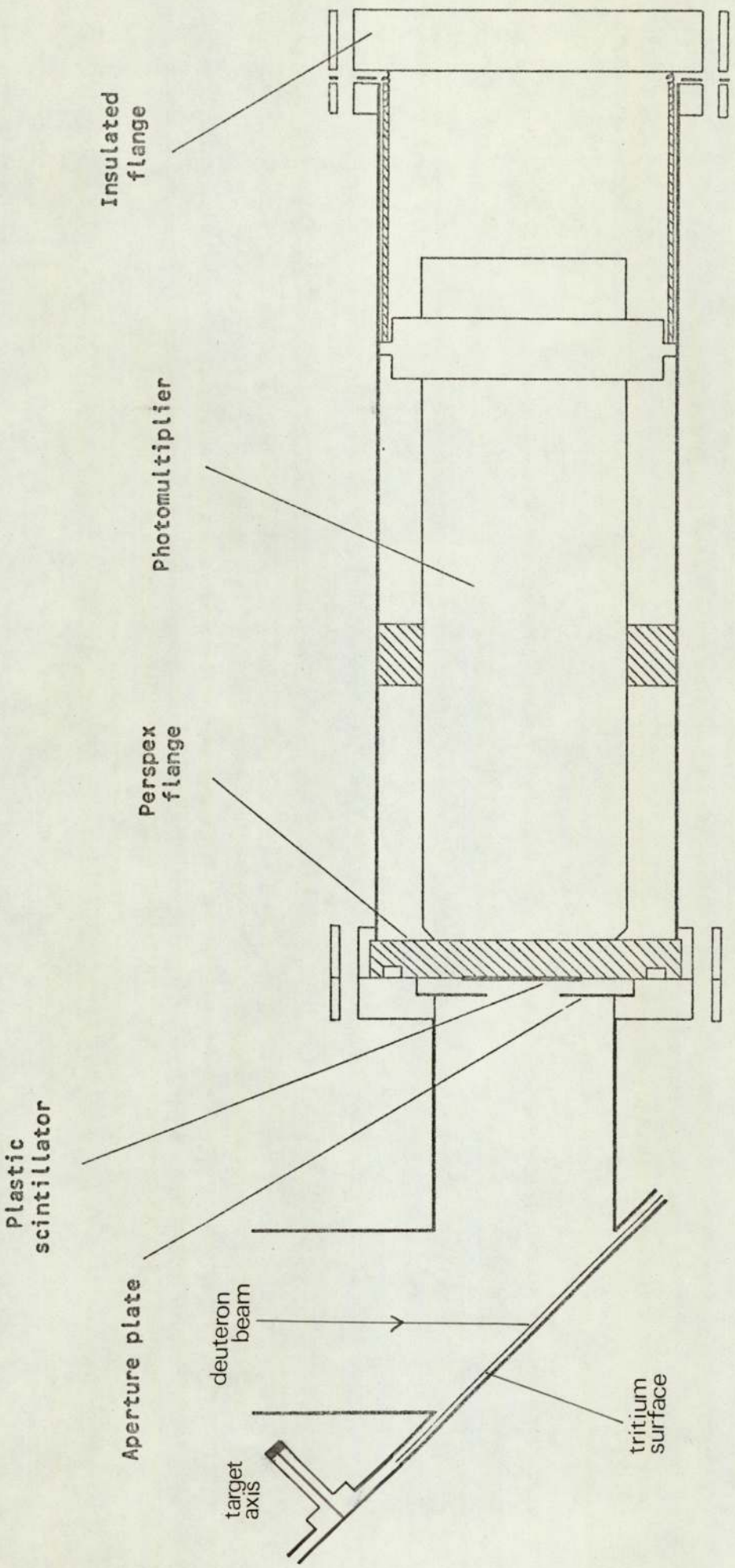

Figure 3.3. The alpha particle detector arrangement.

added advantage of the foil was that it made the scintillator light tight. The exposed area of the scintillator was defined by an aluminium aperture plate placed in front of the scintillator in a recess in the target assembly flange. The plate had a rectangular hole cut out of its centre measuring 15.8 mm horizontally by 10.9 mm vertically. This limited the angular acceptance of alpha particles in the horizontal plane to $90^{\circ} \pm 5^{\circ}$. The alpha detector scintillator light pipe, aperture plate and photomultiplier are shown in figure 3.4.

3.5 Scattering Sample Position

The scattering sample was positioned so that it completely intercepted the neutron beam defined by the associated alpha particles. The most intense part of the neutron beam was at an angle of 83° to the deuteron beam direction, corresponding to the alpha particles detected at 90°, so the scattering sample was centred on this angle. The kinematics of the $^{3}H(d,n)^{4}He$ reaction are discussed in section 5.2. As the defined neutron cone diverged from the target the required sample size depended on the target to sample distance. The scattering sample was positioned 250 mm from the target. At this distance the cross sectional area of the neutron beam, defined by the 10° alpha particle detector aperture, was 68 mm high by 44 mm wide. Figure 3.5 shows the target assembly with a scattering sample in position.

The flight path from the centre of the scattering sample to the face of the neutron detector was fixed at 2 metres. Due to the limited experimental area available in the laboratory the scattering angle range was limited to angles between 0° and 100°. A plan view of the target, scattering sample and shielded neutron detector is shown in figure 3.6.

3.6 The Time of Flight Electronics

A block diagram of the circuitry associated with the two detector channels is shown in figure 3.7. The output pulse from the

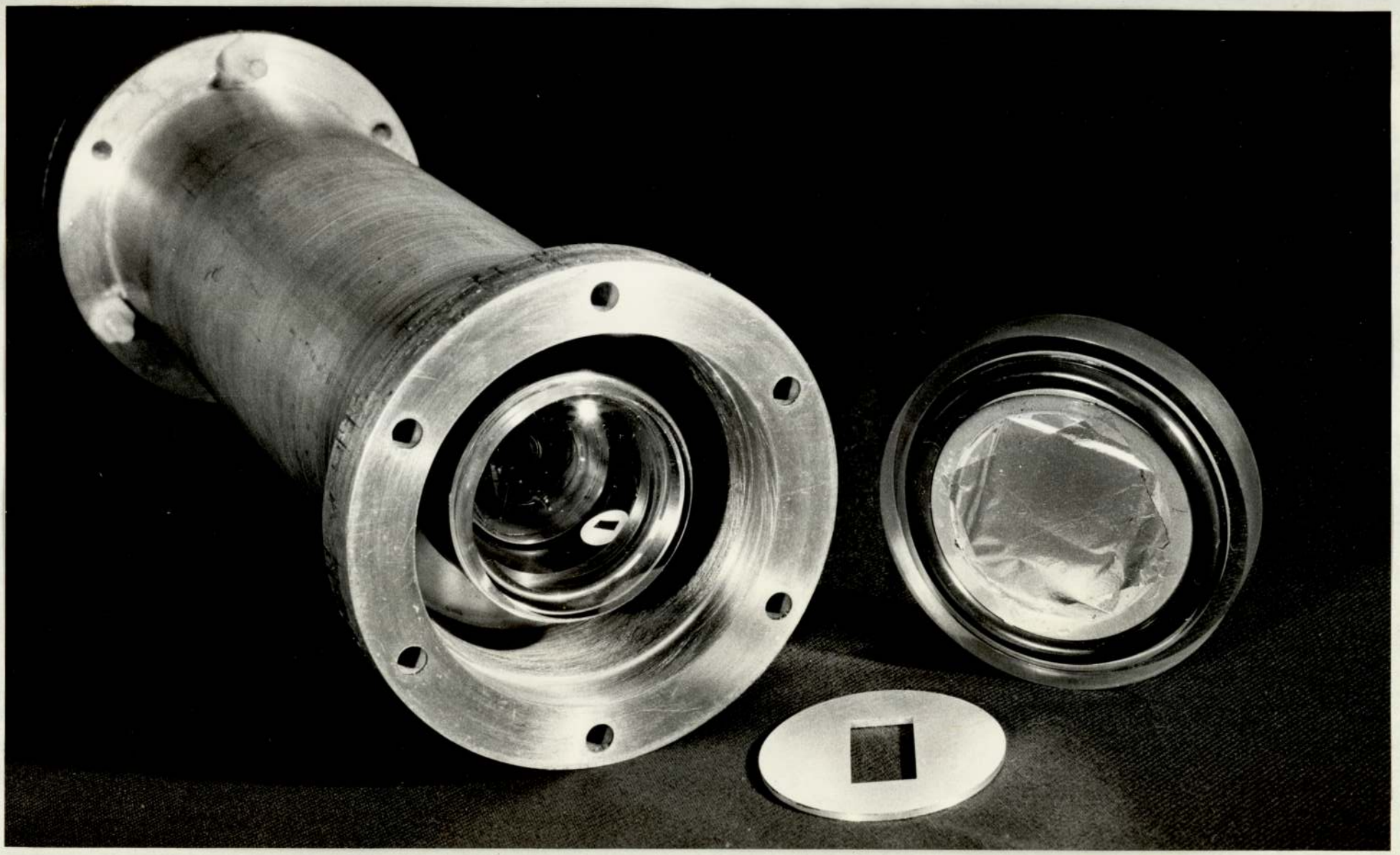

Figure 3.4. The Alpha Detector Scintillator, Light Pipe, Aperture Plate and Photomultiplier.

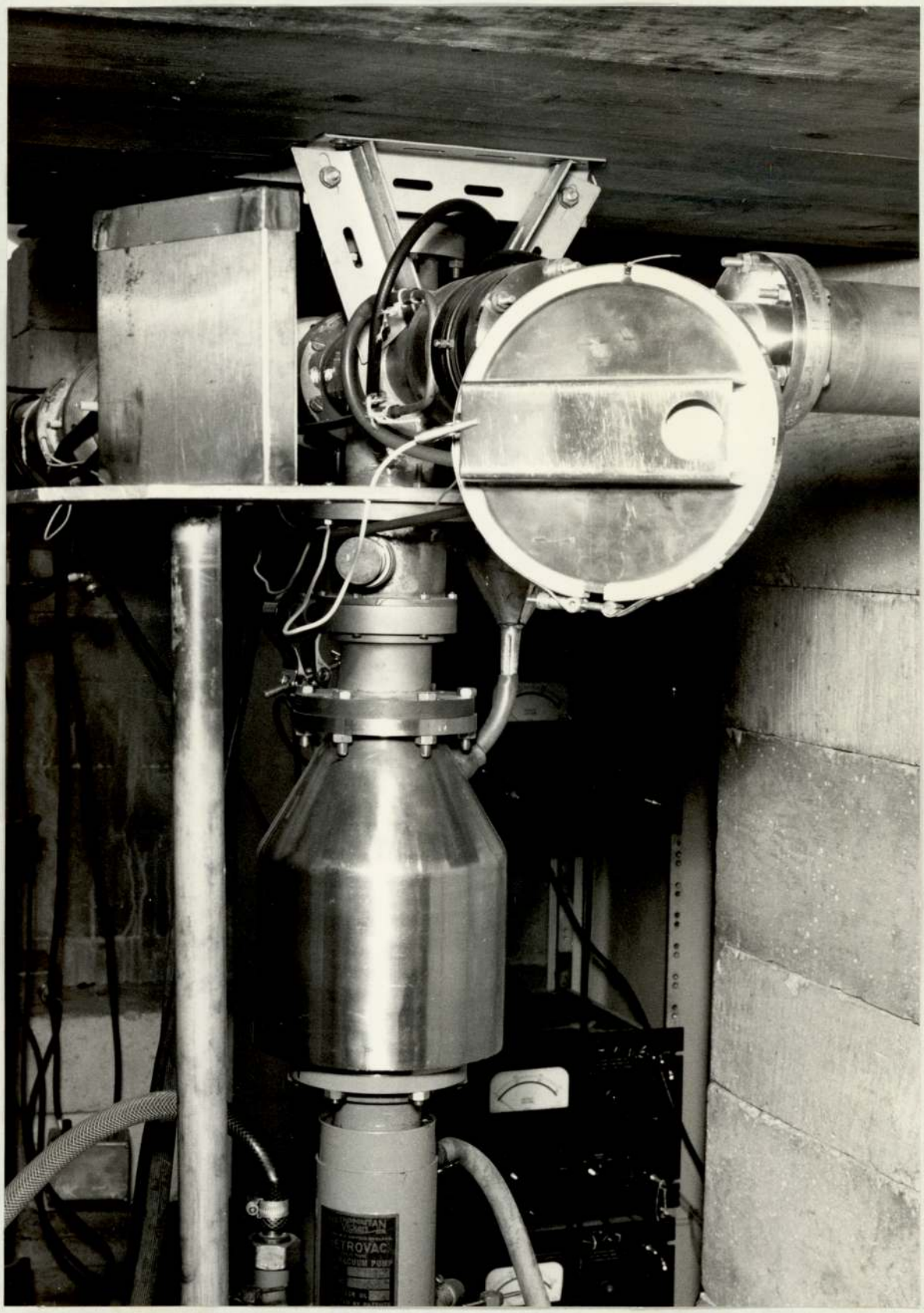

Figure 3.5. The Target Assembly with a Scattering Sample in position.

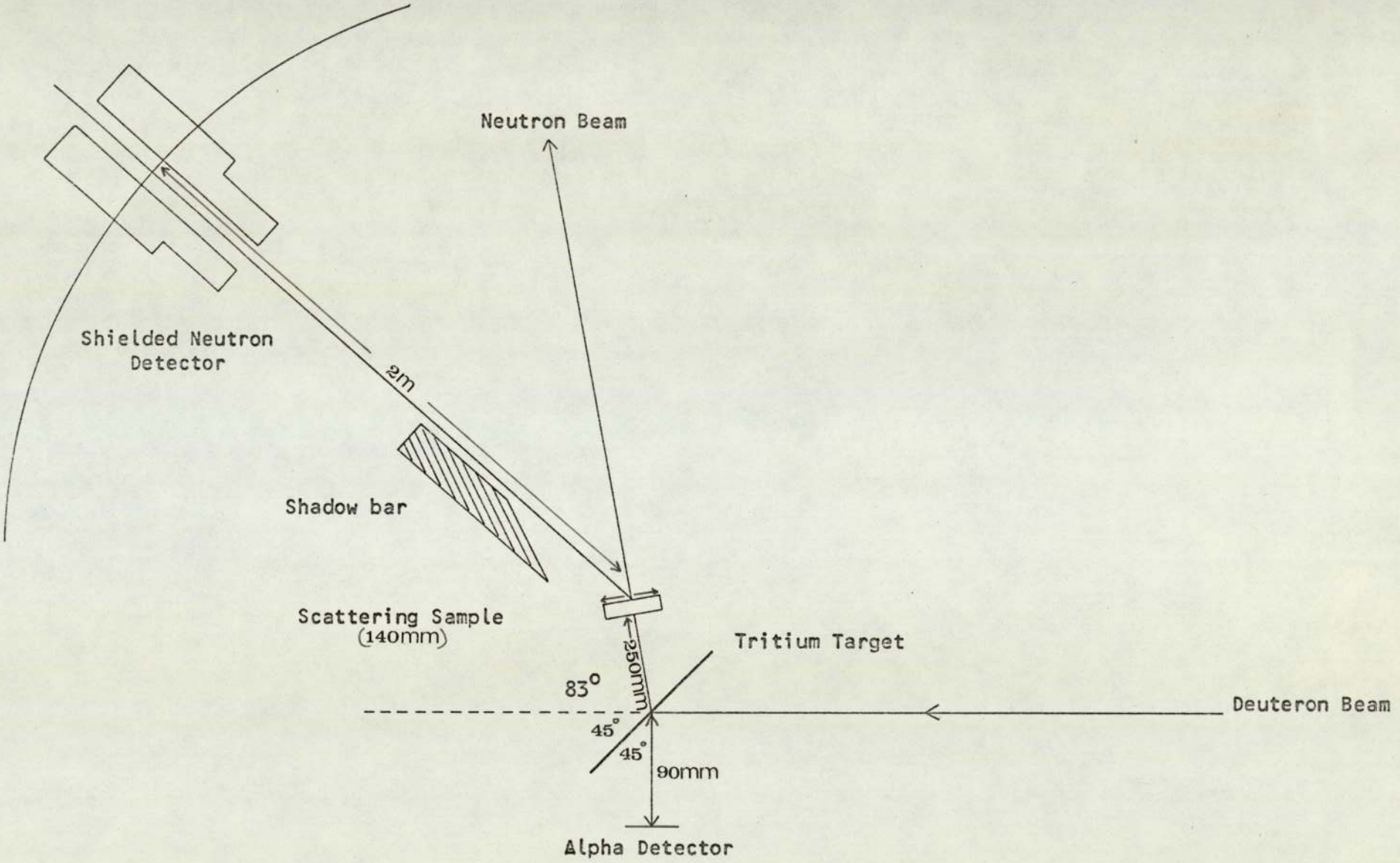

Figure 3.6. Plan view of the target, scattering sample and shielded neutron detector (not to scale).

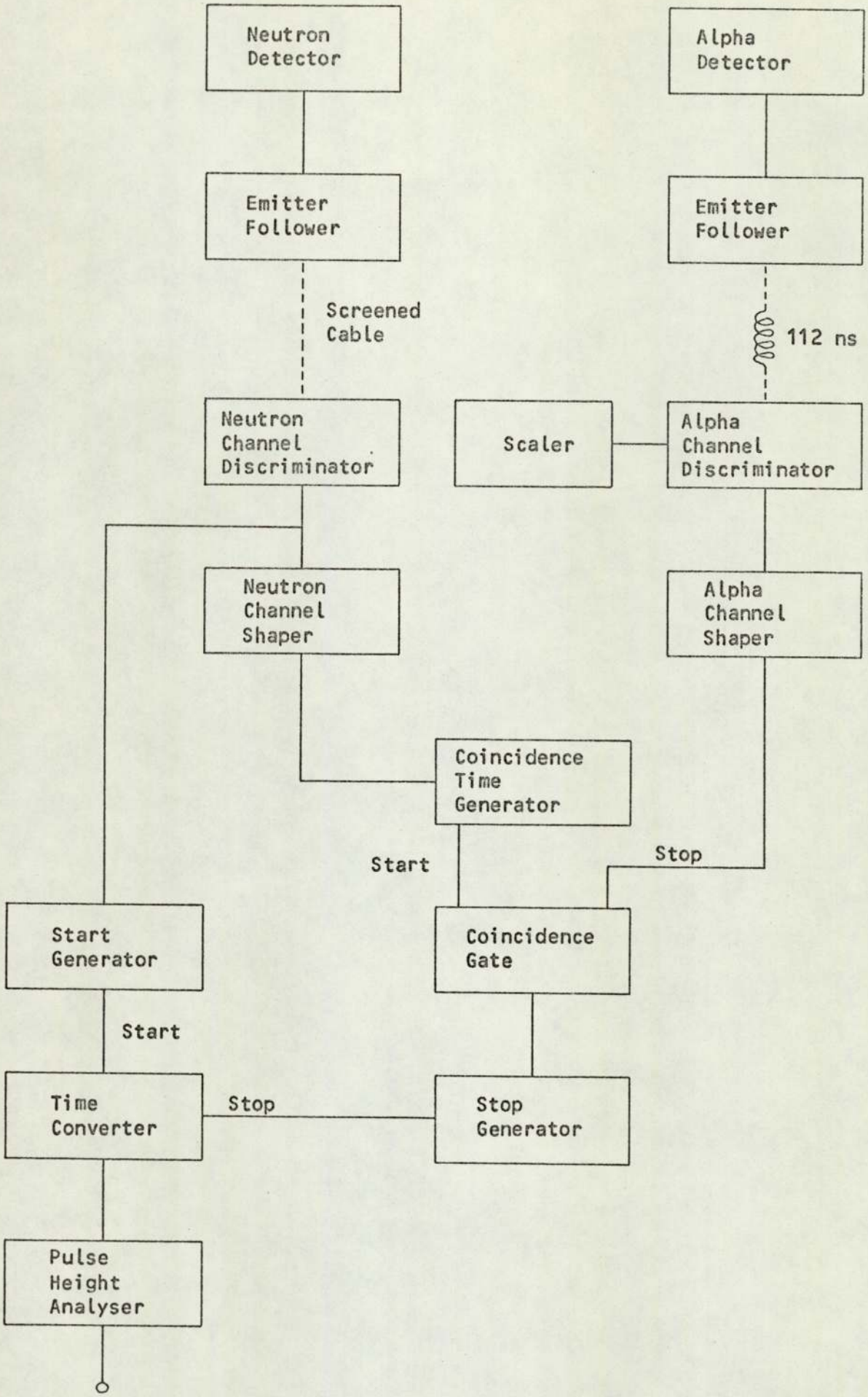

Figure 3.7. Block diagram of the time of flight electronics.

anode of each photomultiplier tube was fed into screened coaxial cable, through an emitter follower designed to provide suitable drive and matching into the coaxial line. Each pulse was then fed to an amplitude discriminator, which accepted the pulse only if it exceeded a pre-set amplitude. The pulse at the discriminator output was then fed to a pulse shaper and then to the coincidence circuit.

Each time a pulse was allowed through the neutron channel discriminator, the output pulse triggered the "start" generator, which was a monostable circuit whose output pulse acted as the start pulse for the time to pulse height converter. Simultaneously, the output pulse from the neutron channel shaper triggered the "coincidence time" generator, which was a 100 ns monostable circuit whose output opened the coincidence gate for the required coincidence time. The suitably shaped pulse corresponding to the associated alpha particle was fed to the second input of the coincidence gate. A pulse at both inputs of the coincidence gate during the coincidence time, caused a pulse to appear at the gate output and this pulse triggered the "stop" generator, which was a monostable circuit whose output pulse acted as the stop pulse for the time to pulse height converter. The output pulses of the time converter were fed into a multi-channel pulse height analyser to build up a time of flight spectrum.

The following sections describe the individual circuits in more detail.

Neutron Channel Discriminator and Shaper

The circuit is shown in figure 3.8. Amplitude discrimination was effected by transistor T_1 and the potential divider action of resistors R_1 and R_2. The extremes of the potentiometer R_2 enabled the base voltage of T_1 to be varied between zero and +2.8 volts. This ensured that T_1 was not conducting and could only be turned on to the conducting state by making the base negative with respect to the

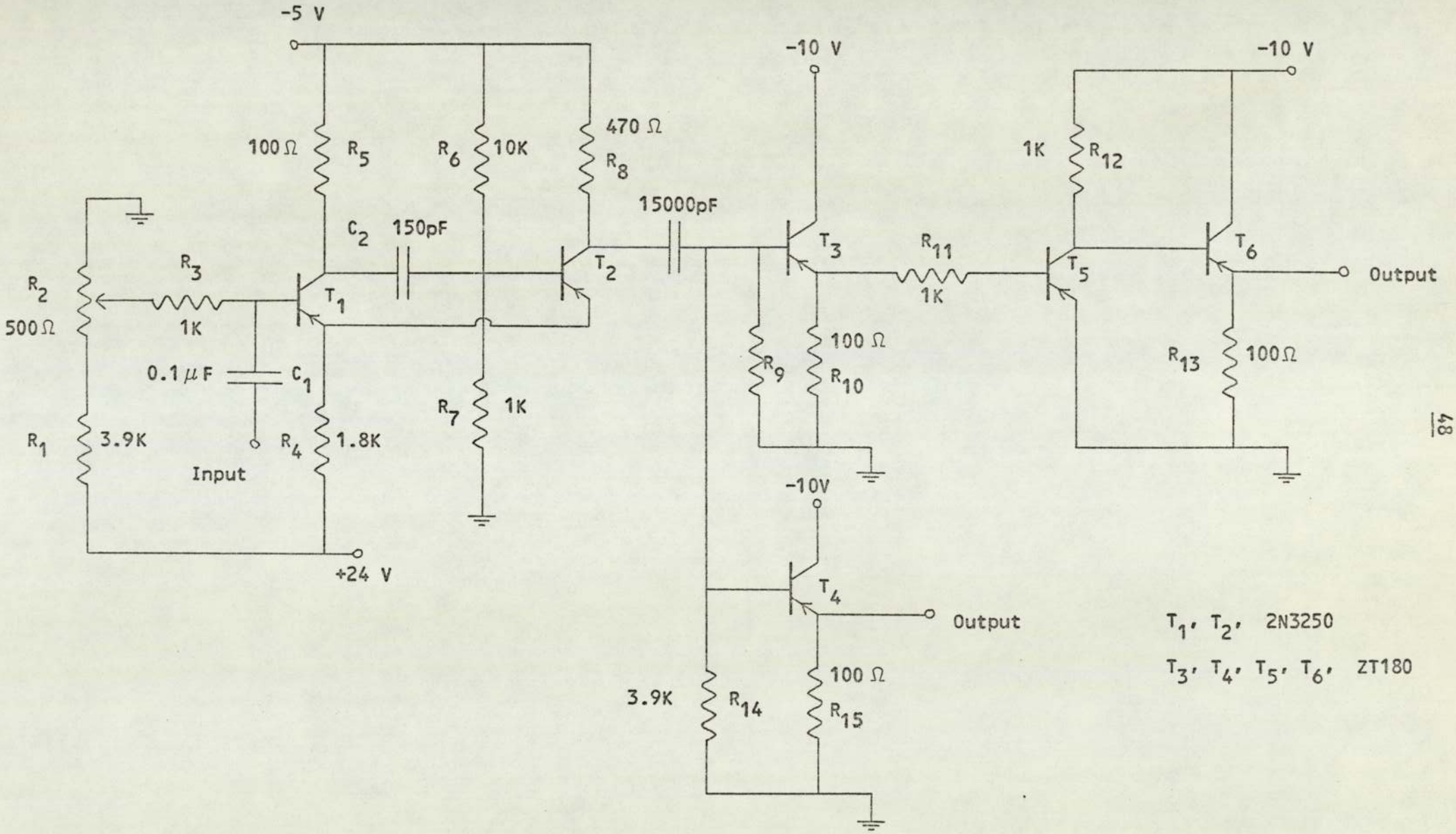

Figure 3.8. Neutron channel discriminator and shaper.

emitter. The base of transistor T_2 was normally held at -0.5 volt by resistors R_6 and R_7, and this ensured that T_2 was conducting, since the common emitter voltage was approximately +1 volt.

The negative pulse derived from the neutron detector was coupled into the base of T_1 through capacitor C_1, and had to be sufficiently negative to overcome the positive bias on the base of T_1. Transistor T_1 conducted for the period during which the input pulse overcame the base bias, and the collector output of T_1 was a positive pulse of the same period. This pulse was coupled through capacitor C_2 into the shaper transistor T_2 switching it off for the duration of the pulse, producing a standard negative pulse of -4 volts amplitude at the collector of T_2. Hence, there was no output if the input pulse was below the discrimination level, but if the input pulse exceeded the discrimination level, a constant amplitude output pulse was obtained, with the same pulse width as the input pulse width.

Two outputs were taken from the discriminator through emitter followers. One output provided a trigger pulse for the "start" generator, and the other output was inverted by transistor T_5, giving a positive pulse which was used to trigger the "coincidence time" generator.

Alpha Particle Channel Discriminator and Pulse Shaper

The circuit for the alpha particle channel amplitude discriminator was identical to that of the neutron channel. Two outputs were taken from the discriminator, one to trigger the alpha particle channel shaper, the other to provide a suitable pulse to drive the alpha particle channel scaler.

The alpha particle channel pulse shaper is shown in figure 3.9 and was a standard monostable circuit. In the stable state, transistor T_1 was switched off and transistor T_2 was fully conducting. A negative pulse applied to the base of T_1 starts to turn the transistor on and its

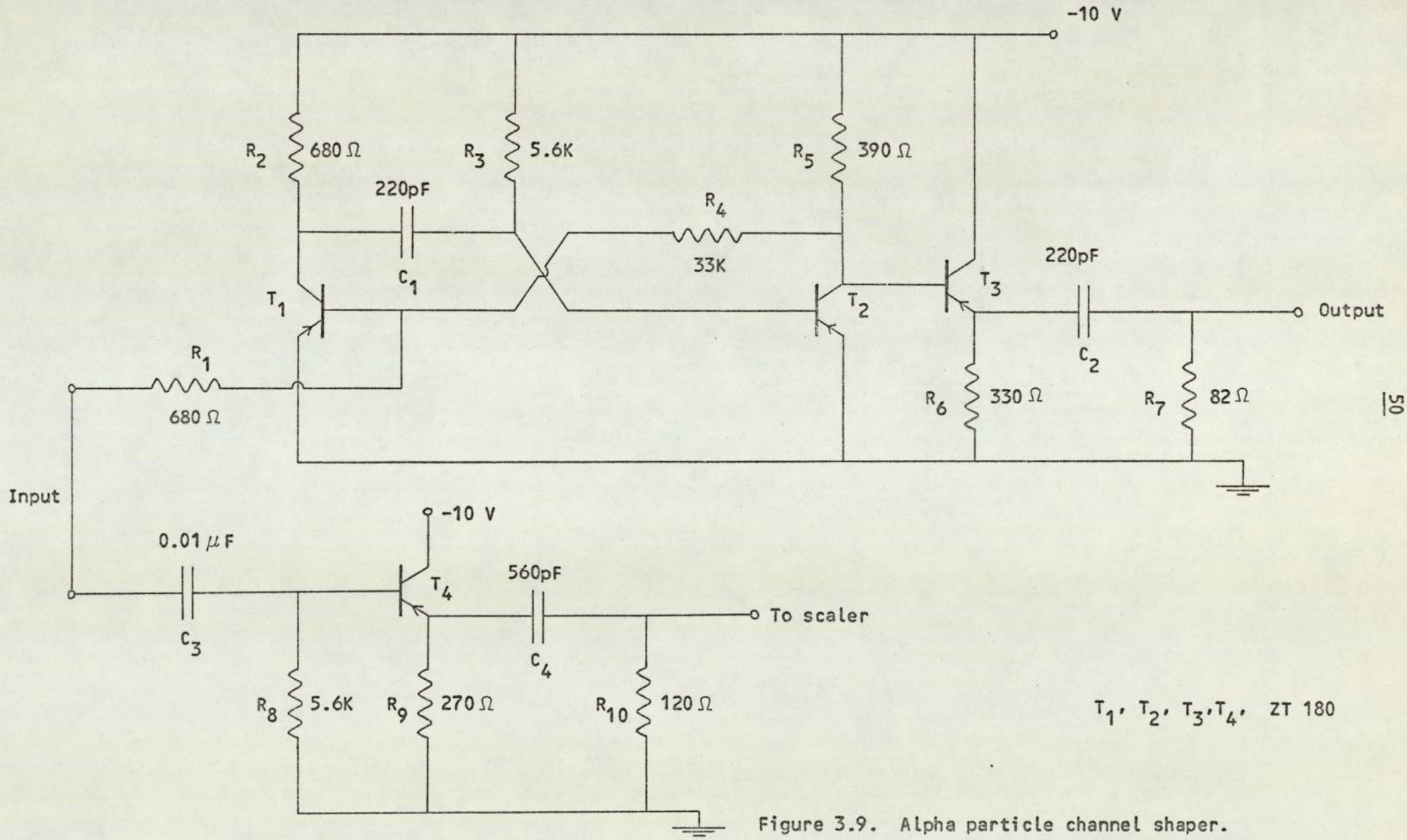

Figure 3.9. Alpha particle channel shaper.

collector voltage begins to rise. This positive excursion is transmitted through capacitor C_1 and starts to turn T_2 off, causing its collector to go negative. This negative signal is fed back to the base of T_1 through the feedback resistor R_4, enhancing the negative input pulse at the base. The circuit remains in the quasi-stable state with T_1 on and T_2 off, until the base voltage of T_2 relaxes from +10 volts to approximately -0.5 volt with time constant C_1R_3. The quasi-stable state lasts for a period $0.7C_1R_3$ and the output pulse at the collector of T_2 is a pulse of -10 volts amplitude and 0.85 μs width. This output pulse was then fed through an emitter follower T_3 and sharply differentiated by C_2 and R_7, giving a -4 volt amplitude output pulse of approximately 20 ns duration. The positive spike resulting from the differentiation of the trailing edge of the shaper output pulse was only of +1 volt amplitude, due to the slow trailing edge of the shaper pulse. The negative output pulse from the differentiator was fed directly to one input of the coincidence gate.

The alpha particle channel scalar required negative pulses of between -2 volts and -3 volts amplitude. It was therefore necessary to feed the alpha particle channel discriminator output pulse through an isolating emitter follower T_4, and a differentiator circuit C_4 and R_{10}, to give -2 volt pulses of 70 ns width. This circuit is shown in figure 3.9.

The Coincidence Circuit

The coincidence circuit consisted of a "coincidence time" generator and a coincidence gate. Figure 3.10 shows the "coincidence time" generator, which was a standard monostable circuit whose output was fed directly to one input of the coincidence gate. In the stable state, transistor T_1 is switched off and transistor T_2 is fully conducting, with the collector voltage of T_2 at approximately zero volts. A positive input pulse, derived from the neutron channel shaper through

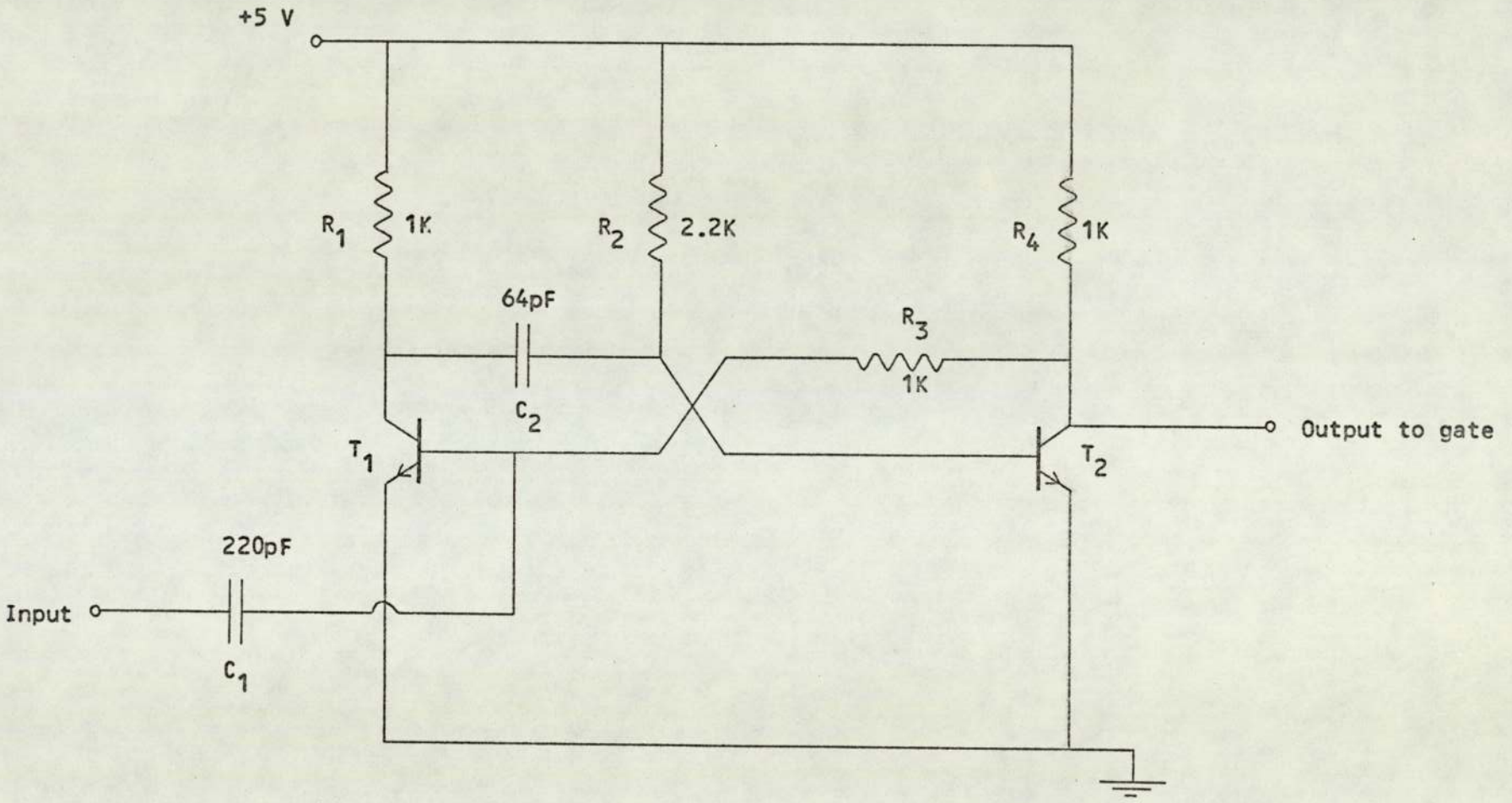

Figure 3.10. Coincidence time generator.

T_1, T_2, ZT2475

capacitor C_1, is applied to the base of T_1, causing the transistor to start conducting. Its collector voltage begins to fall and the negative excursion is transmitted through capacitor C_2 and starts to turn T_2 off, causing its collector to go positive. This positive signal is fed back to the base of T_1 through the feedback resistor R_3, enhancing the positive input pulse at the base. The circuit remains in the quasi-stable state with T_1 on and T_2 off, until the base voltage of T_2 relaxes from - 5 volts to approximately 0.5 volt with time constant C_2R_2. The quasi-stable state lasts for a period $0.7C_2R_2$ and the output pulse at the collector of T_2 is a positive pulse of + 5 volts amplitude and 100 ns width.

The coincidence gate was similar to that used by Oliver et al[41] and is shown in figure 3.11. The zener diode held the emitter of transistor T_3 at +1.5 volts. In the quiescent state the base of transistor T_3 was at zero volts and so T_3 was cut off, since its base was negative with respect to its emitter. The gate output, which was the collector of T_3 was thus held at + 10 volts. The negative input pulses from the alpha particle channel shaper were fed into the grounded base transistor T_4 causing it to saturate, producing negative pulses of 1.5 volts amplitude at its collector. When a neutron was detected the "coincidence time" generator fed a + 5 volt pulse to the base of T_3, causing it to conduct. Thus, with coincident gate input pulses from both neutron and alpha particle channels, a negative pulse of 6 volts amplitude appeared at the collector of T_3. This output was fed through an emitter follower and provided a suitable pulse to trigger the "stop" generator.

The "stop" generator was a standard monostable circuit which produced a standard timing pulse of - 4 volts amplitude and 600 ns duration. This was the stop pulse for the time to pulse height converter. The "start" generator in the neutron channel was an identical monostable circuit, which produced the start pulse for the

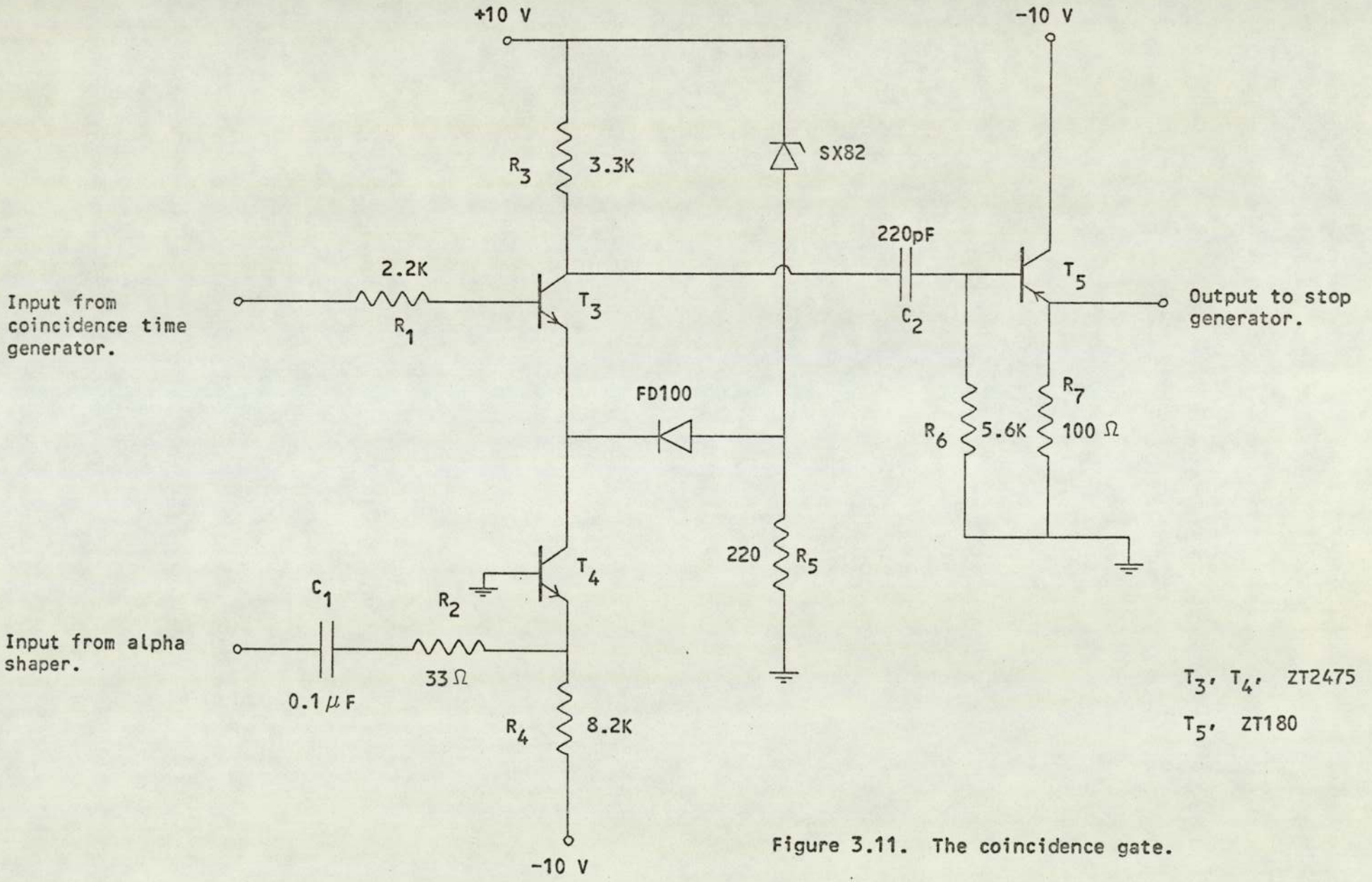

Figure 3.11. The coincidence gate.

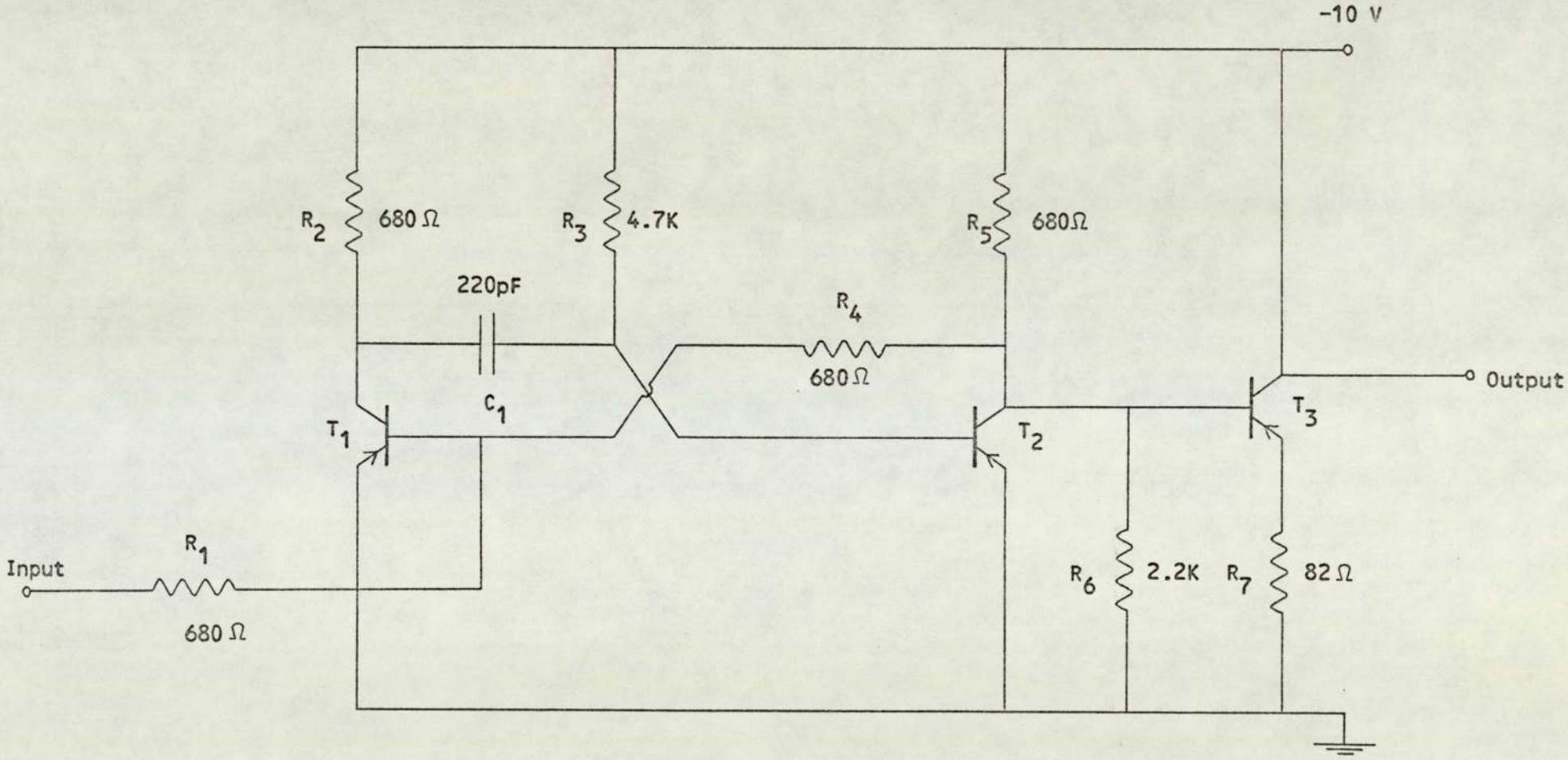

Figure 3.12. Start and Stop generators.

time to pulse height converter. The circuit used is shown in figure 3.12.

The Time Converter

Measurement of time intervals in the nanosecond range is usually made by converting the time interval into a voltage pulse. The time converter generates an output pulse whose amplitude is proportional to the time between the start and stop pulses. When a start pulse is applied it initiates the charging of a capacitor from a constant current source, and when a stop pulse is applied the charging is halted. The voltage across the capacitor is thus proportional to the time interval between the start and stop pulses.

The time converter used in the present work was a Nuclear Enterprises type NE 6250. The amplitude of the output pulse was 0 to + 10 volts with range selections of 0 to 50, 100, 200, 500 or 1000 ns In the absence of a stop pulse after the given time interval, the instrument automatically reset itself to its original mode.

The output pulses of the time converter were analysed in a 100 channel pulse height analyser, a TMC gammascope 1202.

3.7 Setting the Discriminators

It was necessary to set the discriminator levels for both the neutron and alpha particle detectors at a consistently reproducible known level. As was discussed in section 2.4 the neutron discriminator was set to reject pulses due to Na^{22} γ rays interacting in the neutron detector. The experimental arrangement for setting the neutron channel discriminator level is shown in figure 3.13.

With the Na^{22} source placed in front of the neutron detector, the count rate was measured as a function of the voltage on the base of transistor T_1 (figure 3.8), the voltage being adjusted by means of the 0 - 500 Ω potentiometer. Figure 3.14 shows the integral Compton spectrum obtained by plotting the count rate against base voltage. The differential Compton spectrum was obtained from this data by plotting

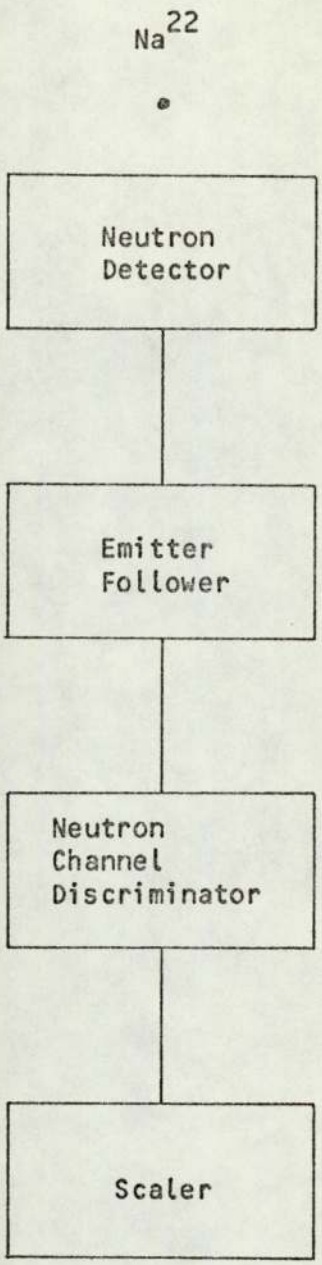

Figure 3.13. Block diagram of the electronics used to set the neutron channel discriminator level.

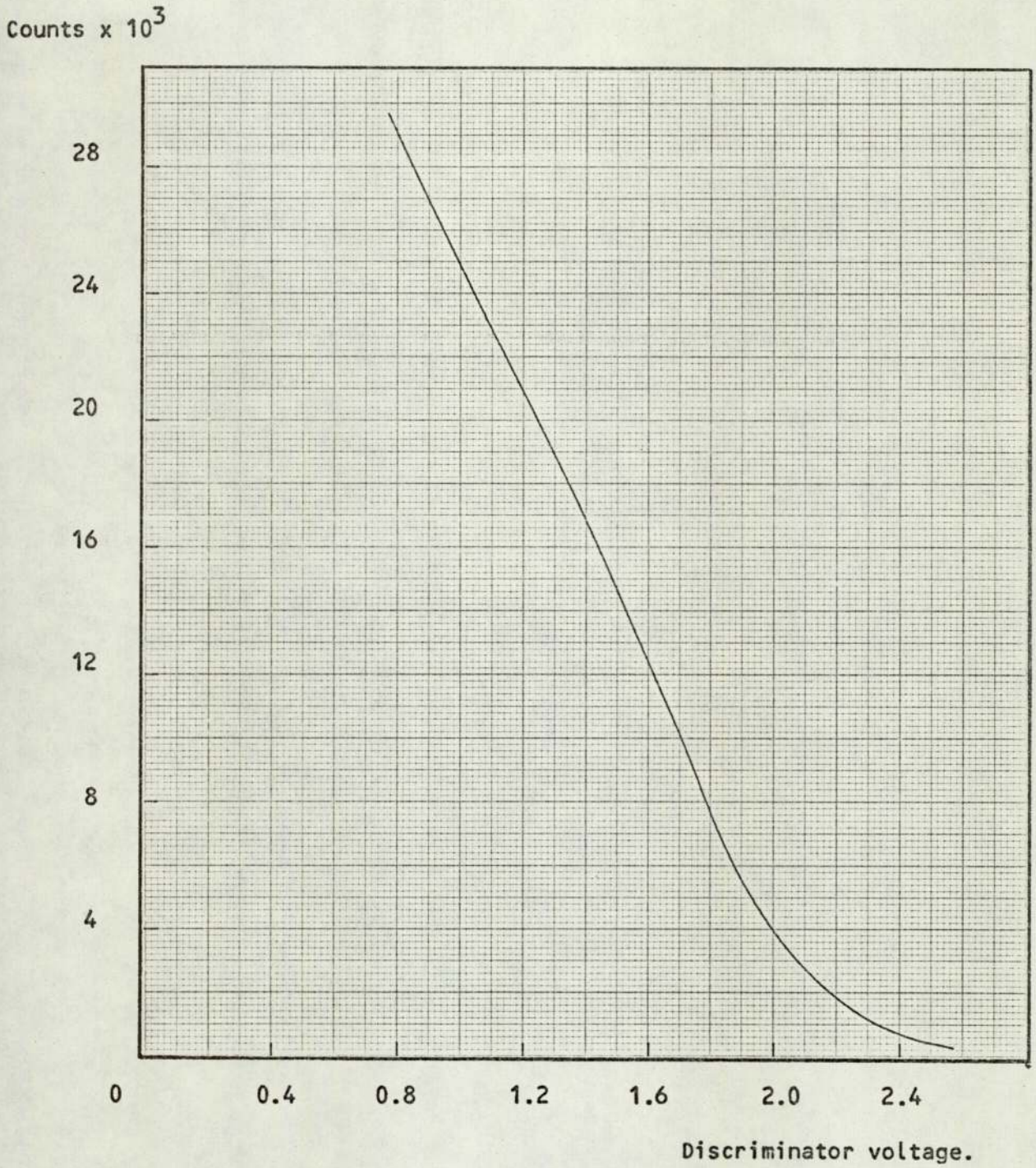

Figure 3.14. Integral Compton Spectrum for Na^{22} γ rays.

the difference in the number of counts in successive voltage intervals against that interval. The resulting spectrum is shown in figure 3.15. The Compton edge of the 1.274 MeV γ rays coincides approximately with the point at which the count rate fell to half its maximum value. At this point the voltage on the base of transistor T_1 was 2.05 volts.

The experimental arrangement used for setting the alpha detector discriminator level is shown in figure 3.16. The negative discriminator output pulses provided suitable gating pulses for the linear gate. As a result, the pulses below the discriminator level were blocked from the multichannel analyser. Figure 3.17 shows the pulse height spectrum of 3.52 MeV alpha particles produced in the deuteron bombardment of the target. The discriminator level as determined by the above method is shown in the figure. The voltage on the base of transistor T_1 in the alpha discriminator circuit was 1.25 volts.

The discriminator levels in both the neutron and alpha particle detector channels were checked before cross section measurements were made.

3.8 Electronic Testing

Linearity

To test that the coincidence gate was functioning correctly the linearity of the time converter-gate combination was examined. A random coincidence spectrum was obtained by using a pulse generator for the stop signal and an americium-beryllium neutron source for the start signal to the time converter. The experimental arrangement is shown in figure 3.18. Since the two signals are randomly related in time an equal number of counts should appear in each channel of the analyser. Linearity tests were performed with the time converter on the 0 - 100 ns, 0 - 200 ns and 0 - 500 ns ranges, with stop pulse repetition rates of 20 - 400 KHz. The best linearity was found on

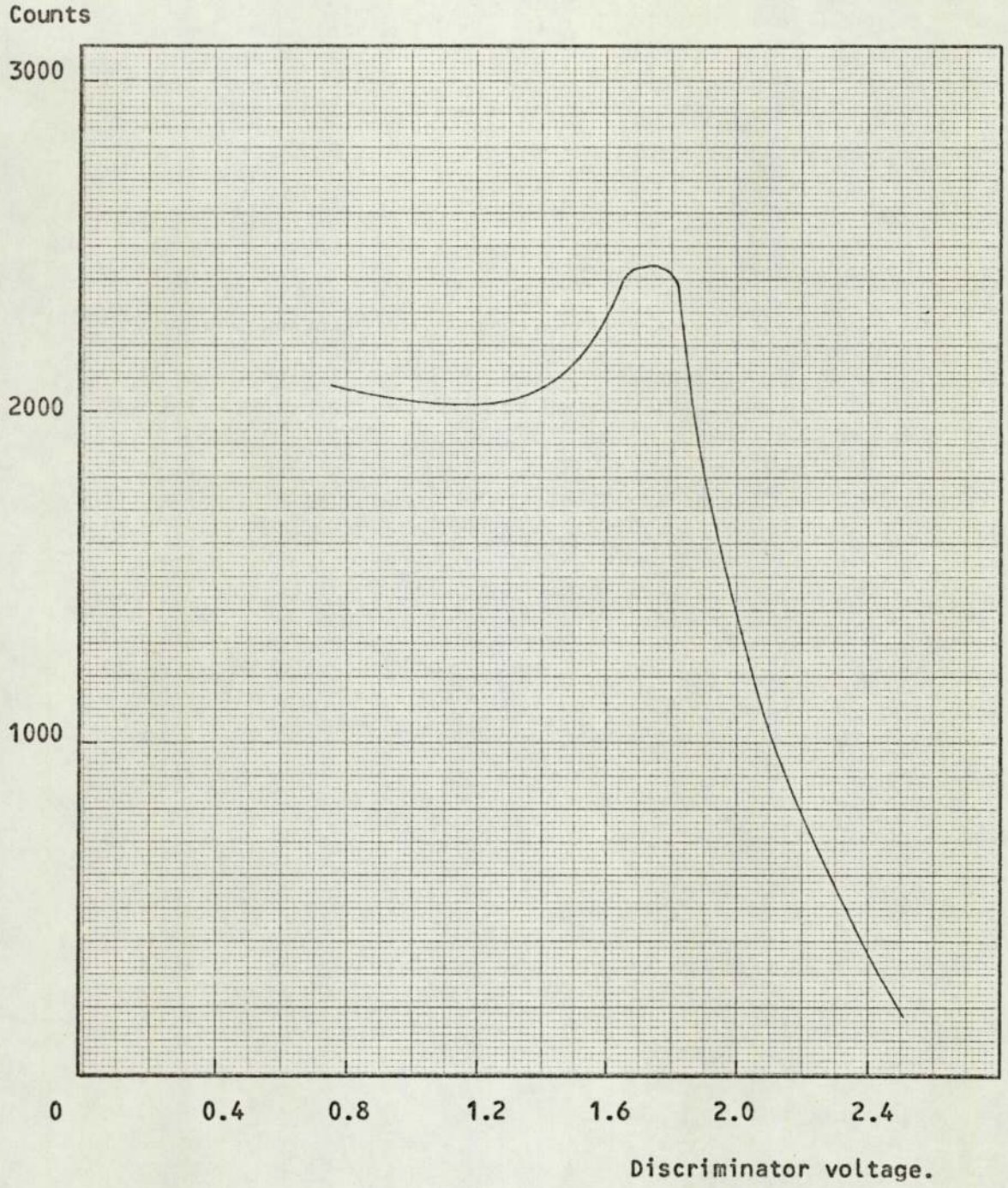

Figure 3.15. Differential Compton Spectrum for Na^{22} γ rays

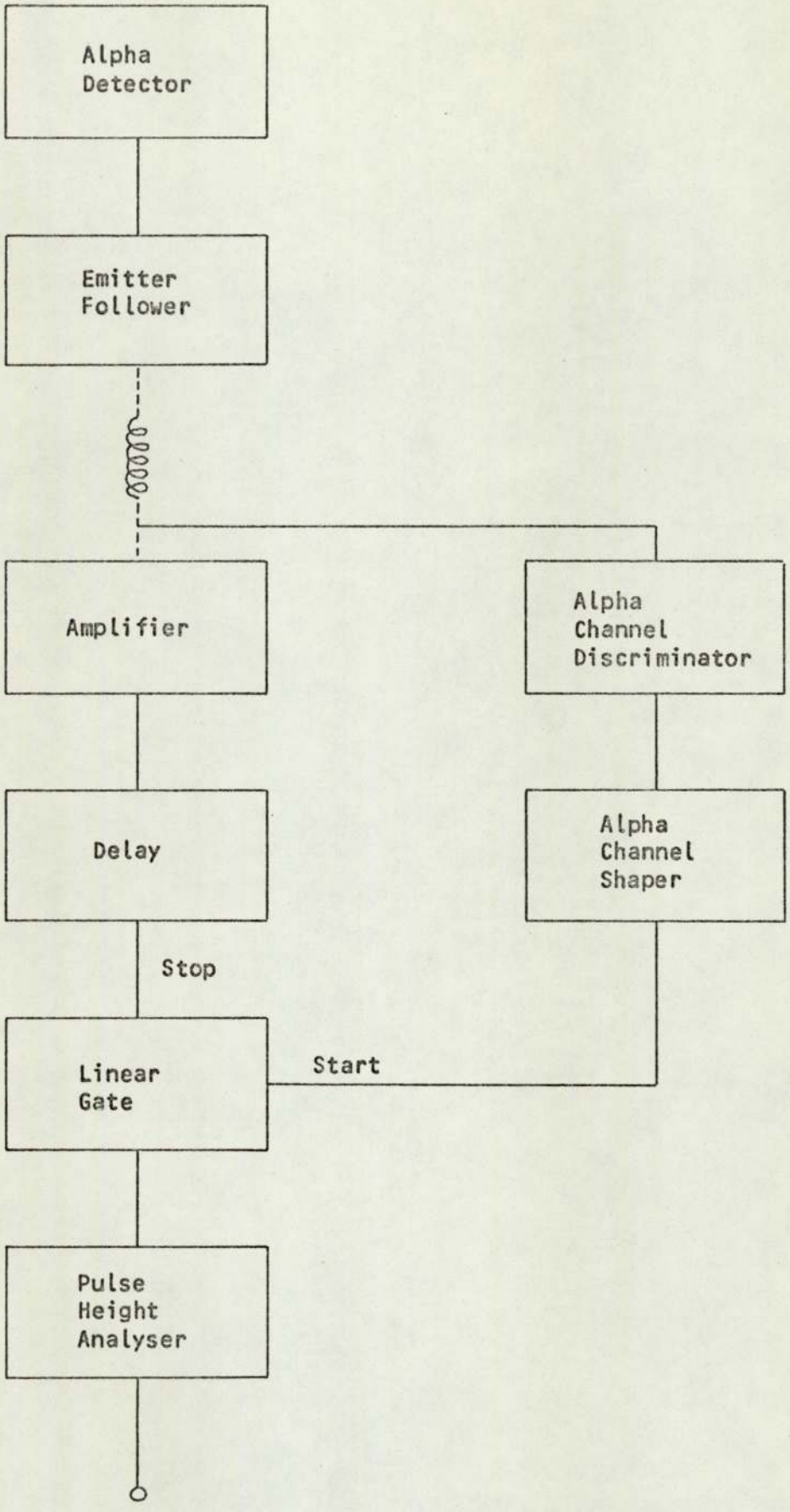

Figure 3.16. Block diagram of the electronics used to set the alpha particle channel discriminator.

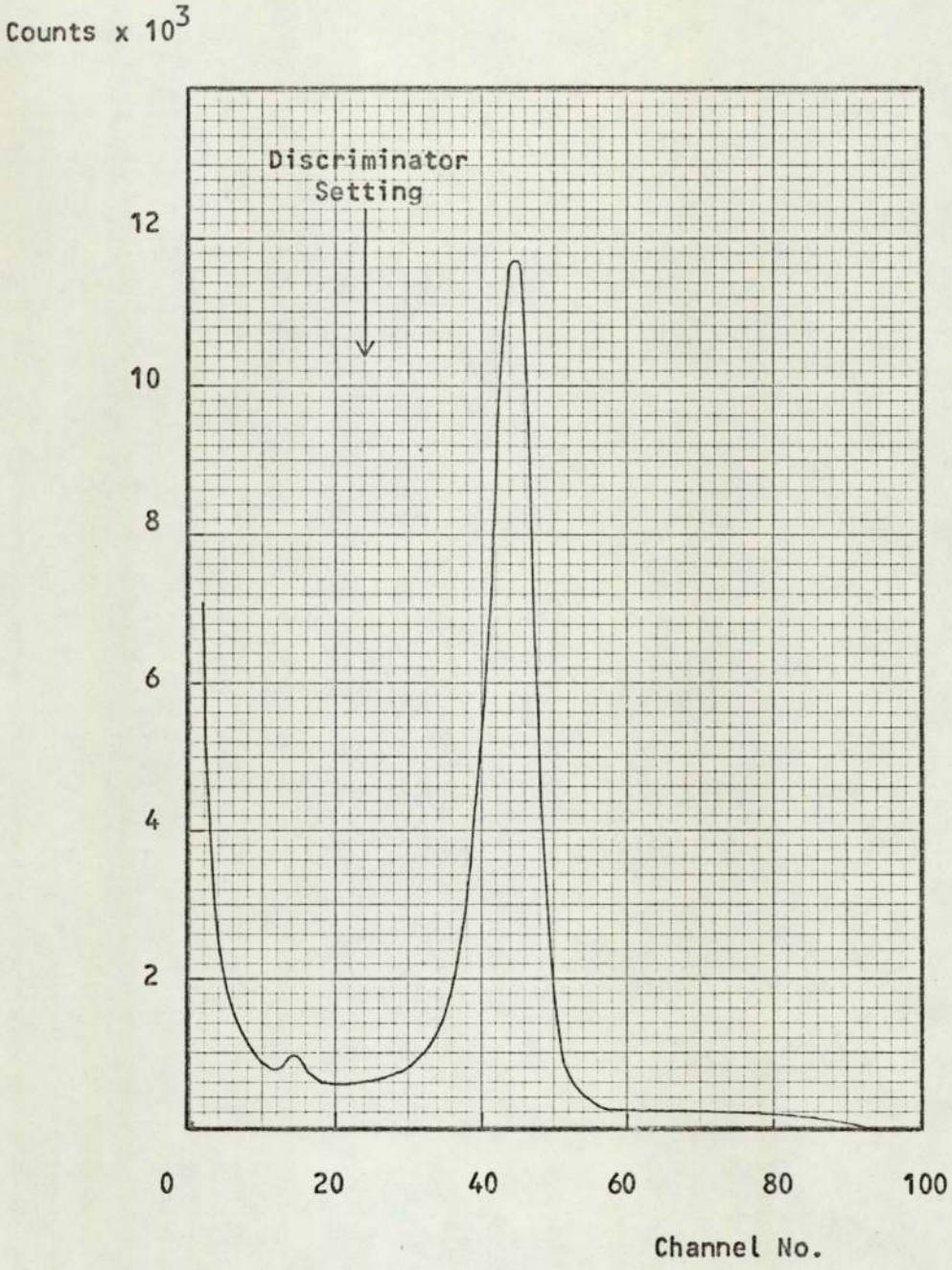

Figure 3.17. The alpha particle pulse height spectrum from the $^{3}H(d,n)^{4}He$ reaction.

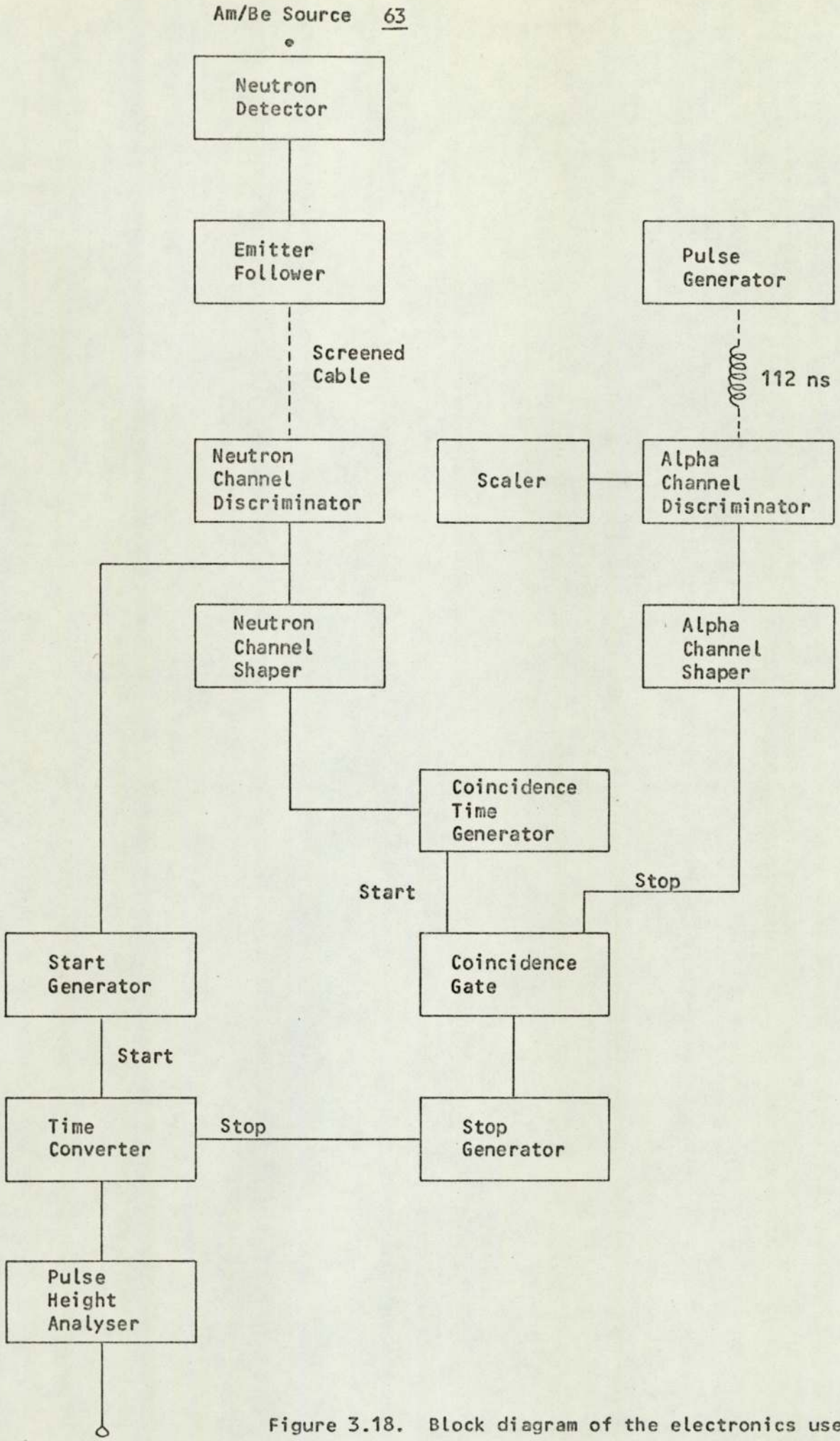

Figure 3.18. Block diagram of the electronics used to test the time linearity of the coincidence gate.

the 0 - 200 ns range, and was relatively insensitive to changes in the stop pulse repetition rate. As a result, all time of flight measurements were made on this range.

The spectrum obtained is shown in figure 3.19. The total length of the gate plateau was approximately 100 ns and the region used is shown in the figure. The spectrum indicates that apart from the non linear region after the start of the coincidence gate, the differential time linearity was $\pm$ 3%. This was considered satisfactory for the present work.

Time Resolution and Spectrometer Performance

There are sources of time uncertainty that arise in the measurement of the time interval between the initiation of an event and the registering of the detection of that event. The folding together of all contributing time uncertainties in production and detection of an event yields a total time uncertainty called the resolving time or time resolution. For analytical purposes this is given by the square root of the sum of the squares of the individual timing uncertainties; and this is equal to the full width at half maximum (FWHM) of a timing peak in a time of flight spectrum. The time resolution was measured by observing the direct neutron beam which was at an angle of 83^{o} to the incident deuteron beam direction. Figure 3.20 shows the coincidence curve obtained for a repetition rate of 100 KHz in the alpha particle channel. The curve shows a FWHM of approximately 2.5 ns.

With the associated particle method the neutron production time can be determined with a very small uncertainty. Most of the line width in the spectrum is due to (i) kinematic variations over the finite angular extent of the detectors, (ii) dispersion in the alpha particle velocities due to the thickness of the tritiated titanium target, (iii) dispersion in the neutron transit times in the neutron scintillator and, (iv) timing uncertainties in the associated electronics.

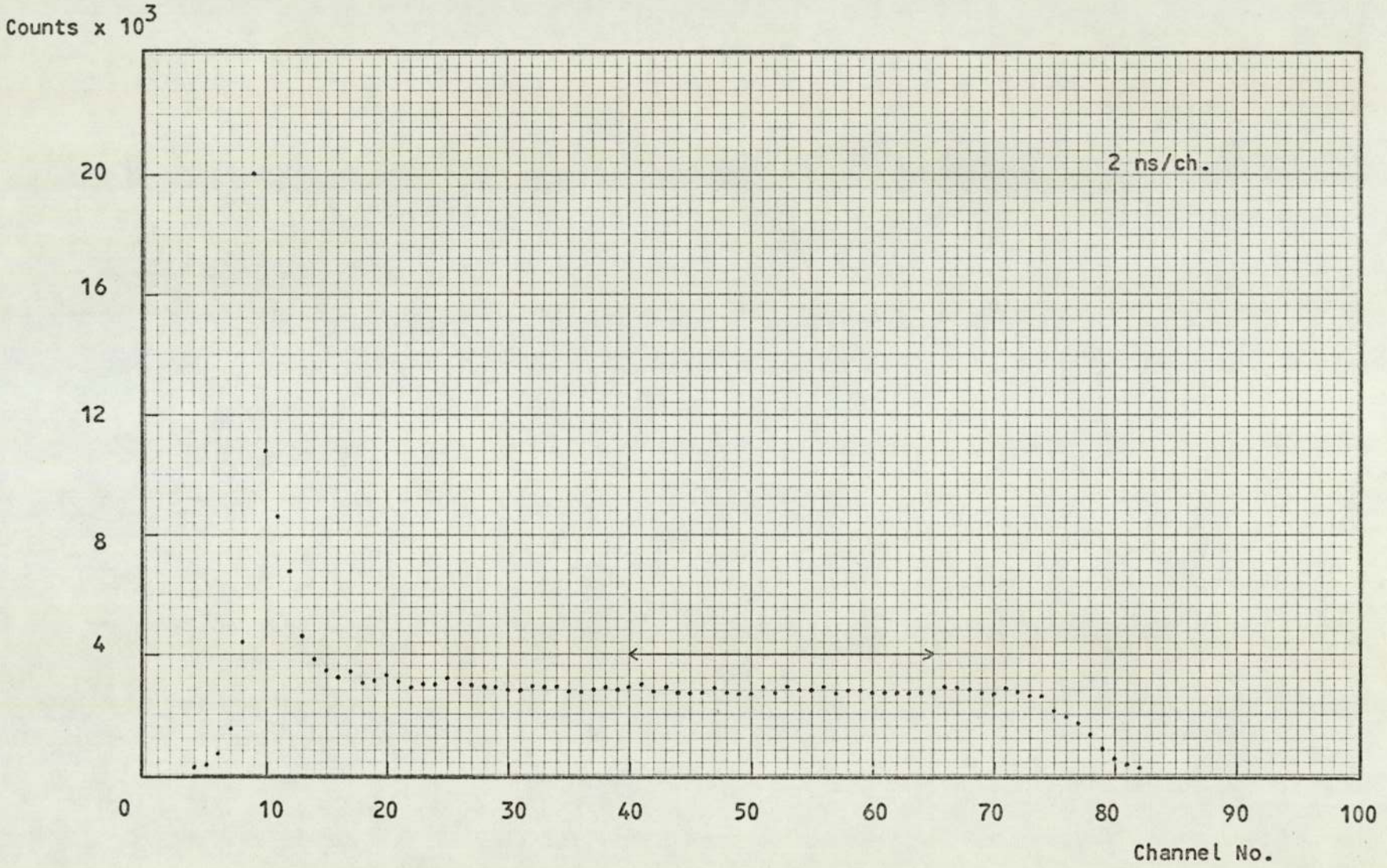

Figure 3.19. A random pulse time spectrum to test the differential timing linearity of the system.

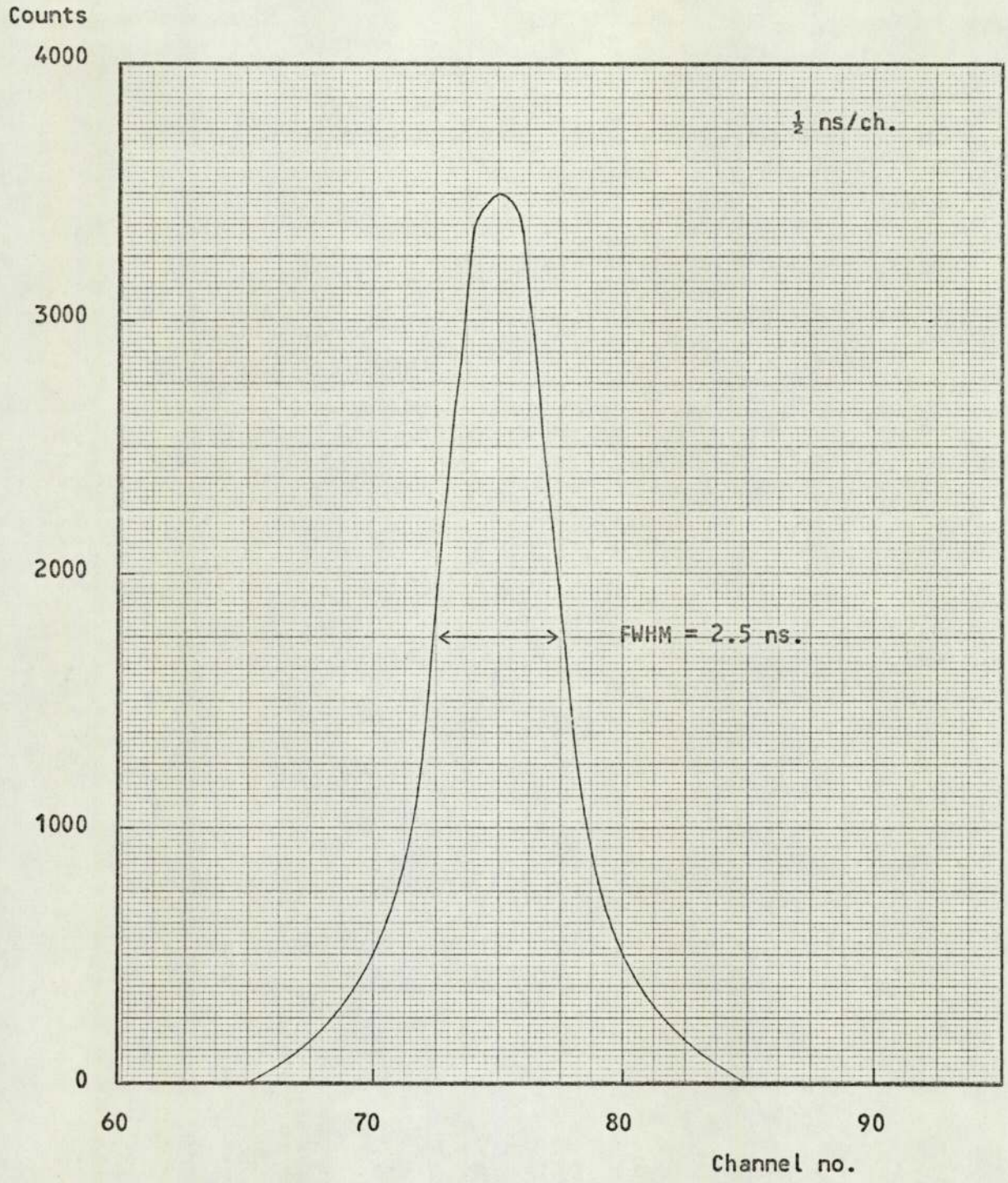

Figure 3.20. Spectrometer resolution.

At the instant of production the alpha particles had an energy of 3.52 MeV with a small energy spread of approximately 60 KeV, due to the ten degree angular range subtended by the alpha particle detector. However, alpha particles produced inside the target by lower energy deuterons lose energy in escaping the target and the effective alpha particle energy range was 3.28 MeV to 3.58 MeV. This resulted in a time spread of 0.4 ns over the 90 mm target to alpha particle detector flight path. The uncertainty in the transit time in the 50.8 mm thick neutron scintillator was 1 ns (section 2.2). Both photomultiplier tubes were Philips 56 AVP's which have a stated transit time spread of 0.5 ns.

The time resolution was also found to be dependent on the repetition rate of the signal in the alpha particle detector channel. The resolution varied from 2 ns for repetition rates up to 60 KHz, to 4 ns for repetition rates exceeding 150 KHz, and was accompanied by a small time shift of the centre of the coincidence curve to a lower channel number of the analyser. These effects were attributed to the change in gain of the alpha particle detector photomultiplier due to the higher count rate.

The time resolution of 2.5 ns indicated in figure 3.20 was sufficient for the present work. To ensure time stability of the associated particle spectrometer throughout all experimental observations, the repetition rate in the alpha particle detector channel was maintained at a constant rate of 100 KHz. The small loss in time resolution due to the higher count rate had obvious advantages over the amount of scattering data acquired.

CHAPTER 4

An Associated Particle Time of Flight System For Use with the Reaction $^{2}H(d,n)^{3}He$ at an incident deuteron energy of 150 KeV

4.1 Experimental Considerations

There are considerable experimental difficulties in applying the associated particle technique to the lower Q-value (3.26 MeV) $^{2}H(d,n)^{3}He$ reaction with incident deuteron energies below 200 KeV, if the associated ^{3}He particles are to be detected unambiguously and good timing resolution obtained. These difficulties arise from a combination of two factors; (i) the associated ^{3}He particles must be distinguished from a very much larger number of charged particles produced in other interactions in the target and, (ii) the low energy of the ^{3}He particles resulting from both the reaction kinematics and energy loss in escaping the target.

In addition to the ^{3}He particles from the $^{2}H(d,n)^{3}He$ reaction, other particles will be emitted from the target namely, (i) deuterons elastically scattered by the Coulomb field of the target nuclei, (ii) protons and tritons both produced in the reaction $^{2}H(d,p)^{3}H$ and, (iii) neutron capture γ rays from surrounding material. The separation of these other particles is especially important since for a determination of the neutron flux at the scattering sample, the number of ^{3}He particles must be accurately known.

Due to the energy loss of the deuterons in the target, the energy distribution of the scattered deuterons is a continuous distribution between zero and E_d, the energy of the incident deuterons from the accelerator. The number of scattered deuterons is higher than the number of ^{3}He particles by a factor of about 10^{5}, and in general, pile up of the deuteron pulses will occur in the ^{3}He particle detector

channel. Therefore, unless the pulse height for the ^{3}He particles is much more than the pulse height for deuterons, a discrimination between deuterons and ^{3}He particles cannot be made in the detector alone.

The cross sections for the ^{2}H(d,n)^{3}He and ^{2}H(d,p)^{3}H reactions are approximately equal for incident deuteron energies up to 200 KeV. Consequently, the number of protons and tritons is of the same order as the number of ^{3}He particles. Due to the higher Q-value (4.032 MeV) in the latter reaction, the proton and triton energies (approximately 1 MeV and 3 MeV respectively) are higher than the ^{3}He particle energy, and it is possible to get different pulse heights for the ^{3}He particles and for the protons and tritons. For an incident deuteron energy of 150 KeV the ^{3}He particle energy is rather low, i.e. ~800 KeV, therefore the main difficulty arises from deuterons elastically scattered from the target. It is extremely difficult under such conditions to avoid events in the associated ^{3}He particle detector which are in no way associated with coincident neutrons. A low deuteron bombarding energy allows better discrimination between scattered deuterons and the associated ^{3}He particles, since the energy difference between them decreases at higher bombarding energies. Various methods have been applied to eliminate some of the difficulties discussed so far.

McFadden et al[42] and Schuster [43] tried to reduce the number of scattered deuterons by using a thin deuterated polytheylene target. While this method has the advantage that the full energy of the ^{3}He particles is available for effecting a detector response, the count rate in the unshielded detector and associated electronics is high and the ^{3}He particle pulses are usually not well resolved in the detector pulse height spectrum. Furthermore, because of the difficulty in producing satisfactory targets for use with low incident deuteron energies, the method is effectively restricted to deuteron energies in the MeV range.

Franzen et al[44] used a gas target, and took an angle greater than 90° between the direction of the ^{3}He particles and the incident deuteron beam. In this way they eliminated the effect of scattered deuterons because no deuterons can be scattered by deuterium gas over angles greater than 90°. However, the use of gas targets introduces considerable problems in that the target must be isolated from the accelerator vacuum system either by thin windows, or by a differential pumping system.

Dixon and Aitken[45], working on the absolute cross section of the $^{39}K(n,p)^{39}Al$ reaction for 2.5 MeV neutrons at an incident deuteron energy of 100 KeV, used a thin CsI(Tℓ) crystal for the ^{3}He particle detector. A crystal of thickness 0.51 mm and diameter 25.4 mm was used, with a film of aluminium evaporated on one side of the crystal. The main disadvantages with a detection system of this type are threefold. (i) The thickness of the foil covering the crystal is critical. The foil thickness must be sufficient to prevent scattered deuterons from reaching the crystal, but must not be thick enough to degrade the ^{3}He particle pulse height to a level comparable with the noise level of the system. (ii) The inherently poor resolution of a CsI(T,ℓ) crystal results in a broad ^{3}He particle peak. Consequently, if genuine ^{3}He particles only are to be selected for neutron flux determination, a narrow pulse height window must be used. Such a restriction would result in a relatively low ^{3}He particle counting rate with consequent poor efficiency. (iii) The sensitivity of the crystal to neutron capture γ radiation is not entirely negligible even for thin crystals.

A considerable improvement is made by the use of a semi-conductor detector as the associated particle detector[46,47,48]. The use of this type of detector has the advantage of giving better discrimination between particles, because the height of the pulses from such a detector is proportional to the energy the particles lose in the

sensitive region of the detector. The intrinsically good resolution of semi-conductor detectors, combined with their low sensitivity to γ rays, reduces considerably the restrictions previously necessary on the foil window in front of the detector. It is only necessary to ensure that the foil thickness is adequate to prevent scattered deuterons from reaching the detector. Bell et al[46], working at an incident deuteron energy of 100 KeV with a gold "drive-in" target, used a silicon surface barrier detector with a separately mounted nickel foil. The thickness of the foil used was sufficient to completely absorb scattered deuterons but allowed the residual ^{3}He particle energy to effect a detector response above the noise level. The upper limit to the deuteron energy at which this method may be usefully employed results from this last requirement, since the deuteron range in the absorber increases more rapidly with energy than that of the ^{3}He particles emitted in the reaction. A marked disadvantage in the use of foils as discussed is that the absorbing foils are extremely thin, and the method is effectively restricted to incident deuteron energies below 100 KeV[45][46].

As is evident from the discussion so far, the discrimination cannot be realised completely by the detector or by an absorber. However, in an attempt to overcome the limitations in detection of the associated ^{3}He particles, a selection system can be introduced before the particles strike the detector. This can be effected by using an electrostatic or magnetic field in which the particles are deflected with curvatures depending on their charge, energy and mass. Both of these methods allow resolution of the ^{3}He particles without the use of a foil in front of the detector. The advantages of such an associated particle detection system are numerous. However, the method requires longer flight paths for the ^{3}He particles, causing a large variation in the flight times of ^{3}He particles of different energies with a resulting loss in the achievable coincidence time resolution between the neutrons and ^{3}He

particles. Magnetic or electrostatic deflection also allows detection of ^3He particles of only one of three stable charge states ($^3He^o$, $^3He^+$ and $^3He^{++}$) emerging from the target, thus decreasing the coincident neutron flux for a fixed incident deuteron beam.

Bartle et al[49], using a magnetic analyser, found that the associated ^3He particles were completely resolved for a range of deuteron energies starting at 100 KeV, even with a detector of medium quality. Increased neutron yields are possible at higher deuteron energies because, since the detector no longer requires an absorbing foil, the danger of detector damage due to window failure is removed. The full energy of the ^3He particles is expended in the detector giving an improved signal response and consequently improved resolution, also the associated particles may be observed at angles for which the ^3He particle energy is relatively small. These same advantages apply to an electrostatic discrimination system[50]. The condition for different deflection is:

$$E_{^3He} > 2E_d \text{ for an electrostatic field} \quad \ldots\ldots 4.1(a)$$

$$E_{^3He} > \frac{8}{3} E_d \text{ for a magnetic field} \quad \ldots\ldots 4.1(b)$$

where $E_{^3He}$ is the energy of the ^3He particles emitted from the target and E_d is the incident deuteron energy. From these conditions it is seen that the best discrimination is possible with an electrostatic system.

The parameters which determine the associated particle method are E_d, the incident deuteron energy and $\theta_{^3He}$, the angle of emission of the ^3He particles. The best discrimination between ^3He particles and deuterons is possible when the ratio $E_{^3He}/E_d$ is as large as possible. This implies that both $\theta_{^3He}$ and E_d have to be as small as possible. However, $\theta_{^3He}$ cannot be too small because the ^3He particles then have

long paths through the target, which implies a large energy loss. Furthermore, at low incident deuteron energies the neutron yield is small and therefore E_d must have an appreciable value.

For a good discrimination a small angular spread in the ^3He particle beam is essential. Therefore a small value of $d\theta_{^3He}/dE_{rt}$ is required, where E_{rt} is the deuteron energy at which the reaction takes place in the target. The requirement for a small value of this quantity is connected with the desirability to use a reasonable thickness of the target in order to get high intensity in the coincident neutron beam.

4.2 The ^3He Particle Detector

A comparison of the methods discussed shows that probably the best associated particle detection system for use with the $^2H(d,n)^3He$ reaction, is discrimination of the particles by an electrostatic field in conjunction with a semi-conductor detector. This was the method adopted in the present work.

Taking into account the limitations on experimental facilities and space available, an electrostatic plate analysing system was used for particle discrimination, with a silicon surface barrier detector as the ^3He particle detector. The associated ^3He particles were detected at an angle of 90^o to the incident deuteron beam. As well as fitting in conveniently with existing experimental arrangements, this was accepted as a reasonable compromise with respect to the problem of energy losses in the target.

4.3 Expected Neutron Yield at 90^o from a Titanium Deuteride Target of Uniform Deuterium Atomic Ratio

The lack of sufficiently accurate experimental data on the cross section of the $^2H(d,n)^3He$ reaction and on the energy loss of deuterons in titanium deuteride at incident energies up to 150 KeV, required calculations in order to obtain a yield curve for titanium

deuteride. These calculations were necessary in order to estimate the number and range of energies of the ^{3}He particles escaping from the target and hence to design a suitable electrostatic deflection system. The deuterated titanium target used was supplied by the Radiochemical Centre and had a deuterium atomic ratio (i.e. loading factor) of 1.2.

Method of Calculation

It was assumed that the deuterium atomic ratio of 1.2 deuterium atoms per titanium atom was constant throughout the whole thickness of the target material, and that any surface contamination layer was of negligible thickness. This assumption has been found to be justified by Gunnersen and James[51] and Woods and Saker[52], in calculating the expected neutron yields from tritiated titanium targets.

From the theory of the yield of a nuclear reaction, the total yield of particles per incident deuteron of energy E is given by:

$$Y = \int_{o}^{E} \frac{n_t \, \sigma(E) dE}{dE/dx} \qquad \ldots\ldots \quad 4.2$$

where n_t is the number of deuterium atoms per cm^3 (assumed constant), $\sigma(E)$ is the cross section at energy E for the $^{2}H(d,n)^{3}He$ reaction, dE/dx is the rate of loss of energy of deuterons of energy E in the titanium deuteride target and dE is a constant small energy interval. The yield per incident deuteron per steradian at 90^{o} in the laboratory system is then given by:

$$dY = \int_{o}^{E} \frac{n_t \left(\frac{d\sigma}{d\omega}\right)_{90^o}(E) \; dE}{dE/dx} \qquad \ldots\ldots \quad 4.3$$

where $\left(\frac{d\sigma}{d\omega}\right)_{90^o}(E)$ is the differential cross section at energy E for

the $^{2}H(d,n)^{3}He$ reaction at 90^{o} in the laboratory system.

The value of the constant n_t is obtained as follows. If the target material TiD_N contains N = 1.2 deuterium atoms per titanium atom, then the density ρ_{TiD_N} of the target material is given by:

$$\rho_{TiD_N} = \frac{48 + 2N}{48} \times \rho_{Ti} \times 0.85 = 4.05 \quad . \; . \; . \qquad 4.4$$

where $\rho_{Ti} = 4.54$. The factor 0.85 arises from the 15% expansion which the deuterium lattice undergoes during deuteration. The number n_t of deuterium atoms per cm^3 is then

$$n_t = \frac{1.2 \times \rho_{TiD_N} \times 6.02 \times 10^{23}}{A_{TiD_N}} = 5.8 \times 10^{22} \quad .. \; 4.5$$

The chief source of error in calculating the yield over an extended energy range is the lack of reliable experimental data on the rate of energy loss dE/dx of deuterons in titanium deuteride. There are no experimental figures available on the rate of energy loss of deuterons in either titanium deuteride, titanium alone, or deuterium alone for the required energy range. Moreover, most available data on the rate of energy loss of deuterons in other metals usually does not extend down to energies less than 100 KeV; Allison and Warshaw[53]. Warshaw[54], however, has made some measurements on the rate of energy loss of protons in aluminium, copper, silver and gold for the proton energy range 50 - 350 KeV, which corresponds to deuteron energies of 100 - 700 KeV.

The data used for the energy loss of deuterons in titanium was that of Woods and Saker[52]. To obtain a curve for titanium they assumed a law relating energy loss to atomic weight, i.e., $dE/dx \propto A^{-\frac{1}{2}}$.

By taking Warshaw's results for the metals quoted overleaf, the assumption was found to be valid at higher deuteron energies between 300 - 400 KeV and only for materials of light atomic weight. The assumption of Segré[55], that $dE/dx \sim A^{-1/3}$ gave no better results. Thus a straightforward interpolation assuming a power law was not regarded as reliable. The method used consisted of plotting dE/dx against $A^{-1/2}$ and also $A^{-1/3}$, using Warshaw's figures, for the points of deuteron energy 200, 150 and 100 KeV, giving reasonably smooth curves, from which the average intercepts corresponding to titanium were obtained. A curve was drawn, and produced to the point dE/dx = 200, E = 60 from where it was joined to the origin by assuming $dE/dx \sim E^{\frac{1}{2}}$. The curve obtained is shown in figure 4.1 and the data given in table 4.1[52]. Obviously, the probable error of points obtained by this method cannot be small, particularly as there exists no adequate theory of stopping power in the region in question, but in the absence of any anomaly an accuracy of $\pm$ 5% should apply.

The rate of energy loss of deuterons in deuterium was obtained from a paper by Dalgarno and Griffing[56] in which experimental results of several workers for proton energy loss in hydrogen are collected. The energy loss in deuterium in KeV/mg.cm^{-2} is equal to one half of the energy loss in hydrogen in KeV/mg.cm^{-2}, since the atomic weight is 2 but the nuclear charge is the same. The data obtained is given in table 4.1. The probable error in figures obtained by Dalgarno and Griffing[56] was estimated to be $\pm$ 5% above 20 KeV deuterons, increasing to possibly $\pm$ 10% for the lower values.

The only known approximation to use for the value of dE/dx for deuterons in titanium deuteride is that value obtained by assuming that Braggs Rule holds, i.e., that the energy loss in a compound is the sum of the energy losses in its separate constituents. Hence,

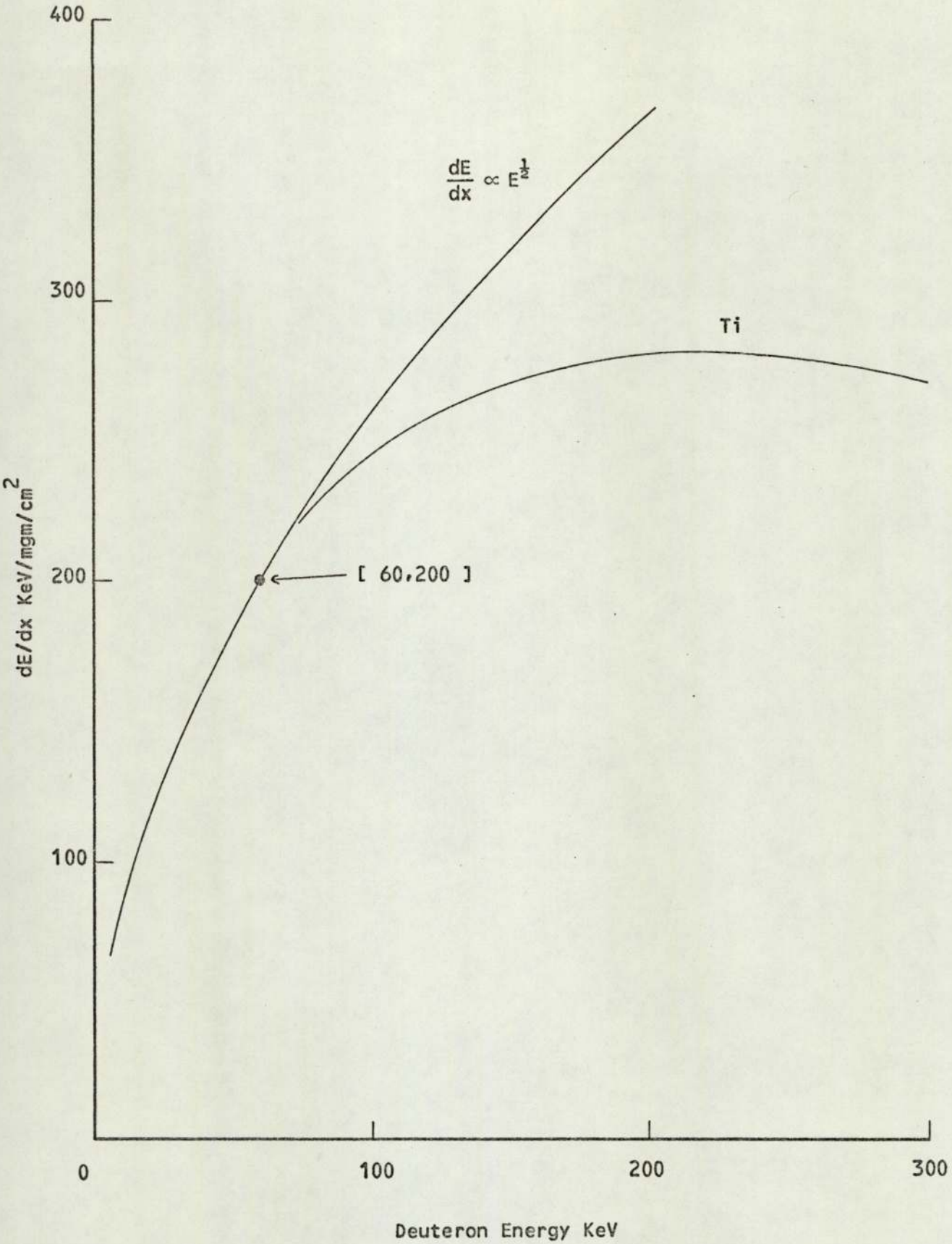

Figure 4.1. Energy loss of deuterons in titanium, from Woods and Saker[52].

Table 4.1

Energy loss data for Titanium, Deuterium and Titanium Deuteride

Deuteron Energy KeV	$(dE/dx)_{Ti}$ KeV/mg.cm^{-2}	$(dE/dx)_{D}$ KeV/mg.cm^{-2}	$(dE/dx)_{TiD}$ KeV/mg.cm^{-2}
10	82	960	124.14
15	100	1080	147.04
20	115	1176	165.93
25	129	1257	183.15
30	141	1341	198.60
35	153	1404	213.05
40	163	1470	225.74
45	173	1524	237.85
50	183	1566	249.39
60	200	1671	270.61
70	214	1758	288.11
80	226	1824	302.70
90	236	1875	314.67
100	245	1905	324.68
110	251	1926	331.40
120	257	1926	337.11
130	262	1917	341.44
140	266	1902	344.53
150	270	1884	347.47
160	273	1860	349.18

$$\frac{dE}{dx} = \frac{48}{48 + 2N}\left(\frac{dE}{dx}\right)_{Ti} + \frac{2N}{48 + 2N}\left(\frac{dE}{dx}\right)_{D} \quad \ldots\ldots \quad 4.6$$

$$= 0.952\left(\frac{dE}{dx}\right)_{Ti} + 0.048\left(\frac{dE}{dx}\right)_{D} \quad \text{for } N = 1.2$$

There is evidence that this law holds sufficiently accurately for those compounds for which it has been investigated provided the incident energy is not less than about 10 KeV[56,57,58]. Just how low in deuteron energy it is possible to go before the law deviates for TiD is uncertain. Using equation 4.6, the curve obtained for the energy loss of deuterons in TiD is shown in figure 4.2, and the data is listed in table 4.1.

The values of the differential cross section at 90^{o} in the laboratory system for the reaction $^{2}H(d,n)^{3}He$ were calculated from the total cross section data measurements of Arnold et al[59]. They measured the differential cross section of the reaction at 90^{o} but published only the total cross section data. Figure 4.3 shows the total cross section of the reaction for the energy range 0 - 150 KeV. The total cross section was calculated by the equation:

$$\sigma_{Total} = 4\pi g h(E)\left(\frac{d\sigma}{d\omega}\right)_{90^{o}} \quad \ldots\ldots\ldots \quad 4.7$$

where 'g' is the correction to the counter solid angle for motion of the centre of mass, and h(E) is the correction factor for the angular anisotropy of the reaction products in the laboratory system. The correction 'g' was applied although its value was only 1.02. The factor h(E) was of the form:

$$h(E) = \frac{1}{1 + \frac{1}{2}C_2 + \frac{3}{8}C_4 + \left\{\frac{3}{2}C_2 + \frac{30}{8}C_4\right\}p^2} \quad \ldots \quad 4.8$$

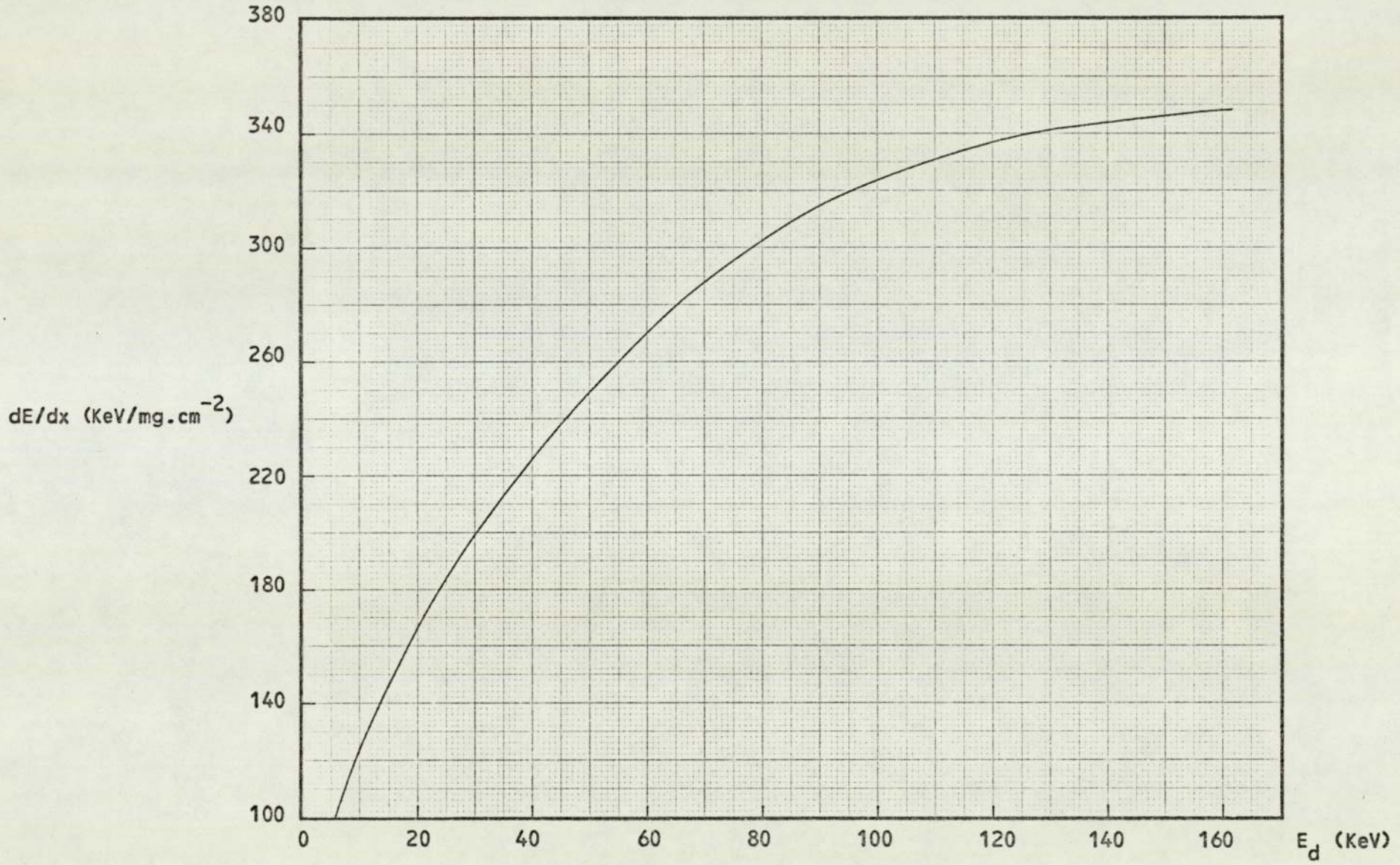

Figure 4.2. Calculated energy loss of deuterons in titanium deuteride.

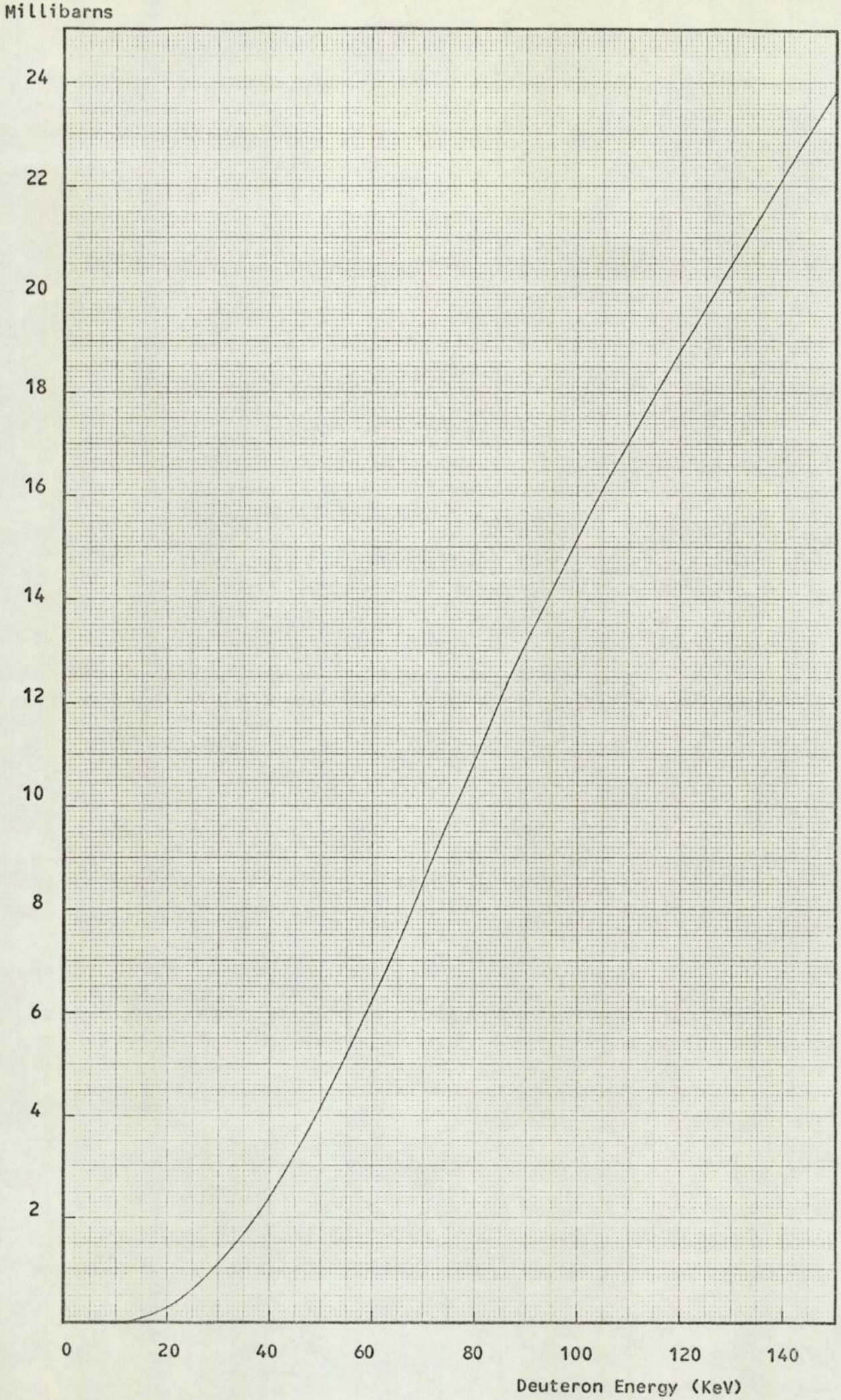

Figure 4.3. Total cross section for the $^{2}H(d,n)^{3}He$ reaction.

where C_2 and C_4 are experimentally determined coefficients in the Legendre polynomial expansion of the anisotropy, taken from the data of Wenzel and Whaling[60] and

$$p^2 = \cos^2\theta = \frac{3E}{(8000 + E)} \quad \ldots\ldots 4.9$$

where θ is the centre of mass angle that corresponds to 90^o in the laboratory system and E is the energy in KeV in the laboratory system. The experimentally determined values of C_2 and C_4 in the Legendre polynomial expansion of the anisotropy viz.,

$$\frac{d\sigma}{d\omega} = \frac{\sigma_T}{4\pi}[1 + C_2P_2(\cos\theta) + C_4P_4(\cos\theta) + \ldots] \quad \ldots 4.10$$

undertaken by Wenzel and Whaling[60] for the five energies considered, are listed in table 4.2.

Using the total cross section data of Arnold et al[59], the data of table 4.2, and equations 4.7, 4.8 and 4.9, the required differential cross section of the reaction $^2H(d,n)^3He$ was calculated for the energy values given in table 4.2. The results are listed in table 4.3. Figure 4.4 shows a curve of the differential cross section as a function of energy, fitted to the data of table 4.3.

By use of equation 4.3, the yield per incident deuteron per steradian at 90^o was calculated as a function of deuteron energy. Figure 4.5 shows the resultant yield curve of neutrons per microcoulomb of deuterons (1.6×10^{-13} particles). The results are listed in table 4.4.

Most of the inaccuracy in these calculations arises from the uncertainty in the energy loss figures for deuterons in titanium deuteride. Because of the extrapolation involved at low energies, it would be unjustifiable to claim an accuracy greater than $\pm$ 10% and it

Table 4.2

Legendre Polynomial Coefficients

E_d KeV	C_2	C_4
35	0.155	0.020
50	0.195	0.020
70	0.247	0.020
100	0.310	0.023
150	0.400	0.031

Table 4.3

Differential Cross Section of the Reaction $^2H(d,n)^3He$

E_d KeV	p^2	h(E)	σ_T mb	$(d\sigma/d\omega)_{90^o}$ mb/st
35	0.0131	0.918	1.7	0.147
50	0.0186	0.899	4.2	0.372
70	0.0260	0.875	8.5	0.773
100	0.0370	0.845	15.2	1.431
150	0.0550	0.799	23.8	2.370

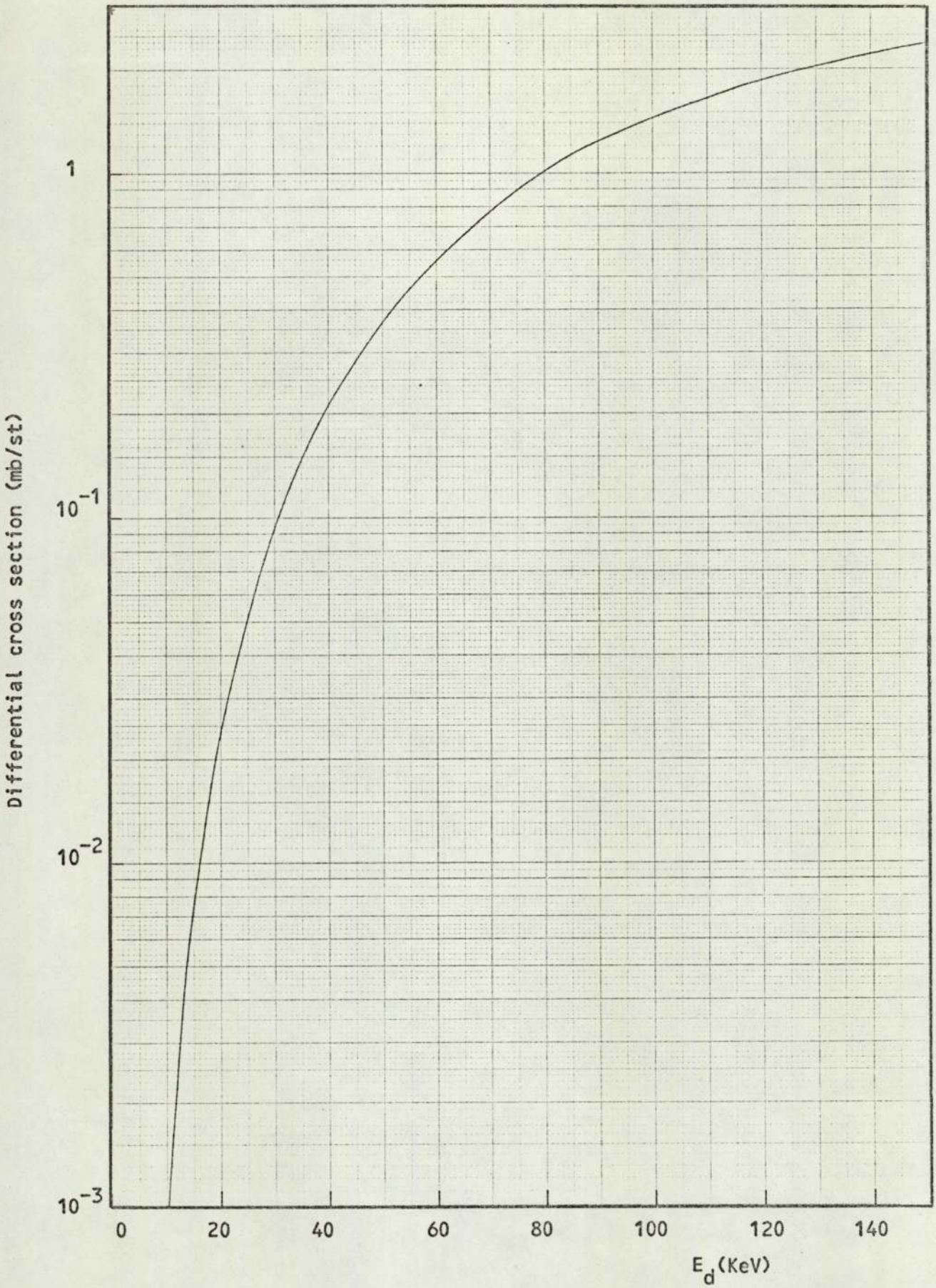

Figure 4.4. The differential cross section for the $^{2}H(d,n)^{3}He$ reaction.

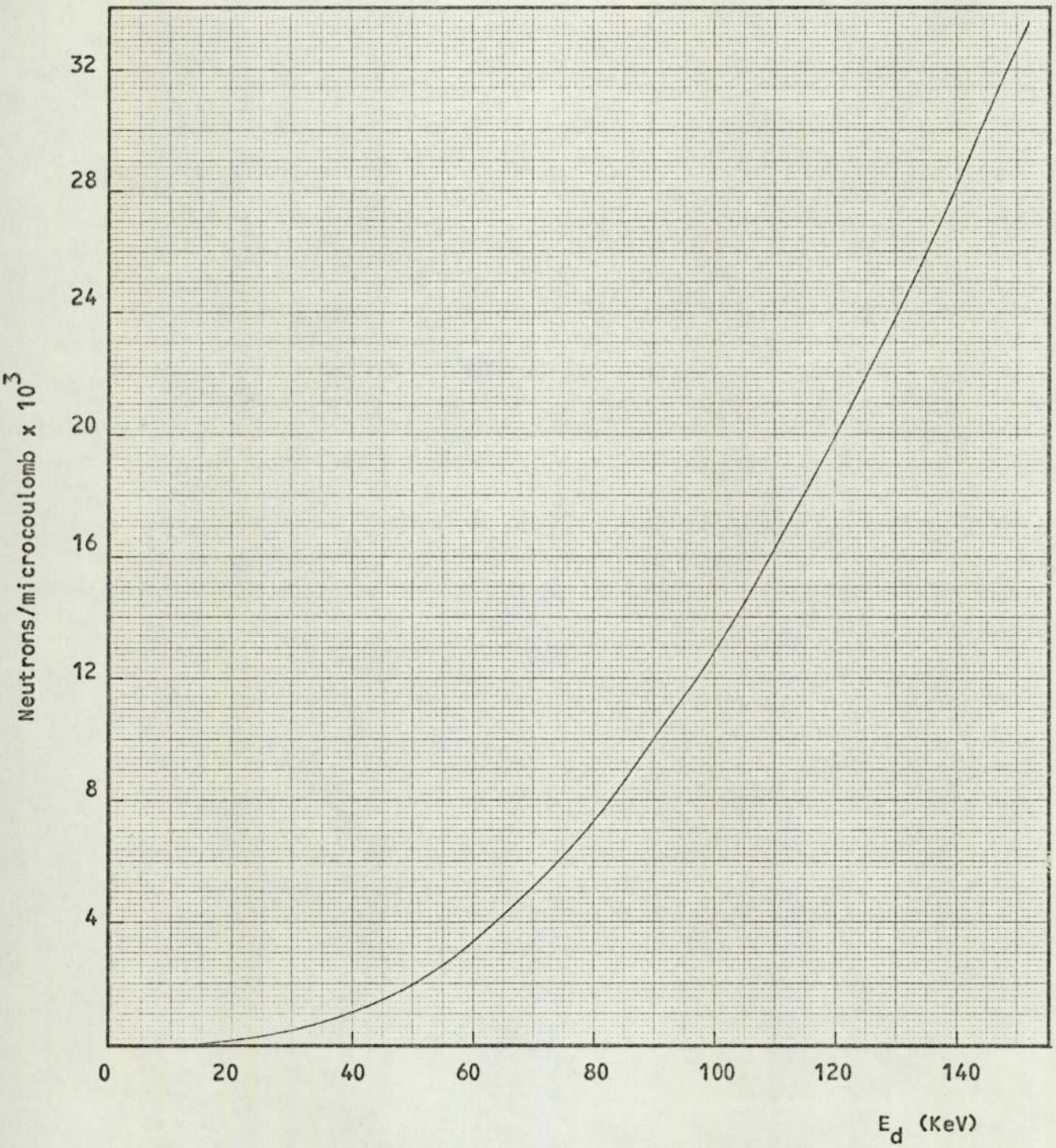

Figure 4.5. Yield of neutrons per microcoulomb of deuterons.

Table 4.4

Yield per Microcoulomb of Deuterons

Energy Interval (KeV)	$dY \times 10^{-4}$ ($mg.cm^{-3}$)	$\frac{dY \times 10^{-7}}{\rho}$	$\sum \frac{dY \times 10^{-7}}{\rho}$	Neutrons per μ coulomb
15 - 25	0.00068	0.000150	0.000150	0.094×10^3
25 - 35	0.00231	0.000508	0.000658	0.411×10^3
35 - 45	0.00454	0.000999	0.001660	1.036×10^3
45 - 55	0.00724	0.001590	0.003250	2.030×10^3
55 - 65	0.00992	0.002180	0.005430	3.390×10^3
65 - 75	0.01300	0.002860	0.008290	5.170×10^3
75 - 85	0.01600	0.003520	0.011810	7.370×10^3
85 - 95	0.01890	0.004160	0.015970	9.970×10^3
95 - 105	0.02150	0.004730	0.020700	12.920×10^3
105 - 115	0.02430	0.005350	0.026050	16.260×10^3
115 - 125	0.02660	0.005850	0.031900	19.910×10^3
125 - 135	0.02860	0.006290	0.038190	23.840×10^3
135 - 145	0.03100	0.006820	0.045010	28.100×10^3
145 - 155	0.03330	0.007330	0.052340	32.670×10^3

may be very much worse than this for incident deuteron energies of less than 20 KeV. It is important to note, however, that above 20 KeV, the general shape of the yield curve is far more likely to be correct than the absolute position of the curve on the ordinate scale. Furthermore, at low incident energies the effect of surface contamination is likely to be serious in reducing incident ion energy. An uncontaminated surface, rather than a high atomic ratio, is the most essential property of a target operating at low incident energies.

4.4 Energy of the ^{3}He Particles Escaping the Target

In order to find the energies with which the ^{3}He particles escape the target, it is necessary to find the range of deuterons in titanium deuteride and the energy loss of ^{3}He particles in titanium deuteride.

The range of a deuteron of incident energy E_d in a material in which its rate of energy loss is dE/dx is given by:

$$R(E_d) = \int_o^{E_d} \frac{dE}{dE/dx} \qquad \ldots\ldots\ldots 4.11$$

For constant energy intervals dE, the range can be written as

$$R(E_d) = \sum_i \frac{\Delta E_i}{dE/dx} \qquad \ldots\ldots\ldots 4.12$$

For a 150 KeV deuteron, using the energy loss data of figure 4.2 and for constant energy intervals of 10 KeV, this gives $R(E_{150})=0.638$ mgm.cm^{-2}. Table 4.5 lists the deuteron range in titanium deuteride as a function of incident energy from 0 - 150 KeV. The table also lists the energy of the ^{3}He particles produced in the reaction ^{2}H(d,n)^{3}He as a function of incident deuteron energy.

It is evident that the energy of the ^{3}He particle produced in the reaction ^{2}H(d,n)^{3}He in the target, is dependent on the energy

Table 4.5

Range of Deuterons in Titanium Deuteride

E_d KeV	Range ($mg.cm^{-2}$)	$E_{^3He}$ KeV
10	0.106	816
20	0.174	814
30	0.229	811
40	0.276	810
50	0.318	806
60	0.356	804
70	0.392	801
80	0.426	799
90	0.459	796
100	0.490	794
110	0.520	791
120	0.550	789
130	0.580	786
140	0.609	784
150	0.638	781

at which the incident deuteron initiates the reaction, i.e., the incident deuteron may travel some range 'r' into the target, losing part of its energy, and there produce a ^{3}He particle of a given energy. Since the target is at 45^o to the incident deuteron beam, the ^{3}He particle has to travel the same range 'r' to escape the target, and in doing so loses part of its energy. In order to estimate the energy loss of the ^{3}He particle consider the diagram shown schematically in figure 4.6.

Let E_1' be the initial energy of a ^{3}He particle produced at a range r_1 in the target, and let E_1'' be the energy with which the ^{3}He particle escapes the target, then:

$$E_1'' = E_1' - \left(\frac{dE}{dx}\right)_{E_1'} .r_1 \qquad \ldots\ldots\ldots 4.13$$

where $\left(\frac{dE}{dx}\right)_{E_1'}$ is the energy loss of a ^{3}He particle of energy E_1' in titanium deuteride. Similarly if E_2' be the initial energy of a ^{3}He particle produced at some second range r_2, then:

$$E_2'' = E_2' - \left\{\left(\frac{dE}{dx}\right)_{E_2'} .r_1 + \left(\frac{dE}{dx}\right)_{\alpha} .r_2 \right\} \quad \ldots\ldots 4.14$$

where $\alpha = E_2' - \left(\frac{dE}{dx}\right)_{E_2'} .r_1$.

To employ equation 4.14 and subsequent equivalent equations, it is required to know the rate of energy loss of ^{3}He particles in titanium deuteride. Energy loss data for deuterons in titanium deuteride was available for higher incident energies up to 1 MeV. The required ^{3}He particle energy losses were thus deduced from this data according to the relationship:

$$\frac{dE}{dx}\left(^3\text{He}\right)_{\frac{3E}{2}} = 4.\frac{dE}{dx}\,(\text{deuteron})_E \qquad \ldots\ldots\ldots 4.15$$

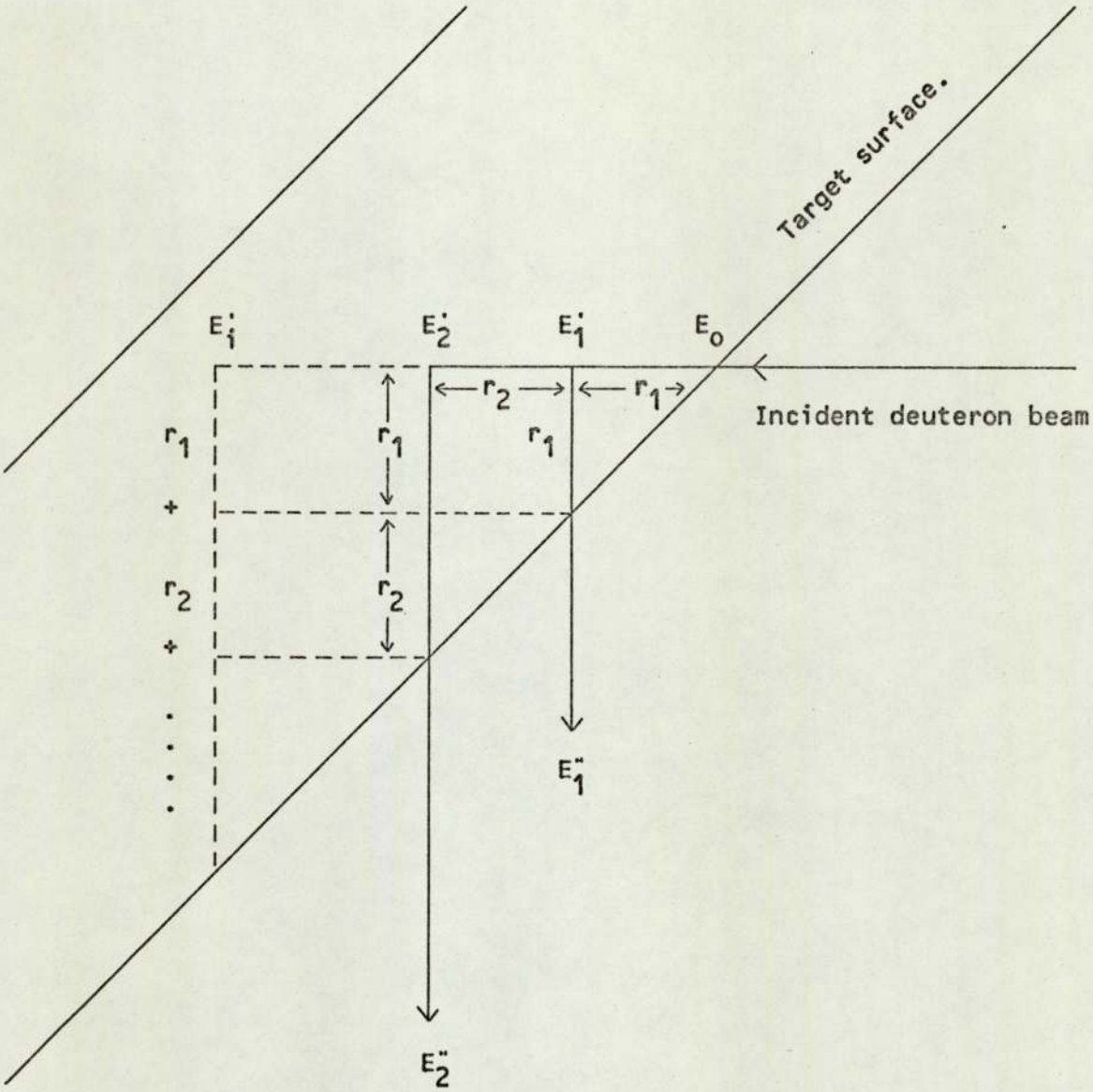
Target surface.
E_i'
E_2'
E_1'
E_o
r_2
r_1
Incident deuteron beam
r_1
r_1
r_1
+
r_2
r_2
+
E_1''
E_2''

Figure 4.6.

The deuteron energy loss data used was that given in LAMS Report No. 2162[61], which was calculated for an atomic ratio of N = 1. No data was available for an atomic ratio of N = 1.2. This was considered adequate in spite of the slight difference in the atomic ratio. Table 4.6 and figure 4.7 show the converted energy loss of ^{3}He particles in titanium deuteride as a function of energy, as defined by equation 4.15. Using the data of tables 4.5 and 4.6, application of equations of the type 4.14 yielded the range of energies of the ^{3}He particles emerging from the target. These values are listed in table 4.7.

4.5 The Electrostatic Deflection System

Theoretical Considerations

Consider a particle of charge 'e' entering into the homogeneous electrostatic field between two plane parallel plates of voltages $\pm V_p$, as shown in figure 4.8.

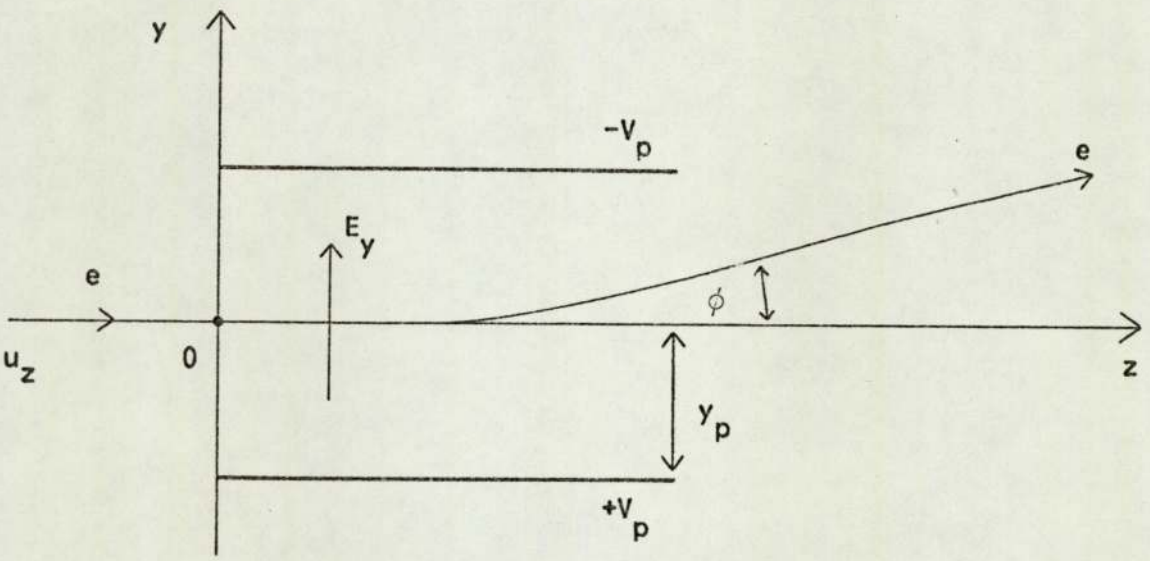

Figure 4.8.

Let the particle move along the Z-axis and let the two plates be arranged symmetrically about the Z-axis, parallel to the X-Z plane.

Table 4.6

Energy loss of ^{3}He Particles in Titanium Deuteride

E_d KeV	(dE/dx) Deuterons KeV/mg.cm^{-2}	$E_{^3He}$ KeV	(dE/dx) ^{3}He KeV/mg.cm^{-2}
600	258.9	900	1035.6
570	265.6	855	1062.4
540	271.0	810	1084.0
510	277.1	765	1108.4
480	283.1	720	1132.4
450	288.6	675	1154.4
420	294.6	630	1178.4
390	300.7	585	1202.8
360	307.3	540	1229.2
330	314.0	495	1256.0
300	320.7	450	1282.8
270	327.9	405	1311.6
240	335.2	360	1340.8
210	341.8	315	1367.2
180	346.1	270	1384.4
150	347.3	225	1389.2
120	342.4	180	1369.6
90	323.1	135	1292.4
60	274.7	90	1098.8
30	177.9	45	711.6

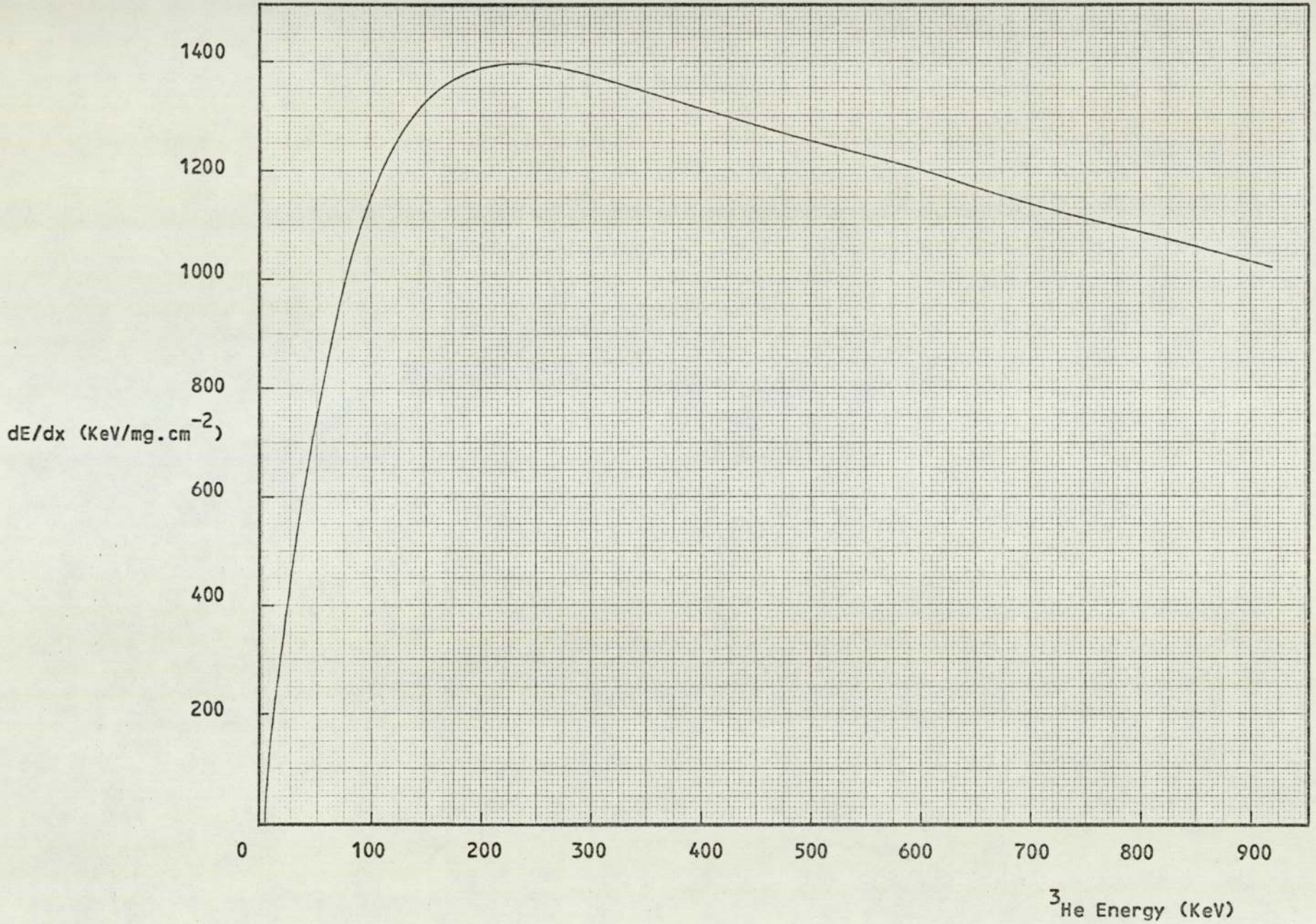

Figure 4.7. Energy loss of ^{3}He particles in titanium deuteride as a function of energy.

Table 4.7

Emergent Energy of ^{3}He Particles Produced in the Titanium Deuteride Target

Deuteron Energy (KeV)	^{3}He Energy (KeV)	Emergent ^{3}He Energy (KeV)
150	781	781
140	784	666
130	786	588
120	789	527
110	791	473
100	794	423
90	796	376
80	799	331
70	801	287
60	804	246
50	806	208
40	810	170
30	811	131
20	814	94
10	816	65

the spacing of the plates being $2y_p$. The electrostatic field vector $\underline{E}_y$ is given by:

$$\underline{E}_y = -\frac{V_p}{y_p} \qquad \ldots\ldots 4.16$$

The equations of motion for the particle are:

$$\left.\begin{aligned} m\frac{d^2y}{dt^2} &= eE_y \\ m\frac{d^2z}{dt^2} &= 0 \end{aligned}\right\} \qquad \ldots\ldots 4.17$$

Subject to the boundary conditions $\left(\frac{dy}{dt}\right)_o = V_o$, $y_o = 0$ and $\left(\frac{dz}{dt}\right)_o = u_z$, $z_o = 0$.

The solutions of equations 4.17 are given by:

$$\left.\begin{aligned} y &= -\frac{e}{2m}E_y t^2 \\ z &= u_z t \end{aligned}\right\} \qquad \ldots\ldots 4.18$$

Elimination of the time 't' gives the equation of the particle orbit i.e.,

$$y = -\frac{e}{2m}E_y\left(\frac{z}{u_z}\right)^2 \qquad \ldots\ldots 4.19$$

But, the initial energy of the particle, E_p, is given by:

$$\tfrac{1}{2}mu_z^2 = E_p \qquad \ldots\ldots 4.20$$

and hence equation 4.19 reduces to

$$y = e\frac{z^2}{E_p}\cdot\frac{V_p}{4y_p} \qquad \ldots\ldots 4.21$$

Differentiation of equation 4.21 gives the angle of deflection ϕ at the end of the plates, i.e.,

$$\tan\phi = \frac{dy}{dz} = e\frac{z}{E_p} \cdot \frac{V_p}{2y_p} \quad \ldots\ldots \quad 4.22$$

Elimination of V_p/y_pE_p between equations 4.21 and 4.22 gives

$$\tan\phi = \frac{y}{z/2} \quad \ldots\ldots \quad 4.23$$

This shows that the tangent to the beam leaving a parallel plate system of length z can be produced back to the centre of the system.

Beam Tube Design

Due to the limited experimental space available the length of the electrostatic separation system was restricted to 0.4 m. The deflector plates were 40 mm wide and 150 mm long, leaving a flight path of 250 mm for an effective separation of particles before the ^{3}He particle detector. The separation of the deflector plates was 30 mm. The deflector plates were fixed in the vertical plane and carried voltages of $\pm$ 3 kV respectively, supplied by two Nuclear Enterprises stabilised power packs type NE 4646.

In view of the need for a small angular divergence in the ^{3}He particle beam, the defining aluminium aperture plate in the target assembly flange (section 3.4) was restricted to 3.2 mm horizontally by 4 mm vertically. This limited the angular acceptance of particles into the electrostatic field to be $90^\circ \pm 1^\circ$ in the horizontal plane.

The displacement from the Z-axis over a flight path of 250 mm after the applied electrostatic field was calculated using equations 4.21 and 4.23 for deuterons of 139 KeV, this being the maximum energy of an incident deuteron of energy 150 KeV scattered through 90° from the titanium deuteride target. Displacements were also calculated

for protons and tritons of energy 972 KeV and 3.06 MeV respectively, this being the maximum energy of the particles emitted in the reaction $^{2}H(d,p)^{3}H$ for an incident energy of 150 KeV, and ^{3}He particles of energy 781 KeV and 300 KeV, these being the extremes of energy considered for ^{3}He escaping the target. The displacements are listed in table 4.8, from which it can be seen that deuterons elastically scattered from the target are well separated from the other particles. Protons and tritons of energies below the stated maxima will incur greater displacements from the Z-axis producing a certain amount of overlap into the ^{3}He particle displacement region. However, since the cross section of the $^{2}H(d,p)^{3}H$ reaction decreases with energy, the effect of these lower energy particles is not serious since their numbers are much smaller than the number of ^{3}He particles.

From these considerations, the beam tube was designed such that the centre of the ^{3}He particle detector was displaced 16 mm from the Z-axis. This allowed detection of the maximum number of the higher energy ^{3}He particles, as well as compensating for the slight angular divergence of the particle beam due to the $\pm 1^{o}$ defining aperture. To prevent unwanted lower energy particles scattered from the inside of the tube from reaching the detector, a rectangular aluminium collimator 70 mm long, and measuring 13 mm horizontally by 15 mm vertically was placed at right angles to the detector face. The silicon surface barrier detector was housed in a suitable end flange piece that formed the end of the vacuum system. The electrostatic deflection system and ^{3}He particle detector are shown in figures 4.9 and 4.10.

4.6 The Time of Flight Electronics

A block diagram of the circuitry associated with the two detector channels is shown in figure 4.11. As Ortec NIM series units were available for use in the time of flight electronics, no gating system was required; these units are capable of coping with pulse repetition rates up to 2MHz.

Table 4.8

Displacement of Particles from the Z-axis

Particle	Energy (MeV)	Displacement (mm)
Deuteron	0.129	37.8
Helium 3	0.300	32.5
Helium 3	0.781	12.5
Proton	0.972	5.0
Triton	3.050	1.6

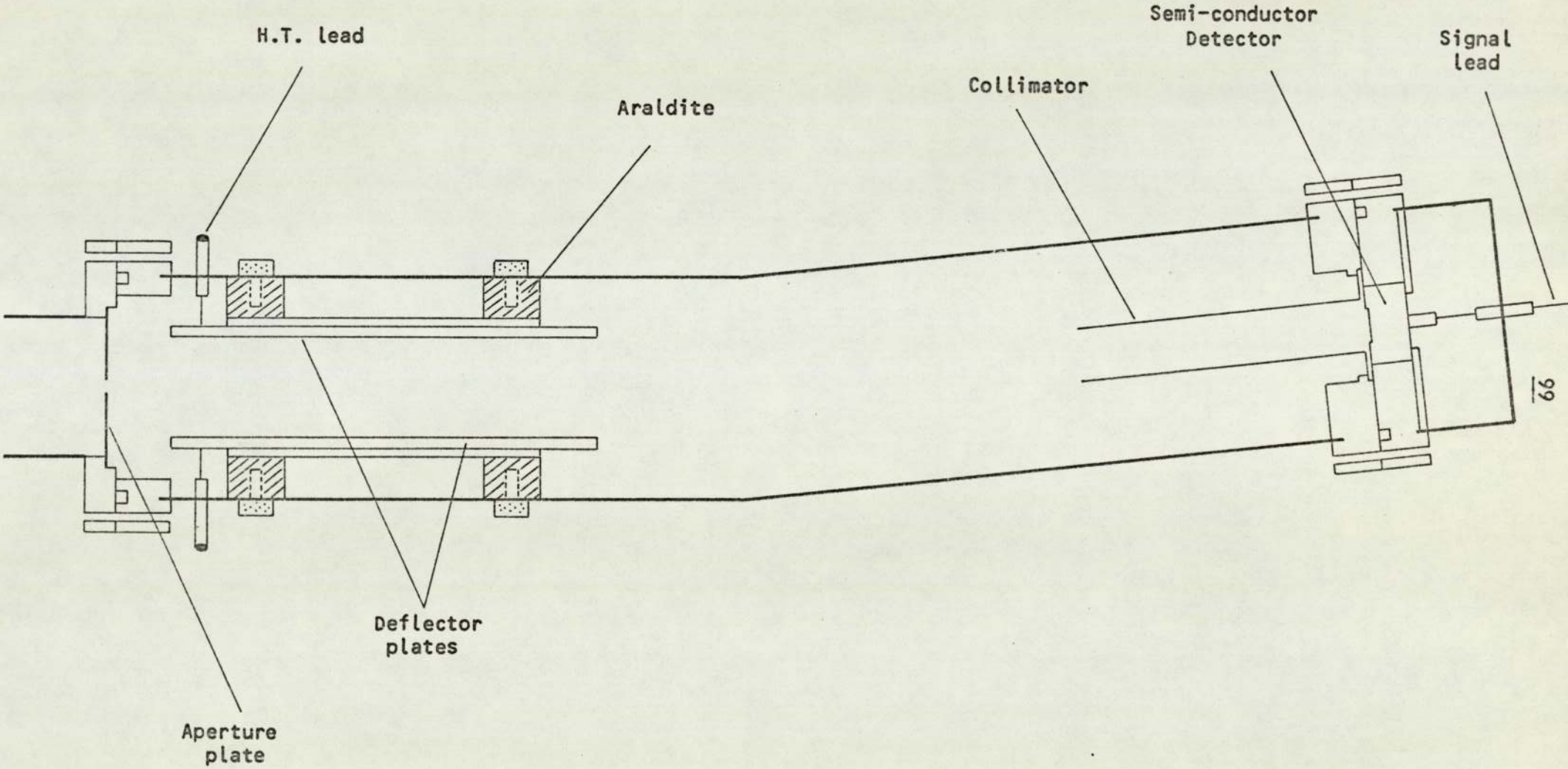

Figure 4.9. Angled beam tube, electrostatic deflection system and ^{3}He particle detector.

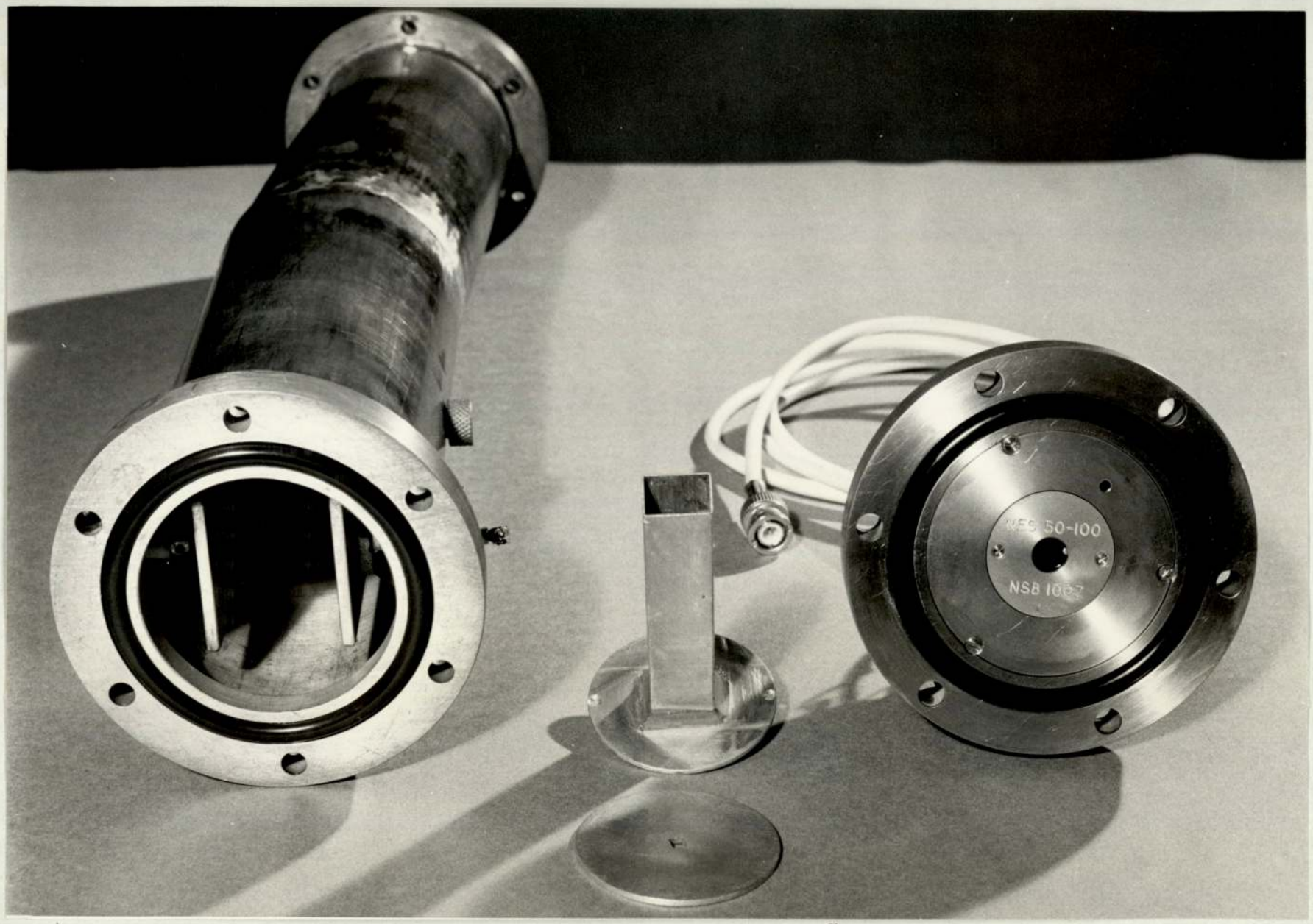

Figure 4.10. The Electrostatic Deflection System and ^{3}He Particle Detector.

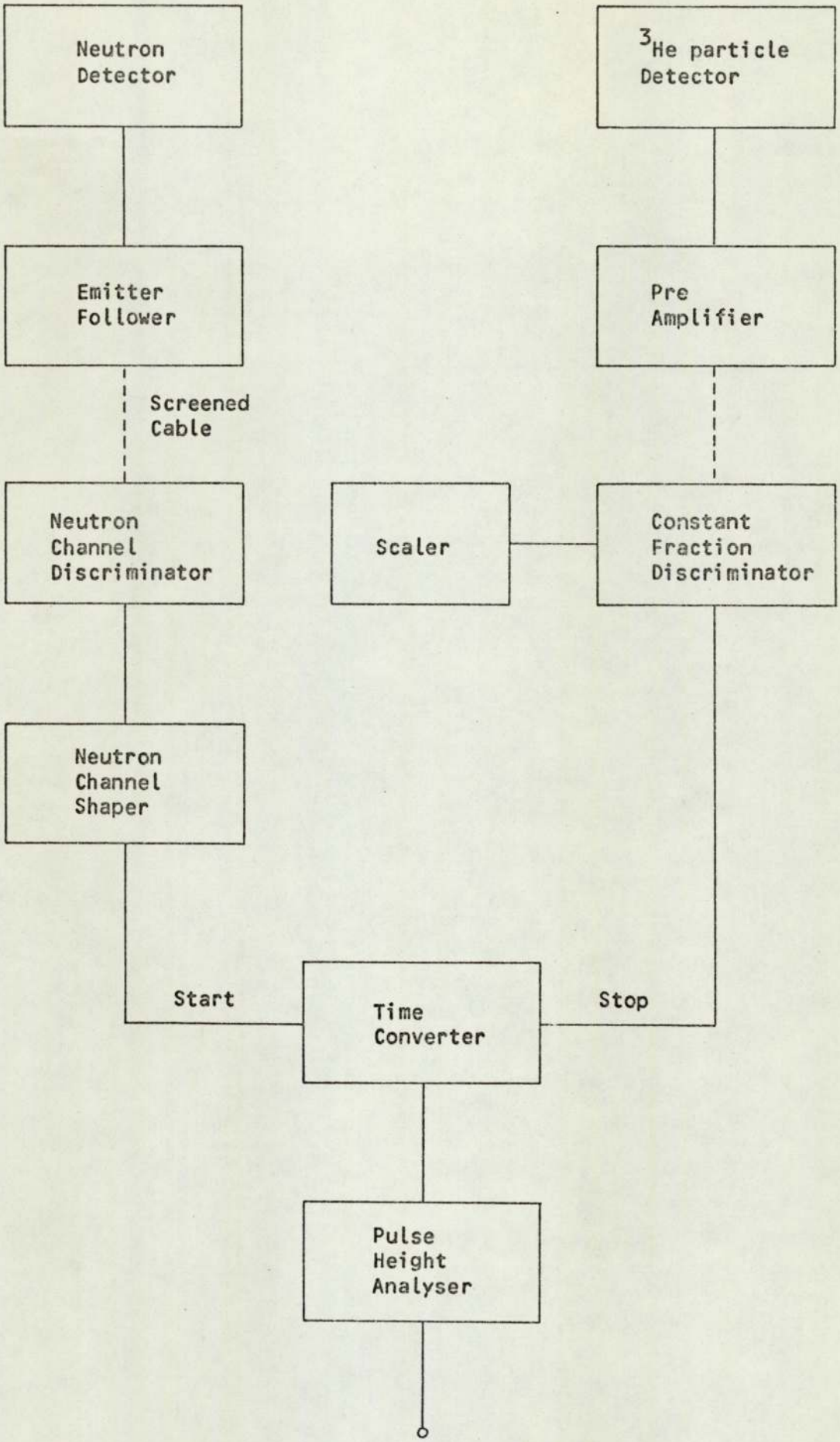

Figure 4.11. Block diagram of the time of flight electronics.

The Neutron Channel

The output pulse from the anode of the neutron detector photomultiplier was fed into screened coaxial cable, through an emitter follower designed to provide suitable current drive and matching into the coaxial line. The pulse was then fed to an amplitude discriminator, which accepted the pulse only if it exceeded a pre-set amplitude. However, in view of the much lower primary energy of 2.5 MeV for neutrons from the $^{2}H(d,n)^{3}He$ reaction, a different discrimination and shaping system was required from that used in the 14 MeV work.

Discrimination in this case was by use of an integrated circuit high-speed differential comparator. The circuit was manufactured by Texas Instruments Ltd., type SN 72710. The device is capable of making a voltage comparison with a resolution of 5 mV, between $\pm$ 5 volts with a response time of 40 ns. The essential function of the circuit was to act as a threshold detector, by comparing a signal voltage with a reference voltage, thus producing either a high level or low level output when one input was higher than the other.

Figure 4.12(a) shows a basic circuit for using the differential comparator. A reference voltage between $\pm$ 5 volts maximum is connected to one input and the signal is fed into the other. When the input exceeds the reference signal, the output changes in state from + 3.1 volts to -0.5 volt as shown in figure 4.12(b). The output switches postively or negatively depending upon how the inputs are connected.

The maximum supply voltages of +14 volts and -7 volts, specified by the manufacturer's data sheet were produced with zener diodes from the 24 volt supplies. The reference voltage, variable from 0 to -1 volt was supplied by a potential divider chain from the -24 volt supply. In order to minimise offset voltage and thermal drift, the manufacturers recommend that the source resistance of the

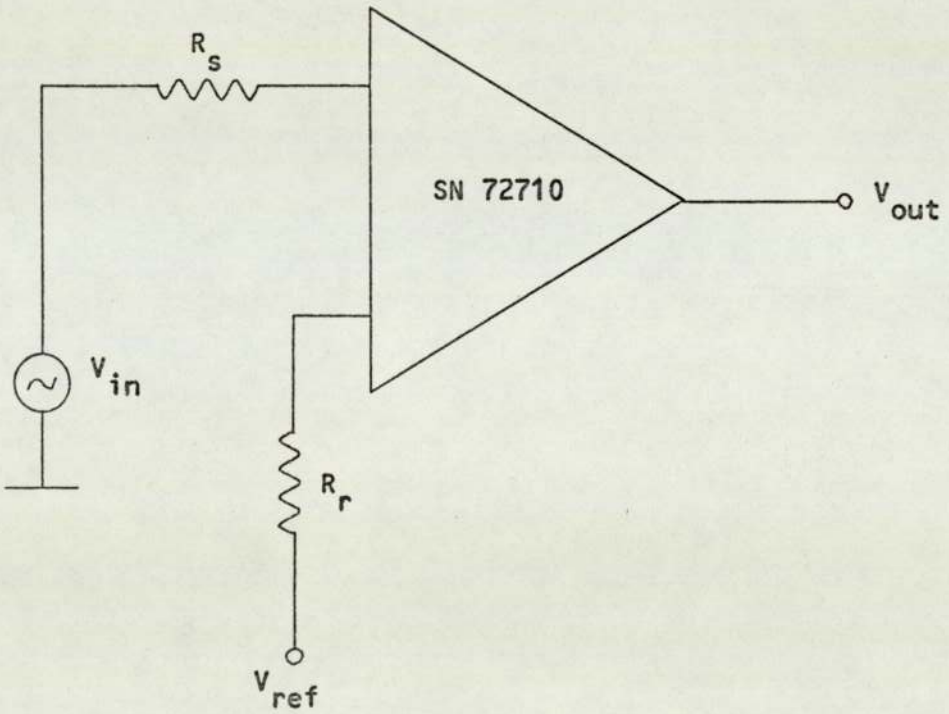

Figure 4.12(a). Differential comparator.

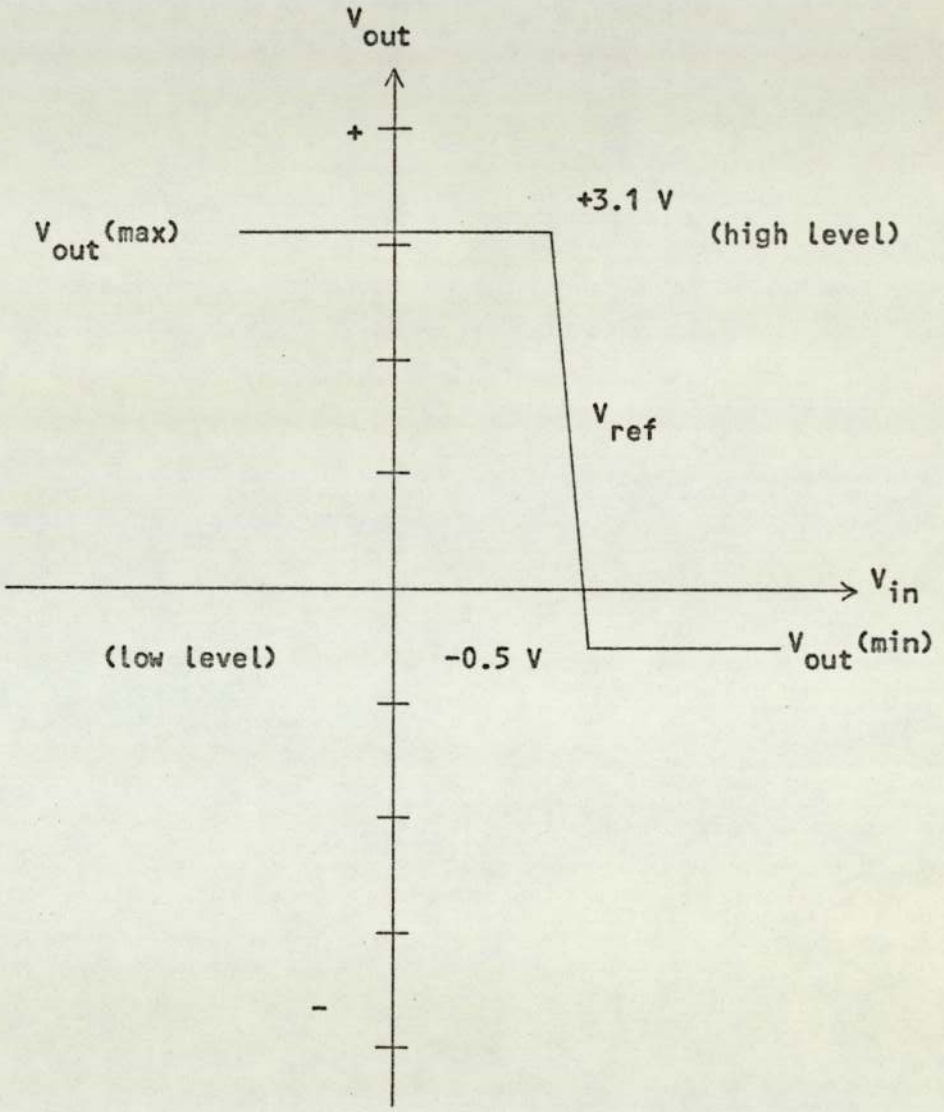

Figure 4.12(b). Transfer function.

signal voltage and the reference voltage should be equal. These resistances should also be made as low as possible, preferably less than 200 Ω for best performance. In order to avoid oscillations in the circuit, it was necessary to by-pass to earth both the positive and negative supplies, using low inductance disc ceramic capacitors of 0.01 μF. The complete discriminator circuit is shown in figure 4.13.

The output from the discriminator was fed to a standard monostable circuit which produced a constant output pulse of -4 volts amplitude and 100 ns duration. This pulse was compatible with the input requirements of the Ortec NIM series time converter, type 447. The circuit is shown in figure 4.14.

The ^{3}He Particle Detector Channel

The silicon surface barrier detector used was a Nuclear Enterprises type NES 50-100, having an area of 50 mm^{2} and a depletion region 100 microns thick. The detector required a bias of +45 volts when in operation and this was supplied by a Nuclear Enterprises power pack, type NE 4646. The output from the detector was fed through a screened coaxial cable into a Nuclear Enterprises pre-amplifier, type NE 5287, which produced pulses of 1000 ns duration and amplitude depending on the energy of the particle striking the detector.

The flight times of the ^{3}He particles over the target to detector flight path of 0.5 m varied from 70 ns for the maximum energy of 781 KeV, to 227 ns for the lower limit of 300 KeV. Therefore no delay was required in the ^{3}He particle detector channel.

When timing from the leading edge of slow rising pulses an electronic error known as "time walk" is introduced. This is the difference in the triggering time due to different amplitude pulses having otherwise identical characteristics. Figure 4.15 illustrates this point. In order to minimise the effects of "time walk", the output pulses from the pre-amplifier were fed to an Ortec constant

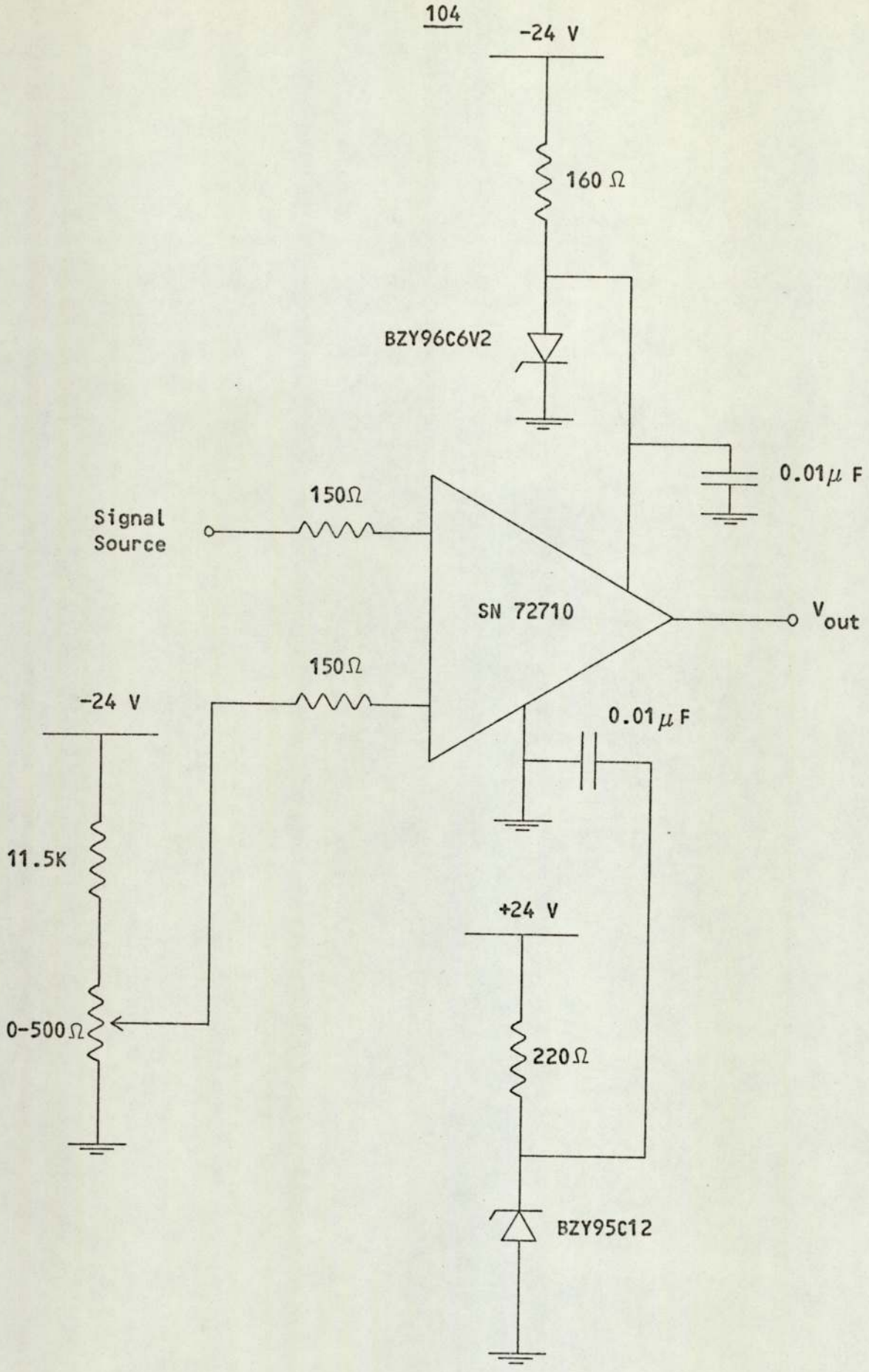

Figure 4.13. The complete neutron channel discriminator circuit.

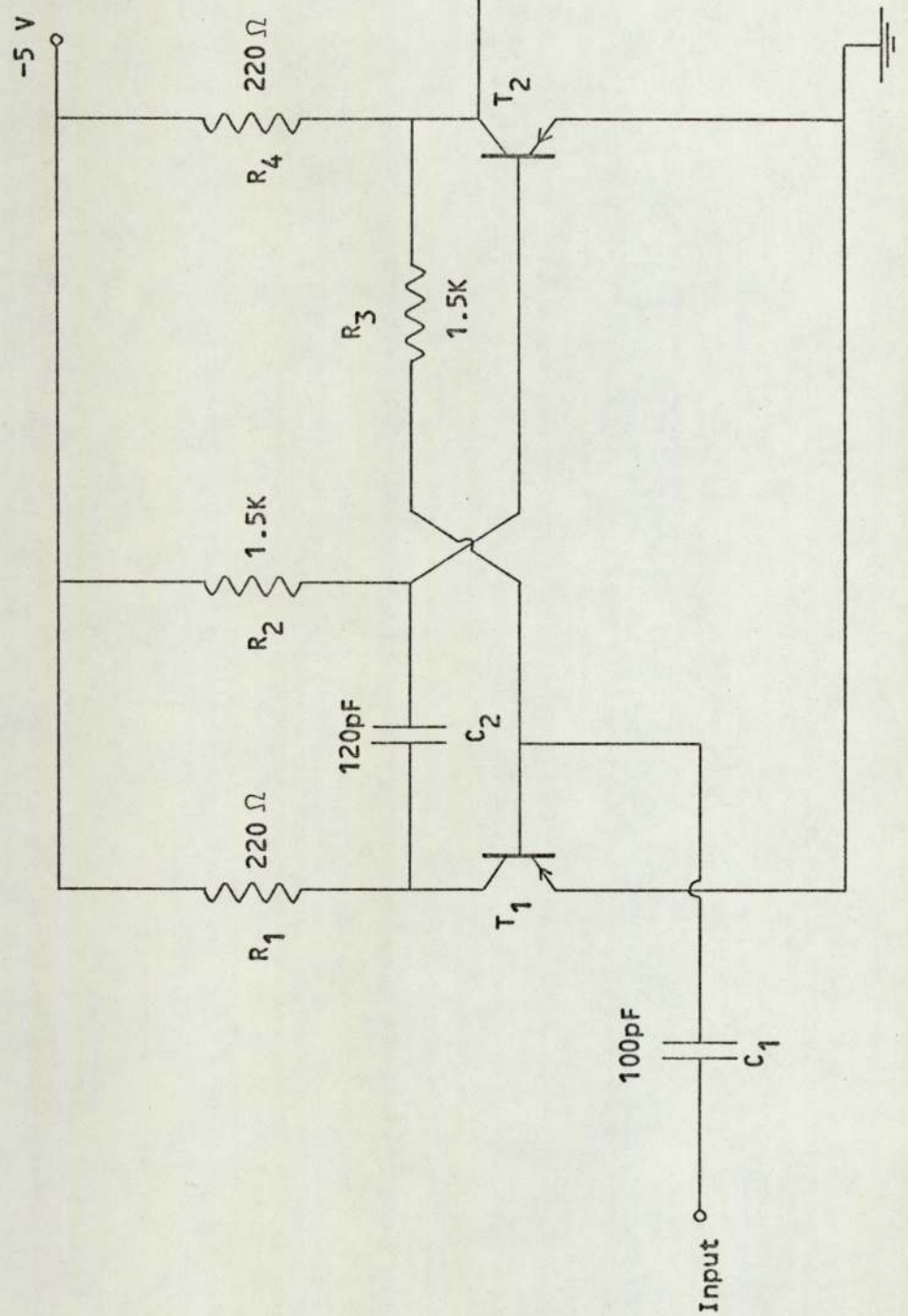

T_1, T_2, 2N2412

Figure 4.14. 100 ns monostable circuit.

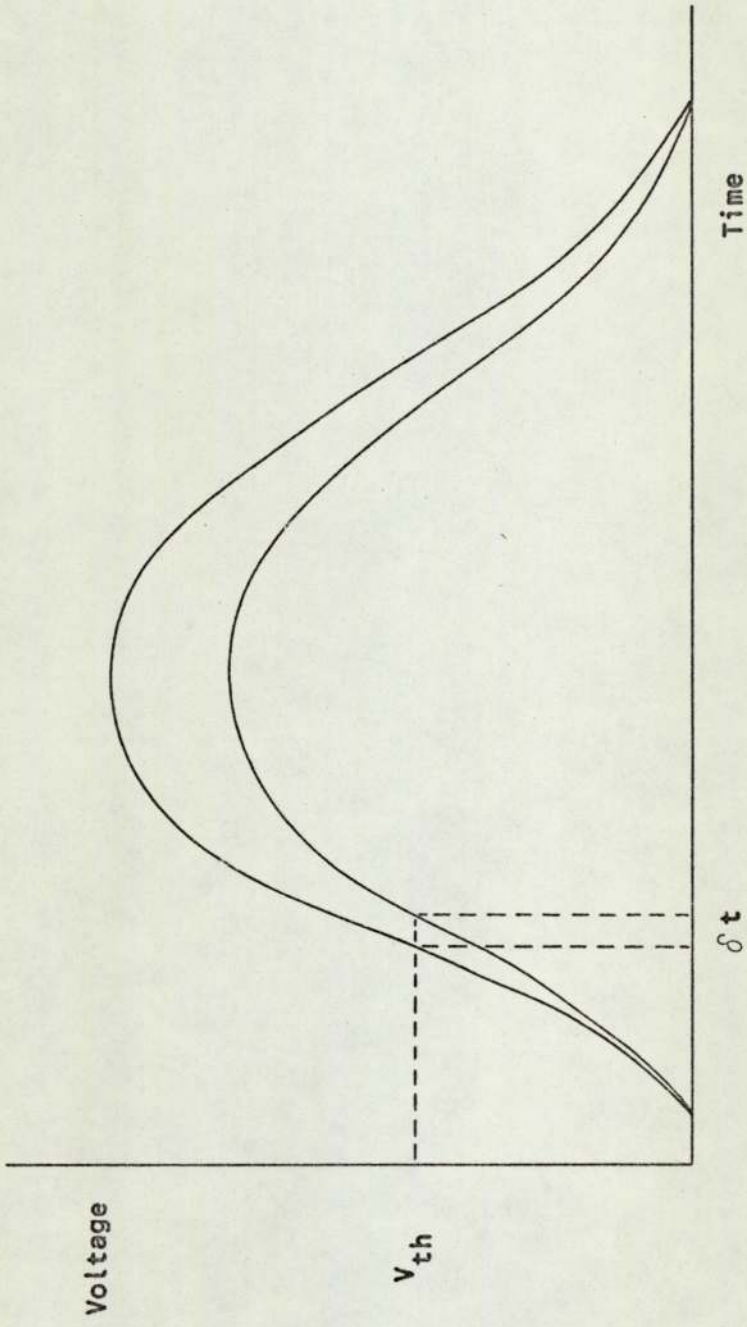

Figure 4.15.

fraction discriminator, type 463. The output from the discriminator was then fed directly to the stop input of the time converter.

4.7 Electronic Testing

The neutron detector was placed at an angle of 71^{o} with respect to the incident deuteron beam direction; corresponding to ^{3}He particles detected at 90^{o}. The flight path from the source to the face of the neutron detector was fixed at 1.25 m.

The discrimination level in the neutron channel was fixed by the reference voltage on the comparator. A reference voltage of -0.5 volt was found to be sufficient to eliminate background noise. Discrimination in the ^{3}He particle channel was by means of a 50 mV to 5 volt threshold level on the constant fraction discrminator. A level of 80 mV was found to be sufficient to eliminate background noise from the detector.

With the electronics set up as shown in figure 4.11, a coincidence spectrum was observed, and this is shown in figure 4.16. The spectrum was consistently reproducible and exhibited the expected increase in time resolution due to the long flight paths of the ^{3}He particles. The resolution compares favourably with that obtained by Okhuysen et al[62], i.e., 10 ns for a deuteron bombarding energy of 100 KeV and Monier et al[47], 10μ sec for a deuteron bombarding energy of 125 KeV.

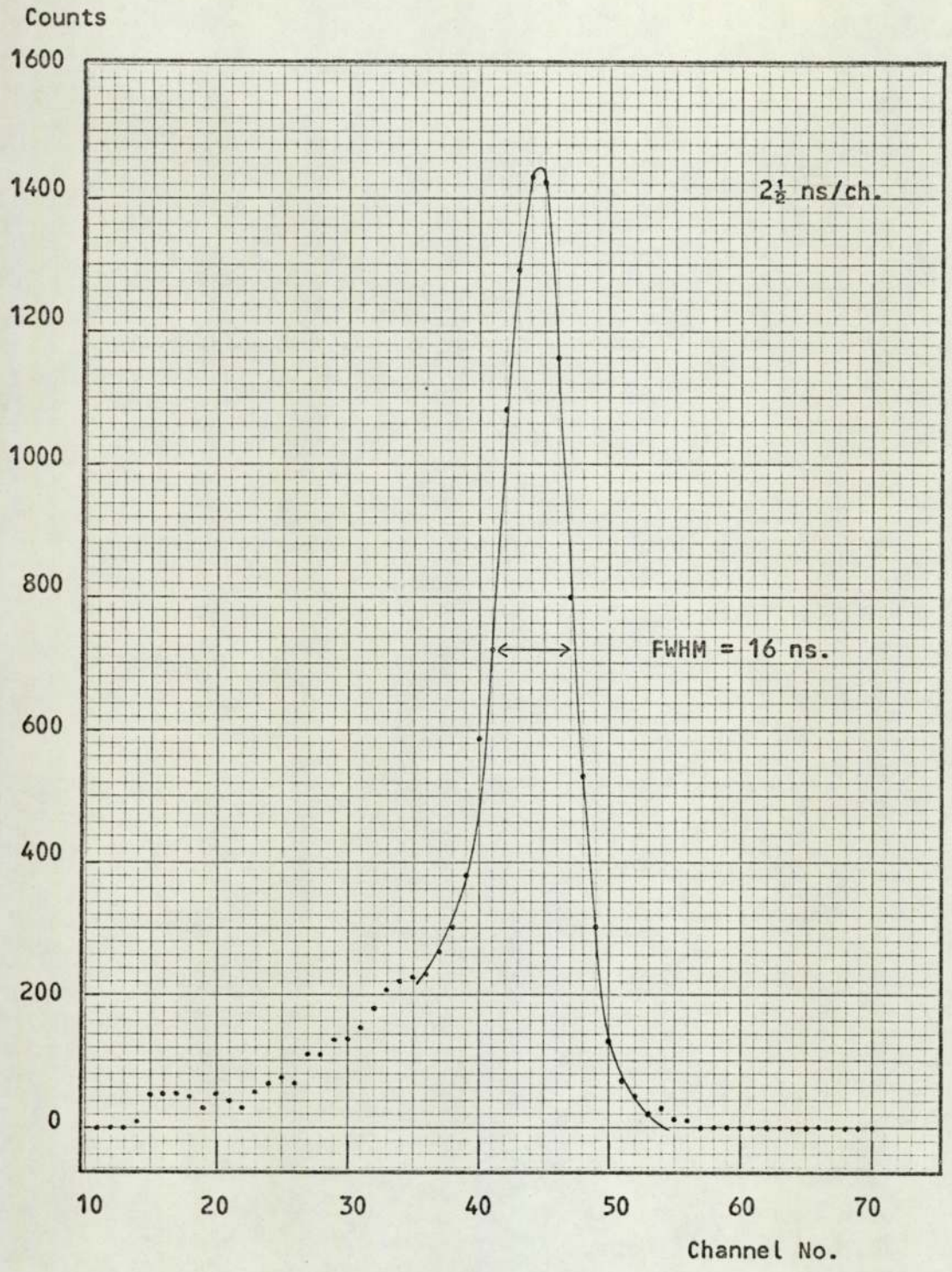

Figure 4.16 Spectrometer Resolution.

CHAPTER 5

Differential Cross Section Measurements

5.1 The Differential Cross Section

In general, neutron scattering is anisotropic. Therefore it is convenient to specify a cross section as a function of the direction in which the neutron is emitted. This is called the differential scattering cross section, normally written as $d\sigma = \sigma(\theta)d\Omega$ (cm^2 per atom or nucleus), and is a measure of the probability of a neutron being scattered into a small solid angle $d\Omega$, at a specified angle θ to the incident neutron direction. Integration of the differential cross section over the 4π solid angle gives the reaction cross section i.e.,

$$\sigma = \int_{4\pi} \sigma(\theta)d\Omega = \int_{\phi=0}^{2\pi} \int_{\theta=0}^{\pi} \sigma(\theta)\sin\theta \, d\theta \, d\phi \qquad . . 5.1$$

If the differential cross section is independent of azimuth about the incident beam direction then:

$$d\Omega = 2\pi \sin\theta \, d\theta \qquad . . . . . 5.2$$

and

$$d\sigma = 2\pi \sin\theta \, \sigma(\theta)d\theta \qquad . . . . . 5.3$$

from which the total reaction cross section is obtained by integration.

$$\sigma = 2\pi \int_0^{\pi} \sigma(\theta)\sin\theta \, d\theta \qquad . . . . . 5.4$$

The quantity $\sigma(\theta) = \frac{d\sigma}{d\Omega}$ gives the angular distribution of the scattering events, and is expressed in cm^2 per scattering centre per steradian.

The angular distribution $\sigma(\theta)$ measured in the laboratory system, is related to the angular distribution in the centre of mass system $\sigma(\phi)$ as follows:

$$\sigma(\phi)\sin\phi\, d\phi = \sigma(\theta)\sin\theta\, d\theta \qquad \ldots\ldots 5.5$$

That is, the same number of events are seen per unit solid angle at corresponding angles in each system. In order to convert the differential cross section from one frame of reference to another, it is required to know the ratio of the related solid angles. This ratio is called the anisotropy of the reaction. If Ω is the solid angle in the laboratory system and Ω' that in the centre of mass system, then equation 5.2 gives:

$$\frac{d\Omega'}{d\Omega} = \frac{\sin\phi\, d\phi}{\sin\theta\, d\theta} \qquad \ldots\ldots 5.6$$

The relation between the centre of mass angle ϕ and the laboratory angle θ is given by[63]

$$\cos\phi = -\gamma\sin^2\theta \pm \cos\theta\,[1 - \gamma^2 \sin^2\theta\,]^{\frac{1}{2}} \qquad \ldots\ldots 5.7$$

with

$$\frac{1}{\gamma^2} = \frac{m_R}{m_n}\left(\frac{m_n + m_T}{m_n}\right)\left[\frac{m_T}{m_n + m_T} + \frac{Q}{E_o}\right] \qquad \ldots\ldots 5.8$$

where m_R is the mass of the recoil nucleus, m_T is the mass of the target nucleus, m_n is the mass of the neutron, Q is the Q-value of the reaction and E_o is the energy of the incident neutron in the laboratory system. Differentiation and rearrangement of equation 5.7 then gives the anisotropy factor.

$$\frac{d\Omega'}{d\Omega} = \frac{\gamma[\cos\theta + (1/\gamma^2 - \sin^2\theta)^{\frac{1}{2}}]^2}{[1/\gamma^2 - \sin^2\theta]^{\frac{1}{2}}} \qquad \ldots\ldots 5.9$$

The present work was concerned with the differential elastic scattering cross section of neutrons. For neutrons incident on a sample of thickness 'x', having 'n' nuclei per unit volume, the total number of elastically scattered neutrons N_{el} is given by:

$$N_{el} = \phi[1 - \exp(-n\sigma_T x)] \frac{\sigma_{el}}{\sigma_T} \qquad \ldots\ldots 5.10$$

where ϕ is the total number of neutrons incident on the sample in a given time, and σ_T is the total neutron cross section for all processes, elastic and inelastic. The number of elastically scattered neutrons $N(\theta)$, in a solid angle $d\Omega$, at an angle θ to the incident beam direction is given by:

$$N(\theta) = \phi[1 - \exp(-n\sigma_T x)] \frac{\frac{d\sigma_{el}}{d\Omega}}{\sigma_T} d\Omega \qquad \ldots\ldots 5.11$$

where $\frac{d\sigma_{el}}{d\Omega}$ is the differential cross section for elastic scattering per unit solid angle. To obtain the true yield of elastically scattered neutrons it was necessary to correct the neutron detector count for the detector efficiency. On re-arrangement, equation 5.11 then gives:

$$\frac{d\sigma_{el}}{d\Omega} = \frac{N'(\theta)\,\sigma_T}{\phi[1 - \exp(-n\,\sigma_T x)]\,\Delta\Omega\,\epsilon(E_n)} \qquad \ldots\ldots 5.12$$

where $N'(\theta)$ is the neutron detector count; $\epsilon(E_n)$ is the detector efficiency as a function of neutron energy and $\Delta\Omega$ is the solid angle subtended by the neutron detector at the sample. In practice, equation 5.12 required corrections for the number of incident neutrons ϕ and the

sample thickness 'x', since with a point neutron source the neutrons incident on the sample do not form a parallel beam but a diverging beam and different parts of the beam pass through different sample thicknesses. The angular range of the source neutrons defined by alpha particles emitted at $90^{o} \pm 5^{o}$ to the incident deuteron beam in the reaction $^{3}H(d,n)^{4}He$ can be calculated from the reaction kinetics. The corrections to equation 5.12 are discussed in section 5.4.

Double Scattering

The differential cross section given by equation 5.12 assumes that the neutron yield is due to neutrons interacting only once in the scattering sample. However, after a neutron has been scattered once, either elastically or inelastically, it is possible that the neutron may interact a second time. Neutron elastic scattering is very forward peaked and the incident neutrons are only slightly reduced in energy (section 5.5). It has been shown by Walt[64] that the effects of multiple scattering can be neglected if the sample thickness is less than 0.2 mean free paths.

The term $[1 - \exp(-n \sigma_T x)]$ in equation 5.12 accounts for the attenuation of the neutron beam in the sample. Therefore, in the case of a thin sample where the attenuation is small, $[1 - \exp(-n \sigma_T x)] \sim n \sigma_T x$. Day[65] and Nishimura et al[66], have proposed that for a thin sample the effects of multiple scattering cancel out the neutron attenuation and that the neutron flux is constant throughout the sample. This criterion was applied in the present work and hence equation 5.12 can be written:

$$\frac{d\sigma_{el}}{d\Omega} = \frac{N'(\theta)}{\phi\, n\, x\, \Delta\Omega\, \epsilon(E_n)} \qquad \ldots\ldots 5.13$$

5.2 Kinetics of the Reaction $^{3}H(d,n)^{4}He$

Collisions of nuclear particles are governed by the laws of energy and momentum conservation. In this reaction the deuteron, mass m_d, is incident on the triton, mass m_t, which is at rest in the laboratory system. The interaction produces a neutron and an alpha particle of masses m_n and m_α respectively. If $(\theta_n, \theta_\alpha)$ and (ϕ_n, ϕ_α) represent the angles of emission of the particles in the laboratory and centre of mass systems of co-ordinates respectively, then the interactions are illustrated by figure 5.1, together with the relationship of the angles in the two systems.

In order to determine the angular range of the source neutrons it is required to know where, in the laboratory frame of reference, the neutron and associated alpha particle from a given encounter are to be found. The following expression given by Benveniste and Zenger[63] relates θ_α and θ_n, the angle made by the alpha particle with the beam direction to the angle made by the neutron and the beam direction:

$$\tan\theta_\alpha = \frac{\frac{1}{2}\sin 2\theta_n + \sin\theta_n[1/\gamma^2 - \sin^2\theta_n]^{\frac{1}{2}}}{-\sin^2\theta_n + \cos\theta_n[1/\gamma^2 - \sin^2\theta_n]^{\frac{1}{2}} - \frac{m_\alpha}{m_n}} \qquad 5.14$$

with

$$\frac{1}{\gamma^2} = \frac{m_\alpha}{m_n}\left(\frac{m_d + m_t}{m_d}\right)\left[\frac{m_t}{m_d + m_t} + \frac{Q}{E_d}\right] \qquad 5.15$$

where E_d is the incident deuteron energy in the laboratory system and Q is the energy released in the reaction, i.e., Q = 17.586 MeV.

Since deuterons lose energy in penetrating the tritium target to the point of interaction, neutrons are produced in collisions with E_d varying between zero and 120 KeV. Equations 5.14 and 5.15 show that the relationship between the angles of emission of the alpha particle and neutron are dependent on the incident deuteron energy E_d. The related

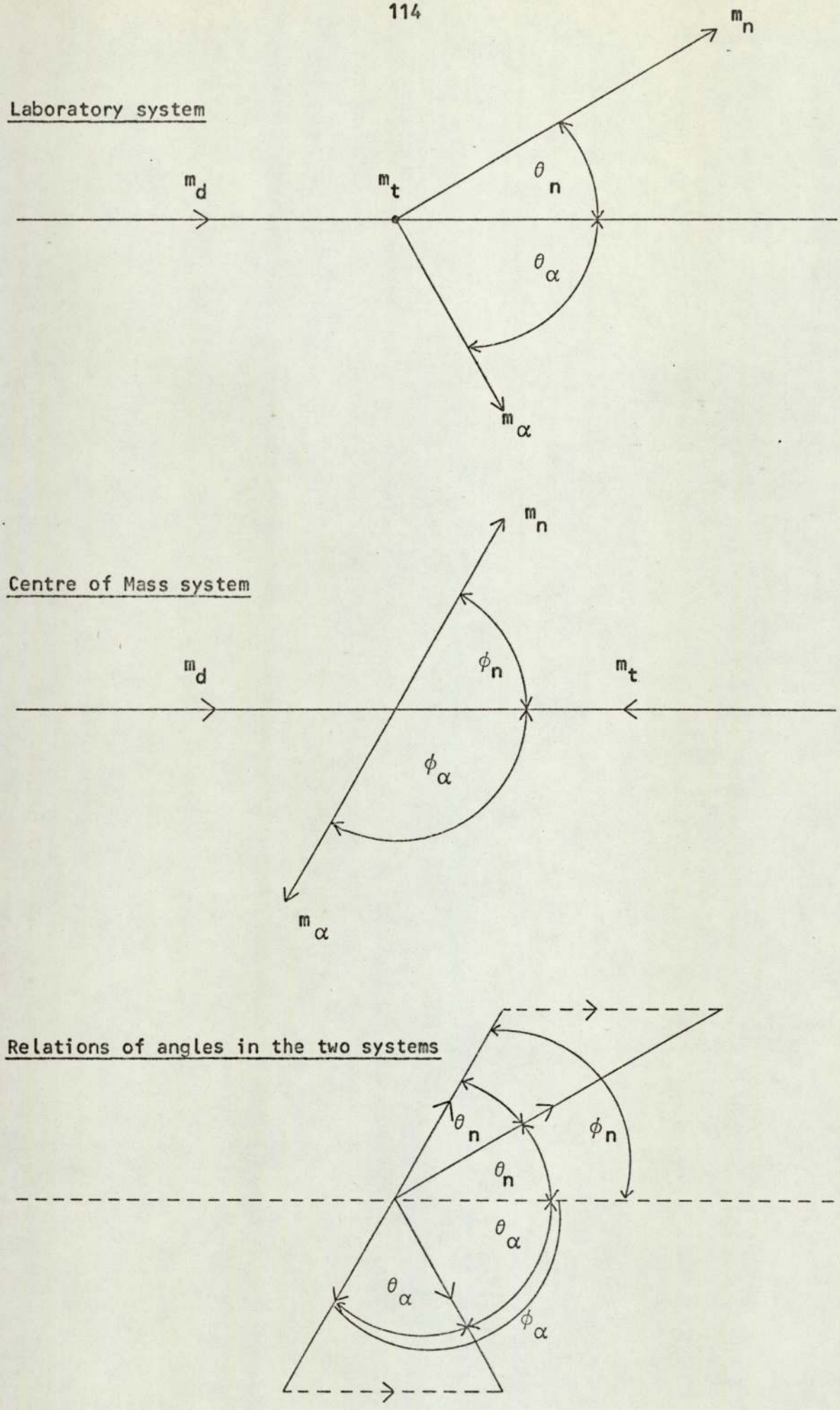

Figure 5.1. Kinetics of nuclear collisions.

angles were obtained using equations 5.14 and 5.15 for incident deuteron energies between zero and 120 KeV in steps of 20 KeV; the results of which are shown in figure 5.2. It can be seen from figure 5.2 that alpha particles detected at $90^{o} \pm 5^{o}$ define a neutron beam over the angular range 77.6^{o} to 95^{o}.

In view of the variation of the cross section of the $^{3}H(d,n)^{4}He$ reaction with incident deuteron energy, the neutron yield is not uniform over the specified angular range of the alpha particle detector in the reaction plane. This fact is illustrated by figure 5.2, i.e., at $\theta_{n} = 79^{o}$ the neutron yield is due only to deuteron interactions with energies from 120 KeV to 80 KeV, whilst at 85^{o} the yield is due to deuteron interactions over the entire energy range. In order to determine the relative neutron yield over the angular range $\theta_{n} = 77.6^{o}$ to 95^{o}, it was necessary to calculate the variation of neutron yield with incident deuteron energy.

5.3 The Neutron Yield as a Function of Deuteron Energy

The method of calculation of the neutron yield was similar to that given in section 4.3 for the reaction $^{2}H(d,n)^{3}He$. The total thick target yield of neutrons per incident deuteron of energy E is given by:

$$Y = \int_{o}^{E} \frac{n_{t}\,\sigma(E)de}{dE/dx} \qquad \ldots\ldots 5.16$$

where n_{t} is the number of tritium nuclei per cm^{3}, $\sigma(E)$ is the cross section at energy E for the $^{3}H(d,n)^{4}He$ reaction and dE/dx is the rate of loss of energy of deuterons of energy E in the tritiated titanium target.

The neutron yield dY per incident deuteron per steradian at a neutron angle θ_{n} is given by:

$$dY = \int_{o}^{E} \frac{n_{t}\,\frac{d\sigma}{d\Omega}(E)dE}{dE/dx} \qquad \ldots\ldots 5.17$$

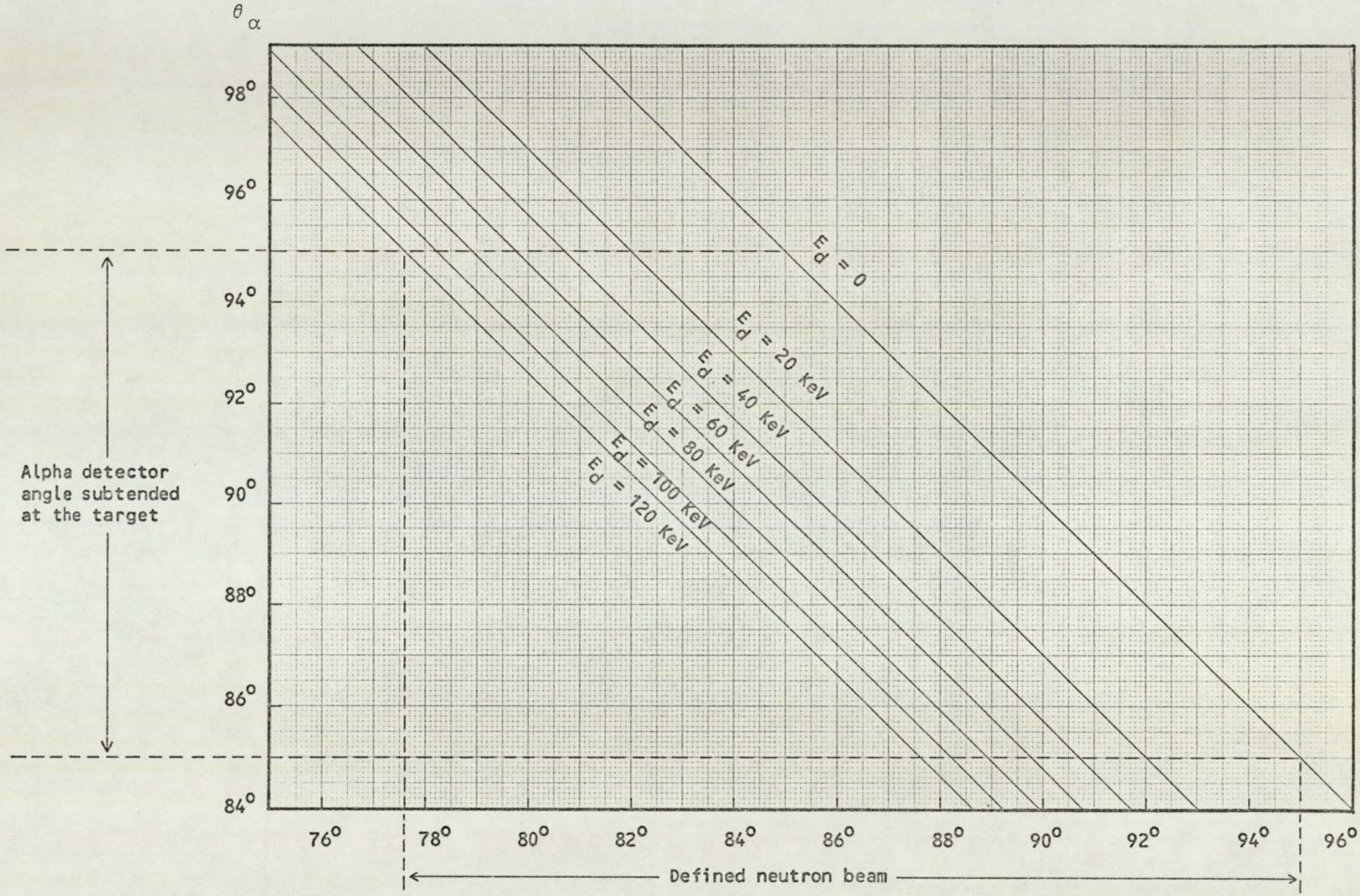

Figure 5.2. Related neutron and alpha particle angles of emission in the laboratory system.

where $\frac{d\sigma}{d\Omega}(E)$ is the differential cross section in the laboratory system at an incident deuteron energy E and neutron angle θ_n.

The angular dependence of the differential cross section of the $^3H(d,n)^4He$ reaction has been found to be isotropic in the centre of mass system for deuteron energies up to 200 KeV by Allen and Poole[67] and up to 570 KeV by Argo et al[68]. The data used for the differential cross section in the present calculations was that of Benveniste and Zenger[63]. The data is given in the centre of mass system and is shown in figure 5.3.

The data used for dE/dx, the rate of loss of energy of deuterons in the target, was that of Gunnersen and James[51]. They measured dE/dx for deuterons in a tritiated titanium target experimentally for incident deuteron energies up to 170 KeV. The curve obtained is shown in figure 5.4.

In contrast to the calculation of the neutron yield from the $^2H(d,n)^3He$ reaction, where it was required to obtain an estimate of the actual numbers of neutrons available, the $^3H(d,n)^4He$ reaction is known to be a copious source of neutrons, therefore it was sufficient to calculate only the relative neutron yield. With the data of figures 5.3 and 5.4, the relative neutron yield dY per steradian, at an angle θ_n, from deuterons in a small energy interval dE is obtained using equation 5.17 and can be written:

$$dY(\theta_n, E) \propto \frac{\frac{d\sigma}{d\Omega}\,\frac{d\Omega'}{d\Omega}}{\frac{dE}{dx}}\,dE \qquad \ldots\ldots 5.18$$

n_t, the number of tritium nuclei per cm^3 is assumed constant. The anisotropy factor defined by equation 5.9 was found to be constant to within 1% over the deuteron energy range, and its value was considered

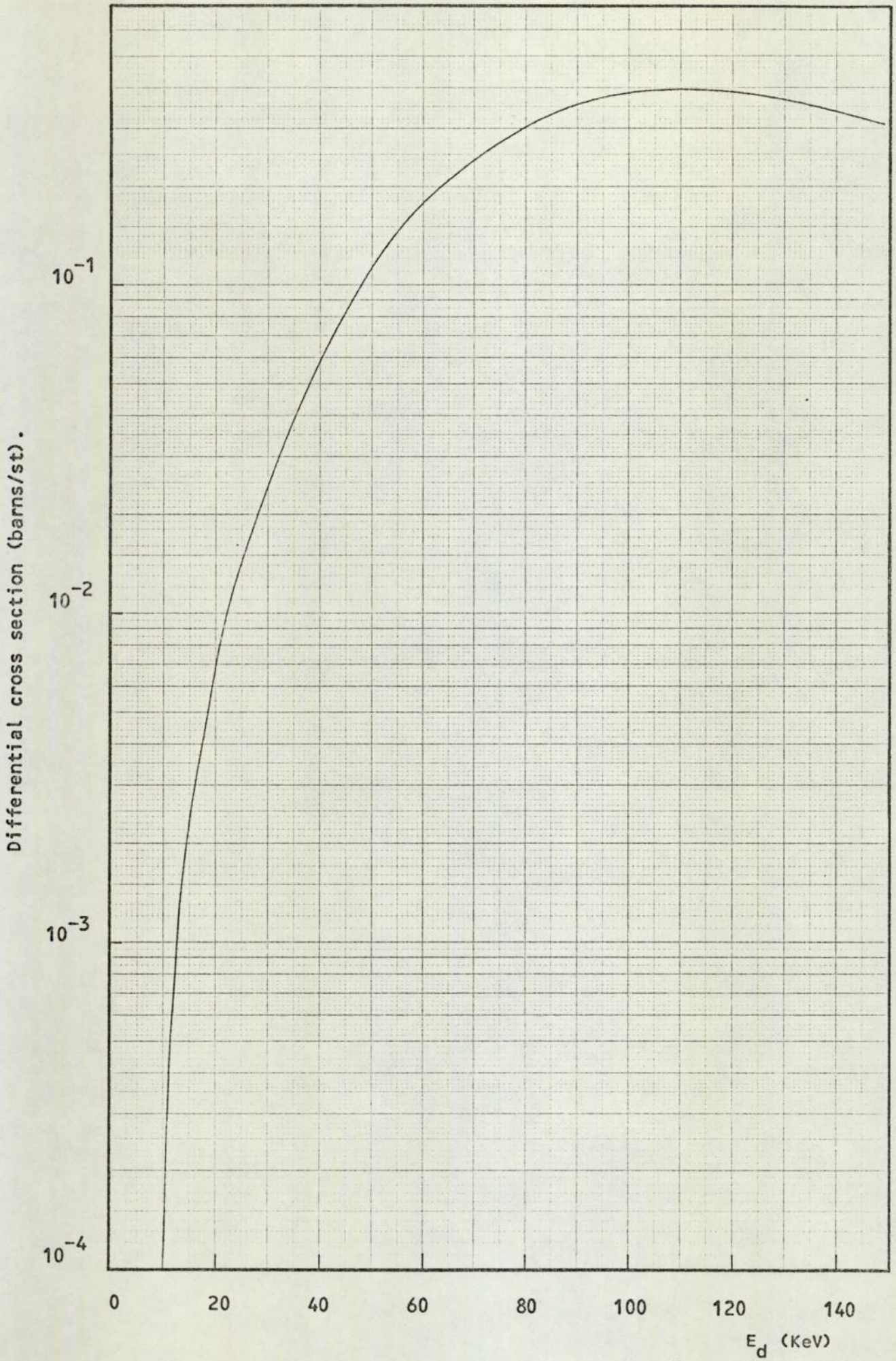

Figure 5.3. The differential cross section for the $^{3}H(d,n)^{4}He$ reaction.

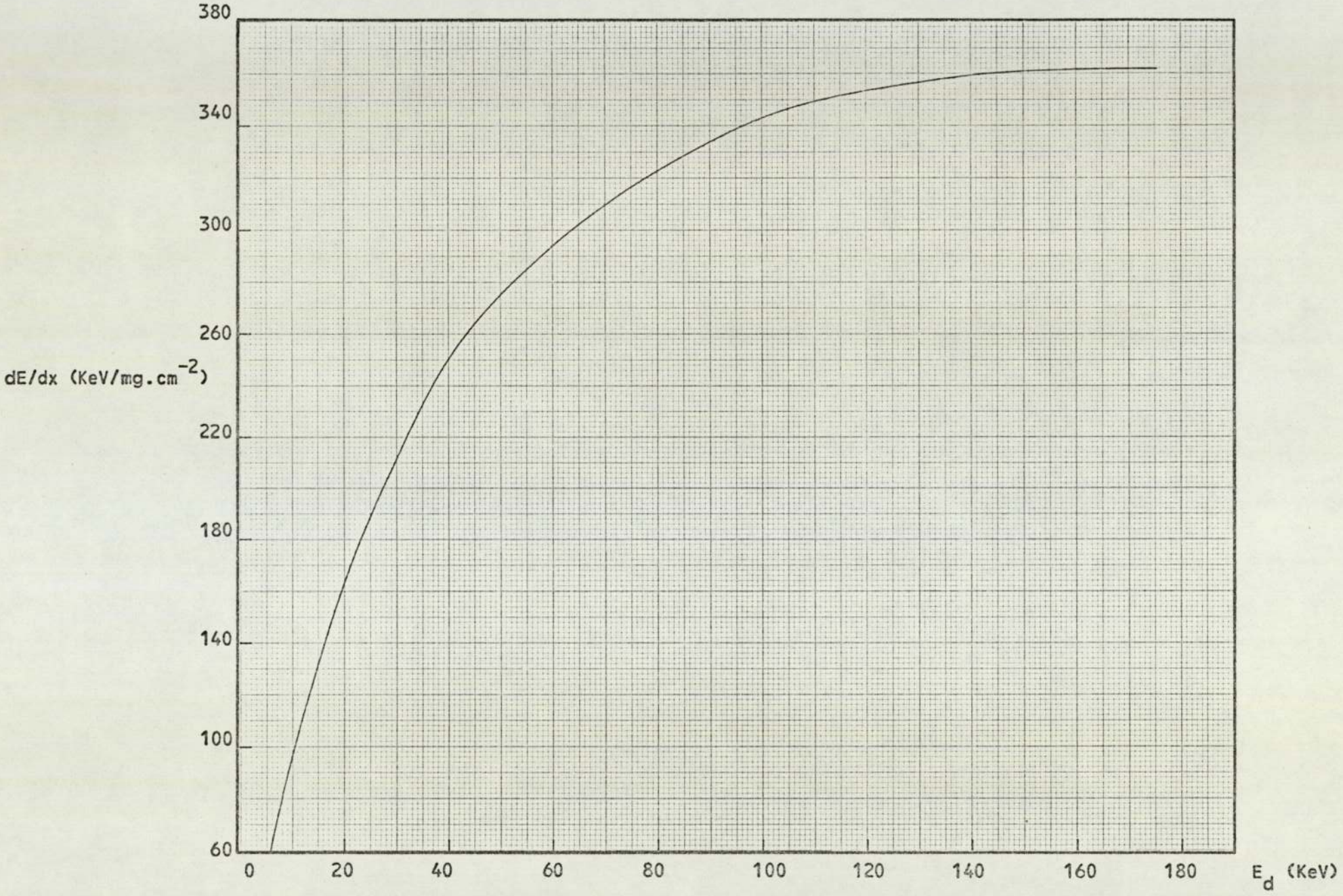

Figure 5.4. Energy loss of deuterons in titanium tritide[51].

as unity. The yield curve obtained is shown in figure 5.5.

With the information on the neutrons produced in the $^{3}H(d,n)^{4}He$ reaction found so far, it was possible to calculate the neutron beam profile, i.e., the relative neutron yield at each angle θ_n, as defined by the alpha particle detector. This was obtained using the data of figures 5.2 and 5.5. For example, from figure 5.2 at $\theta_n = 79^{o}$, the emitted neutrons having detected associated alpha particles are produced only by deuterons with incident energies between 120 KeV and 80 KeV. Using figure 5.5 it can be seen that the area under the curve in the energy interval 120 KeV to 80 KeV is proportional to the neutron yield. Calculation of the relative neutron yield at each angle θ_n over the defined neutron beam produced the beam profile shown in figure 5.6. The defined beam was centred at approximately 83.7^{o} to the incident deuteron beam, with a full width at half maximum of 10^{o}.

Implicit in the calculation of the neutron beam profile were the following assumptions; (i) the reaction products are isotropically distributed in the centre of mass frame of reference over the range of incident deuteron energies, (ii) uniform loading of tritium atoms to a depth at least equal to the range of the incident deuterons and, (iii) no scattering of the incident deuterons.

A comprehensive study of the problem of determining the absolute yield of 14 MeV neutrons from the $^{3}H(d,n)^{4}He$ reaction has been undertaken by Schrader et al[69], who concluded that these assumptions introduce little effect on the shape of the profile.

5.4 Corrections to the Differential Cross Section Equation

The differential elastic scattering cross section as defined by equation 5.12 required corrections for the sample thickness 'x' and the number of neutrons incident on the sample ϕ. Each of these are now considered separately.

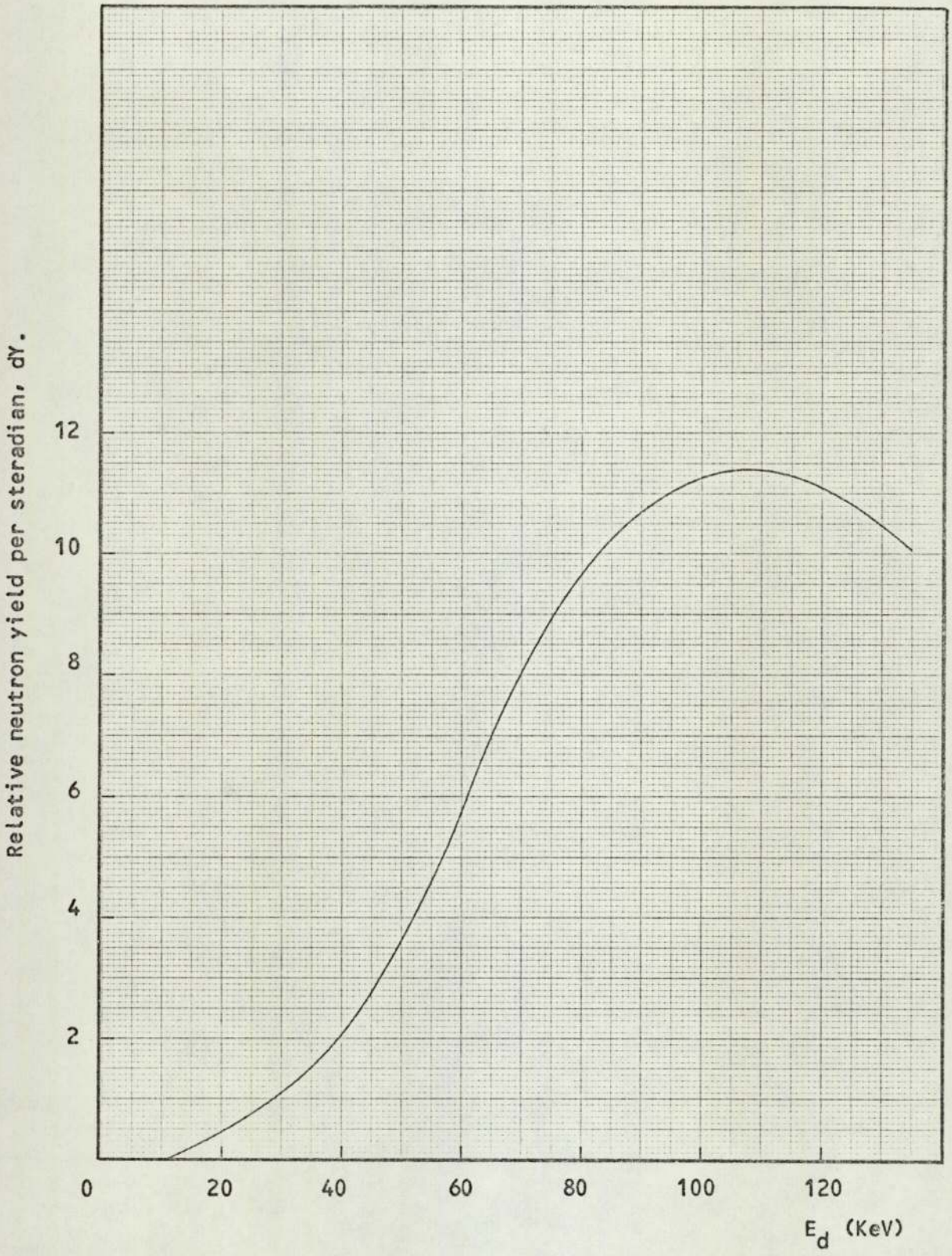

Figure 5.5. The relative neutron yield as a function of deuteron energy.

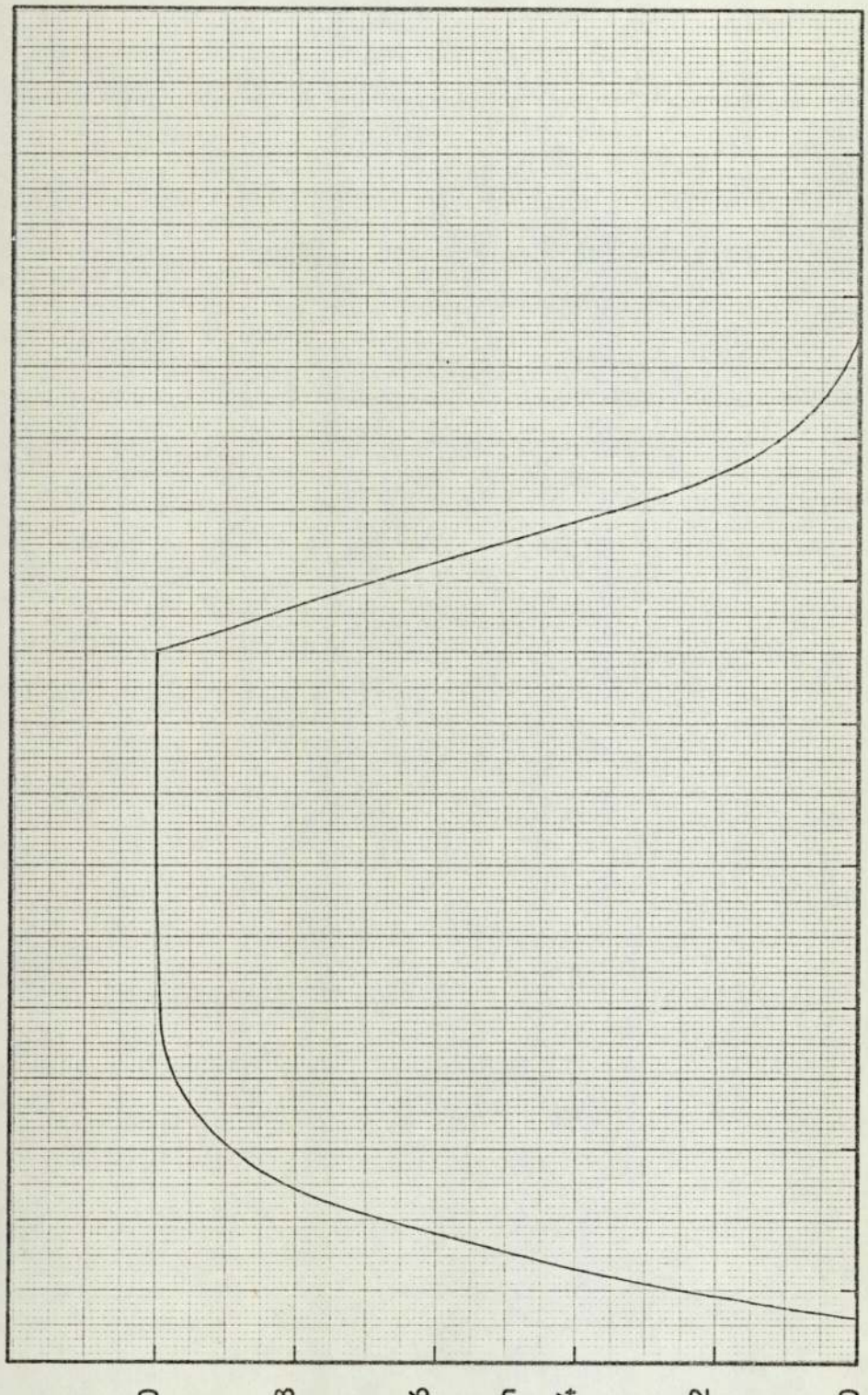

Figure 5.6. The neutron beam profile defined by the $90^{\circ} \pm 5^{\circ}$ alpha detector aperture.

The Sample Thickness

From figure 5.6 it can be seen that the neutron beam diverges over an angular range of 14^{o}. Therefore, for a scattering sample which completely subtends the defined neutron beam, the sample thickness varies with the neutron angle of emission. Since the intensity of the neutron beam also varies across the angular range it was necessary to replace the sample thickness term 'x' by a weighted average thickness.

The weighted average thickness was calculated using the neutron beam profile. The ratio r_i of the area under the curve in a small angular interval to the total area under the curve, gave the intensity of the beam passing through the sample at a given thickness x_i. The weighted sample thickness was then given by $\Sigma r_i x_i$, where i defines the angular range of the neutron beam. This expression was evaluated over one degree intervals using the data of figure 5.6.

The angle between the scattering sample and the incident neutron beam could be positioned to one degree, introducing a possible error in the sample thickness of 1.7%.

The Neutron Flux ϕ

The number of neutrons ϕ, incident on the sample, was determined by the number of counts in the alpha particle detector channel. This count had to be corrected for two effects, namely, (i) the background radiation in the alpha particle detector, which consisted of source neutrons and γ rays promptly emitted in fast neutron interactions with the material of the target assembly, and γ rays and β particles resulting from the activation of the target assembly; (ii) the absorption of source neutrons in the target assembly.

At the end of each data cycle the background count rate in the alpha particle detector was noted. This background was due entirely to the activation of the target assembly. The total background count over each data cycle was subtracted from the detector count.

To measure the neutron and γ ray prompt background correction factor, the alpha particle detector count rate was first recorded for a number of different deuteron beam target currents. The alpha particle detector aperture was then replaced by a blank aluminium plate of the same thickness, so that all alpha particles were completely shielded from the detector. The detector count rate was then noted for the same target currents. This count was due to the neutron and γ ray background. The detector counts were corrected for the activation background giving a value of 5.5% for the percentage of the alpha particle detector count due to prompt neutrons and γ rays. The prompt background correction factor, C_1, was then equal to 0.945.

In view of the design of the target holder, the neutrons had to penetrate 2.5 mm of steel and 1.3 mm of water in order to escape from the target assembly. The number of neutrons incident on the scattering sample was thus reduced due to neutron elastic scattering and inelastic reactions with these materials. However, neutron elastic scattering is very forward peaked, so that a large fraction of the source neutrons elastically scattered by the materials in the target assembly would still pass through the scattering sample. The fraction of source neutrons escaping the target assembly, C_2, was estimated to be:

$$C_2 = \exp - [\alpha_{Fe} x_1 + \alpha_{H_2O} x_2] \qquad \ldots\ldots 5.19$$

where α_{Fe} and α_{H_2O} are the absorption coefficients for iron and water, and x_1, x_2 are the thicknesses of iron and water respectively. The absorption coefficients were calculated using the total cross section data given in the Barn Book[70]. The fraction of source neutrons escaping the target assembly was calculated as 0.937.

In applying these three corrections the neutron flux was determined with an estimated error of less than 1%.

5.5 Experimental Determination of the Efficiency of the Neutron Spectrometer

The efficiency of the alpha particle detector was assumed to be 100%. No error resulted from this assumption because those neutrons associated with lost alpha events were not part of the coincident beam.

The energy of neutrons elastically scattered in the laboratory system by potassium and lithium nuclei varies slightly with scattering angle, affecting both the efficiency of detection in the neutron detector and their flight time. For a neutron scattering collision in the laboratory system, the energy of the scattered neutron is a function of the scattering angle and the mass of the scattering nucleus. The general expression for the energy of a neutron in the laboratory system may be written in the form[63]:

$$E_n(E_o, \theta) = \left(\frac{m_n}{m_n + m_N}\right)^2 E_o \cos 2\theta + \left(\frac{m_N}{m_n + m_N}\right)\left[\frac{m_N}{m_n + m_N} E_o + Q\right]$$

$$\pm \frac{2\cos\theta}{m_n + m_N} \sqrt{m_n^2 \cdot \frac{m_N}{m_n + m_N} E_o \left(\frac{m_N}{m_n + m_N} E_o + Q\right)}$$

$$\times \sqrt{1 - \frac{m_n^2}{m_n + m_N} \cdot \frac{E_o \sin^2\theta}{m_N \left(\frac{m_N}{m_n + m_N} E_o + Q\right)}} \qquad \ldots\ldots 5.20$$

where E_o is the energy of the incident neutron in the laboratory system, θ is the laboratory angle made by the scattered neutron with the incident beam direction, m_n is the mass of the neutron and m_N is the mass of the scattering nucleus. Figure 5.7 shows the neutron energy as a function of laboratory scattering angle for potassium and lithium; evaluated by equation 5.20 over the angular range $0^\circ - 100^\circ$.

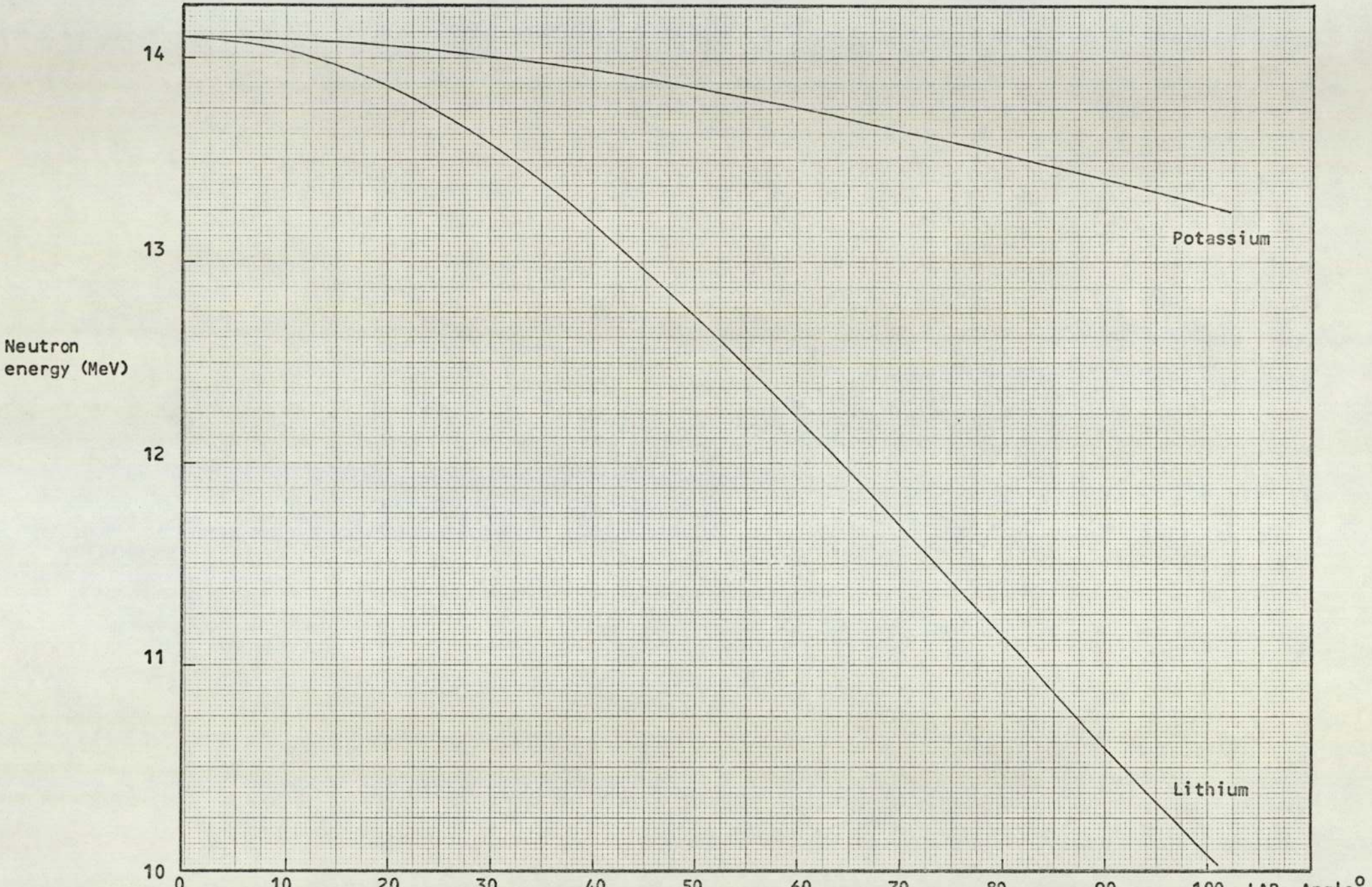

Figure 5.7. Neutron energy as a function of laboratory scattering angle for potassium and lithium.

In order to apply the correct value of the efficiency term, $\epsilon(E_n)$ in equation 5.13, it was necessary to determine experimentally the efficiency of the neutron detector as a function of the energy of the scattered neutron.

Neutron Detector Efficiency

The efficiency of the neutron detector for 14.1 MeV neutrons was measured using the direct beam. The centre of the face of the neutron detector was positioned 150 mm from the neutron source, so as to completely encompass the defined cone of associated neutrons. In view of the very short neutron flight path, the pulse repetition rate in the alpha particle detector channel was restricted to 1 KHz, and a number of coincidence spectra were observed. The efficiency of the neutron detector was then given by the ratio of the total number of coincidences to the total number of neutrons incident on the detector, as defined by the alpha particle detector count. When employing this method, the efficiency of the neutron detector for 14.1 MeV neutrons was determined to be 9.4% $\pm$ 0.1%.

The relative sensitivity of the neutron detector to neutrons of lower energies was determined by measuring the yields of neutrons scattered by hydrogen at known angles, and assuming that this scattering is isotropic in the centre of mass system[22,71,72]. The energy and yield can then be related to the laboratory angle. The hydrogen was in the form of a flat sheet of polyethylene, which is a polymerised form of ethylene, $CH_2:CH_2$.

For the particular case of neutron-proton scattering in the laboratory system, the energy of the scattered neutron as defined by equation 5.20 reduces to the much simpler form:

$$E_n = \frac{E_o}{2}[1 + \cos 2\theta] \qquad \ldots\ldots 5.21$$

where the terms are as defined previously. Figure 5.8 shows the neutron

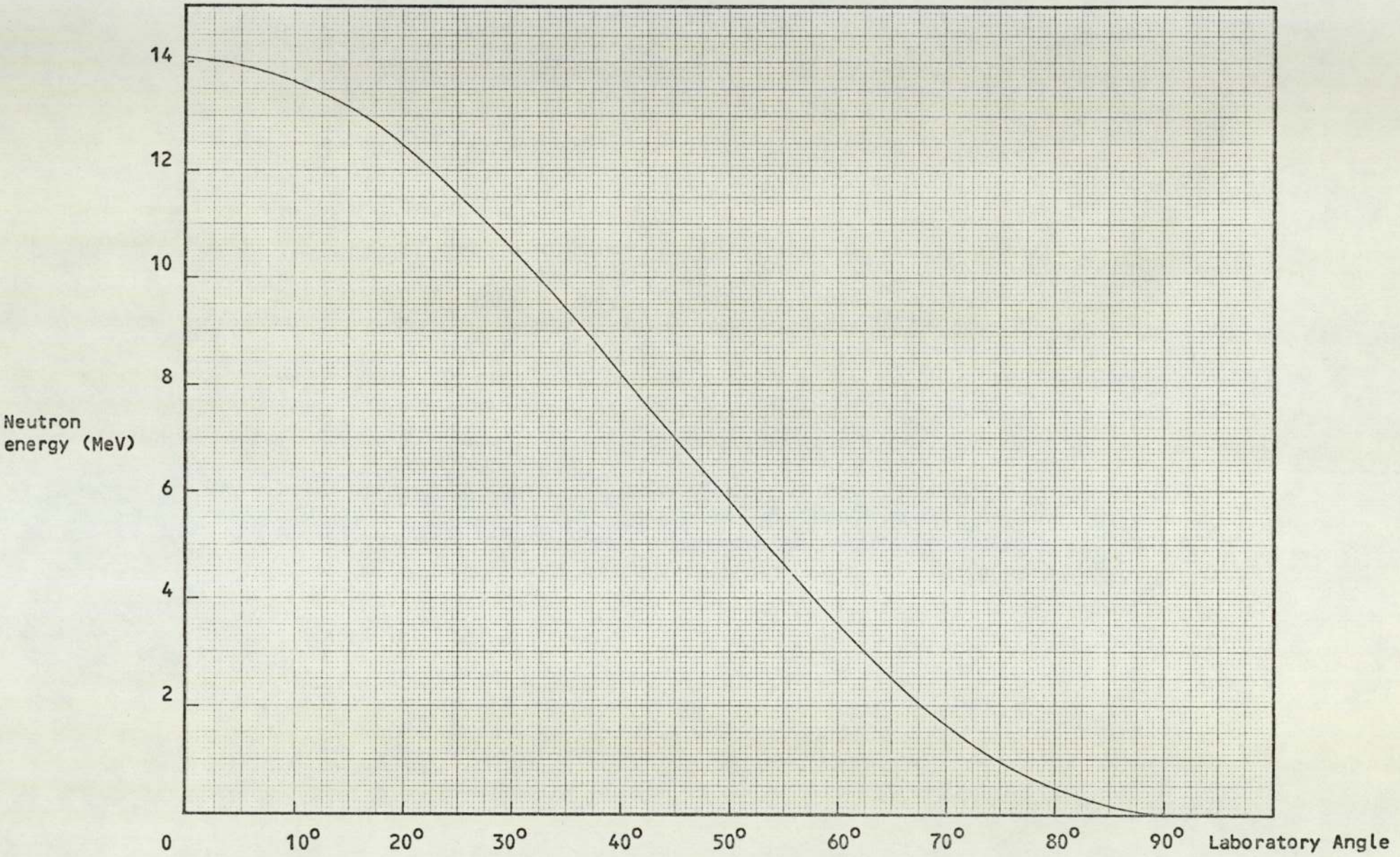

Figure 5.8. Neutron energy as a function of laboratory angle for scattering from hydrogen.

energy as a function of laboratory angle for incident neutrons of 14.1 MeV, as evaluated by equation 5.21.

When measuring the yield of neutrons scattered by the hydrogen content of a polyethylene sample, it is found that at certain angles the hydrogen peak overlaps with those of the neutrons elastically scattered by carbon and inelastically scattered to the 4.43 MeV state in carbon. It was therefore necessary to subtract from the polyethylene spectra the contribution due to neutron scattering from the carbon content of the sample. Two approaches are available for this correction. The first is by taking time of flight spectra for both the polyethylene and a graphite sample; the known response of the system to elastic and inelastic scattering from carbon can then be subtracted from the polyethylene spectra. The second approach is to use a graphite sample of equivalent thickness to the carbon content of the polyethylene; the contribution due to scattering from carbon can then be subtracted directly. This approach was used in the present work, the main advantage being in the amount of experimental time required for data accumulation.

The thickness of graphite required to make a direct subtraction of the scattering due to carbon was deduced using equation 5.10. For the same incident neutron flux ϕ, the number of neutrons scattered by carbon nuclei in a polyethylene sample and graphite sample respectively, is given by:

$$N_{CP} = \phi[1 - \exp(-ax_p)] \frac{n_{CP}\sigma_C}{a} \quad \ldots\ldots 5.22(a)$$

with $a = n_{HP}\sigma_H + n_{CP}\sigma_C$, and

$$N_C = \phi[1 - \exp(-n_C\sigma_C x_C)] \quad \ldots\ldots 5.22(b)$$

where n_{HP} = number of hydrogen atoms per cm^3 of polyethylene

n_{CP} = number of carbon atoms per cm^3 of polyethylene

n_C = number of carbon atoms per cm^3 of graphite

σ_H = total cross section for hydrogen

σ_C = total cross section for carbon

x_p = thickness of the polyethylene sample

x_C = thickness of the graphite sample.

Solution of equations 5.22(a) and 5.22(b) showed that to a good approximation, the thickness of graphite required to make a direct subtraction was given by:

$$x_C = \frac{1 \pm [1 - 2x_p(1 - ax_p/2)n_{CP}\sigma_C]^{\frac{1}{2}}}{n_C\sigma_C} \quad \ldots\ldots 5.23$$

To minimise multiple scattering effects, the thickness of the polyethylene sample was chosen to be 20 mm. Using equation 5.23, this required a graphite sample of thickness 8.28 mm for the direct subtraction of scattering due to the carbon content of the polyethylene sample.

To further minimise the effects of carbon scattering, the scattering angles were chosen where the flight times of the neutrons scattered from the carbon and hydrogen were well separated. These angles were 25^o, 40^o and 50^o in the laboratory system. Figure 5.8 shows that at these angles the energy of the neutron scattered from hydrogen is 11.58 MeV, 8.27 MeV and 5.83 MeV respectively.

The energy of a neutron scattered by hydrogen falls very sharply with laboratory angle. This results in a relatively wide range of flight times for the scattered neutrons. To minimise this effect the angular acceptance of the associated alpha particles was reduced to $\pm 2^o$ in the reaction plane. The minimum acceptance is limited by

straggling due to scattering of the alpha particles in the target.

Experimental Procedure

With the electronic system set up as described in section 3.6, time of flight spectra were observed at laboratory angles of 25^{o}, 40^{o} and 50^{o}. The neutron detector face was positioned 2m from the centre of the scattering sample. The experimental configuration is shown in figure 5.9. Prior to taking experimental measurements, the electronics was switched on for two hours to allow the system to stabilise. The neutron source was also run to allow the induced activity in the target assembly to become reasonably constant. Alternate runs were made with the polyethylene sample in position, and with the graphite sample to correct for the contribution due to carbon scattering in the spectra. A single run corresponded to an alpha monitor count of 10^{8}. The time of flight spectra obtained are shown in figures 5.10, 5.11 and 5.12. On examination of the spectra, the energy spread of the neutrons scattered by hydrogen becomes apparent, indicated by the deterioration in the time resolution (FWHM) with increasing laboratory angle.

The sensitivity of the neutron detector as a function of energy was determined by use of the equation:

$$\epsilon(E_n) = \frac{N'(\theta)}{C_1 C_2 \phi n \Sigma r_i x_i \Omega \left(\frac{d\sigma}{d\Omega}\right)_H} \qquad \ldots\ldots 5.24$$

where $\left(\frac{d\sigma}{d\Omega}\right)_H$ is the differential cross section in the laboratory system for scattering from hydrogen and the remaining terms are as defined previously. The value of $\left(\frac{d\sigma}{d\Omega}\right)_H$ was calculated from the results of the angular distribution measurements of neutron-proton scattering obtained by Seagrave[71]. The results are presented in the centre of mass system as an isotropic distribution, with a differential cross section of 52 ± 2.4 mb/sr. In order to convert the differential cross section in

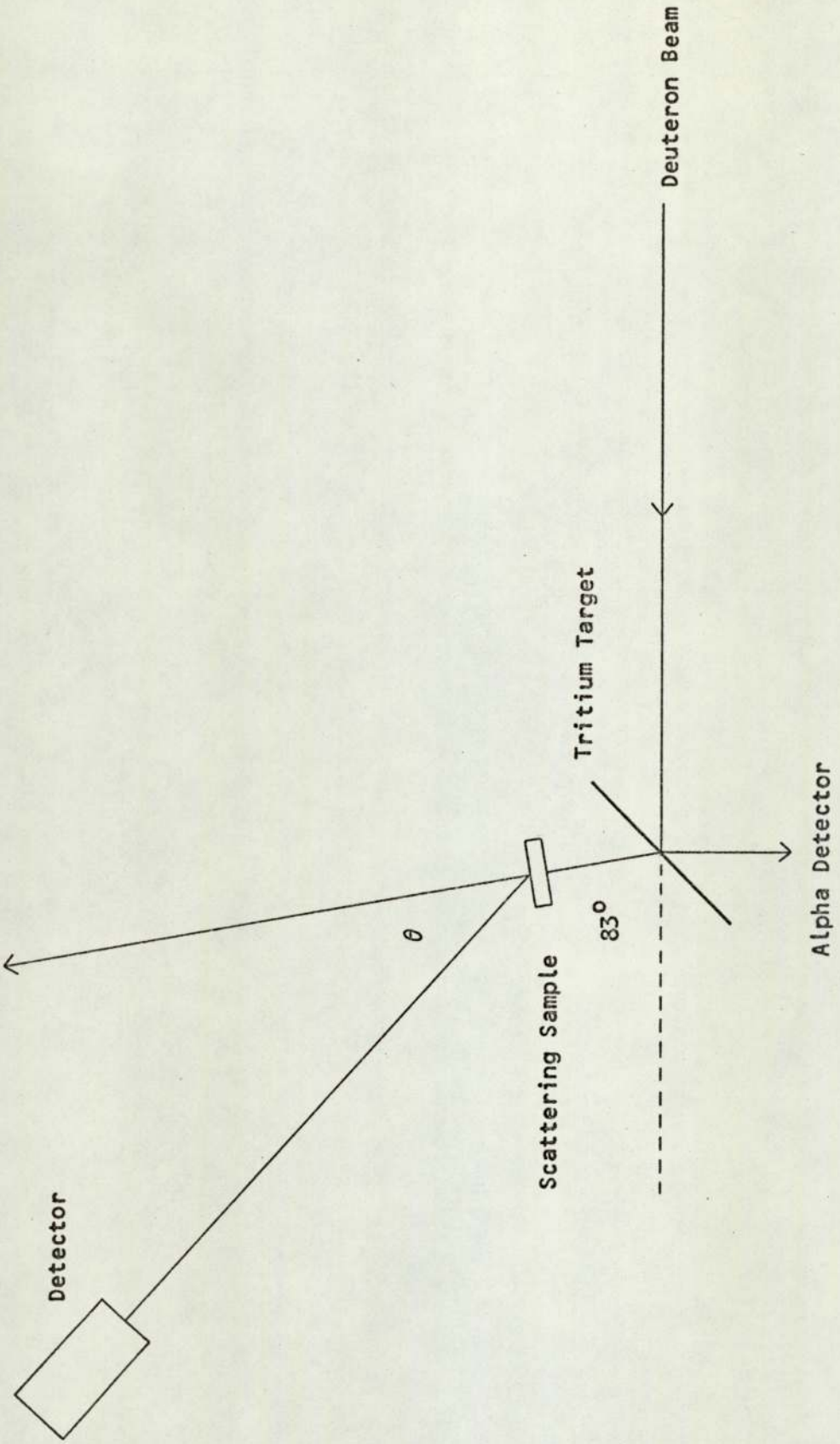

Figure 5.9. Experimental configuration.

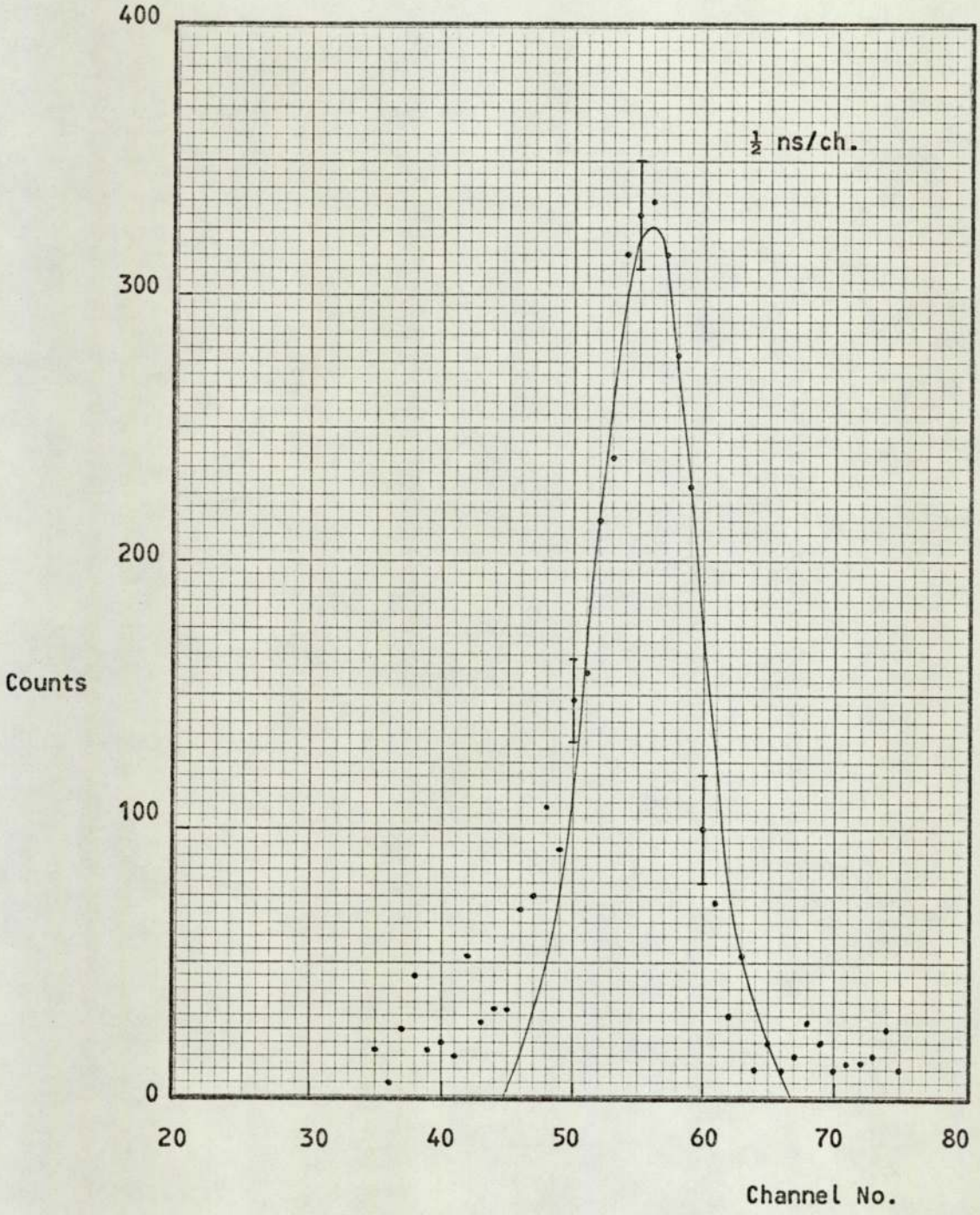

Figure 5.10. Time of flight spectrum for scattering from hydrogen at 25^{o} in the laboratory system.

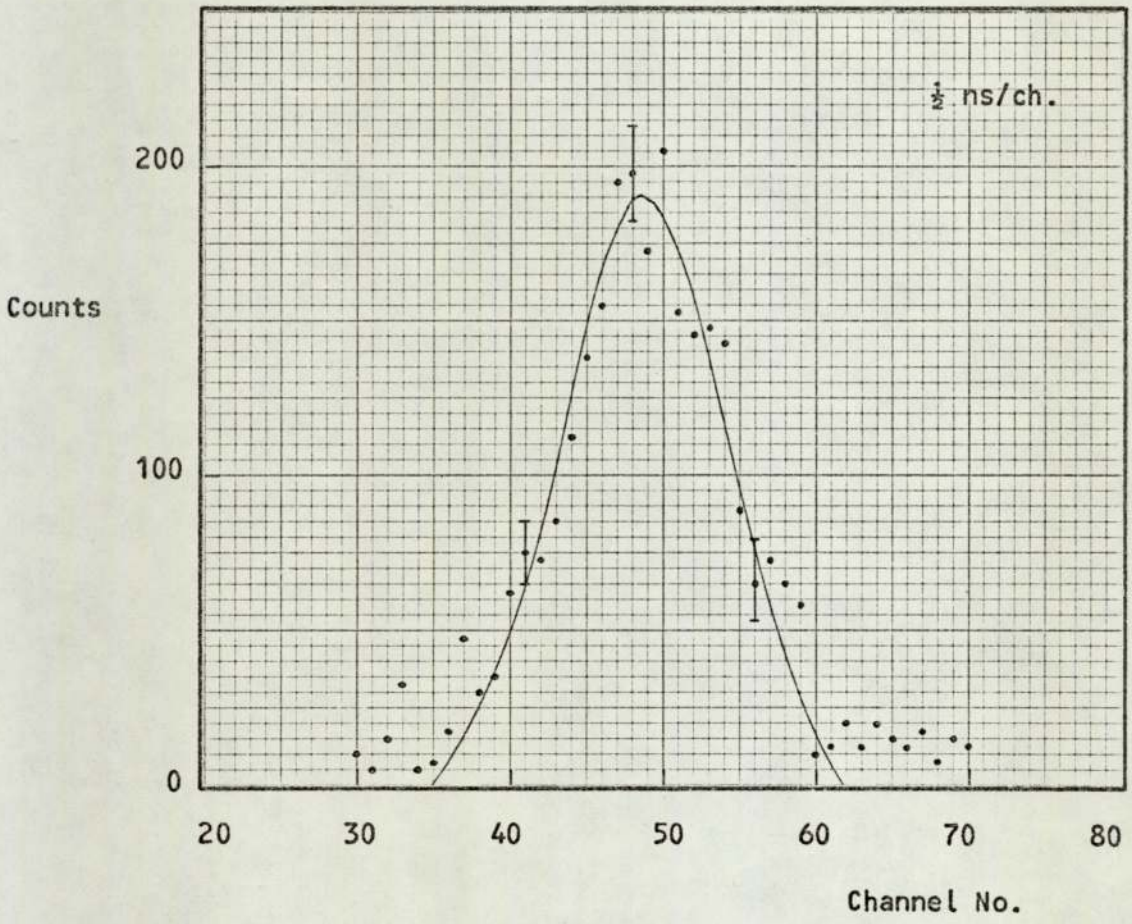

Figure 5.11. Time of flight spectrum for scattering from hydrogen at 40^{o} in the laboratory system.

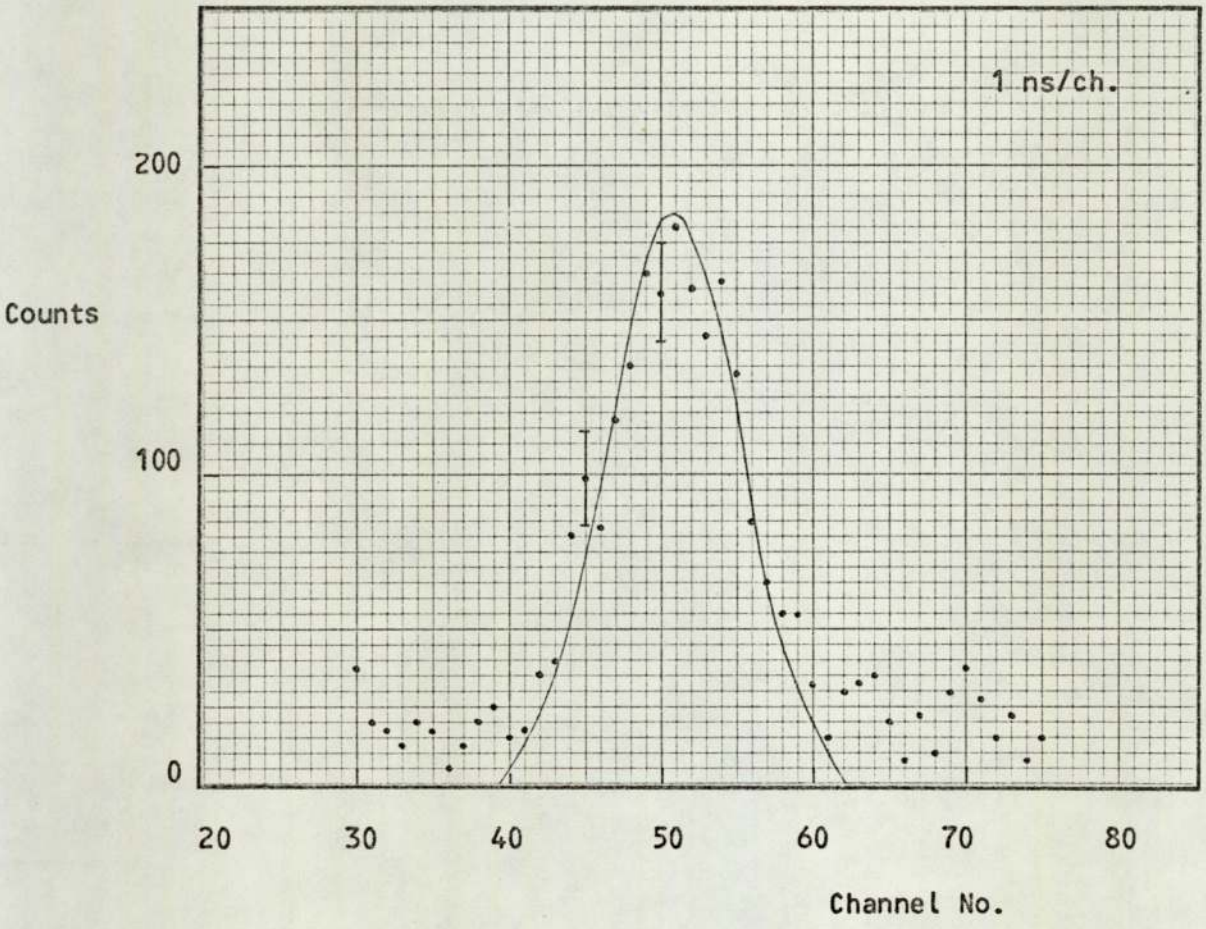

Figure 5.12. Time of flight spectrum for scattering from hydrogen at 50^{o} in the laboratory system.

the centre of mass system to the laboratory system, it was necessary to determine the anisotropy factor as defined by equation 5.9. For the particular case of neutron-proton scattering, the relationship between the scattering angles in the two systems is that the centre of mass angle is twice the laboratory angle. Equation 5.9 then reduces to

$$\frac{d\Omega'}{d\Omega} = 4\cos\theta \qquad \ldots\ldots 5.25$$

The relative sensitivity of the neutron detector determined experimentally as a function of energy is shown in figure 5.13.

For the points obtained by scattering from hydrogen, the errors indicated in the energy values represent the energy spread of the scattered neutrons due to the finite angular acceptance of the spectrometer. The largest single source of error in the sensitivity was the error in the estimation of the hydrogen peak intensity. If A_i is the count added into the ith channel and S_i is the background counts subtracted from the ith channel, then the standard error in A_i, given by a_i, is[73]

$$a_i = (A_i + S_i)^{\frac{1}{2}} \qquad \ldots\ldots 5.26$$

The total error on a peak is then given by $(\Sigma a_i^2)^{\frac{1}{2}}$. The errors in each term of equation 5.24 are summarised in table 5.1. The error in the relative sensitivity was obtained by adding the errors in each term quadratically to give an estimated experimental error.

5.6 ^{39}K Differential Cross Section Measurements

The Scattering Sample

The potassium sample was of solid metal moulded into a thin walled (1.2mm) aluminium container. To prevent oxidation, the moulding process was carried out by melting the potassium under paraffin. The top of the sample was then sealed by a thin layer of paraffin wax. An

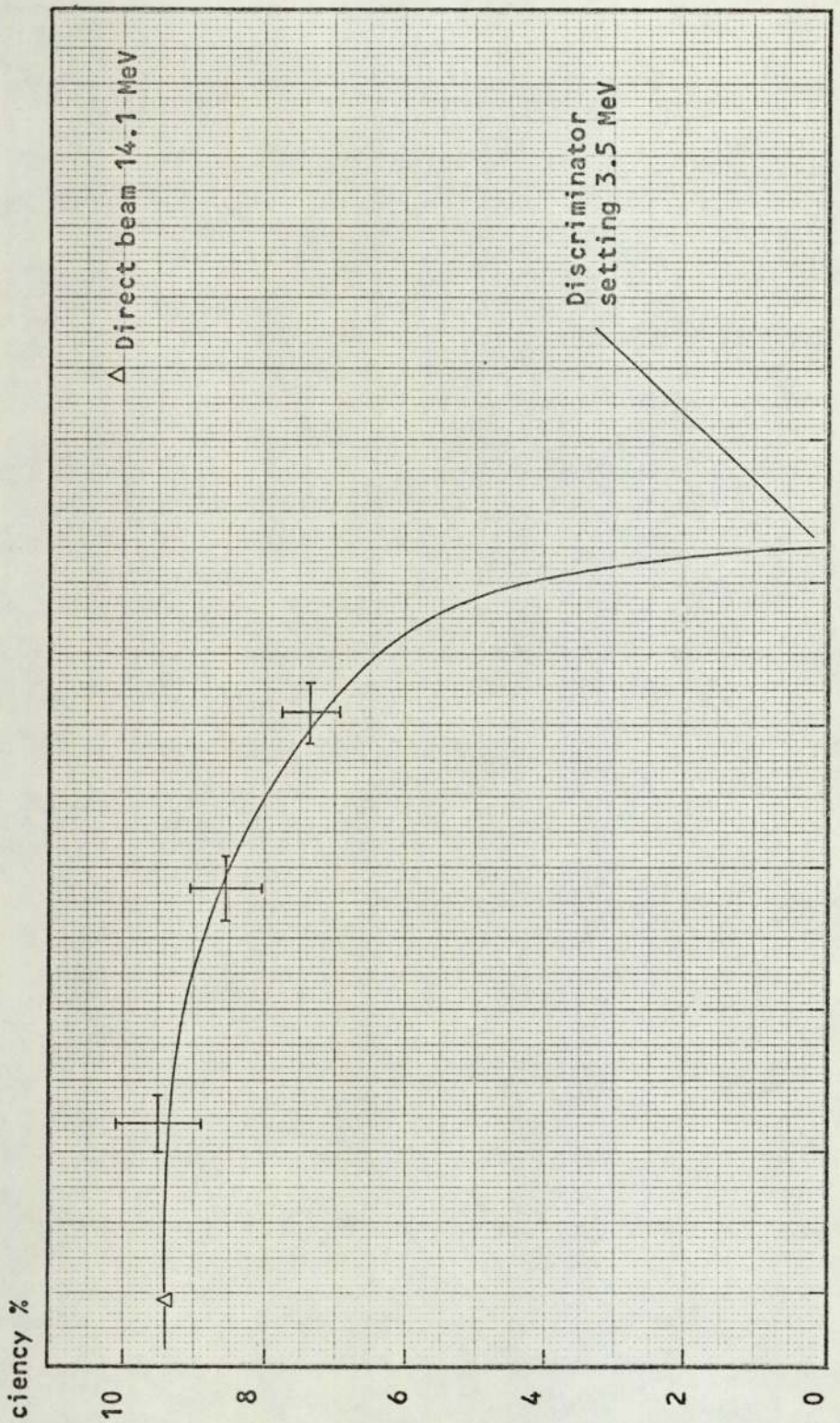

Figure 5.13. Measured efficiency of the neutron detector as a function of neutron energy.

Table 5.1

Term	Estimated Error
Peak counts, $N'(\theta)$	$(\Sigma a_i^2)^{\frac{1}{2}}$
Sample thickness, $\Sigma r_i x_i$	1.7%
Solid angle, $\Delta\Omega$	1.0%
Corrected flux, $C_1 C_2 \phi$	1.0%
Hydrogen differential cross section, $(d\sigma/d\Omega)_H$	4.5%

X-ray radiograph of the constructed sample showed good uniformity of the potassium metal inside the container. The sample measured 120 mm by 140 mm and was 25 mm thick. An identical empty aluminium container was used for background subtraction.

Time of Flight Spectra

The experimental procedure for accumulating time of flight spectra was as described in section 5.5. Alternate runs were made with the potassium sample in position, and with the empty aluminium container to subtract the background contribution. Time of flight spectra were accumulated at nine laboratory angles between 20^{o} and 100^{o}, in ten degree intervals. Typical spectra obtained are shown in figures 5.14, 5.15 and 5.16, corresponding to laboratory angles of 20^{o}, 40^{o} and 60^{o} respectively. For each time of flight spectrum obtained a normal error curve was applied to the elastic scattering peak.

Differential Elastic Scattering Cross Sections

The equation used to evaluate the differential elastic scattering cross sections was:

$$\frac{d\sigma_{el}}{d\Omega} = \frac{N'(\theta)}{C_1 C_2 \phi n(\Sigma r_i x_i) \Delta\Omega \ \epsilon(E_n)} \qquad \ldots\ldots 5.27$$

where all the terms are as defined previously. The results obtained were transferred to the centre of mass system by use of equations 5.6 and 5.7, and are given in table 5.2, together with those of Frasca et al[8]. The angular distributions are shown in figure 5.17.

Each experimental point in the present work is subject to an angular uncertainty of $\pm 5^{o}$ due to the angular acceptance of the defining alpha particle detector aperture. The errors indicated in the differential cross sections were obtained by adding the errors in each term of equation 5.27 in quadrature, to give an estimated experimental error.

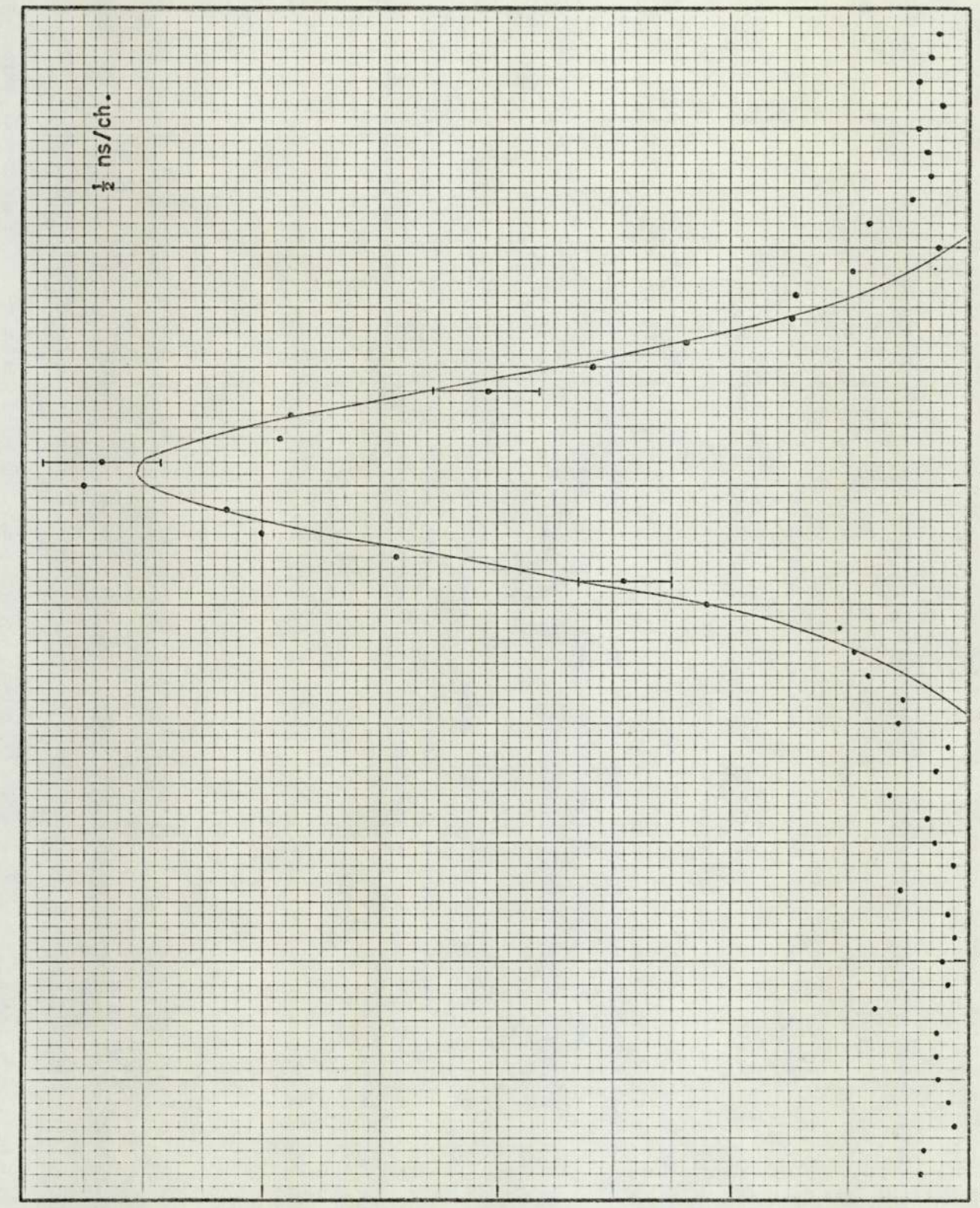

Figure 5.14. Time of flight spectrum for scattering from ^{39}K at 20° in the laboratory system.

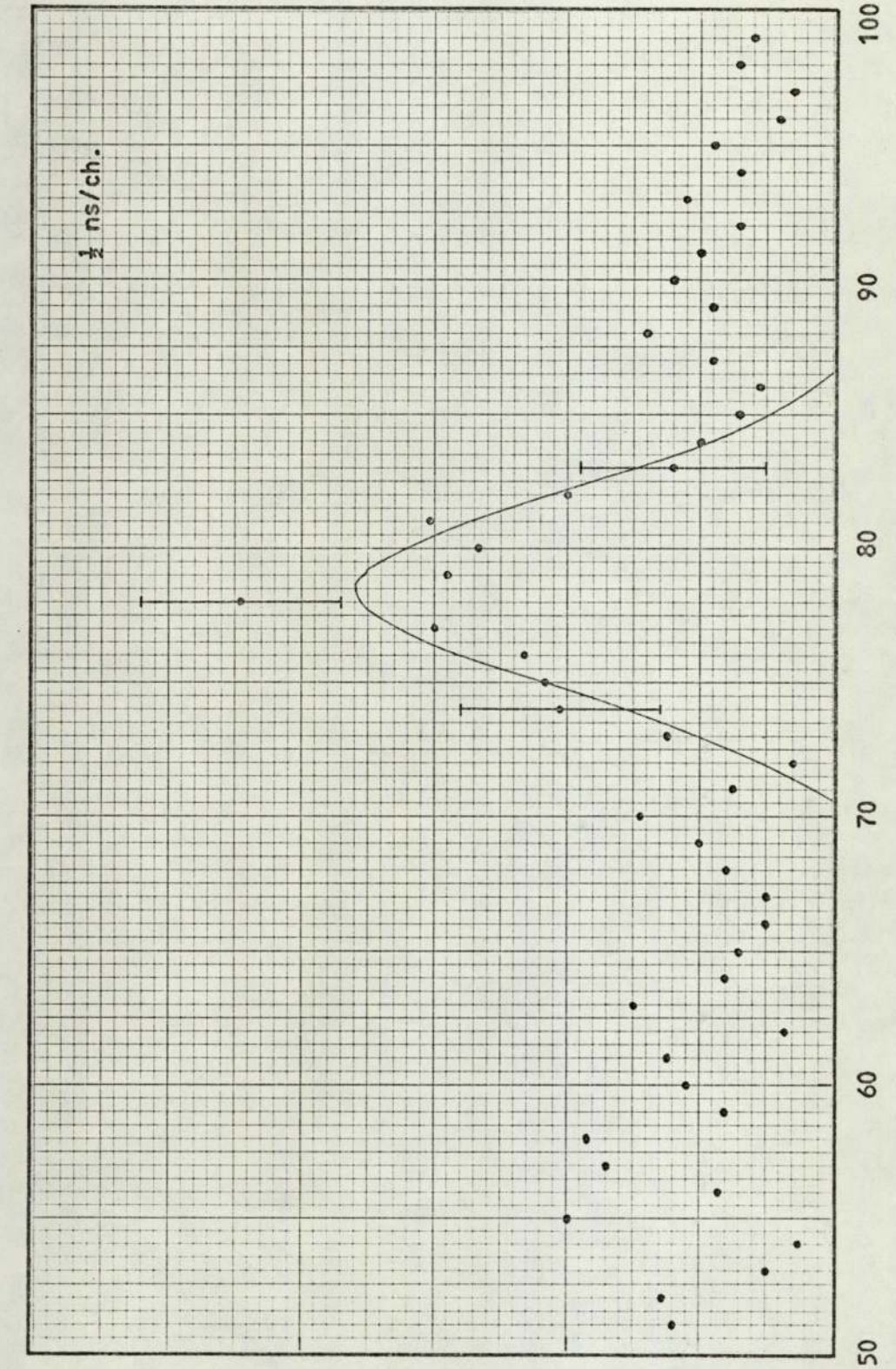

Figure 5.15. Time of flight spectrum for scattering from ^{39}K at 40^{0} in the laboratory system.

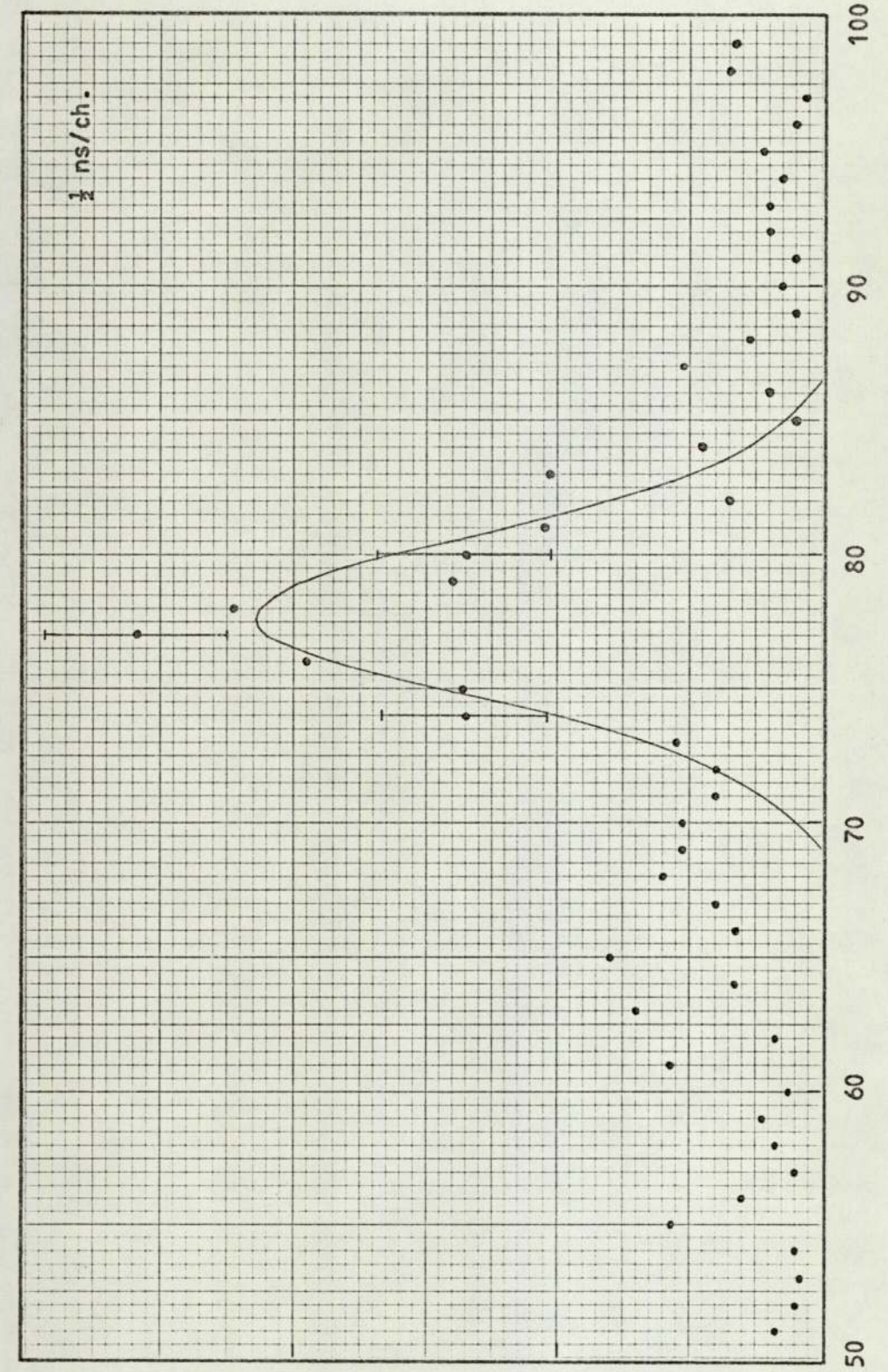

Figure 5.16. Time of flight spectrum for scattering from ^{39}K at 60^{o} in the laboratory system.

Table 5.2

^{39}K Differential Elastic Scattering Cross Section Data

Present Work			Frasca et al		
Centre of Mass Scattering Angle (degrees)	Differential Cross Section (mb/st)	Experimental Error (mb/st)	Centre of Mass Scattering Angle (degrees)	Differential Cross Section (mb/st)	Experimental Error (mb/st)
20° 30'	584.4	39.7	20° 36'	740	35
30° 45'	148.5	12.2	30° 54'	168	10
40° 57'	52.4	6.1	41° 6'	45.8	3.2
51° 7'	80.8	9.2	51° 18'	94	5.5
61° 16'	68.6	6.3	61° 30'	74.8	3.8
71° 23'	29.2	4.9	71° 36'	40.7	2.9
81° 27'	25.7	5.4	81° 42'	22.6	2.1
91° 28'	32.4	5.1	91° 42'	31.1	2.8
101° 26'	38.8	6.0	102° 6'	37.6	3.4

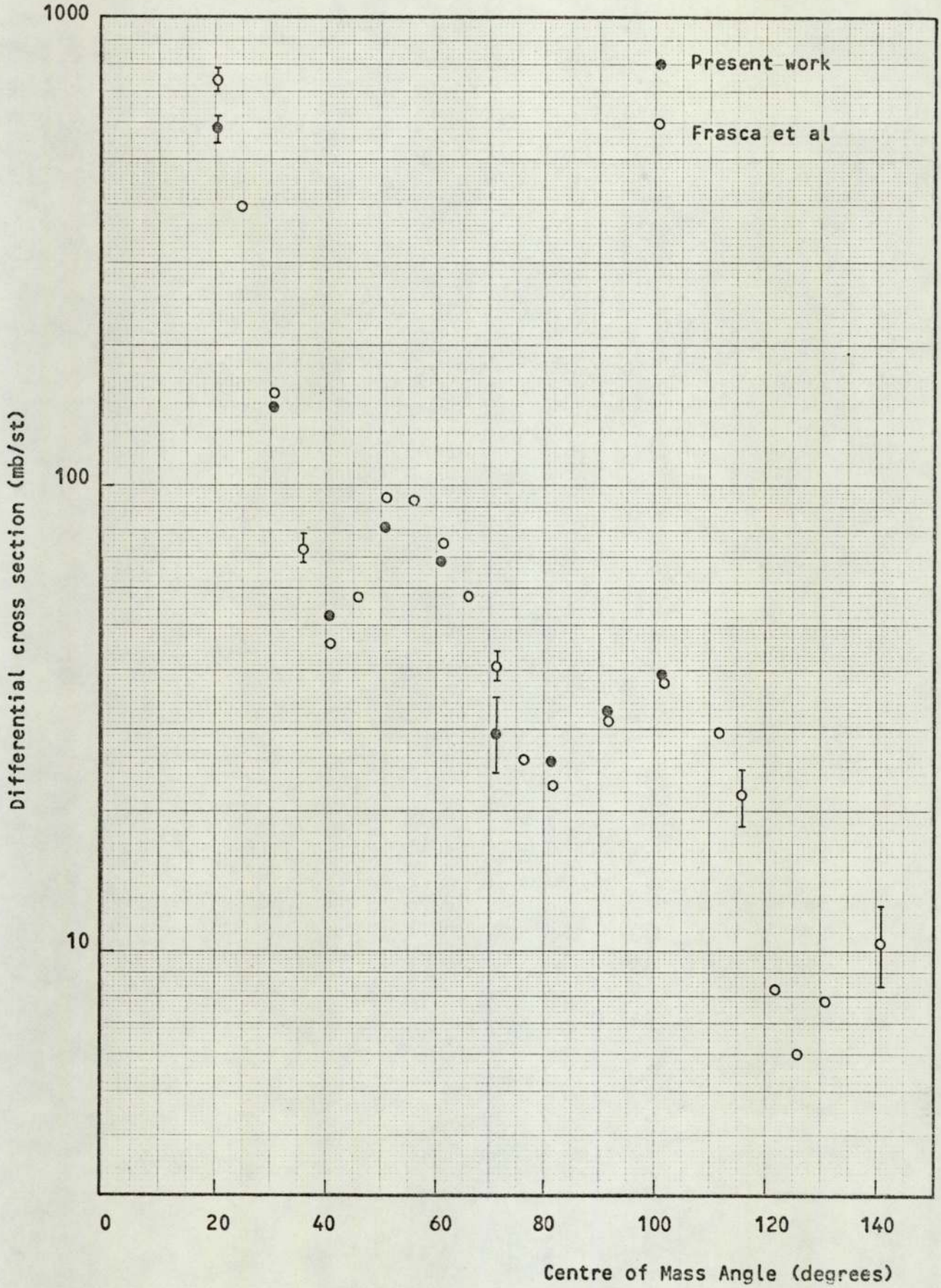

Figure 5.17. Comparison of the measurements of the differential elastic scattering cross section from ^{39}K at 14.1 MeV.

The results obtained for potassium using flat plate geometry are in good agreement within experimental errors with those obtained by Frasca et al[8] using cylindrical geometry, except for the 20° (LAB) measurement. However, with the exception of the values at 20° and 30° (LAB), the experimental errors quoted by Frasca et al are approximately a factor of two better than those of the present work. The data of Frasca et al was not corrected for multiple scattering or absorption, but was corrected for the finite angular resolution of the spectrometer, this being ± 3.5° in the scattering plane. The effect of the angular resolution, and a comparison of the present measurements with the optical model predictions is discussed in Chapter 6.

5.7 ^{7}Li Differential Cross Section Measurements

The Scattering Sample

The lithium sample was of solid metal and was initially moulded into a thin walled aluminium container; a method similar to that used by Cookson et al[74]. To prevent any oxidation the moulding process was carried out by melting the lithium in an argon atmosphere. However, the combination of these two metals was found to form a solid solution. On the recommendation of Whittaker[75], the lithium metal was enclosed in a thin walled (0.7 mm) stainless steel container. An X-ray radiograph of the constructed sample showed good uniformity of the lithium inside the container. The sample measured 120 mm by 140 mm and was 20 mm thick. Again, an identical empty container was used for background subtraction.

Time of Flight Spectra

Time of flight spectra were accumulated at the same nine laboratory angles as for potassium. Typical spectra obtained are shown in figures 5.18, 5.19 and 5.20, corresponding to laboratory angles of 20°, 50° and 100° respectively. The inelastic neutrons from the 4.61 MeV level are clearly resolved at 20° and 50°. Neutrons from the 0.477 MeV level are included in the elastic peaks since they were not resolved from

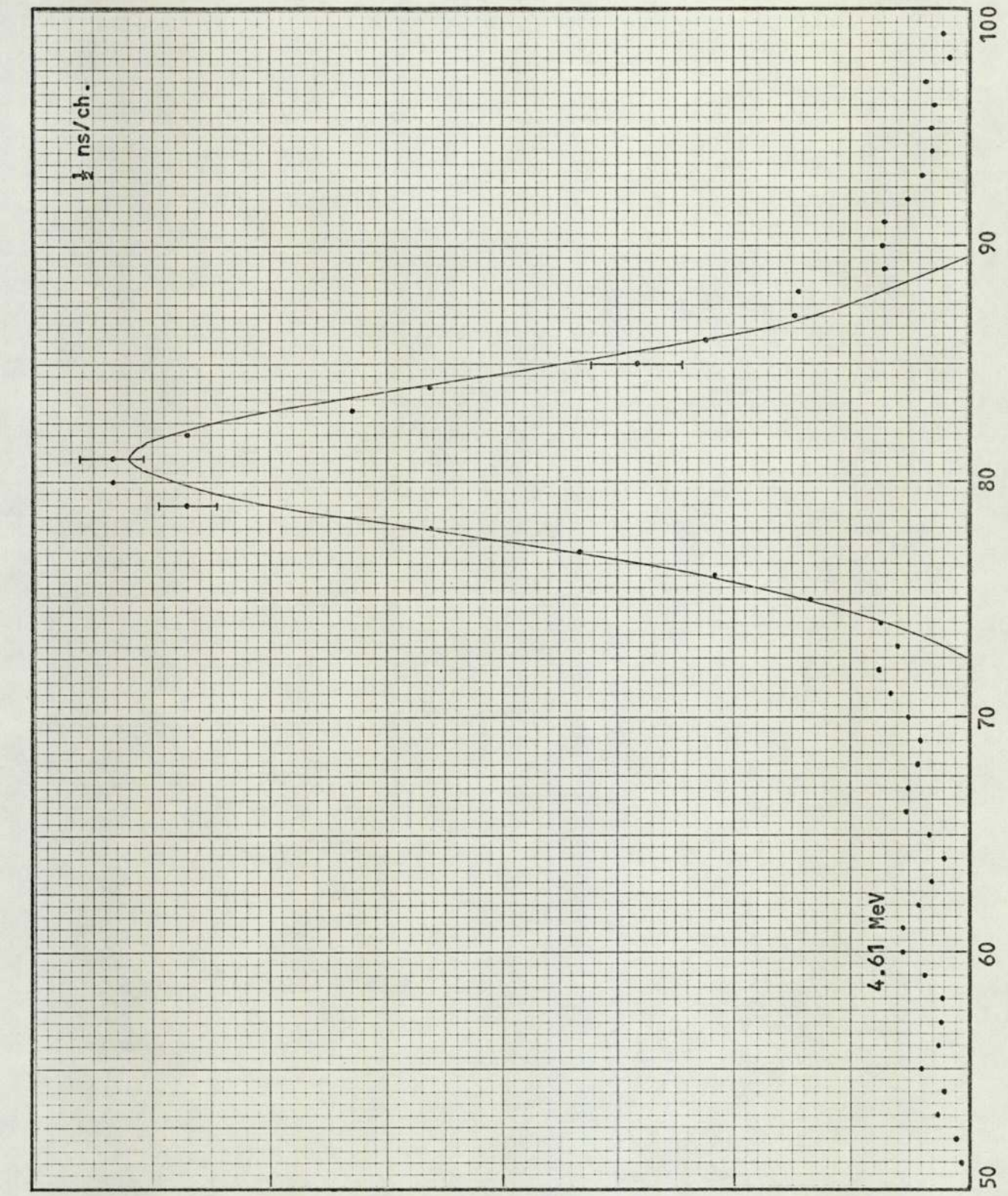

Figure 5.18. Time of flight spectrum for scattering from ^{7}Li at 20° in the laboratory system.

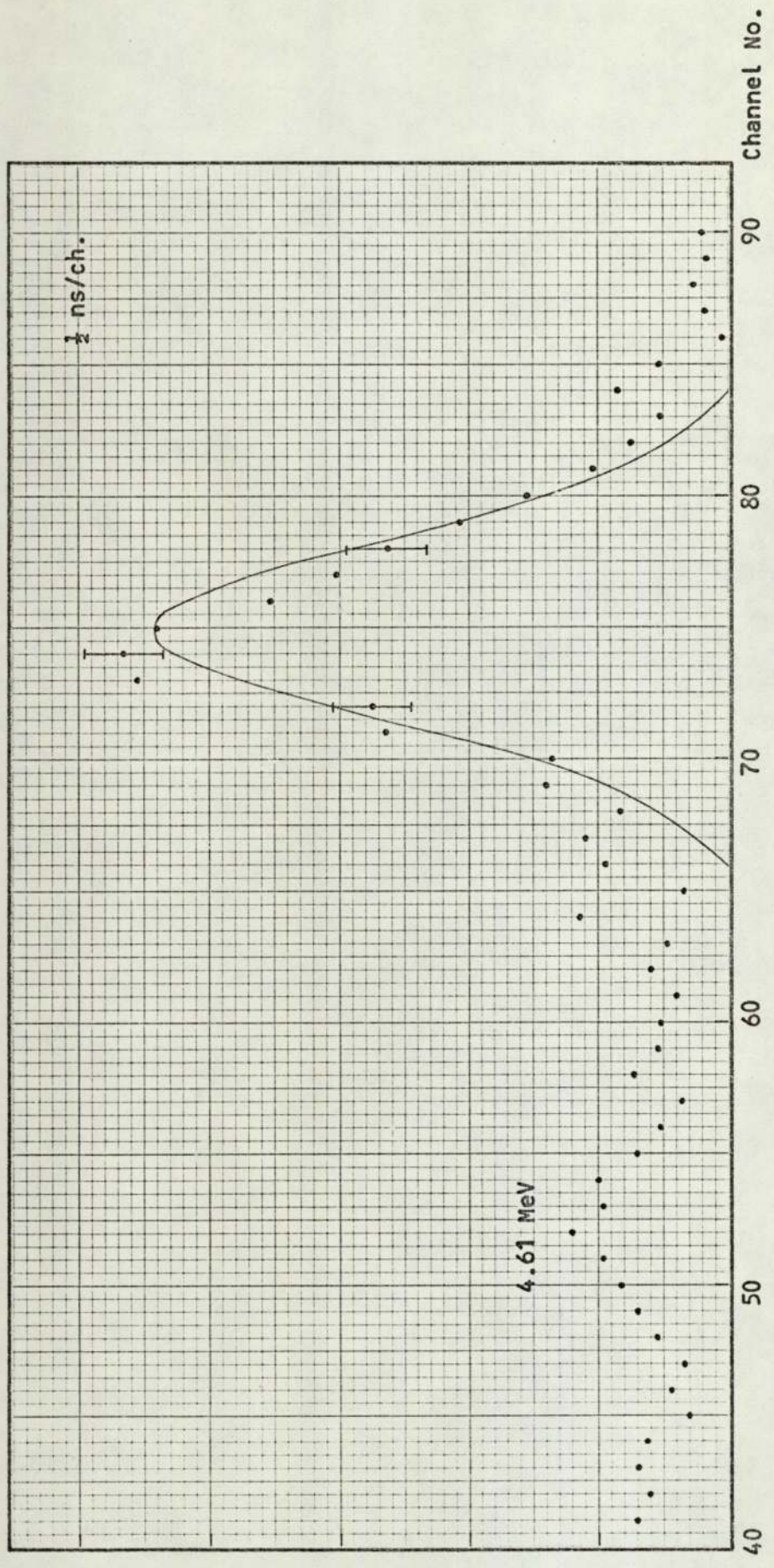

Figure 5.19. Time of flight spectrum for scattering from ^{7}Li at 50^{o} in the laboratory system.

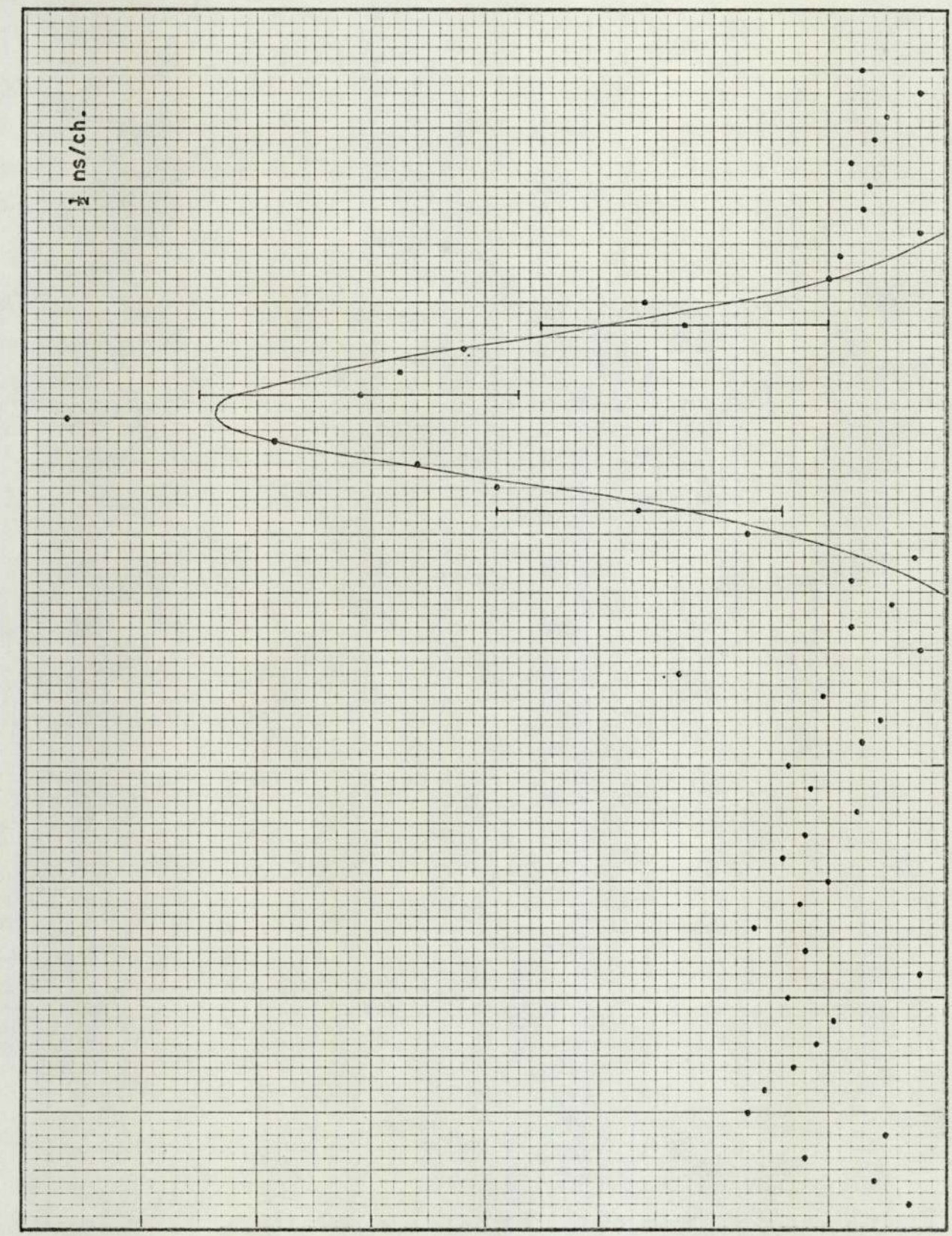

Figure 5.20. Time of flight spectrum for scattering from ^{7}Li at 100° in the laboratory system.

the elastically scattered neutrons. The only γ rays from ^{7}Li are from the 0.477 MeV level, since the higher levels decay by the emission of an alpha particle and a triton, i.e.,

(i) $^{7}Li + ^{1}n = ^{3}H + ^{4}He + ^{1}n' - 2.465$ MeV

(ii) $^{7}Li + ^{1}n = ^{3}H + ^{5}He - 3.423$ MeV $= ^{3}H + ^{4}He + ^{1}n' - 2.465$ MeV

(iii) $^{7}Li + ^{1}n = ^{7}Li^{*} + ^{1}n' = ^{3}H + ^{4}He + ^{1}n' - 2.465$ MeV

reaction (iii) being mainly via the 4.61 MeV state.

Differential Elastic Scattering Cross Sections

The differential elastic scattering cross sections obtained for ^{7}Li are presented in table 5.3, together with those of Wong et al[17] and Armstrong et al[16]. The data of both these other studies also includes scattering to the 0.477 MeV level. The angular distributions are shown in figure 5.21.

The treatment of experimental errors was the same as that used for the differential cross section results for potassium.

The results obtained for lithium show good agreement within experimental error up to 70° with both Wong et al[17] using ring geometry, and Armstrong et al[16] using nuclear emulsions. The three angular distributions shown in figure 5.21 differ however, in that Armstrong et al found a pronounced secondary maximum, whereas the present results indicate this to be very shallow.

The data of Armstrong et al was not corrected for multiple scattering. The data of Wong et al was corrected for multiple scattering, absorption, and angular resolution due to finite ring size which, although not stated, was probably inferior to that in the present work. The experimental error in the present results is a factor of between two and eight better than that of Armstrong et al, but a factor of two greater than that of Wong et al.

The agreement of the present measurements with the optical model predictions is discussed in Chapter 6.

Table 5.3

^{7}Li Differential Elastic Scattering Cross Section Data

Present Work

Centre of Mass Scattering Angle (degrees)	Differential Cross Section (mb/st)	Experimental Error (mb/st)
22° 48'	404.5	25.4
34° 6'	260.8	16.6
45° 17'	126.4	8.0
56° 17'	75.2	5.0
67° 7'	34.8	3.4
77° 44'	25.9	3.1
88° 6'	23.9	2.6
98° 13'	24.9	2.9
108° 6'	21.3	2.7

Table 5.3 contd.

Wong et al			Armstrong et al		
Centre of Mass Scattering Angle (degrees)	Differential Cross Section (mb/st)	Experimental Error (mb/st)	Centre of Mass Scattering Angle (degrees)	Differential Cross Section (mb/st)	Experimental Error (mb/st)
25° 26'	437.7	19	22° 54'	376	71
36° 18'	305.6	10.4	34° 12'	267	40
43° 22'	200.5	8.9	45° 24'	160	32
52° 59'	113.1	3.3	56° 24'	55.4	13
66° 33'	38.1	2.8	67° 12'	62.8	25
75° 6'	23.6	1.7	77° 54'	19.9	10
84° 30'	14.5	1.4	88° 12'	15.3	8
94° 42'	13.3	1.3	98° 24'	22.2	8
105° 8'	18.7	1.1	108° 12'	34.4	10

Data supplied by Brookhaven National Laboratory, New York.

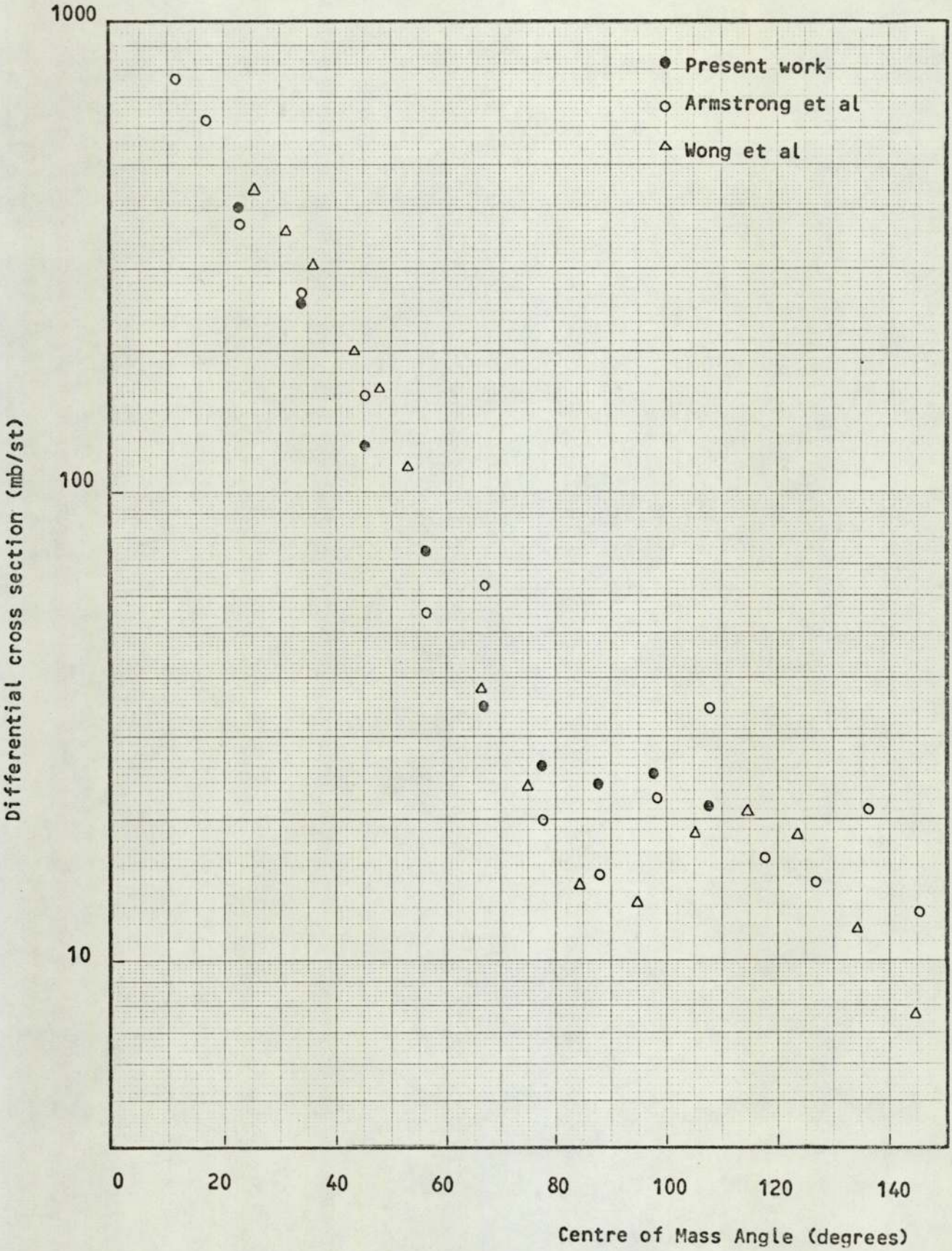

Figure 5.21. Comparison of the measurements of the differential elastic scattering cross section from ^{7}Li at 14.1 MeV.

CHAPTER 6

Optical Model Analysis of the Differential Cross Sections

6.1 Optical Model Analyses

The optical model has been used extensively for the analysis of elastic scattering data for a wide variety of particles and over a wide range of energies. Many investigations have shown that neutron elastic scattering cross sections can be well fitted by the optical model with a complex potential and suitably adjusted parameters. Much of the data has been analysed individually in terms of the model, and in several instances the individual parameters have been used to give information about the energy and isospin dependence of the optical model potentials. However, because of the inherent potential ambiguities, the parameters found by various authors differ somewhat and make interpolation between different energies and nuclei uncertain. Besides the utilitarian value of such parameters, there is reason to believe that useful information about nuclear forces and structure can be obtained from the systematic analysis of neutron elastic scattering.

In view of the amount of data available and the inherent parameter ambiguities in the optical model potentials, it is clearly impractical to analyse individual data sets and subsequently determine an optimum parameter set. The usual approach is to combine a large number of individual data sets taken over a range of energies and nuclei, include explicit energy and mass terms as variable parameters in the optical model potentials, and fit simultaneously all of the data.

An extensive analysis of experimental data by Perey and Buck[76] showed that the differences in parameters found by various investigators were mainly explained by the experimental uncertainties and differences in techniques of the optical model analysis used. They found it was possible to find a single optical potential that gives cross sections in

excellent agreement with the data for medium and heavy nuclei for incident neutron energies from 1 - 25 MeV. This optical potential is non-local in form. In general, non-local potentials seem to give better results than those obtained with local potentials. At present, however, it is not clear whether this improvement is a direct result of the increased validity of the non-local potential, or simply follows from the greater number of adjustable parameters that are included in the non-local potential analysis.

In view of the increased numerical complexity due to the greater number of adjustable parameters, Wilmore and Hodgson[77] calculated an equivalent local potential, from which a set of equivalent local optical model parameters have been derived. The use of this potential gives good agreement with experimental data for medium and heavy nuclei in the neutron energy range 1 - 15 MeV.

More recently, a large amount of accurate data from proton and neutron elastic scattering on medium to heavy weight nuclei have appeared, which has allowed an improved set of nucleon-nucleus optical model parameters to be determined. This has been done by Becchetti and Greenlees[78], using much of the elastic scattering data for energies less than 50 MeV and nuclei with $A \geq 40$. The parameters were determined by fitting simultaneously a large sample of the available proton data, and independently, a large sample of the available neutron data. Explicit energy and isospin-dependent terms were included and their coefficients obtained directly from the data analysis.

The neutron data were analysed using the derived proton parameters as starting values. The results, however, were found to be insensitive to small changes in the energy and (N-Z)/A terms. Consequently, the energy dependence of the central strengths was set equal to that of the corresponding proton terms. The real potential geometry and the spin orbit strength and geometry did not change

significantly from the proton parameters, and these were also set equal to the proton values. The most significant changes were in the strength and geometry of the absorptive potential, which indicated a smaller radius and an increased volume strength for neutrons.

In the present analysis, the optical model parameters of Becchetti and Greenlees[78] were used as starting values for the optical model searches on both potassium and lithium. The parameters are presented in detail in section 6.3.

The differential elastic scattering cross sections obtained in the present work were compared with the theoretical predictions of the optical model using the computer search code RAROMP, (Regular And Reformulated Optical Model Programme)[18]. The programme was run at the Rutherford High Energy Laboratory, via the link line from the Physics Department of the University of Birmingham.

6.2 The Optical Potential

The optical potential used was a combination of Woods-Saxon volume and surface derivative forms given by:

$$U_{OPT}(r) = U_R(r) + iU_I(r) + U_{SO}(r) \qquad \ldots\ldots 6.1$$

where $U_R(r)$ is the real central potential and its form is taken to be that of a Woods-Saxon well[79], written in the conventional form:

$$U_R(r) = -V_R\left\{1 + \exp\left(\frac{r-R_R}{a_R}\right)\right\}^{-1} \qquad \ldots\ldots 6.2$$

with a radius prameter defined as $R_R A^{-1/3}$. The primary effect of this potential is on the shape elastic scattering cross section and it has three parameters, V_R, r_R and the diffuseness a_R.

$U_I(r)$ constitutes the imaginary central potential and has the usual combination of volume and surface terms given by:

$$U_I(r) = -W_v f(r,R_I.,a_I.) + 4a_I W_d \frac{d}{dr} f(r,R_I,a_I) \quad .. \quad 6.3$$

$$\text{where} \quad f(r,R,a) = \left\{ 1 + \exp\left(\frac{r-R}{a}\right)\right\}^{-1} \quad ..... \quad 6.4$$

These terms are responsible for the absorption which takes place in the scattering process. The first corresponds to absorption occuring within the nuclear volume and is assumed to possess the same general form as the real central potential. The second term is the shape for the potential which characterises the absorption taking place near the nuclear surface, and is proportional to the derivative of the Woods-Saxon well. Again, it is convenient to introduce the radius parameter $r_{I.,I} = R_{I.,I}A^{-1/3}$, and the imaginary potential thus has six parameters $W_v, r_{I.}, a_{I.}, W_d, r_I$ and a_I. and a_I. The spin orbit potential $U_{SO}(r)$ is given by the usual Thomas form:

$$U_{SO}(r) = -[V_{SO} + iW_{SO}]\left(\frac{h}{m_\pi c}\right)^2 \frac{1}{r}\frac{d}{dr} f(r,R_s,a_s)\bar{\ell}.\bar{\sigma} \quad 6.5$$

$$\text{with} \quad f(r,R_s,a_s) = \left\{ 1 + \exp\left(\frac{r-R_s}{a_s}\right)\right\}^{-1} \quad ..... \quad 6.6$$

where the coefficient is the square of the pion Compton Wavelength, which appears because the potential was originally derived from the meson theory of nuclear forces and serves to keep the dimensions correct. It is convenient that $(h/m_\pi c)^2 \sim 2.00$. $\bar{\ell}.\bar{\sigma}$ is the scalar product of the intrinsic and orbital angular momentum operators.

In the absence of convincing evidence to the contrary it is usual to take W_{SO} equal to zero[80]. The primary effect of the spin orbit potential is in the polarisation of the scattered particles[80]. With the introduction of the radius parameter $r_s = R_s A^{-1/3}$, the potential has the three parameters, V_s, r_s and a_s.

6.3 Optical Model Parameters

The appropriate optical potential cannot be deduced directly

from the experimental data, so it is necessary to begin with a suitable potential and iterate the numerical values of its parameters, in order to optimise the fit to the data. The optical model parameters used as starting values to evaluate the potentials defined in the previous section, were the best fit parameters of Becchetti and Greenlees[78], given by:

VR	V_R	= 56.3 - 0.32E - 24.0(N-Z)/A	6.7
RR	r_R	= 1.17	6.8
AR	a_R	= 0.75	6.9
WV	W_v	= 0.22E - 1.56 or zero, whichever is greater.	6.10
RV	r_v	= 1.26	6.11
AV	a_v	= 0.58	6.12
WD	W_d	= 13.0 - 0.25E - 12.0(N-Z)/A or zero, whichever is greater.	6.13
RD	r_d	= 1.26	6.14
AD	a_d	= 0.58	6.15
VS	V_s	= 6.2	6.16
RS	r_s	= 1.01	6.17
AS	a_s	= 0.75	6.18

where all potential strengths are in MeV and E is the incident neutron energy in MeV in the laboratory system.

With the optical potential defined by equation 6.1, it is possible, by systematic adjustment of the parameters, given by equations 6.7 - 6.18, to obtain a good over-all fit to elastic scattering data. In practice, however, it is necessary to limit the number of variable parameters so that meaningful information can be obtained.

Experience with conventional optical model analyses has shown that for incident neutron energies of less than 20 MeV, it is not necessary to include a volume absorption term because these neutrons are

not sufficiently energetic to penetrate deeply into the nucleus[6,76,81,82]. Pyle and Greenlees[82][83] have shown this also to be true for proton scattering in this energy range, where the data can be satisfactorily represented using a pure surface form for the imaginary part of the potential. The variability of the potential of equation 6.1 can be further restricted by requiring that no parameters in the spin orbit term be allowed to vary. The justification for this choice is that the spin orbit term influences the elastic scattering in a minor way only, and its effect on the cross section is confined to scattering angles in the backward hemisphere, i.e., for angles greater than about 150° [6][84].

6.4 Fitting Procedure

In view of the above limitations on the number of variable optical model parameters, the analysis undertaken in the present work was mainly focused on the effect on the surface interaction. For completeness, however, the effect of volume absorption alone was also examined, as was a combination of surface and volume terms. In all analyses the three spin orbit parameters defined by equations 6.16, 6.17 and 6.18 remained fixed.

The general problem in the fitting procedure was that of obtaining the parameters of the optical model which gave a best fit of the predictions to the experimental data. The criterion most widely used for this purpose, and the one used by RAROMP in the present analysis is the χ^2 criterion[6,76,85]. χ^2 is a measure of the discrepancy between the experimental data and the theoretical values found from an assumed optical potential, and is defined by:

$$\chi^2 = \sum_i^{N_d} \left\{ \frac{\sigma_{th}(\theta_i) - \sigma_{ex}(\theta_i)(p)}{\Delta\sigma_{ex}(\theta_i)} \right\}^2 \qquad \ldots\ldots 6.19$$

where $\sigma_{ex}(\theta_i) \pm \Delta\sigma_{ex}(\theta_i)$ is the experimentally determined differential

cross section at a particular angle θ_i, and $\sigma_{th}(\theta_i)(p)$ is the theoretically predicted differential cross section in terms of the optical model parameters (p), the summation running over all the experimental points N_d. Hence the quantity χ^2 is a function of the (p) optical model parameters, with minima at the positions where:

$$\frac{\partial \chi^2}{\partial p} = 0 \qquad \ldots\ldots 6.20$$

Thus the lower χ^2 the better the fit. It is difficult to specify the range of χ^2 for which a fit is acceptable, but in general a value of $\chi^2 \leq 10$ is satisfactory[6,80,85].

The experimental data obtained in the present work were not corrected for the angular resolution of the spectrometer. This introduced appreciable experimental averaging into the measured differential cross sections. In view of this the 'averaging option' in the programme was used, which averages the theoretically predicted differential cross section over the experimental angular resolution before making the χ^2 comparison, i.e.,

$$\bar{\sigma}(\theta) = \int_{-\Delta\theta}^{\Delta\theta} \sigma(\theta) d\theta \qquad \ldots\ldots 6.21$$

where $\Delta\theta$ is the experimental angular resolution.

A suitable set of optical model parameters should not only give good fits to angular distributions, but should also predict accurately the reaction cross section. In the analyses on both ^{39}K and ^{7}Li, the experimentally determined reaction cross section was read in and fitted as an extra data point.

6.5 Optical Model Analysis of ^{39}K

In the first instance, the three energy and (N-Z)/A dependent potentials defined by equations 6.7, 6.10 and 6.13, were evaluated for an

incident neutron energy of 14.1 MeV, giving:

$$VR = 51.173 \text{ MeV}, \quad WV = 1.542 \text{ MeV}, \quad WD = 9.167 \text{ MeV} \quad \ldots\ldots 6.22$$

Keeping all geometrical parameters fixed at the values given by Becchetti and Greenlees[78], the three potentials were optimised by searching on the parameters VR, WD, WV,(6). (The number in parenthesis after the varied parameters indicates the number of iterations carried out). The optimum values of the three potentials were found to be:

$$VR = 51.3 \text{ MeV}, \quad WD = 9.56 \text{ MeV}, \quad WV = 0.73 \text{ MeV} \quad \ldots\ldots 6.23$$

and the fit obtained is shown in figure 6.1. The figure shows the fit to be poor, and it would appear that the parameters of Becchetti and Greenlees are not sufficient to fit potassium differential cross sections, although potassium just lies within the target mass range for which the parameters should be suitable. This inadequacy has recently been found for other elements of mass number greater than forty by Hoffman and Coker[86] and Carlson et al[87]. A typical output of iteration number six of the search VR, WD, WV,(6) is shown in Appendix A.1.

The next stage of the analysis was to investigate the effects of surface absorption alone. The value of the real radius parameter RR was fixed at 1.17 fm, and using the optimum values of VR and WD from equation 6.23 three searches were executed to obtain an optimum fit. The first was to investigate the effect of the surface radius parameter RD, i.e., a search VR, WD, RD,(6). The fit obtained is shown in figure 6.2 and although it is an improvement on the first, with a value of $\chi^2 < 2$ per point, it was not satisfactory over the region of the first sharp minimum. The second search varied the diffuseness parameters, i.e, a search VR, AR, WD, AD,(6) was performed. The fit is shown in figure 6.3

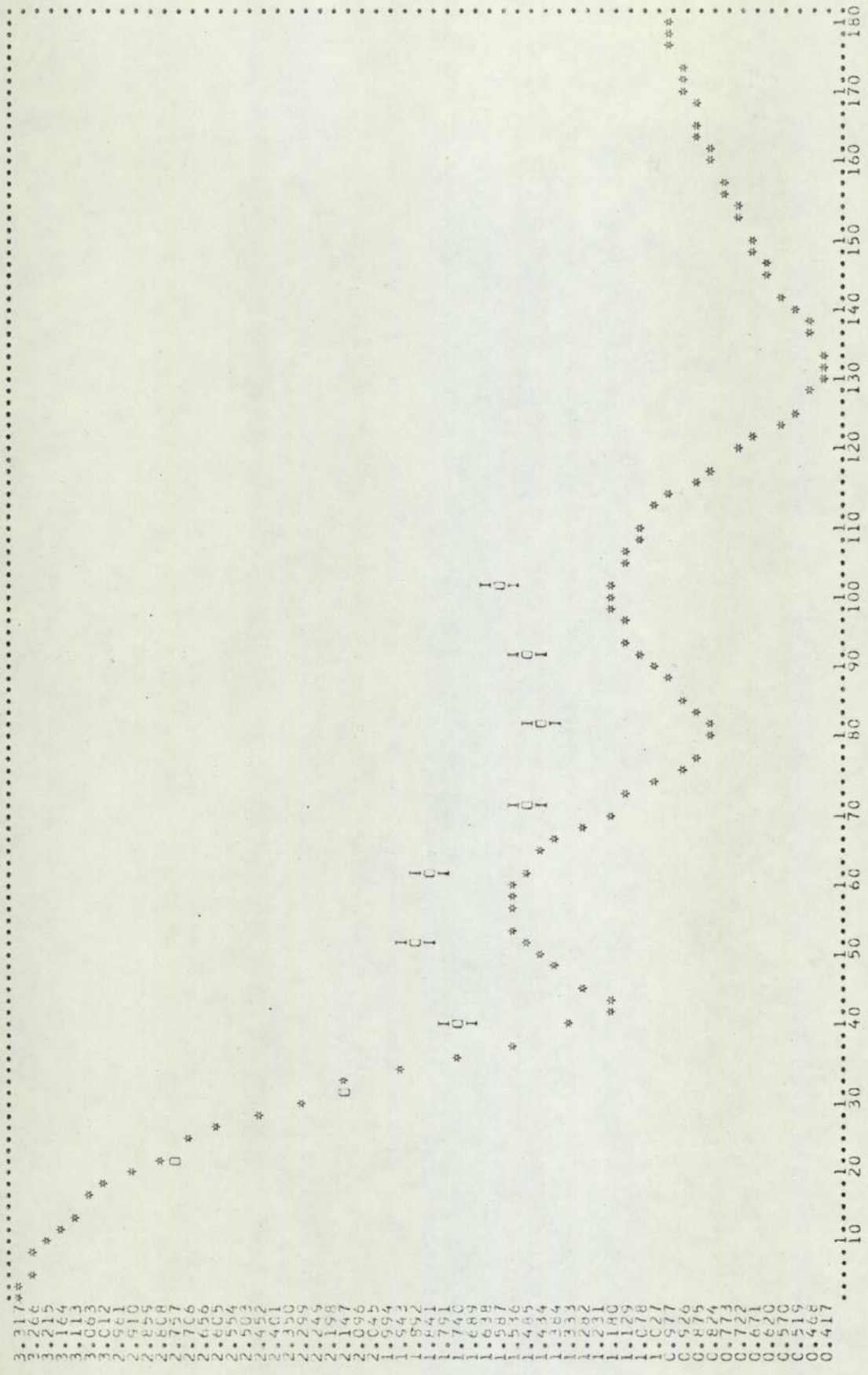

Figure 6.1 VR, WD, WV,(6)

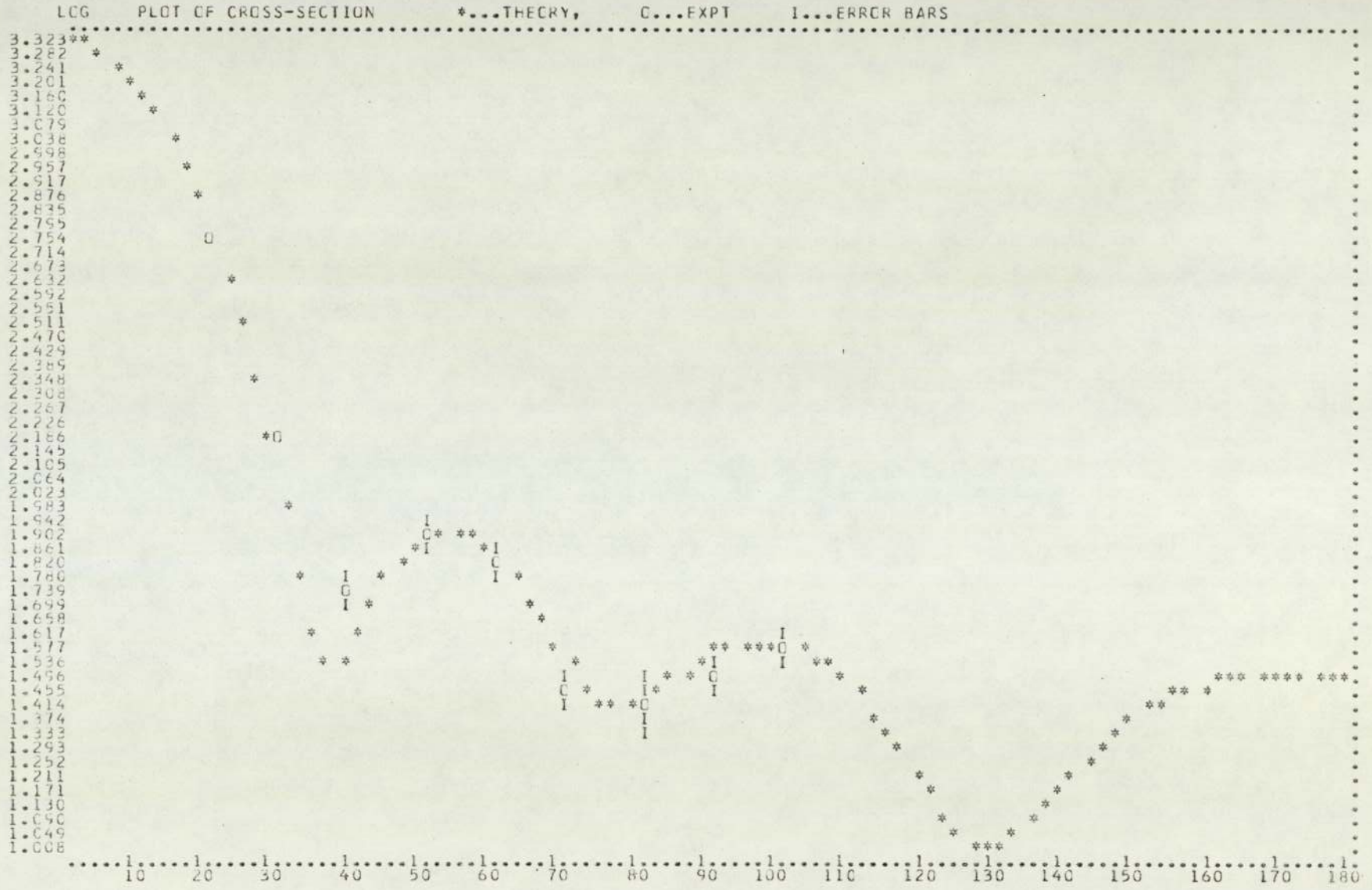

Figure 6.2 VR, WD, RD.(6)

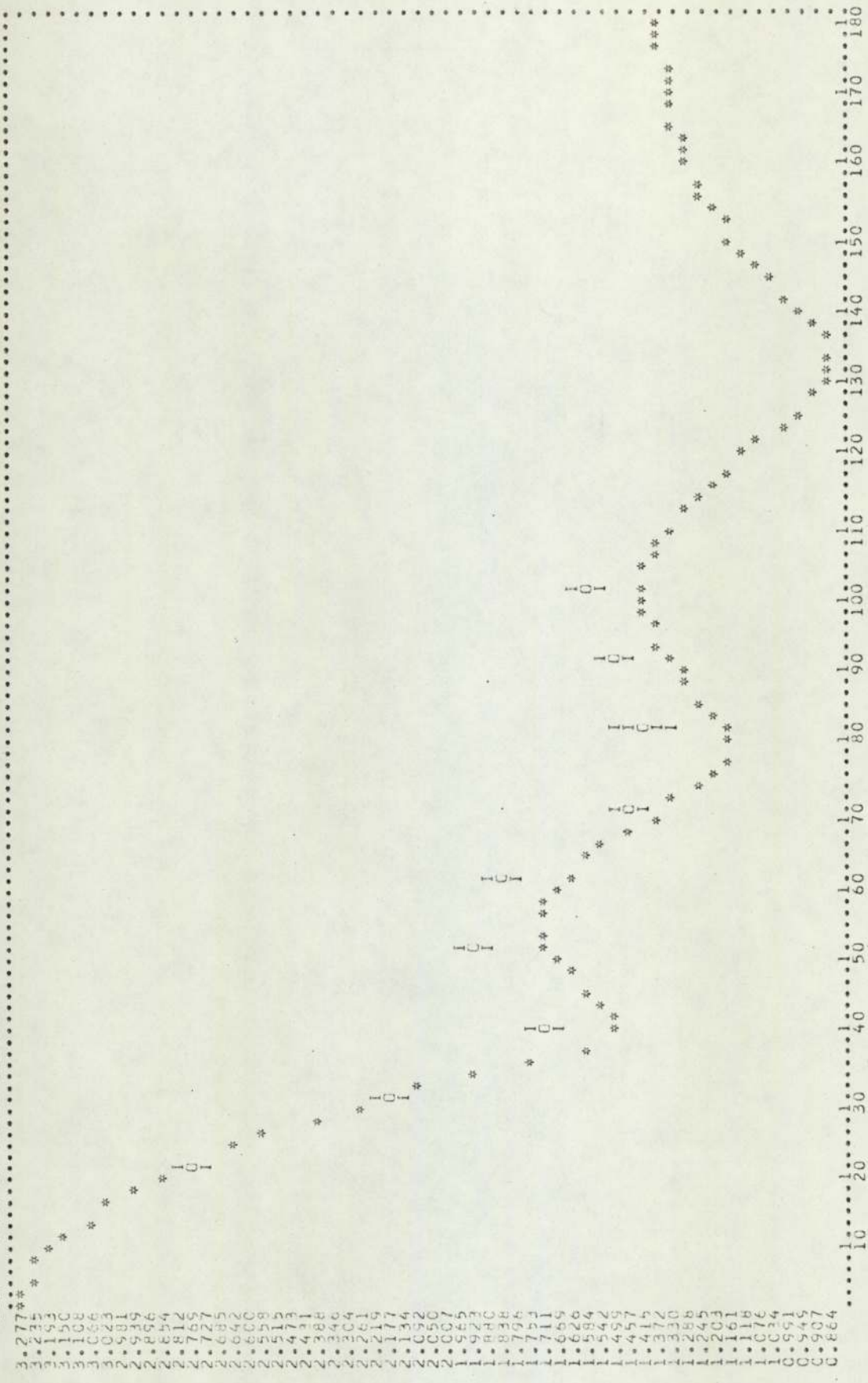

Figure 6.3 VR, AR, WD, AD,(6)

and is seen to be worse than the previous one. Hence, a combination of the two was investigated, i.e., a search VR, AR, WD, RD, AD,(10). The fit, shown in figure 6.4, gives good agreement between theoretically predicted and experimentally determined cross sections, with a value of $\chi^2 < 0.5$ per point.

So far the real radius parameter RR has not been included in any of the searches undertaken. This is because of the well known $V_R r_R$ ambiguity[6,80,88]. In the case of the real central potential it is found that as long as the product $V_R r_R$ is kept constant, r_R can often be varied over quite a large range without substantially affecting the fit to the experimental data, i.e., a change in the parameter r_R results only in a small change in χ^2, provided V_R is varied at the same time to keep the product constant. To overcome this ambiguity a grid search was performed in order to find an optimum value of the real radius parameter RR[89].

Grid Search

The grid search technique consists of varying the particular parameter singly to reduce the value of χ^2 as much as possible. In general the parameter is varied up or down in arbitrary steps in order to obtain the direction of decreasing χ^2. The parameter then is repeatedly varied in that direction until the value of χ^2 starts to increase, indicating that the minimum has been straddled. It is then possible to either 'close in' on the solution in decreasing steps, or simply fit a parabola to the three points closest to the minimum and calculate the position of the minimum. Having obtained three points near the minimum, say P_1, P_2 and P_3, χ^2 can be expanded about the point P_2, giving

$$\chi^2 = \chi_2^2 + a(P - P_2) + b(P - P_2)^2 \qquad \ldots\ldots 6.24$$

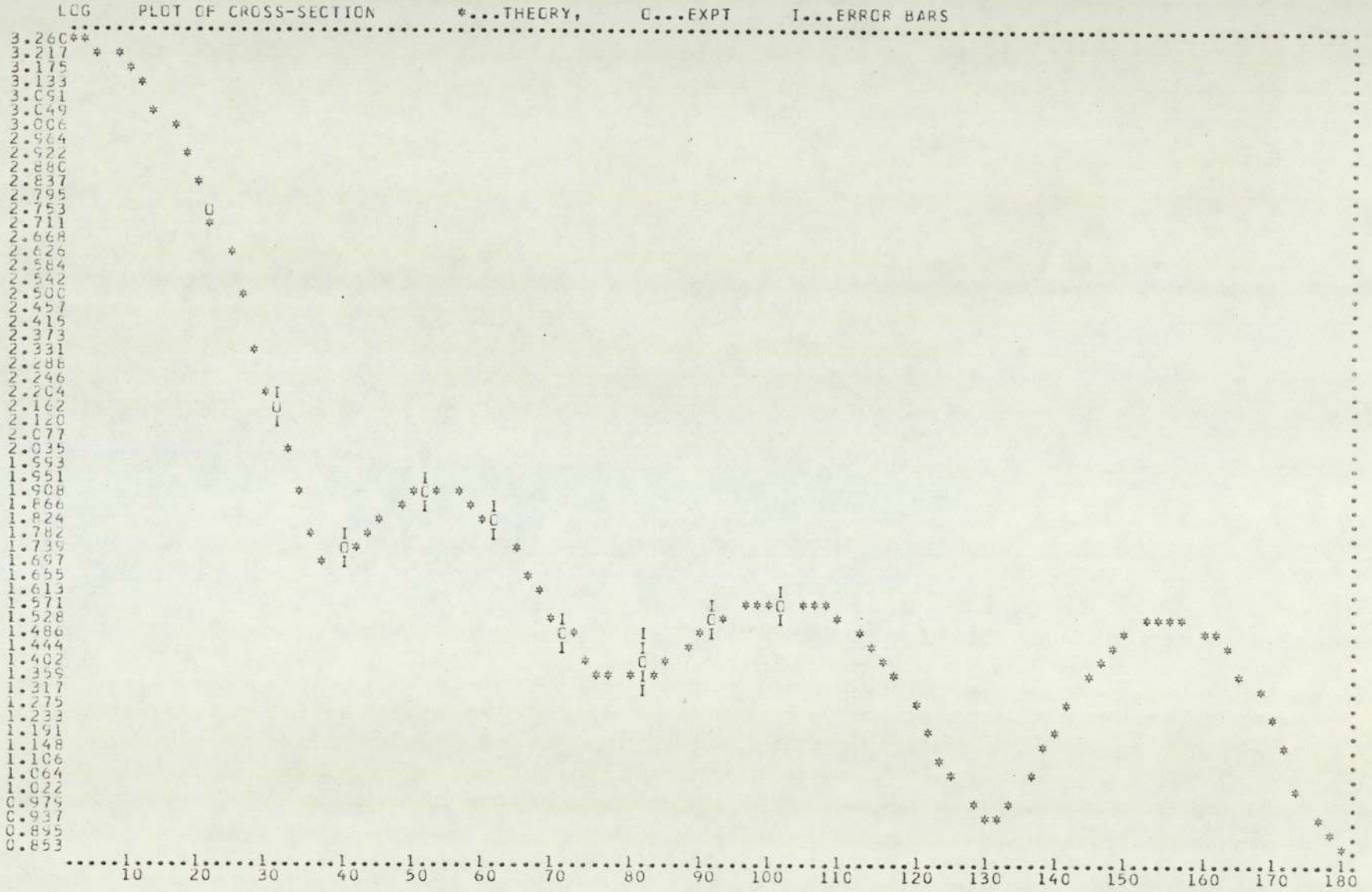

Figure 6.4 VR, AR, WD, RD, AD.(10)

Partial differentiation with respect to P gives:

$$P_{min} = P_2 - (a/2b) \qquad \ldots\ldots 6.25$$

'a' and 'b' can then be obtained from the equations:

$$\chi_3^2 = \chi_2^2 + a(P_3 - P_2) + b(P_3 - P_2)^2 \qquad \ldots\ldots 6.26$$

$$\chi_1^2 = \chi_2^2 + a(P_1 - P_2) + b(P_1 - P_2)^2 \qquad \ldots\ldots 6.27$$

This was the method used in the present analysis.

Using the optimum fit obtained by the search VR,AR,WD,RD,AD,(10), the value of the real radius parameter RR was varied in steps of 0.05 fm between 1.17 fm and 1.42 fm. The three points found closest to the minimum are listed below:

RR (fm)	χ^2 per point
1.22	0.33257
1.27	0.28474
1.32	0.29157

Application of equations 6.25, 6.26 and 6.27, showed the optimum value of of RR to be 1.29 fm. The curve of χ^2 versus RR is shown in figure 6.5.

The optimum value of RR was then substituted in the three searches VR, WD, RD,(6); VR, AR, WD, AD,(6) and VR, AR, WD, RD, AD,(10). Improved fits were found for the first two, and the final fit for the third search is shown in figure 6.6. The value of χ^2 for this search was reduced to less than 0.3 per point. This search also gave good agreement between the theoretical and experimental reaction cross sections viz; 1200 $\pm$ 72 mb experimental[90], compared to 1102 mb theoretical.

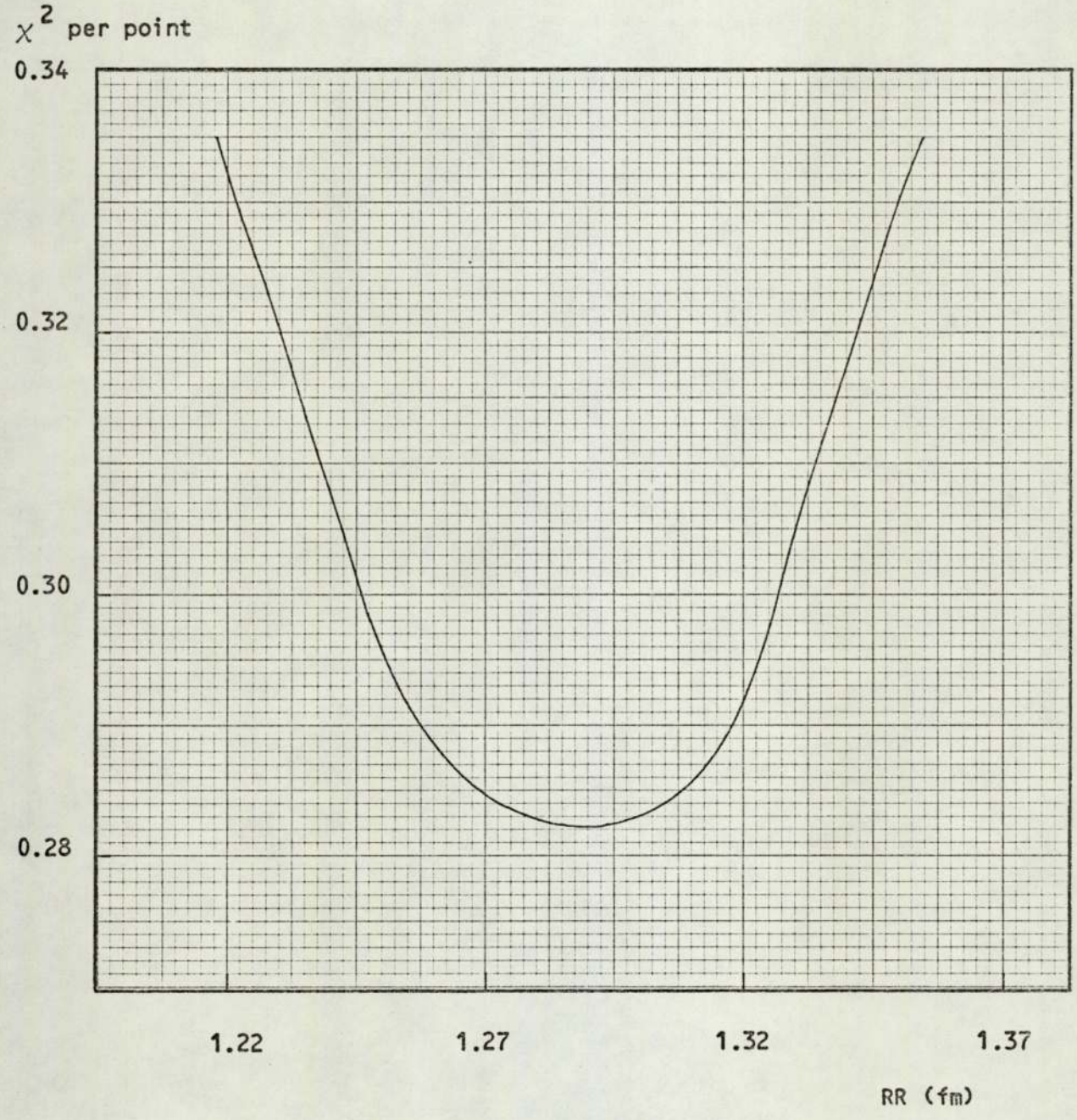

Figure 6.5. χ^2 per point versus RR for potassium.

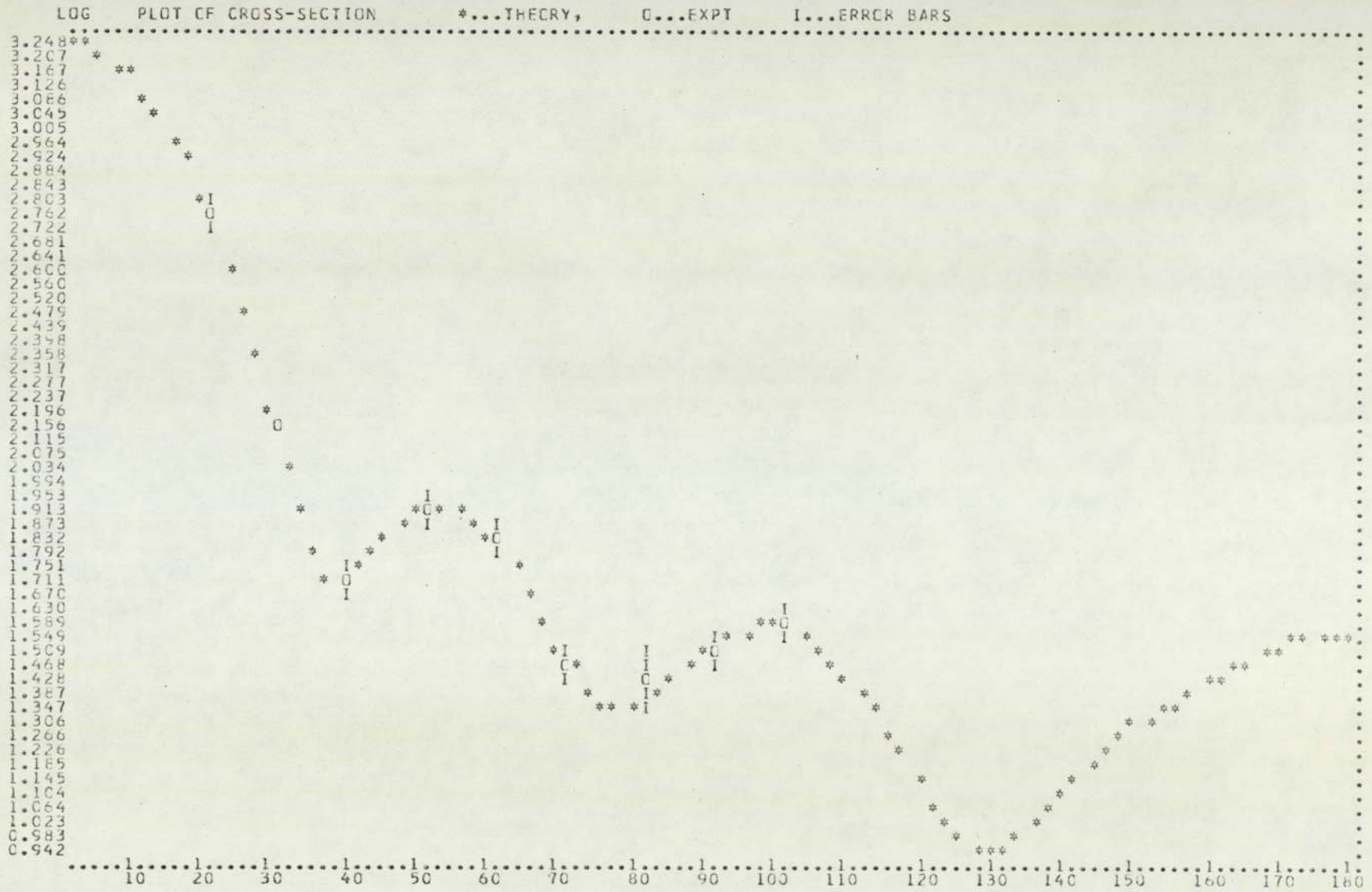

Figure 6.6 VR, AR, WD, RD, AD,(10) with RR = 1.29 fm.

It is appropriate at this point to compare the present optical model analysis of potassium, with that undertaken by Frasca et al[8].

In this previous analysis, the volume terms were set to zero, and a Gaussian surface form factor was used. The real radius parameter was initially fixed at 1.25 fm but no satisfactory fit was found. In subsequent calculations all parameters were allowed to vary, although it is not clear whether the variation of the real radius parameter was by grid search, or whether it was allowed to vary freely. In the calculations the best fits were obtained only with regard to the angular distributions. No attempt was made to obtain a best value for the reaction cross section. The value of χ^2 was 307 and the fit obtained is shown in figure 6.7.

A further optical model analysis of the data of Frasca et al[8] has been undertaken by Cassola and Koshel[88], using a Woods-Saxon surface derivative form. With the optimum parameters determined by Frasca et al, the main objective of the analysis was to determine an optimum value of the surface radius parameter RD. Keeping VR, AR, and WD fixed at the optimum values, RD was varied from 1.24 fm to 1.49 fm. The optimum value was found to be 1.49 fm, and the value of χ^2 for the fit was 394. (In the present analysis the optimum value of RD was determined to be 1.442 fm). Again, no attempt was made to obtain an optimum fit with respect to the reaction cross section.

A comparison of the optimum optical model parameters determined by the analyses discussed is given in table 6.1.

Volume Absorption

The entire searching procedure was repeated using only volume absorption. With the optimum values for VR and WV given by equation 6.23, three searches were executed; VR, WV, RV,(6); VR, AR, WV, AV,(6) and VR, AR, WV, RV, AV,(10). When using volume absorption alone, however, it is necessary to use a different value of the radius parameter RV. This is explained by figure 6.8. The new value required can be deduced from

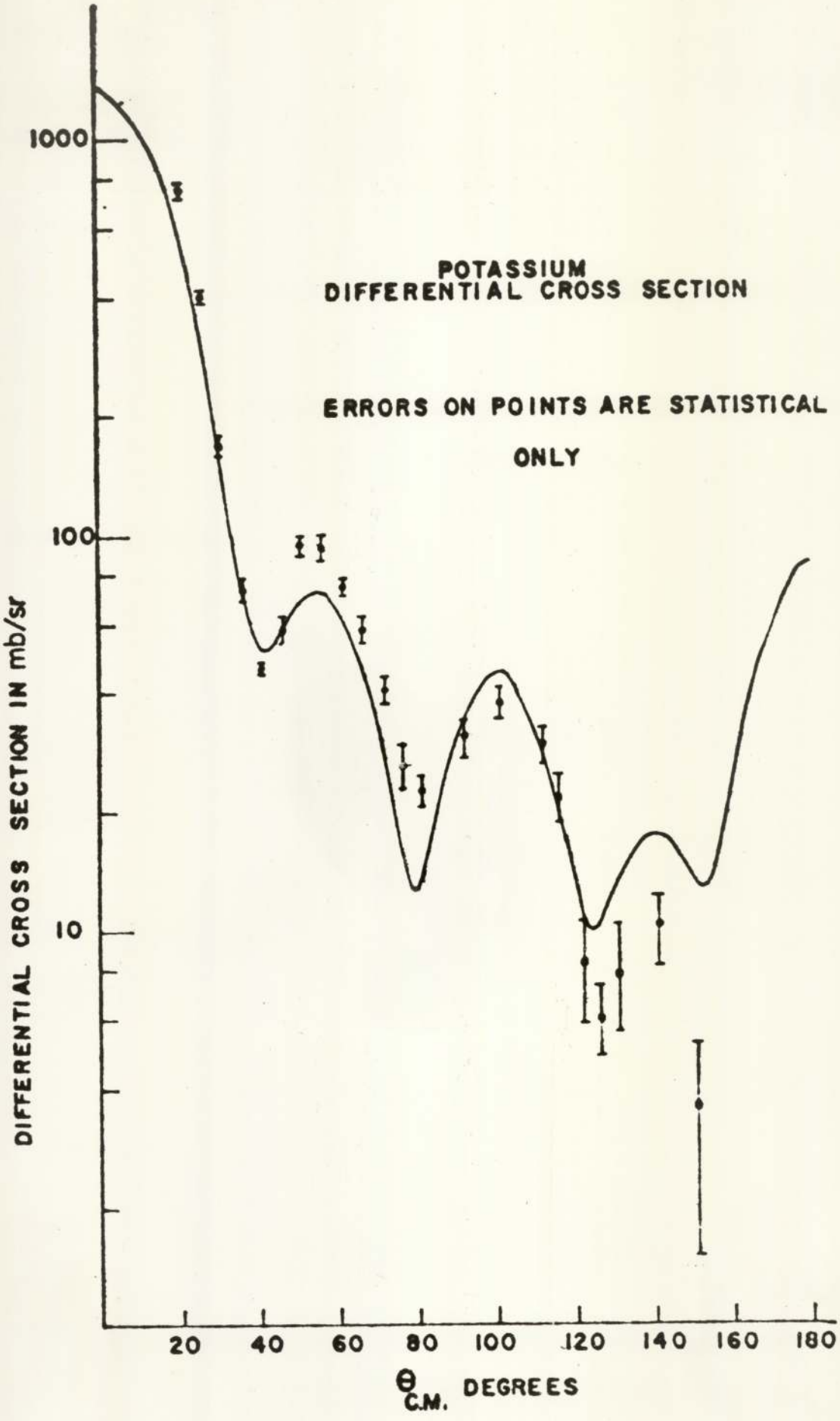

Figure 6.7. The Optical Model fit for ^{39}K obtained by Frasca et al.

Table 6.1

Optical Model Parameters used to fit Potassium Elastic Scattering Data

Parameter	Present Work	Frasca et al	Cassola and Koshel
VR (MeV)	44.78	46.1	46.1
RR (fm)	1.295	1.3	1.25*
AR (fm)	0.620	0.58	0.76
WD (MeV)	5.97	6.7	6.9
RD (fm)	1.442	-	1.49
AD (fm)	0.455	-	0.47*
b (fm) Gaussian	-	0.88	-
VS (MeV)	6.2	2.09	7.5*
RS (fm)	1.01	-	1.25*
AS (fm)	0.75	-	0.65*
σ_R^{th} (mb)	1102	908	1310
σ_R^{ex} (mb)	1200 $\pm$ 72	-	-
χ^2	< 0.3	307	394

* Parameters of Perey and Buck.

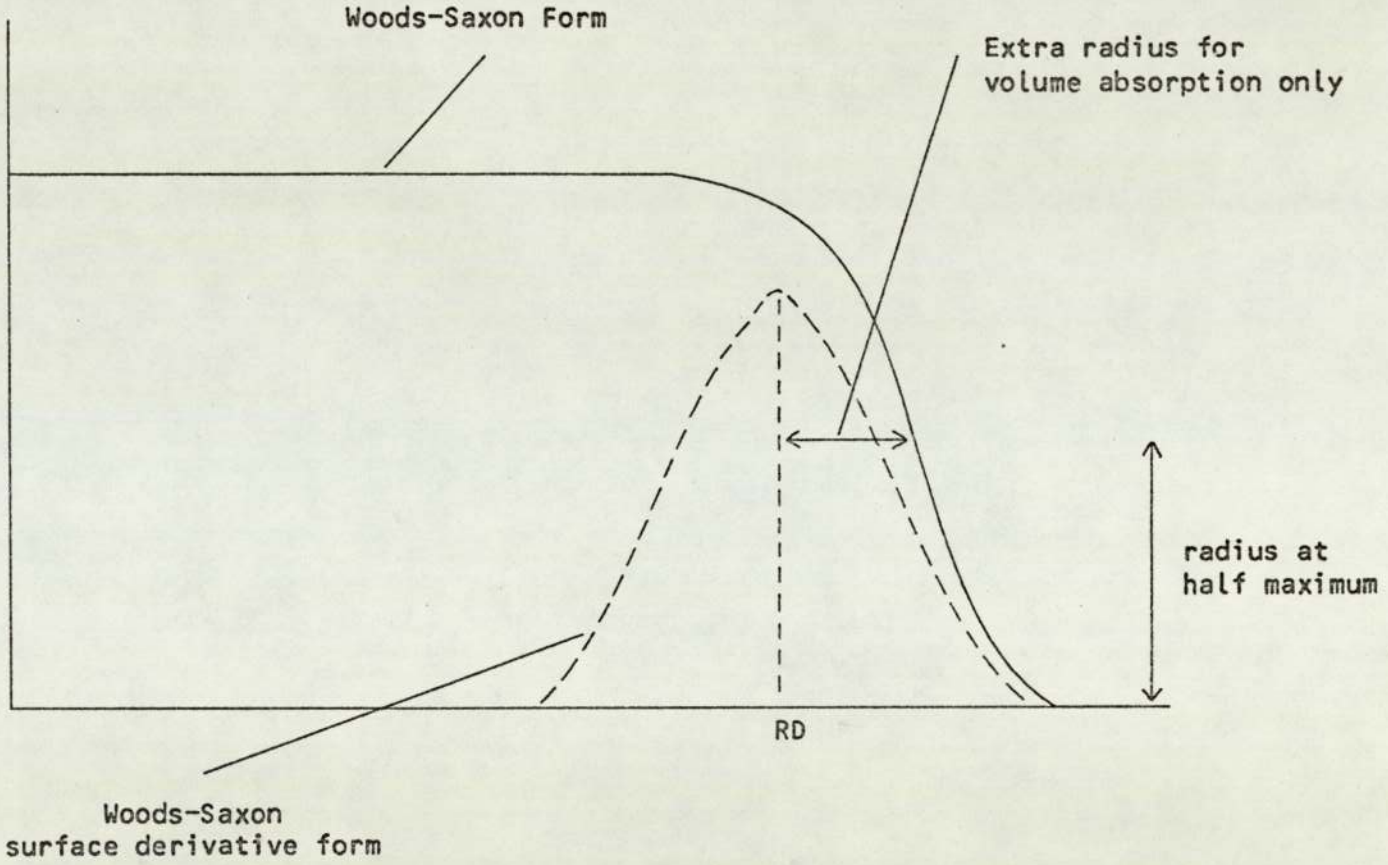

Figure 6.8. Radius for volume absorption only.

the surface geometry and is given by[91]:

$$RV \simeq RD + 2AD \qquad \ldots\ldots 6.28$$

where RD and AD are the optimum values given in table 6.1. For potassium, RV = 2.352 fm. No reasonable fits were obtained for volume absorption alone, and a typical fit for VR, WV, RV,(6) is shown in figure 6.9(a).

Finally, a combination of surface and volume terms was used. The optimum value of WV was included in the three searches used for surface absorption, i.e., VR, WD, RD, WV,(6); VR, AR, WV, WD, AD,(6) and VR, AR, WD, RD, AD, WV,(10). Again, no reasonable fits were obtained and a typical fit for the five parameter search is shown in figure 6.9(b).

6.6 Optical Model Analysis of ^{7}Li

The procedure for the analysis of the lithium differential cross sections was exactly the same as that for potassium. The three energy and (N-Z)/A dependent potentials defined by equations 6.7, 6.10 and 6.13, were evaluated for the incident neutron energy of 14.1 MeV, giving:

$$VR = 48.359 \text{ MeV}, \quad WV = 1.542 \text{ MeV}, \quad WD = 7.761 \text{ MeV} \qquad \ldots\ldots 6.29$$

With all geometrical parameters fixed at the starting values of Becchetti and Greenlees[78], the three potentials were optimised using the search VR, WD, WV,(6), giving:

$$VR = 48.35 \text{ MeV}, \quad WV = 2.98 \text{ MeV}, \quad WD = 6.74 \text{ MeV} \qquad \ldots\ldots 6.30$$

and the fit obtained is shown in figure 6.10. As expected, the fit is a poor one, since the overall parameters are not suitable to describe light

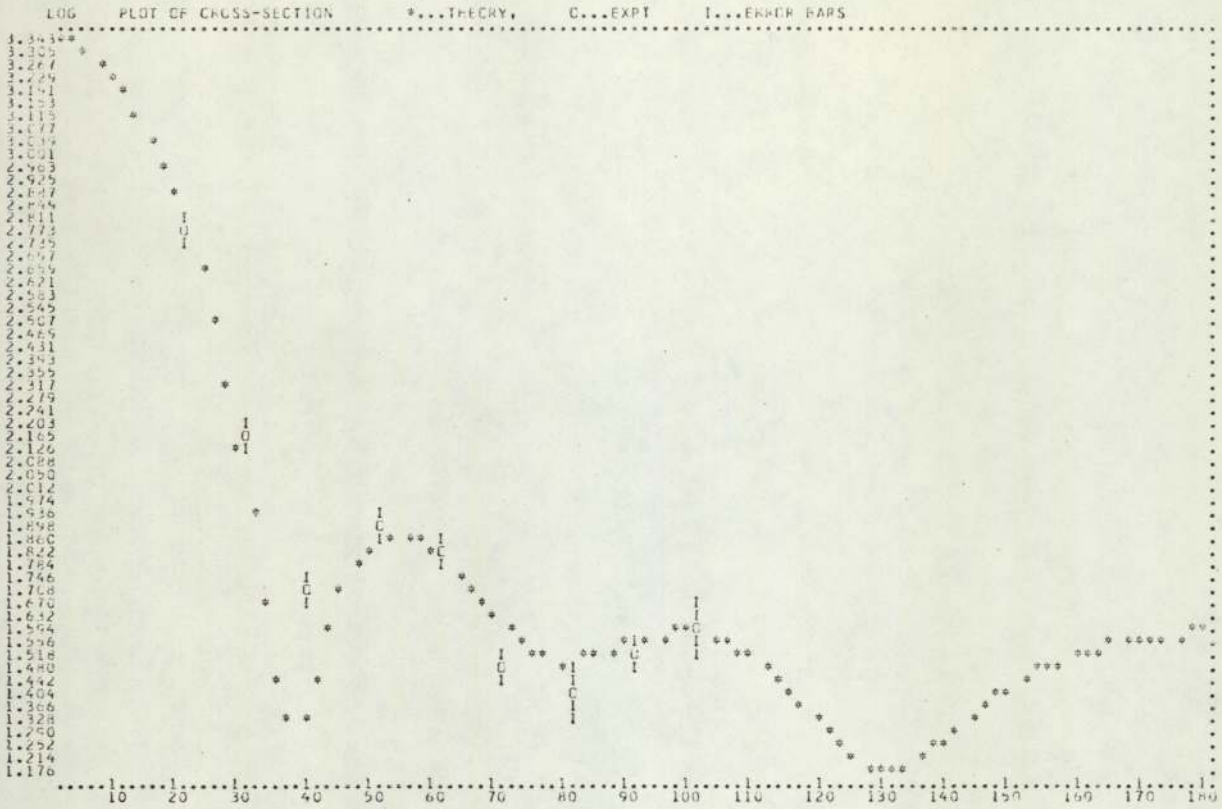

Centre of Mass Angle (Degrees)

Figure 6.9(a) VR, WV, RV,(6)

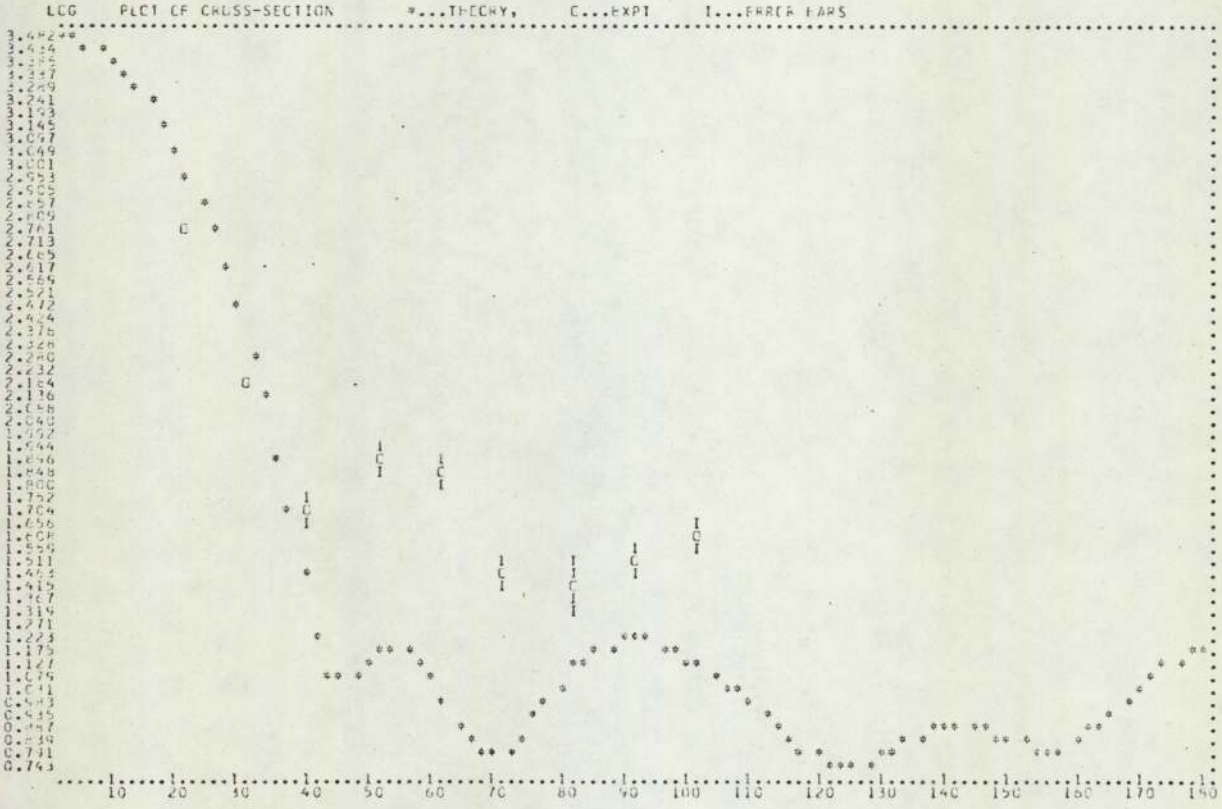

Centre of Mass Angle (Degrees)

Figure 6.9(b) VR, AR, WV, WD, AD,(6)

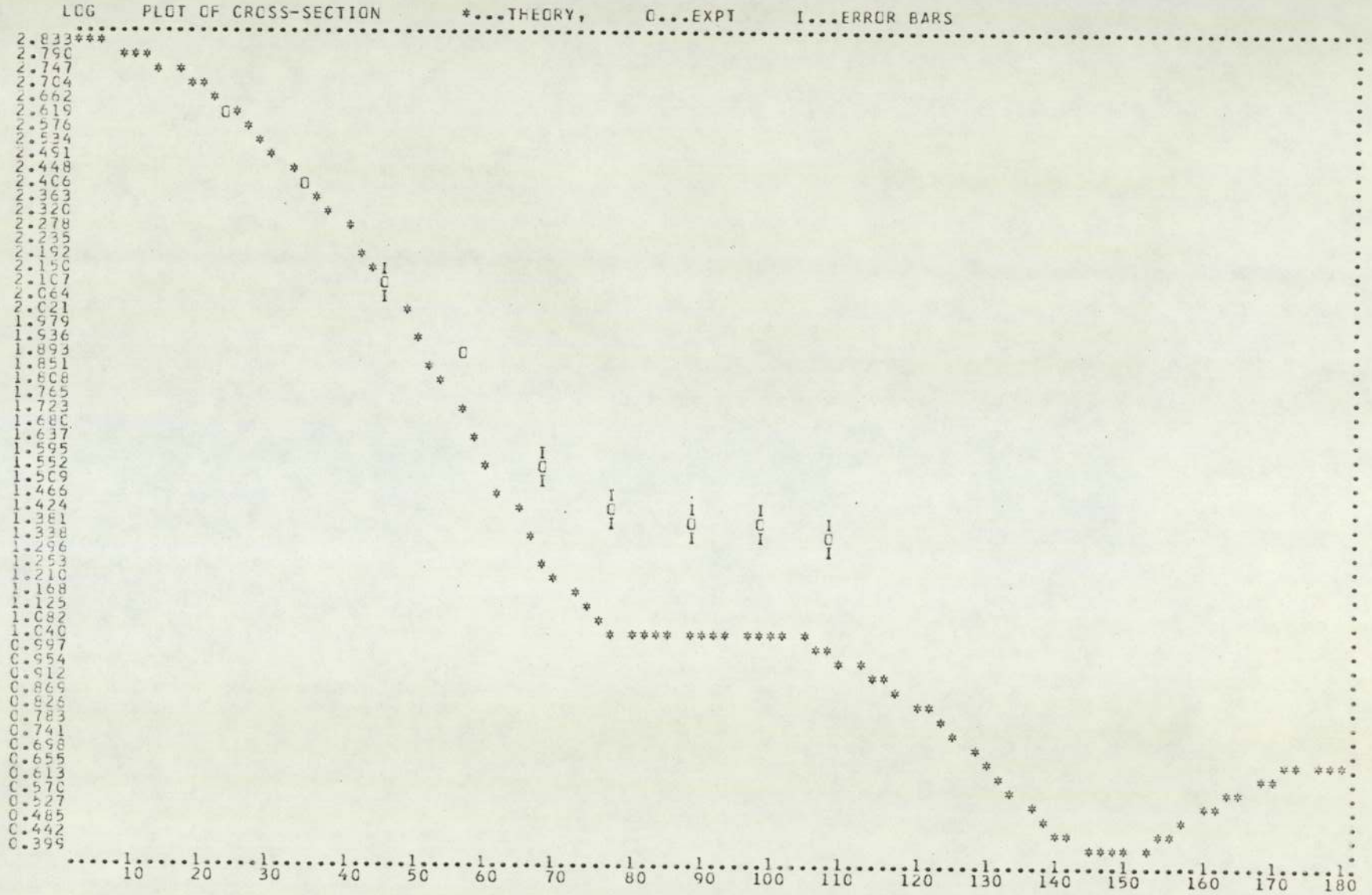

Figure 6.10 VR, WD, WV,(6)

nuclei. There is no reason, however, why these parameters should not be used for starting values. A typical output for this search is shown in Appendix A.1.

With the real radius parameter fixed at 1.17 fm, three searches were executed using surface absorption only, VR, WD, RD,(6); VR, AR, WD, AD,(6) and VR, AR, WD, RD, AD,(10). The fits obtained are shown in figures 6.11, 6.12 and 6.13 respectively. All three searches give good fits to the experimental data, but for the four and five parameter searches the value of χ^2 was a factor of three better than for the three parameter search. In view of the lesser number of variable parameters, the search VR, AR, WD, AD,(6) was used in the optimisation of the real radius parameter RR.

A grid search was again used on the parameter RR, its value being varied in steps of 0.05 fm between 1.17 fm and 1.47 fm. The three points found closest to the minimum are listed below;

RR (fm)	χ^2 per point
1.32	0.46445
1.37	0.46396
1.42	0.46568

Application of equations 6.25, 6.26 and 6.27 showed the optimum value of RR to be 1.356 fm. The curve of χ^2 versus RR is shown in figure 6.14. It should be noted that although an optimum value of the parameter could be determined, the fits obtained for lithium appear to be relatively insensitive to changes in this parameter, the value of χ^2 per point being less than one over the entire grid range.

The optimum value of RR = 1.356 fm was substituted into the three searches VR, WD, RD,(6); VR, AR, WD, AD,(6); VR, AR, WD, RD, AD,(10). Although the visual fit was not improved, the value of χ^2 was reduced for

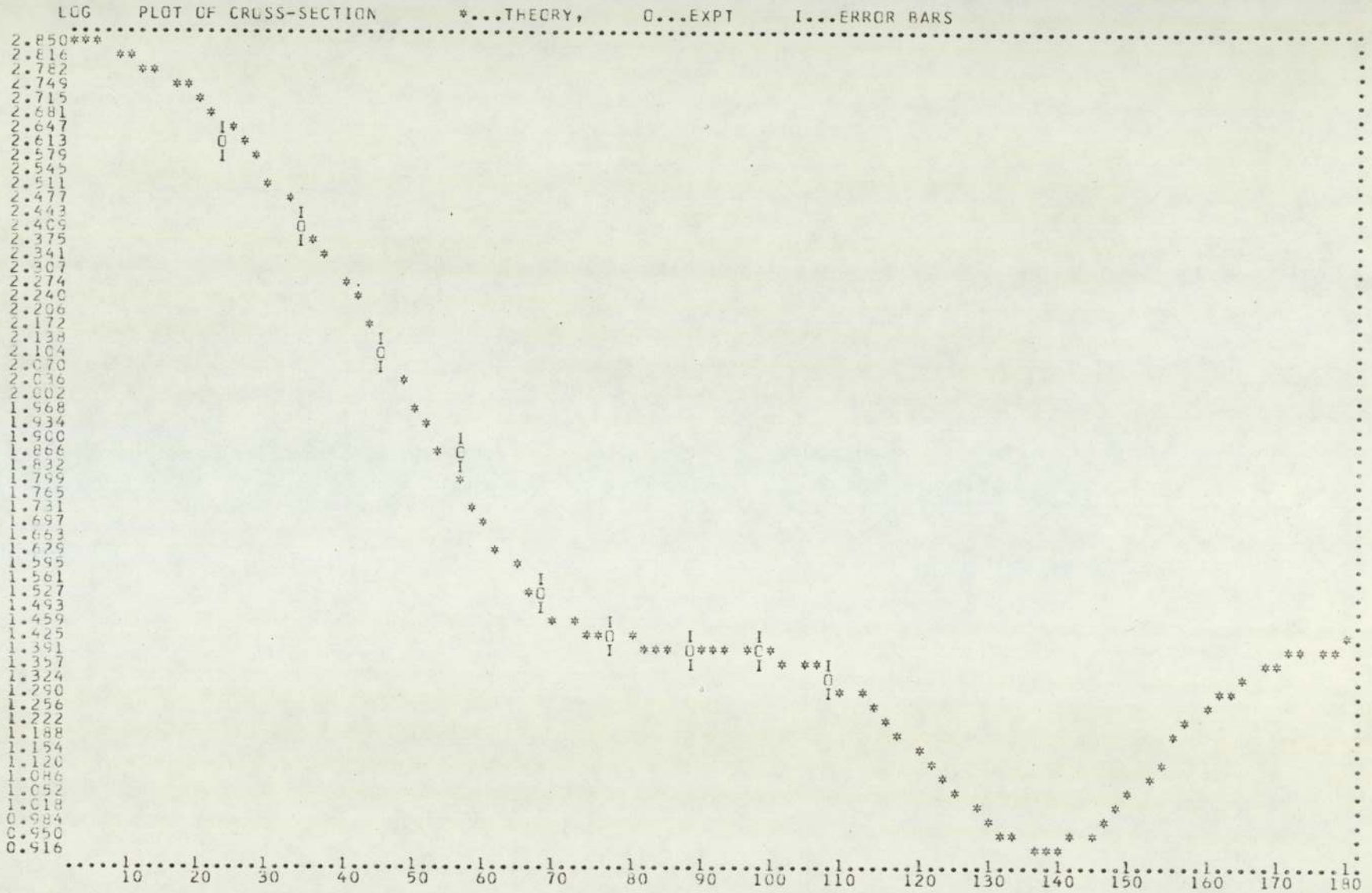

Figure 6.11 VR, WD, RD,(6)

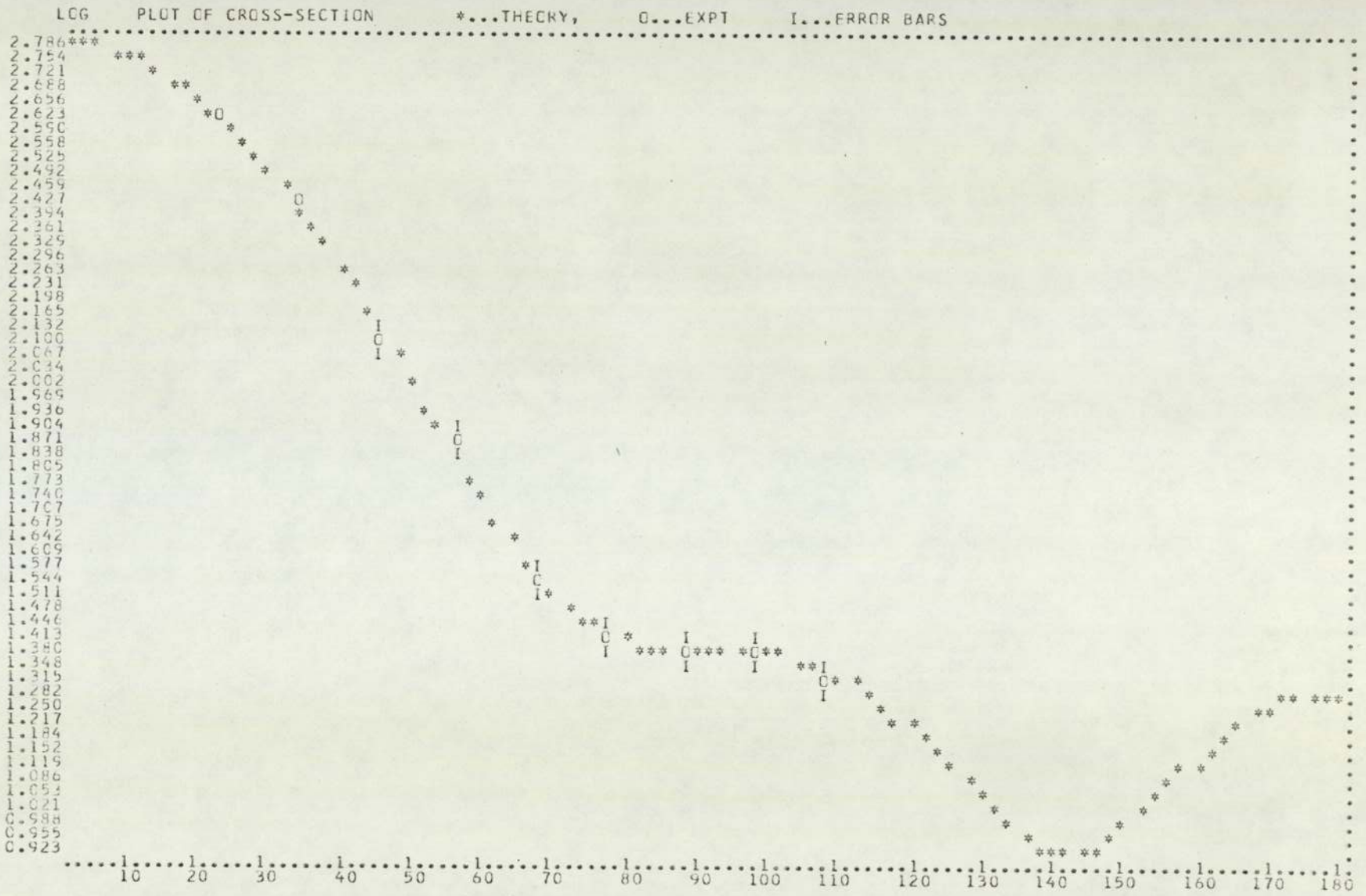

Figure 6.12 VR, AR, WD, AD,(6)

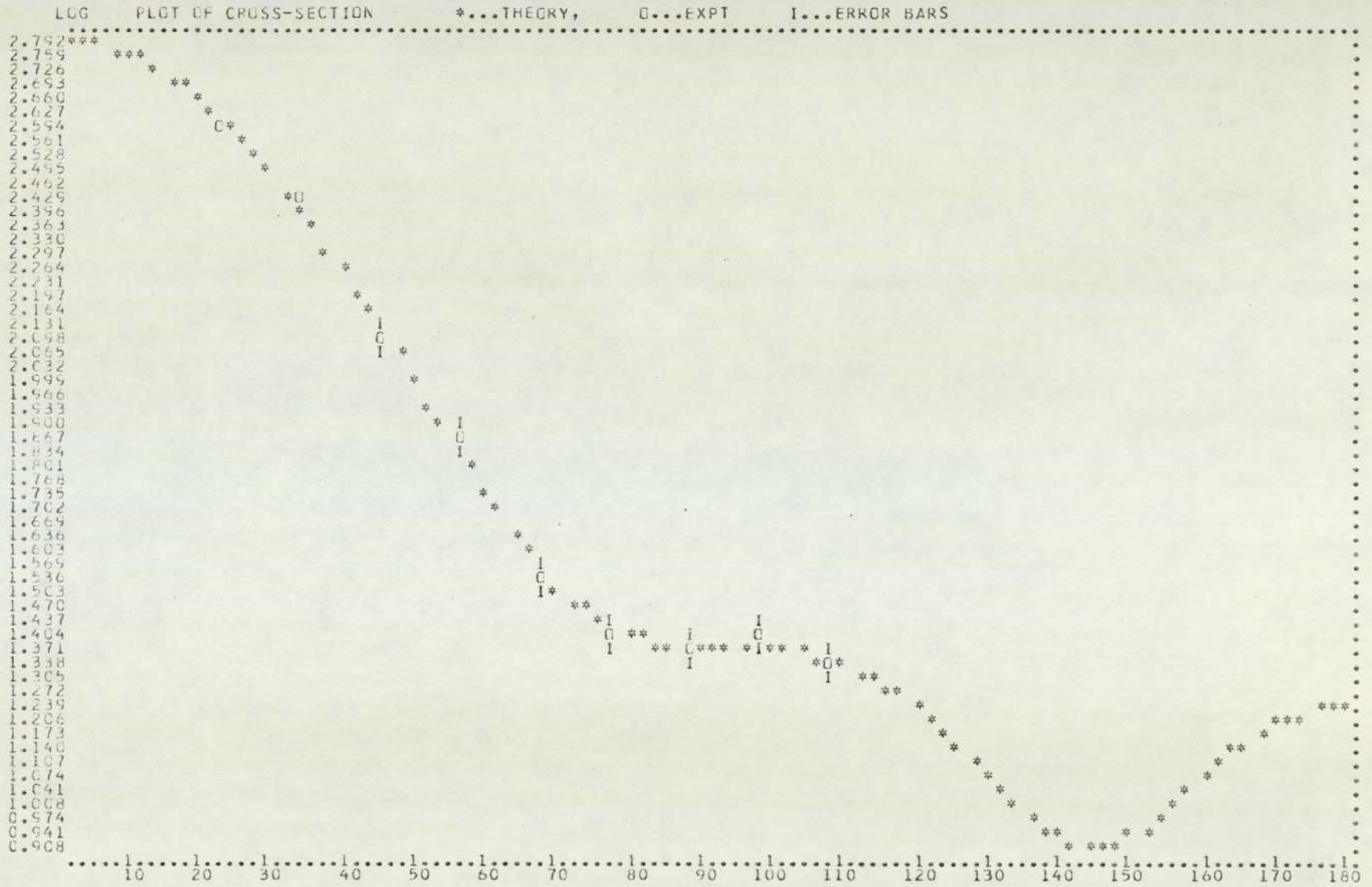

Figure 6.13 VR, AR, WD, RD, AD,(10)

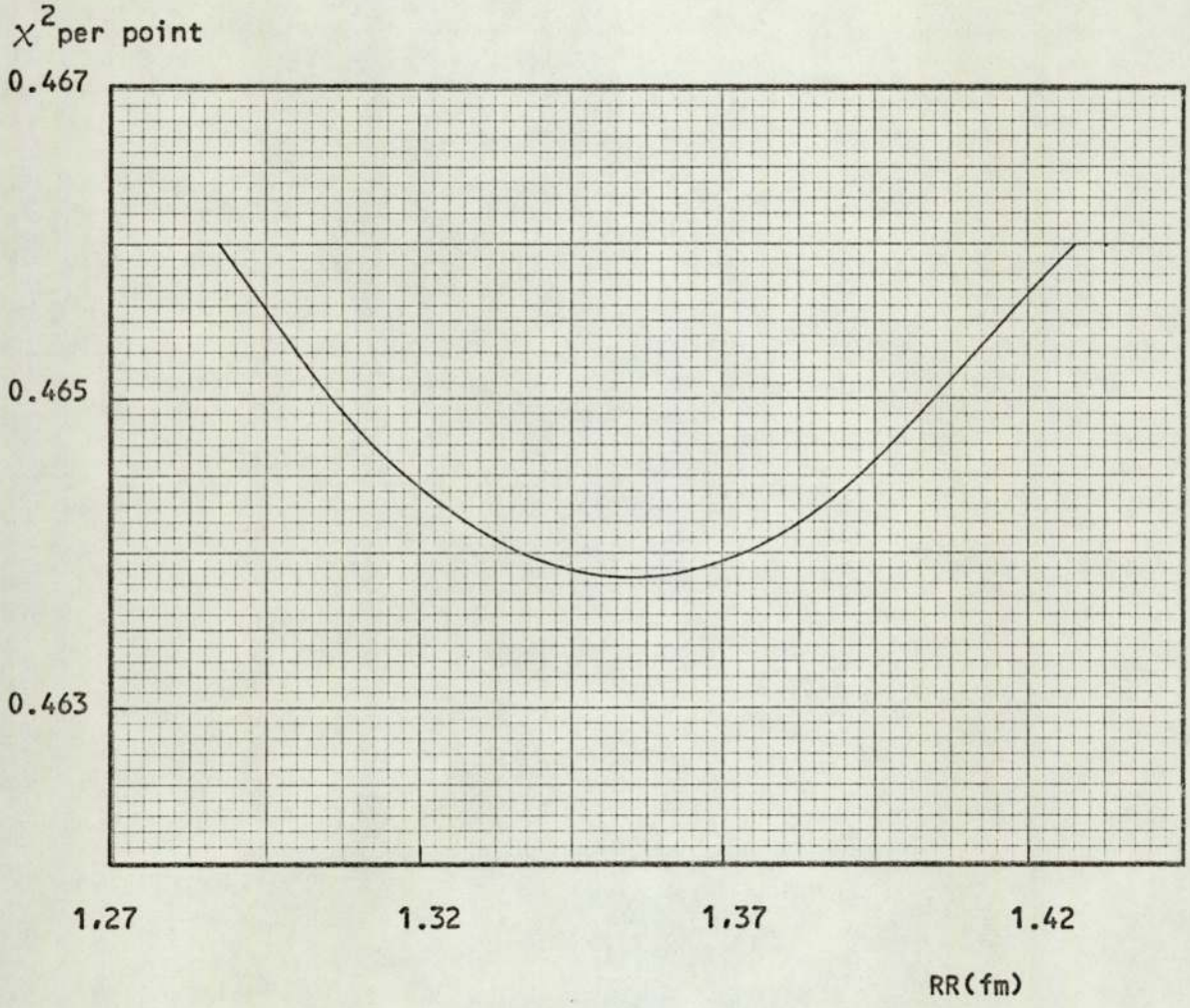

Figure 6.14. χ^2 per point versus RR for lithium.

all searches. The final optimum fit for the search, VR, AR, WD, AD,(6) is shown in figure 6.15. This search also gave good agreement between the theoretical and experimentally determined reaction cross sections viz; 531 ± 102 mb experimental[16], compared to 473 mb theoretical.

In a previous analysis of lithium by Armstrong et al[16], the optical model parameters used were those of Bjorklund and Fernbach[81]. No further information is presented for this analysis, so a comparison of the optimum parameter values is not possible. In using these parameters, however, the volume absorption is set to zero and a Gaussian surface form factor is used. The fit obtained by Armstrong et al is shown in figure 6.16.

No optical model analysis was made of the angular distribution for ^{7}Li obtained by Wong et al[17].

The optimum parameter values obtained for lithium in the present work are listed in table 6.2.

Volume Absorption

The search procedure was repeated using volume absorption alone, and a combination of surface and volume terms. The analysis was exactly the same as that for potassium. As expected, no reasonable fits were obtained. Typical fits for searches VR, WV, RV,(6) and VR, AR, WD, RD, AD, WV,(10) are shown in figures 6.17(a) and 6.17(b) respectively.

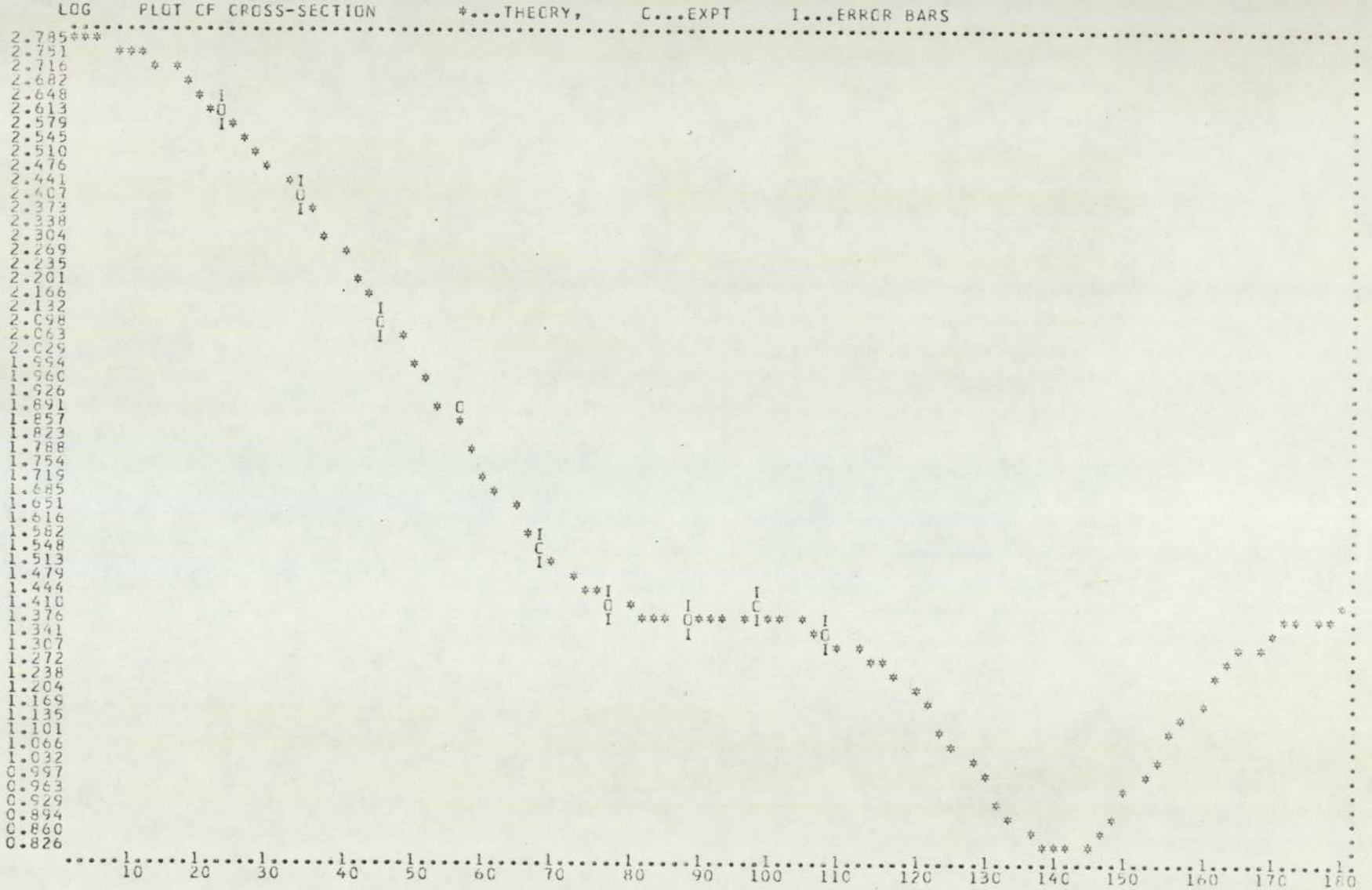

Figure 6.15 VR, AR, WD, AD,(6) with RR = 1.356 fm.

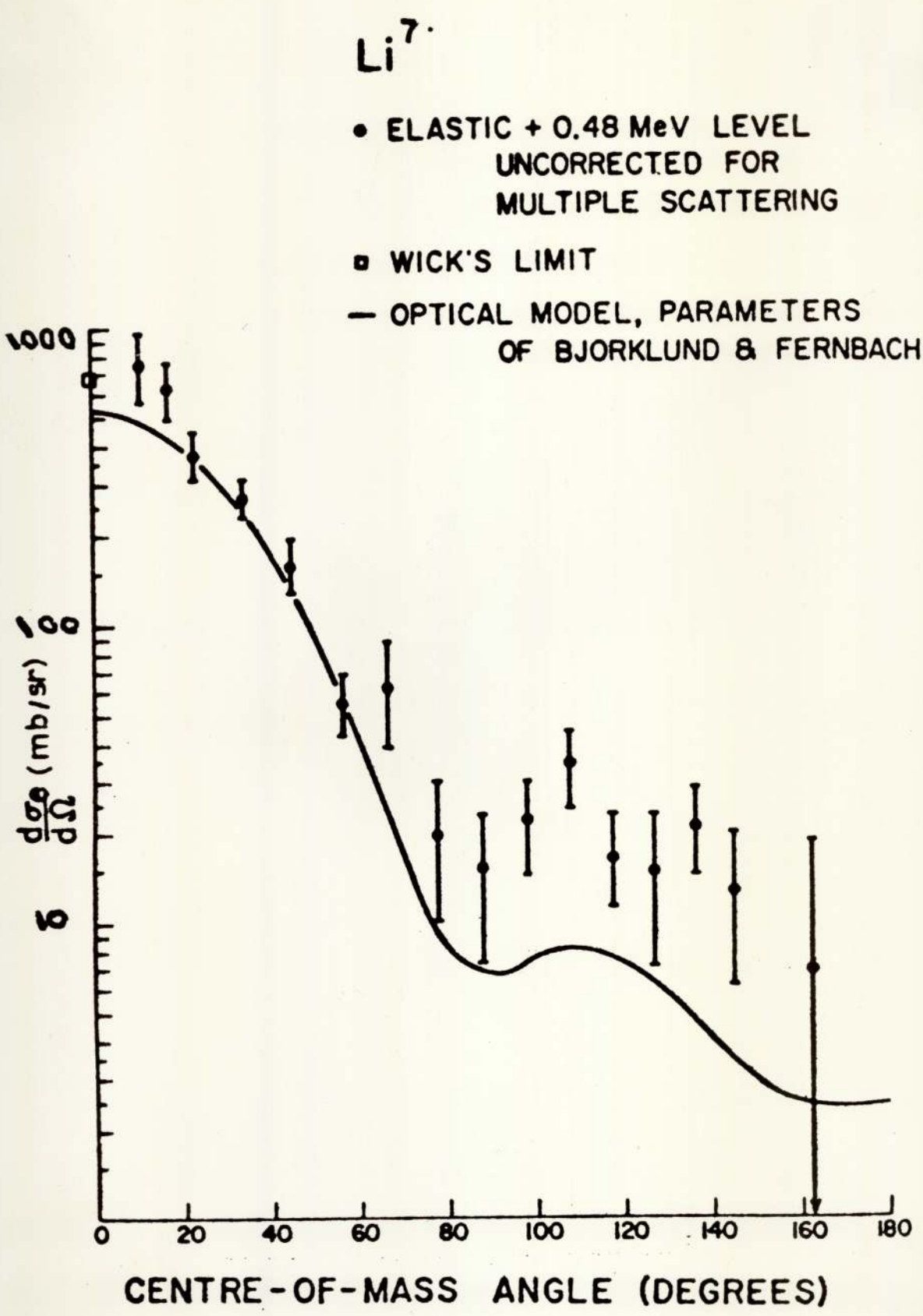

Figure 6.16. The Optical Model fit for ^{7}Li obtained by Armstrong et al.

Table 6.2

Optical Model Parameters used to fit Lithium Elastic Scattering Data

Parameter	Present Work
VR (MeV)	48.37
RR (fm)	1.356
AR (fm)	0.654
WD (MeV)	15.65
RD (fm)	1.278
AD (fm)	0.200
VS (MeV)	6.2
RS (fm)	1.01
AS (fm)	0.75
σ_R^{th} (mb)	473.3
σ_R^{ex} (mb)	531 $\pm$ 102
χ^2	< 0.3

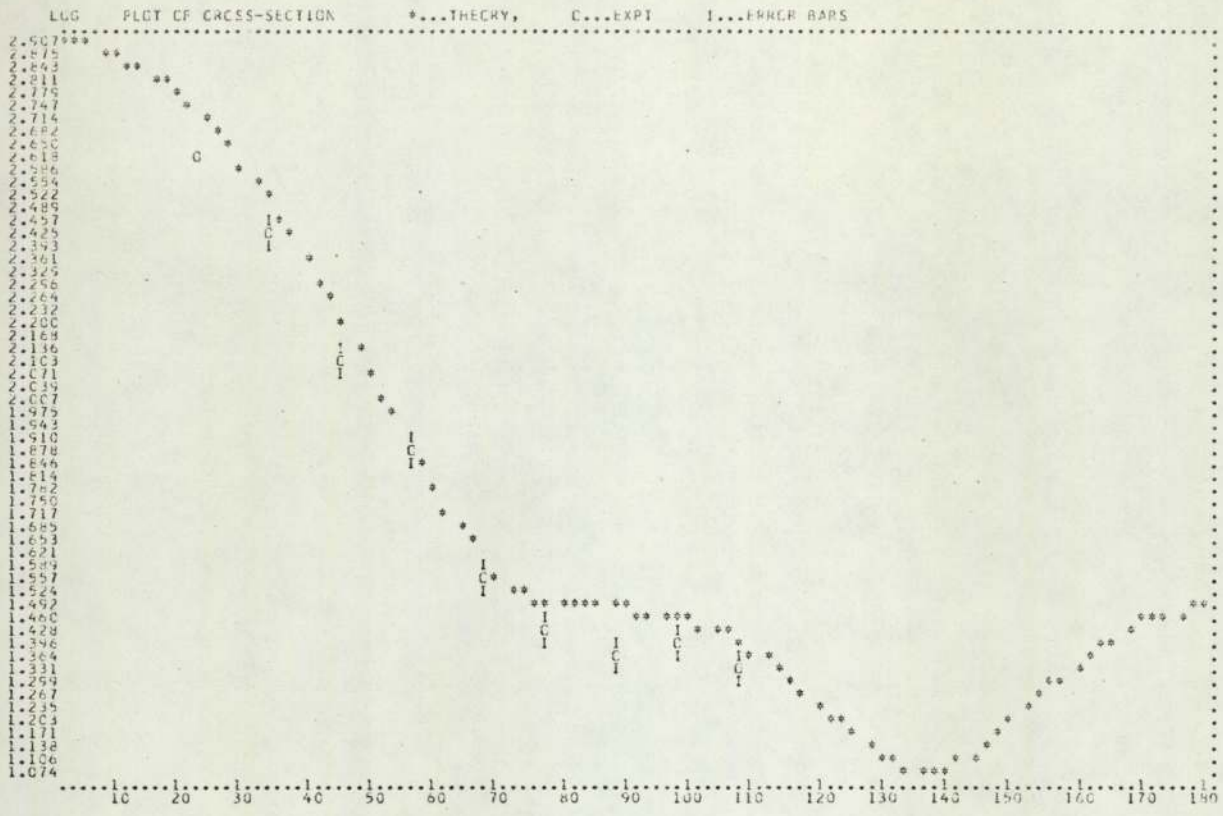

Centre of Mass Angle (Degrees)

Figure 6.17(a) VR, WV, RV,(6)

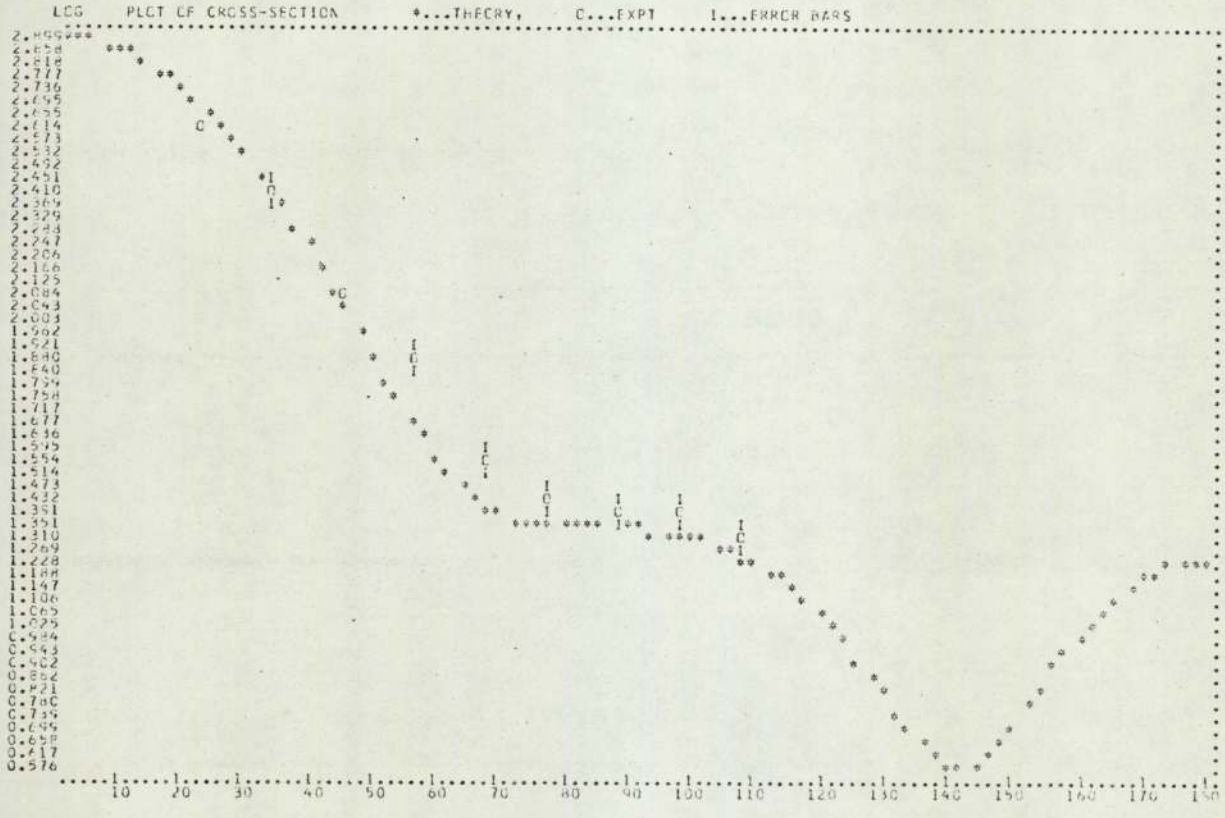

Centre of Mass Angle (Degrees)

Figure 6.17(b) VR, AR, WD, RD, AD, WV(10)

CHAPTER 7

Conclusions and Recommendations

The differential elastic scattering cross sections obtained in the present work for potassium at 14.1 MeV, using flat plate geometry, agree within experimental errors with those obtained by Frasca et al[8], using cylindrical geometry. The optical model with derivative surface absorption gives better agreement between theoretically predicted and experimentally determined values, ($\chi^2 < 0.3$), than the use of a Gaussian surface absorption form ($\chi^2 = 307$)[8]. In addition, the model predicts a value within experimental errors for the reaction cross section, showing that the model can successfully describe the elastic scattering from potassium.

The differential elastic scattering cross section measurements obtained for lithium, fall between the results of Wong et al[17], using the pulsed beam method, and Armstrong et al[16], using nuclear emulsions. Again, the use of the optical model with derivative surface absorption and the parameters of Becchetti and Greenlees[78], gives much better agreement with experimental data over the angular range 0° - 100° ($\chi^2 < 0.5$), than the use of a Gaussian surface form with the parameters of Bjorklund and Fernbach[81], as undertaken by Armstrong et al. In addition, the good agreement between the theoretically predicted and experimentally determined values of the reaction cross section for lithium, would indicate that for a light nucleus the use of the optical model is valid for the description of elastic scattering.

Although a good optical model fit was obtained for lithium in the present work, it would be unjustifiable to claim a completely successful analysis in view of the limited angular range examined. This could be remedied, however, by a repositioning of the existing accelerator facility in order to obtain measurements in the backward hemisphere.

This would require the development of one or two more time of flight systems, since the accumulation of data at the backward angles would be prohibitively slow in view of the very small differential cross sections predicted by optical model calculations.

An optical model analysis with the same parameter variation as that undertaken in section 6.6 should be sufficient to examine a complete angular distribution for lithium. An improvement on the reliability of the analysis could be made by using the method developed by Thomas and Burge[92]. Here, the quantity analysed is the difference in cross section from neighbouring nuclei, i.e.,

$$D(\theta) = \frac{\sigma_1(\theta) - \sigma_2(\theta)}{\sigma_1(\theta + \sigma_2(\theta)} \qquad \ldots\ldots 7.1$$

where the σ s are the differential cross sections and the subscripts refer to the two nuclei. This method eliminates many of the usual sources of statistical uncertainty and gives more accurate results.

In all future measurements, the determination of the relative sensitivity of the neutron detector as a function of energy could be determined more accurately using the triple coincidence method[12]. With the experimental arrangement described in section 5.5, the polyethylene sample is replaced by a sample of plastic scintillator coupled to a photomultiplier tube. Neutrons scattered by hydrogen in the scintillator produce an output pulse from the photomultiplier tube and complete the triple coincidence requirement when they are also registered by the neutron detector. The use of this method gives a negligible background, since scattering from carbon produces a negligible pulse from the scintillator, and the spectrum obtained is effectively from hydrogen alone.

The development of the associated particle time of flight spectrometer for use with the reaction $^2H(d,n)^3He$, shows that such systems

can be constructed on a reasonably economical basis, although its use for neutron scattering studies with existing facilities is limited by the low yield of neutrons obtainable with the 150 KeV incident deuteron energy available from the accelerator. However, the basic design of the system does form a useful starting point for the development of a system for use with the new Dynamitron facility, where higher incident deuteron energies are available for an increased neutron yield. In this case it would be an advantage to use a more restricted energy range of ^{3}He particles in order to obtain better time resolution in the coincidence spectrum.

Neutron elastic scattering data obtained for incident neutron energies of 2.5 - 4 MeV, would have to be corrected for compound elastic scattering contributions. Such a correction could be applied by assuming the compound elastic scattering, σ_{CE}, to be isotropic, and the formation of a quantity.

$$\sigma_{el}(\text{true}) = [\sigma_{exp} - \sigma_{CE}(\text{assumed})] \qquad \ldots\ldots 7.2$$

The numerical value of the assumed compound elastic scattering cross section would be dependent on the experimentally determined values, i.e., if these values range from several hundred millibarns per steradian at 20^{o}, down to 10 or 20 mb/st. at 90^{o} - 100^{o}, then as a starting point it would be feasible for the compound elastic scattering cross section to be 1 mb/st. An optical model analysis similar to that described in Chapter 6, with the same objects in mind, i.e., the optimisation of potentials and geometrical parameters, would give a best fit value for χ^{2}. The entire procedure should then be repeated with other assumed values of σ_{CE}, i.e., the values of σ_{CE} are, in effect, investigated by a grid search. A graph of χ^{2} per point versus σ_{CE} would then very nearly determine the true value of σ_{CE}.

With the experimentally determined differential cross sections

corrected for the optimum value of σ_{CE}, the entire analysis should then be repeated to obtain meaningful results.

APPENDIX A.1

**** REGULAR OPTICAL MODEL CALCULATION ****

DIFFERENTIAL ELASTIC SCATTERING POTASSIUM

ELAB = 14.100 MEV MI = 1.0087 AMU ZI = 0. K = 0.8040 H = 0.3731 F (N-Z)/A = 0.0256
MT = 38.9637 AMU ZT = 19. ETA = 0.0 R = 11.1943 F

ITERATION NO... 6 OF SEARCH... VR,WD,WV,(6)

PARAMETERS VARIED... VR,WD,WV
CHISQ(CROSS SECTION) = 1.8160D+02 = 2.0177D+01 PER POINT PREDICTED CROSS SECTION AVERAGED OVER 10.000 DEGREES
CHISQ(POLARISATION) = 0.0 = 0.0 PER POINT PREDICTED POLARISATION AVERAGED OVER 10.000 DEGREES
CHISQ(REACTION XSEC) = 5.1175D+00
CHISQ(TOTAL) = 1.8672D+02 = 1.8672D+01 PER POINT

						R.A**1/3	M.S.RAD	R.M.S.RAD	JD,JR	JT
	PARAMETER VALUES									
VR = 51.3005	RR = 1.1700	AR = 0.7500				3.966	17.184	4.145	461.589	0.0
WV = 0.7284	RV = 1.2600	AV = 0.5800				4.272	23.323	4.829	144.322	
WD = 9.5551	RD = 1.2600	AD = 0.5800				4.272				
VS = 6.2000	RS = 1.0100	AS = 0.7500				3.424	17.234	4.151	13.605	
WS = 0.0										
	RC = 0.0	AC = 0.0				0.0	0.0	0.0		

EXPERIMENTAL REACTION CROSS SECTION = 0.1200D+04 MB
EXPERIMENTAL ERROR = 0.7200D+02 MB
THEORETICAL REACTION CROSS SECTION = 0.1363D+04 MB

**** REGULAR OPTICAL MODEL CALCULATION ****

DIFFERENTIAL ELASTIC SCATTERING LITHIUM

ELAB = 14.100 MEV MI = 1.0087 AMU ZI = 0. K = 0.7211 H = 0.4160 F (N-Z)/A = 0.1429
MT = 7.0160 AMU ZT = 3. ETA = 0.0 R = 9.5684 F

ITERATION NO... 6 OF SEARCH... VR,WD,WV,(6)

PARAMETERS VARIED... VR,WD,WV
CHISQ(CROSS SECTION) = 1.3585D+02 = 1.5094D+01 PER POINT PREDICTED CROSS SECTION AVERAGED OVER 10.000 DEGREES
CHISQ(POLARISATION) = 0.0 = 0.0 PER POINT PREDICTED POLARISATION AVERAGED OVER 10.000 DEGREES
CHISQ(REACTION XSEC) = 9.2984D-01
CHISQ(TOTAL) = 1.3678D+02 = 1.3678D+01 PER POINT

						R.A**1/3	M.S.RAD	R.M.S.RAD	JD,JR	JT
	PARAMETER VALUES									
VR = 48.3530	RR = 1.1700	AR = 0.7500				2.240	10.714	3.273	660.818	0.0
WV = 2.9801	RV = 1.2600	AV = 0.5800				2.412	10.697	3.271	230.903	
WD = 6.7401	RD = 1.2600	AD = 0.5800				2.412				
VS = 6.2000	RS = 1.0100	AS = 0.7500				1.934	9.120	3.020	43.749	
WS = 0.0										
	RC = 0.0	AC = 0.0				0.0	0.0	0.0		

EXPERIMENTAL REACTION CROSS SECTION = 0.5310D+03 MB
EXPERIMENTAL ERROR = 0.1020D+03 MB
THEORETICAL REACTION CROSS SECTION = 0.6294D+03 MB

REFERENCES

1. H.A. Bethe, Phys. Rev., 47, 747, (1935).
2. N. Bohr, Nature, 137, 344, (1936).
3. R.E. Le Levier and D.S. Saxon, Phys. Rev., 87, 40, (1952).
4. H. Feshbach, C.E. Porter, and V.F. Weisskopf, Phys. Rev., 96, 448, (1954).
5. J.M. Blatt and V.F. Weisskopf. "Theoretical Nuclear Physics." Wiley & Sons, 1952.
6. P.E. Hodgson. "Nuclear Reactions and Nuclear Structure." Oxford University Press, 1971.
7. S. Fernbach, R. Serber, and T.B. Taylor, Phys. Rev., 75, 1352, (1949).
8. A.J. Frasca et al. Phys. Rev., 144, 854, (1966).
9. W.G. Cross and R.G. Jarvis, Nucl. Phys., 15, 155, (1960).
10. W.J. McDonald and J.M. Robson, Nucl. Phys., 59, 321, (1965).
11. K. Tesch, Nucl. Phys., 37, 412, (1962).
12. R. Bouchez, J. Duclos, and P. Perrin, Nucl. Phys., 43, 628, (1963).
13. R.L. Cassola and R.D. Koshel, Bull. Am. Phys. Soc., 12, 212 C3, (1967).
14. M.P. Nakada et al. Phys. Rev., 110, 1439, (1958).
15. R.W. Bauer, J.D. Anderson, and L.J. Christensen, Nucl. Phys., 47, 241, (1963).
16. A.H. Armstrong et al. Nucl. Phys., 52, 505, (1964).
17. C. Wong, J.D. Anderson, and J.W. McClure, Nucl. Phys., 33, 680, (1962).
18. RAROMP. (Regular And Reformulated Optical Model Programme). G.J. Pyle.
19. Nuclear Enterprises Ltd., Catalogue, 1970.

20. J.B. Marion and J.L. Fowler. "Fast Neutron Physics, Part I." Interscience Publishers, Inc., New York, 1960.

21. H.H. Barshall and M.H. Kanner, Phys. Rev., 58, 590, (1940).

22. Wilmot N. Hess, Rev. Mod. Phys., 30, 368, (1958).

23. J.B. Birks, Proc. Phys. Soc., (London), 64A, 874, (1951).

24. H.C. Evans and E.H. Bellamy, Proc. Phys. Soc., (London), 74, 483, (1959).

25. M. Rich and R. Madey. Range Energy Tables, UCRL. 2301 (1954).

26. Philips Ltd., Technical Data Memo.

27. R. W. Engstrom et al. Nucleonics, 10, 58, (1952).

28. R. Connor and M. Hussain, Nucl. Instr. and Methods, 6, 337, (1960).

29. P.A. Tove, Rev. Sci. Instr., 27, 143, (1956).

30. J.B. Ashe, J.D. Hall, and I.L. Morgan, Rev. Sci. Instr., 37, 1559, (1966).

31. J.C. Hopkins, J.T. Martin, and J.D. Seagrave, Nucl. Instr. and Methods, 56, 175, (1967).

32. L.W. Alvarez, Phys. Rev., 54, 486, (1938).

33. G.E.F. Fertel, P.B. Moon, G.P. Thompson, and C.E. Wynn-Williams, Nature, 142, 829, (1938).

34. J.M.W. Milatz and D. Th. J. ter Horst, Physica, 5, 796, (1938).

35. L. Cranberg and J.S. Levin, Phys. Rev., 100, 435, (1955).

36. G.K. O'Neill, Phys. Rev., 95, 1235, (1954).

37. D.E. Baynham, Ph.D. Thesis, University of Aston in Birmingham (1971).

38. D.L.E. Smith, AWRE Report No. O - 52/67, (1967).

39. G. Dearnaley and A.B. Whitehead, Nucl. Instr. and Methods, 12, 205, (1961).

40. W. Whaling, Handbuch der Physik, Vol. XXXIV, 193. Springer Verlag, (Berlin).

41. C.J. Oliver, B. Collinge, and G. Kaye, Nucl. Instr. and Methods, 50, 109, (1967).

42. R. McFadden, P.W. Martin, and B.L. White, Nucl. Instr. and Methods, 92, 563, (1971).

43. D.G. Schuster, Nucl. Instr. and Methods, 76, 35, (1969).

44. W. Franzen, P. Huber, and L. Schellenberg, Z. Naturforsch, 10a, 820, (1955).

45. W.R. Dixon and J.H. Aitken, Nucl. Phys., 24, 456, (1961).

46. R.A.I. Bell, N.G. Chapman, and P.B. Johnson, Nucl. Instr. and Methods, 33, 13, (1965).

47. L.F.C. Monier, G.E. Tripard, and B.L. White, Nucl. Instr. and Methods, 45, 282, (1966).

48. V. Naggiar, L. Lafaye, and P. Breonce, Nucl. Instr. and Methods, 41, 77, (1966).

49. C.M. Bartle et al. Nucl. Instr. and Methods, 63, 39, (1968).

50. L.W. Put et al. Physica, 32, 1397, (1966).

51. E.M. Gunnersen and G. James, Nucl. Instr. and Methods, 8, 173, (1960).

52. J.D.L.H. Woods and E.W. Saker, Private Communication and SERL Technical Report M.61, (1958).

53. S.K. Allison and S.D. Warshaw, Rev. Mod. Phys., 25, 779, (1953).

54. S.D. Warshaw, Phys. Rev., 76, 1759, (1948).

55. E. Segre. "Experimental Nuclear Physics, Vol.I." Wiley & Sons, 1953.

56. A. Dalgarno and G.W. Griffing, Proc. Phys. Soc., (London), 232A, 423, (1955).

57. J.A. Phillips, Phys. Rev., 90, 532, (1953).

58. H.K. Reynolds et al. Phys. Rev., 92, 742, (1953).

59. W.R. Arnold et al. Phys. Rev., 93, 483, (1954).

60. W. Wenzel and W. Whaling, Phys. Rev., 88, 1149, (1952).

61. J.D. Seagrave. LAMS Report No. 2162, (1958).

62. P.L. Okhuysen et al. Rev. Sci. Instr., 29, 982, (1958).

63. J. Benveniste and J. Zenger, UCRL. 4266 (1954).

64. M. Walt, "Fast Neutron Physics, Part II." J.B. Marion and J.L. Fowler, Interscience Publishers, Inc., New York, 1963.

65. R.B. Day, Phys. Rev., 102, 767, (1956).

66. K. Nishimura, K.O. Kano, and S. Kikuchi, Nucl. Phys., 70, 421, (1965).

67. D.L. Allen and M.J. Poole, Proc. Phys. Soc.,(London), A204, 500, (1951).

68. H.V. Argo et al. Phys. Rev., 87, 612, (1952).

69. C.D. Schrader et al, Nucl. Instr. and Methods, 7, 306, (1960).

70. Neutron Cross Sections, BNL. 325 (1964) Supplement No.2.

71. J.D. Seagrave, Phys. Rev., 97, 957, (1955).

72. J.C. Allred, A.H. Armstrong and L. Rosen, Phys. Rev., 91, 90, (1953).

73. J. Topping. "Errors of Observation and their Treatment." The Institute of Physics and the Physical Society Monograph.

74. J.A. Cookson, D. Dandy, and J.C. Hopkins, Nucl. Phys., 91, 273, (1967).

75. V.N. Whittaker, Department of Metallurgy, The University of Aston in Birmingham. Private Communication.

76. F. Perey and B. Buck, Nucl. Phys., 32, 353, (1962).

77. D. Wilmore and P.E. Hodgson, Nucl. Phys., 55, 673, (1964).

78. F.D. Becchetti and G.W. Greenlees, Phys. Rev., 189, 1190, (1969).

79. R.D. Woods and D.S. Saxon, Phys. Rev., 95, 577, (1954).

80. P.E. Hodgson. "The Optical Model of Elastic Scattering." Oxford University Press, 1963.

81. F. Bjorklund and S. Bernbach, Phys. Rev., 109, 1295, (1958).

82. G.J. Pyle and G.W. Greenlees, Phys. Rev., 181, 1444, (1969).

83. G.J. Pyle, G.W. Greenlees and Y.C. Tang, Phys. Rev., 171, 1115, (1968).

84. W.R. Gibbs, Bull. Amer. Phys. Soc., 11, 43, (1966).

85. J.S. Nodvik, C.B. Duke, and M.A. Melkanoff, Phys. Rev., 125, 975, (1962).

86. G.W. Hoffman and W.R. Coker, Phys. Rev. Lett., 29, 227, (1972).

87. J.D. Carlson, D.A. Lind, and C.D. Zafiratos, Phys. Rev. Lett., 30, 99, (1973).

88. R.L. Cassola and R.D. Koshel, Nuovo Cimento, 53B, 363, (1968).

89. "Methods in Computational Physics". Edited by B. Alder, S. Fernbach, and M. Rotenberg, Vol. 6. Academic Press 1966.

90. J.H. Coon, E.R. Graves, and H.H. Barshall, Phys. Rev., 88, 562, (1952).

91. G.J. Pyle, Private Communication.

92. G.L. Thomas and E.J. Burge, Nucl. Phys., 128, 545, (1969).